Acoustical Physics, Vol. 47, No. 4, 2001, pp. 371–375. Translated from Akusticheskiĭ Zhurnal, Vol. 47, No. 4, 2001, pp. 437–441.
Original Russian Text Copyright © 2001 by Averbakh, Artel'nyĭ, Bogolyubov, Zaslavskiĭ, Kukushkin, Lebedev, Maryshev, Postoenko, Talanov.

Seismoacoustic Survey of Artificial Inhomogeneities in the Ground

V. S. Averbakh, V. V. Artel'nyĭ, B. N. Bogolyubov, Yu. M. Zaslavskiĭ, V. D. Kukushkin,
A. V. Lebedev, A. P. Maryshev, Yu. K. Postoenko, and V. I. Talanov

Institute of Applied Physics, Russian Academy of Sciences,
ul. Ul'yanova 46, Nizhni Novgorod, 603600 Russia
e-mail: zaslav@hydro.appl.sci-nnov.ru

Received August 7, 2000

Abstract—The results of processing the field test data obtained for the seismoacoustic system designed at the Institute of Applied Physics of the Russian Academy of Sciences for the visualization of underground engineering structures are presented. The described experiment is the first demonstration of the use of a high-power, high-stability transmitting–receiving system for producing a coherent insonification with a frequency of 195 Hz. The receiving element of the system is a synthetic aperture array. With the use of focusing as a method of the final signal processing, an image of a tunnel lying at a depth of 30 m is obtained in three spatial cross-sections, which demonstrates the possibility of a three-dimensional, coherent, high-frequency seismic survey of engineering structures. © *2001 MAIK "Nauka/Interperiodica".*

Along with the conventional problems facing the engineering seismic survey, the problem of the detection of artificial inhomogeneities in shallow layers is quite topical. It explains the permanent interest to the development of new approaches to finding structural anomalies [1] and to monitoring the geological medium in both quiet and seismically active regions [2–5]. In this paper, we present the results of the experiments on the seismoacoustic survey with the use of highly stable acoustic fields in combination with the methods of coherent signal processing. This work is the first step toward the development of a system of acoustic visualization of natural and artificial underground inhomogeneities and, in prospect, toward the development of a system for seismoacoustic tomography of the Earth's shallow structure.

Now, we briefly describe the geological conditions at the experimental site and the main features of the transmitting-receiving system. The field experiments were carried out at a testing ground near Obninsk, Kaluga region, in November–December 1997. The object of investigation was a tunnel with a cross-section of 2×3 m^2 lying at a depth of 30 m. The data obtained in a borehole located at a distance of 200 m from the tunnel provide evidence that, with an increase in depth from 0 to 40 m, the velocity of P waves grows from 500 to 1800 m/s, and the depths from 25 to 40 m correspond to a limestone layer subjected to karst processes.

The radiator was designed on the basis of an electromagnetic hydroacoustic transducer mounted in a metal cylindrical container whose diameter and height were equal to 1.5 m. The container was buried in the ground and filled with water. According to the results of the previous papers [6, 7], in this case the surface waves are only weakly excited by the acoustic source, and the acoustic energy is about evenly divided between P and S waves. At a frequency of 195 Hz, the source radiated about 100 W of acoustic power. A rubidium frequency standard was used as the primary generator, which determined the radiating signal and was also used in the receiving channel to provide the synchronization of the processes of radiation and recording. For receiving, we used accelerometers with a sensitivity of 100 mV/ms^{-2}; their output signal was amplified, filtered, and fed to a 16-bit A/D-converter, which made it possible to obtain a high signal-to-noise ratio. The measurement of the seismoacoustic field was performed for two rectilinear profiles, the positions of which are shown in Fig. 1. In this figure, the layout of the investigated area is presented with a cross array and the projection of the central axis of the main tunnel and its branches on the Earth's surface (the coordinates are given in meters). The following designations are used: the source of the signal (with the coordinates (0, 0)) is denoted by the dotted empty circle, the tunnel at a depth of 30 m is denoted by full circles, and the receiving array is denoted by two intersecting straight lines.

The first profile is almost perpendicular to the tunnel and has a longitudinal displacement of 12 m relative to the source. Its length was 45 m, and the measurements along it were performed with a step of 0.5 m. The second profile is parallel to the tunnel. This profile was investigated with a step of 1 m. Because of the high stability of radiation and reception, it was found to be possible to survey along both profiles by successive repositioning of a single geophone while retaining the locking to the phase at the carrier frequency, which

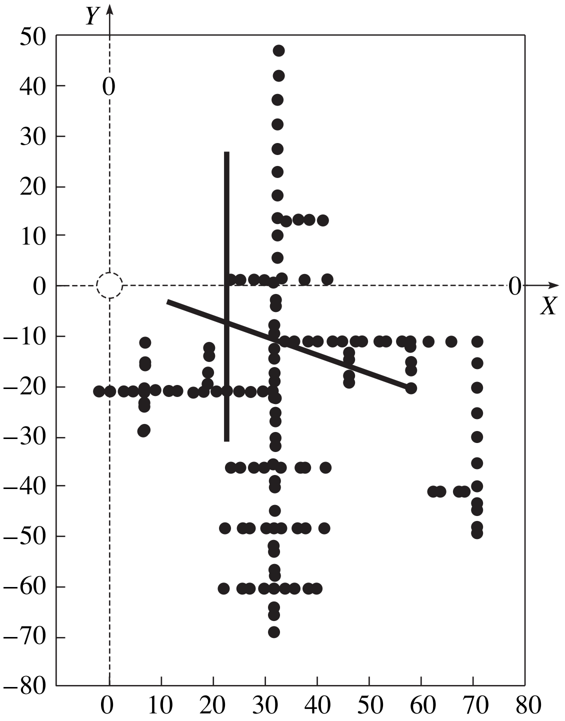

Fig. 1. Schematic representation of the tunnel (full circles) and the positions of the seismic source (empty circle) and the receiving array (intersecting solid lines).

provided the possibility of the following coherent processing, i.e., of synthesizing a cross array. Travelling along both profiles with recording at every point of reception was carried out with a fixed position of the source (see Fig. 1). For an additional increase in the signal-to-noise ratio of the sounding signals, the coherent accumulation of 64 pulses with durations of 10 periods each and with the carrier frequency 195.31 Hz was performed. The pulse duration ratio was equal to 25. The records spoiled by the malfunction of equipment or by an increase in the level of seismic noise were rejected and replaced by the records obtained in repeated cycles of measurements.

The result of recording the initial signal received by transverse and longitudinal arms of the array is given in the form of brightness pictures in Figs. 2a and 2b. In these figures, the vertical axis corresponds to the time-base of the oscillogram and the horizontal axis corresponds to the number of the measuring point along the profile (the steps of space quantization are 0.5 and 1 m). The level of the signal is represented by the intensity of the black color on the light background; the full dynamic range of the signal level variation is 40 dB. The observation of the phase variation clearly seen in Fig. 2 is possible only owing to the use of the highly stable seismic radiator in the experiment. The constant slope of the phase variation gives the values of the apparent velocity of waves: 460 m/s for the initial part of the profile and 630 m/s for its terminal part. In the middle of the profile, it is easy to see the presence of strong phase fluctuations testifying to the interference of many types of waves that contribute to the total seismic response. From the view of the wave field displayed in the figures, it is impossible to make an unambiguous conclusion about the presence or absence of any anomalies at the depths comparable with the horizontal dimensions of the area under study.

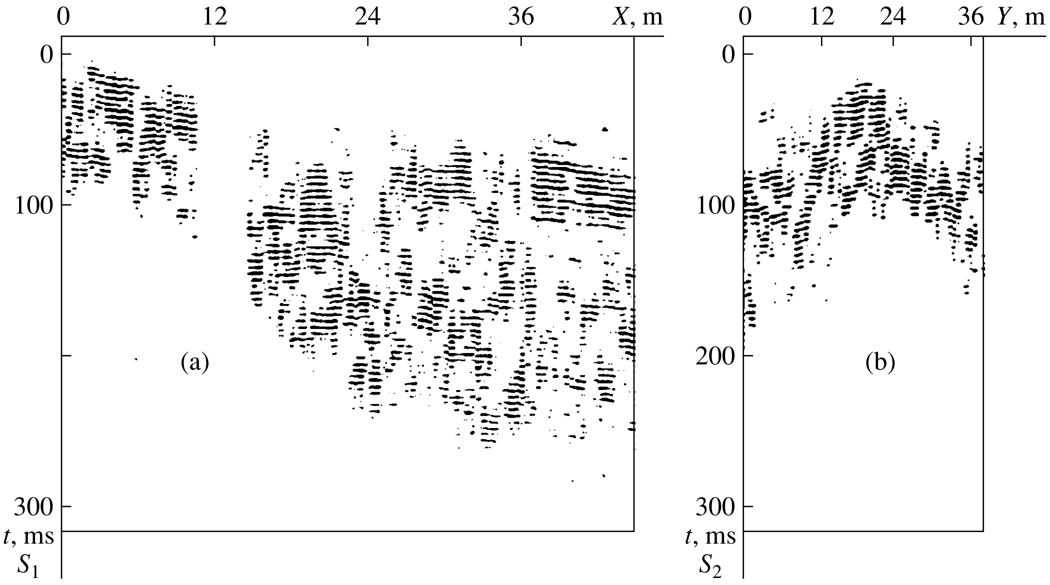

Fig. 2. Equiphase lines for the (a) transverse and (b) longitudinal arms of the array.

The total number of spatial points to which the array was focused in solving the three-dimensional problem was equal to 130 × 90 × 40, the bandwidth was 40 Hz, and the number of the frequency readings was 27. All this forms the whole set of data. From the formal point of view, the acoustical reconstruction of the image of the inhomogeneous medium can be considered as a matched signal reception from multiple scatterers with the coordinates $\mathbf{r}_m = (x, y, z)_m$. The model of the main signal arrival received by the array is described as

$$S_p(t) = \sum_m A_m S_0(t - \tau(\mathbf{r}_s, \mathbf{r}a_p, \mathbf{r}_m)),$$

where p is the index of the array element (receiver); $\mathbf{r}_s$, $\mathbf{r}a_p$, and $\mathbf{r}_m$ are the coordinates of the radiator, receivers, and scatterers, respectively; S_0 is the radiated (reference) signal accurate to the amplitude-frequency distortion due to the attenuation and excitation of waves of the useful type; and τ is the time delay of the received signals. The algorithm of the acoustic image reconstruction maximizes the energy of signals received in the form of scattered waves from every point of space, including the unknown coordinates of actual scatterers

$$FS(\mathbf{r}) = \left|\sum_p \int_{t \in \tau_u} S_0^*(t - \tau_0(\mathbf{r}_s, \mathbf{r}a_p, \mathbf{r}_m))S_p(t)dt\right|^2 \quad (1)$$

or, in the frequency form,

$$FS(\mathbf{r}) = \left|\sum_p \sum_{f_0 - \frac{\Delta f}{2}}^{f_0 + \frac{\Delta f}{2}} X_p(f)X_0^*(f)\exp(2i\pi f\tau_0(\mathbf{r}_s, \mathbf{r}a_p, \mathbf{r}_m))\right|^2, \quad (2)$$

where τ_u is the duration of the signal; $X_p(f)$ and $X_0(f)$ are the Fourier spectra of the signal at the array and of the reference signal, respectively; f_0 and Δf are the carrier frequency and the bandwidth of the signal; and τ_0 is the trial delay.

For lack of reliable information about the depth dependence of the elastic parameters of the medium, as a zeroth approximation, it is possible to use a homogeneous model for which the following relation is valid: $\tau_0 = (|\mathbf{r} - \mathbf{r}a_p| + |\mathbf{r} - \mathbf{r}_s|)/MC$, where MC is the mean velocity of propagation. The mean velocity can be obtained by maximizing the functional

$$Q = \max_{MC}\left[\frac{\max(FS_{12})_r}{MC(FS_{12})_r}\right],$$

where the subscripts 1 and 2 correspond to the perpendicular arms of the array and $MC(FS_{12})$ is the median of the amplitude distribution of the focusings taken over the whole space of focusings

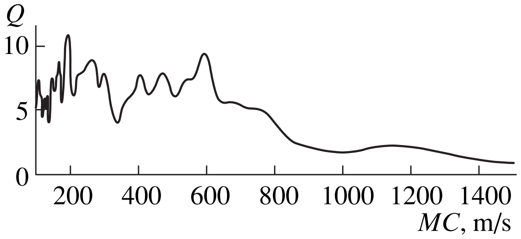

Fig. 3. Criterion Q as a function of the propagation velocity of the seismic wave.

$$FS_{12}(\mathbf{r}) = \left|\sum_f \sum_{p_2} \sum_{p_2} X_{1p_1}(f)X_{2p_2}^*(f)|X_0(f)|^2 \times \exp\left(i2\pi f\frac{|\mathbf{r} - \mathbf{r}a_{1p_1}|}{MC}\right)\exp\left(-i2\pi f\frac{|\mathbf{r} - \mathbf{r}a_{2p_2}|}{MC}\right)\right|^2.$$

The maximum-to-median ratio Q is one of the criterions of the contrast, because the median gives the mean probable level of the background of the image and the peaks are additionally maximized when the mean velocity is chosen correctly [8]. Figure 3 presents the plot of the criterion Q as a function of the mean velocity. One can see several maximums, which correspond to the velocities 200, 340, 480, 580, and 1200 m/s. Only the value 580 m/s was later used for focusing.

We now consider the results of focusing on the basis of Eqs. (1) and (2). Figure 4a shows the image of the tunnel cross-section in the XY plane at a depth of 30 m, and Fig. 4b shows the tunnel cross-section in the XZ plane at the point $Y_0 = 10$ m. The YZ cross-section of the tunnel for $X_0 = 30$ m is given in Fig. 4c. The light regions of the black and white representation of the image correspond to the higher level of the scattered field and reveal the outline of the main shaft of the tunnel and some of its branches. The maximal difference in the signal levels represented by light and dark regions of the monochrome images in Fig. 4 is 40 dB. The incomplete visualization of the details of the structure is related to their shielding by the main body of the tunnel with the given location of the source, or to increased distances from the receivers and scatterers to the source. However, the visualization system implies signal radiation from several source positions, which will later make it possible to obtain fuller and more detailed images. As a whole, the obtained set of the tunnel cross-sections provides a qualitative picture of the tunnel structure. One should note the correct values obtained for the coordinates of the reference points of the structure, although some distortions are also

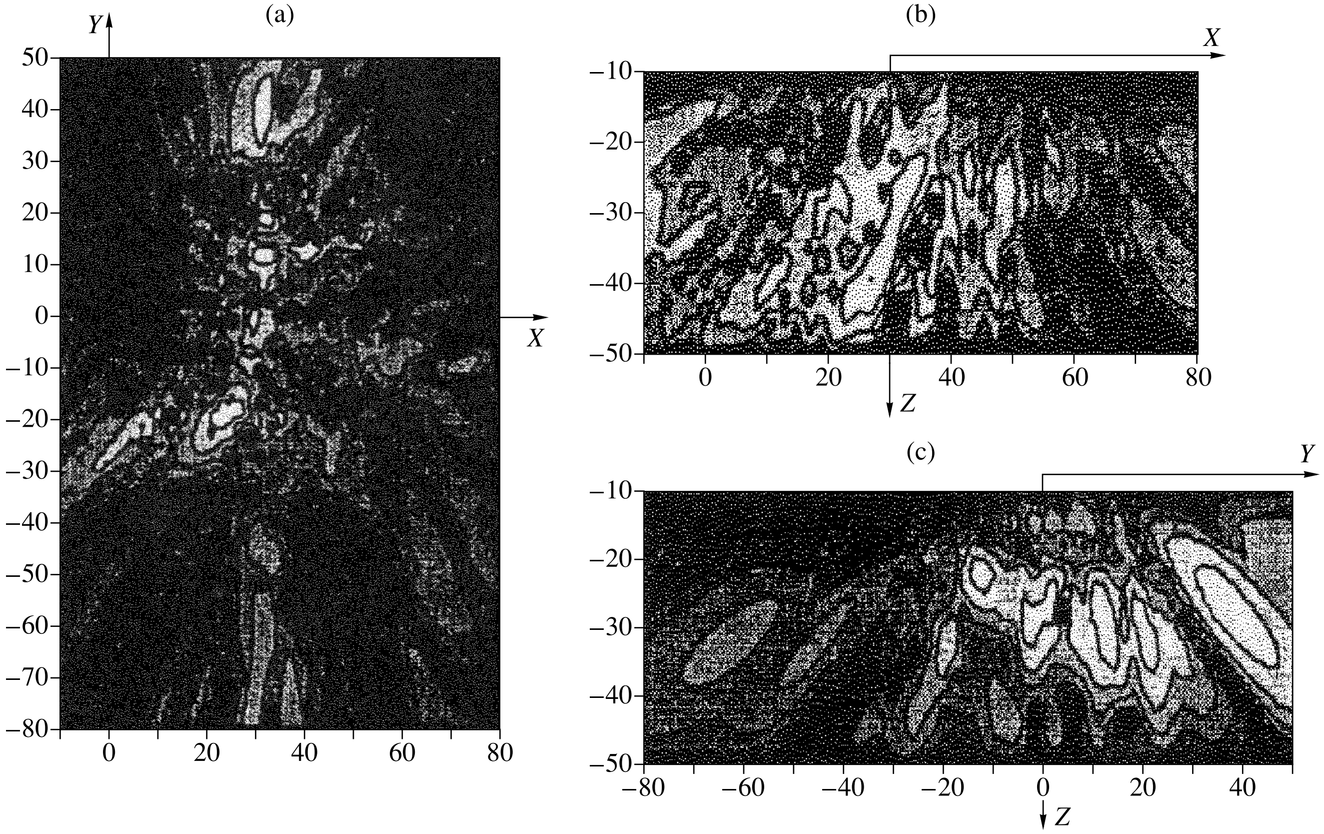

Fig. 4. Brightness image of the tunnel cross-sections (the ratio of the levels of the black to white background is 40 dB): (a) in the *XY* plane at the depth 30 m, (b) in the *XZ* plane at the point Y_0 = 10 m, and (c) in the *YZ* plane at the point X_0 = 30 m.

observed; for instance, the scale along *Y* axis in the *XY* cross-section is distorted because of the finiteness of the array aperture and the scattering by inhomogeneities in the medium near the Earth's surface.

Summarizing the results of the experiments, we can conclude that the use of a single buried source of vibrations (of the pressure center type) with the seismoacoustic radiation power reaching several tens of watts makes it possible to create a coherent, high-frequency seismic field in the region of the Earth's medium within the radius 60–70 m and within the depth of the same order of magnitude. The bistatic arrangement of the source and the receiving array (a synthetic cross-shaped aperture) allows one to obtain initial data on the seismic signal scattered by an artificial inhomogeneity (a tunnel at a depth of 30 m) and arriving together with the reverberation noise transferred by the set of additively excited bulk and surface waves of various types. In the course of secondary processing of the recorded signals with the use of the method of focusing, it proves to be possible to select the desired scattered signal on the background of the interfering reverberation field and to reconstruct the image of three spatial cross-sections of the underground engineering structure. The comparison with the experimental data obtained for a monostatic source–receiver arrangement shows the way for further improvement of the quality of the inhomogeneity image in seismic waves by selecting a rational arrangement of the source–array system. In particular, it is expedient to place the primary source of a coherent seismic field between the transducers forming the receiving array. The necessity of using a number of positions for the source of vibrations is obvious. The advantage of employing high seismic frequencies about several hundreds of hertz should also be noted. The accuracy of the localization of engineering structures several tens of meters underground is within one to two meters along the horizontal and vertical axes.

ACKNOWLEDGMENTS

This work was supported by the Ministry of Science and Technologies of the Russian Federation (contract no. 4 of March 14, 1997) and by the Russian Foundation for Basic Research (project no. 99-02-16957), and the Leading Scientific School Support Program (grant no. 96-15-96592).

The authors are grateful to A.V. Nikolaev for the interest taken in this work.

REFERENCES

1. C. H. Frazier, N. Cadalli, D. C. Munson, Jr., and W. D. O'Brien, Jr., J. Acoust. Soc. Am. **108**, 147 (2000).
2. W. J. Stephenson, R. B. Smith, and J. R. Pelton, J. Geophys. Res. B **98**, 8211 (1993).
3. R. D. Miller, W. Don Steeples, and P. B. Myers, GSAB **102**, 18 (1990).
4. R. D. Miller, W. Don Steeples, and M. Brannan, Geophysics **54**, 1528 (1989).
5. E. Kozlov, J. Bouska, D. Medvedev, and A. Rodenko, Geofizika, No. 6, 3 (1998).
6. V. S. Averbakh and Yu. M. Zaslavskiĭ, Fiz. Zemli, No. 12, 1 (1997).
7. A. V. Lebedev and A. M. Sutin, Akust. Zh. **42**, 812 (1996) [Acoust. Phys. **42**, 716 (1996)].
8. N. N. Puzyrev, *Temporal Fields of Reflected Waves and the Effective Parameter Method* (Nauka, Novosibirsk, 1979).

Translated by A. Svechnikov

Acoustical Physics, Vol. 47, No. 4, 2001, pp. 376–383. Translated from Akusticheskiĭ Zhurnal, Vol. 47, No. 4, 2001, pp. 442–450.
Original Russian Text Copyright © 2001 by Alekseev, Andreev, Romanenko, Rybak.

Study of the Cavitation Region and the Evolution of the Acoustic Spectrum

V. N. Alekseev*, V. G. Andreev, G. A. Romanenko**, and S. A. Rybak***
** Andreev Acoustics Institute, Russian Academy of Sciences, ul. Shvernika 4, Moscow, 117036 Russia*
*** Moscow State University, Vorob'evy gory, Moscow, 119899 Russia*
e-mail: bvp@akin.ru

Received September 8, 2000

Abstract—An experimental setup and a technique for measuring the transient period before a stationary cavitation in a liquid by the evolution of the cavitation noise spectrum are described. The time dependences of harmonic amplitudes both near the radiator and outside the cavitation region are presented. From the form of these dependences, the characteristic transient periods preceding the stage of a fully developed cavitation in water and in transformer oil are calculated. A formal scheme for describing the cavitation region is proposed. *© 2001 MAIK "Nauka/Interperiodica".*

Unlike the description of the behavior of a single bubble in a sound field, the study of the cavitation process by describing this phenomenon as a whole presents certain difficulties. Already for many years, the dynamics of single cavities had been much studied both experimentally and theoretically [1–3]. A whole set of approximate equations were derived for describing the behavior of bubbles of different nature, and practically no considerable discrepancies were obtained between theoretical and experimental results [1]. Although the studies of the dynamics of isolated cavities are very important for the understanding of the cavitation process as a whole, there is still no complete formal description of the cavitation region. A limited number of theoretical papers describing various features of the cavitation region can be found in the literature, and the pioneering work by Rozenberg [4] must be mentioned among them. Starting from the times of Blake and Willard who proposed several descriptive models of the cavitation process, many researchers had been particularly interested in the problem of the transient period of cavitation. The determination of the characteristic transient periods preceding the stage of fully developed cavitation in fluids is of fundamental significance for the choice of optimal regimes in technologies using ultrasonic cavitation [5, 6]. This is especially important to sonochemistry for the initiation of fast chemical reactions that have several stages [7]. Rapid photography is the best-known method used for the investigation of the process of the development of a cavitation region. The initiation and development of cavitation was recorded by Sirotyuk with the help of an SFR superfast camera [8]. The cavitation was observed in water, in the focus of an acoustic concentrator operating at a frequency of 500 kHz. It was found that, in the case of the intensities used, the time of the cavitation region formation in the concentrator focus was 15–45 periods of ultrasonic oscillations. A similar experiment was performed by Akulichev [9] who studied the initiation and development of a cavitation region in the focus of a low-frequency (15 kHz) radiator. The process of the development was recorded using an SSKS-3 motion-picture camera with a recording speed of 200000 frames per second, which provided an opportunity to investigate in detail the behavior of a single bubble within a single period and within many periods. The number of cavitation bubbles increased from period to period and reached saturation approximately after 10 periods.

However, such a technique can be used only in transparent liquids and, what is most important, it allows one to determine only the time of the formation of the cavitation region, but not the transient period for the stationary cavitation regime. As our measurements have demonstrated, these times differ essentially. Here, we investigate the evolution of the spectrum of cavitation noise and make a conclusion about the transient process preceding the regime of stationary cavitation on the basis of the form of the time dependences of harmonic amplitudes. Some modern representations used for describing a cavitation region, which may be useful to explain the experimental data, are given in the last part of the paper.

The excitation of the cavitation in our experiments was performed by an ultrasonic generator (Fig. 1). An industrial ultrasonic generator of the UZGZ-4 type with a power of 4 kW and a frequency of 18 kHz was used to feed a PMS 15A-18 magnetostrictive transducer. The magnetostrictive transducer was equipped with a dumbbell-shaped titanium radiator. Its dumbbell shape provided an opportunity to obtain an increase in the amplitude of end vibrations by a factor of 1.5–2, while the area of the radiating surface remained the same. The end of the radiator was immersed in a plexiglas basin with the dimensions 400 × 63 × 63 mm. The inlet aperture of the basin had the diameter slightly exceeding the diameter of the radiator end, which provided an opportunity to reduce capture of air from the liquid surface in the cavitation regime. The basin was filled with the liquid under investigation. We used settled boiled water and transformer oil with a higher cavitation strength compared to water. A spherical hydrophone with diameter 7 mm and the resonance frequency 230 kHz was used to measure the field of acoustic pressure in the basin. The hydrophone size was small relative to the ultrasonic wavelength $\lambda = 8.3$ cm. Therefore, its presence almost did not disturb the structure of the sound field. On the other hand, it was sufficiently large to measure the average field caused by the collapse of many bubbles near its surface. Its high resonance frequency provided the opportunity to detect the first 8–10 harmonics of the fundamental frequency with equal sensitivity. The signal received by the hydrophone was fed to the input of a Tektronix TDS 520A digital oscilloscope. The oscilloscope memory was capable of storing four realizations of 50000 points. The data from the oscilloscope memory were recorded to the memory of a computer with the help of a code written using LabView.

In studying the cavitation field, the hydrophone was positioned at a fixed distance from the radiator surface and in the basin center. First, the development of acoustic pressure oscillations at a fixed point of the field was recorded starting from the moment of turning on the ultrasonic generator. An analogous record at the same point of the field was made for comparison after 5–7 s after turning on the generator. It was visible in the oscilloscope screen that the signal structure after this time interval almost did not change, and, therefore, this record was considered to be the realization of the process of stationary cavitation. The maximal length of the process record was determined by the technical characteristics of the oscilloscope. The total recorded realization consisted of 50000 points. The horizontal scan was selected to be equal to 10 ms per division, which made it possible to record the data within the time interval equal to 0.1 s. In this case, 28 points corresponded to one period of oscillation with the frequency $f = 18$ kHz, which provided an opportunity to determine 14 harmonics of the fundamental frequency. Measurements using scans twice as long were also performed, which allowed us to record realizations two times greater in length.

Multiple cavitation bubbles appeared near the radiator immediately after the ultrasonic generator was turned on. The cavitation region was about 10 cm in length. Only single random bubbles were observed at greater distances. The hydrophone was positioned both in the cavitation region (2–4 cm from the radiator) and at a distance of 10–15 cm from the lower boundary of the bubbles. In the first case, a pronounced variability of the wave profile was expected due to multiple bubble collapse near the hydrophone. In the second case, cavitation noise of the whole cavitation region was detected.

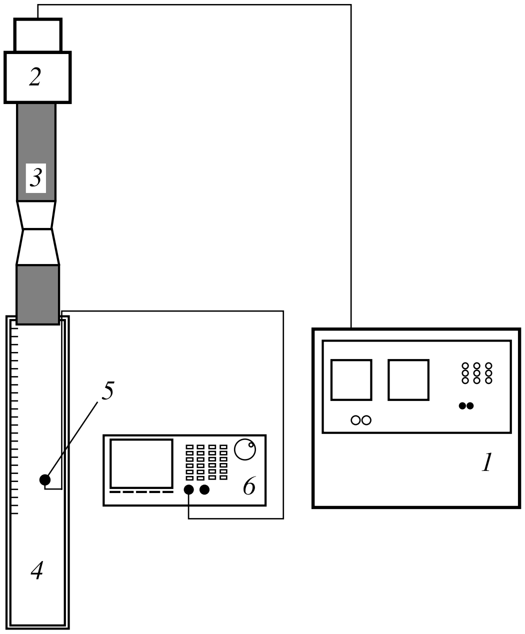

Fig. 1. Experimental setup: (*1*) generator, (*2*) magnetostrictive transducer, (*3*) titanium radiator, (*4*) basin with a liquid, (*5*) hydrophone, and (*6*) digital oscilloscope.

An emitter of ultrasonic oscillations has a finite quality factor as any oscillating system does and, therefore, a certain time is needed for its oscillations to become stationary. The analysis of the behavior of the pressure amplitude in the process of turning on and off the ultrasonic generator allowed us to estimate the transient period for the oscillation amplitude as approximately 80–85 oscillation periods. The fact that this period turned out to be considerably shorter than the characteristic times of cavitation development was important for our experiments.

Already from the form of the pressure profiles recorded at different instants of time after turning on the ultrasound, it was possible to conclude that a certain time is needed for the system to reach the stage of stationary cavitation (Fig. 2). At the beginning of the cavitation development, the wave has an almost sinusoidal form disturbed by the oscillations due to bubble cavitation (Fig. 2a). Intense bubble collapse near the hydrophone occurs rarely, and, therefore, the disturbances of the wave profile are weakly pronounced. As cavitation develops, the disturbances of the wave form become stronger, and the detected wave becomes similar to a sequence of pulses with the pulse rate equal to the frequency of the initial harmonic wave (Fig. 2b). Each of these pulses corresponding to the compression phase of the ultrasonic wave is produced due to a strong collapse of a cavitation bubble near the hydrophone. Thus, the structure of the wave profile is quite complex and sub-

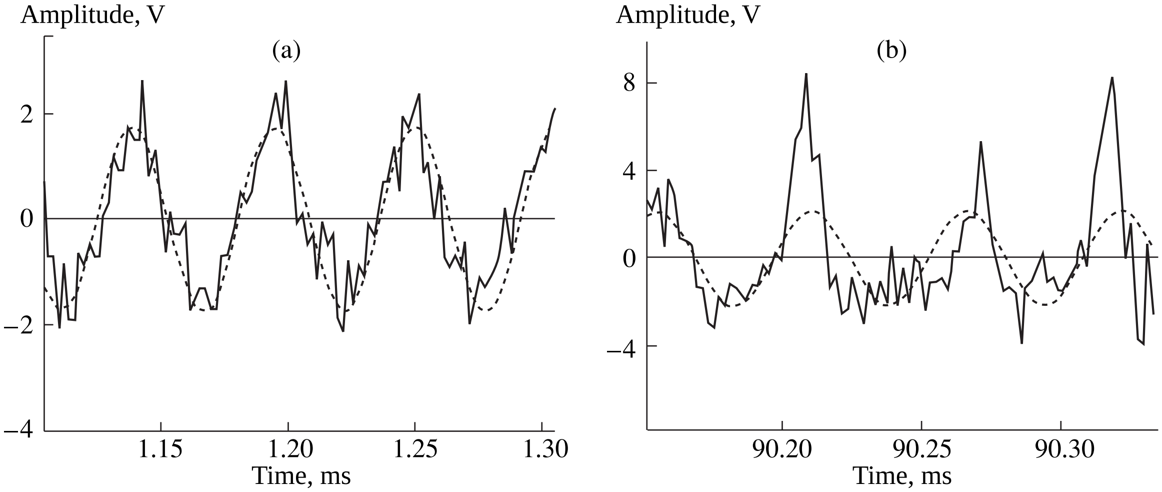

Fig. 2. Pressure profile in water 4 cm from the radiator (a) 1 and (b) 90 ms after turning on the ultrasound. A harmonic oscillation with the amplitude of the first harmonic is shown by the dashed line.

jected to fluctuations due to both the process of bubble collapse and the chaotic character of bubble oscillations. Therefore, it is rather difficult to determine the exact time intervals of the evolution of a wave profile by its form. It is desirable to use some averaged quantities that characterize slow (compared to the period of oscillations) evolution of the wave. On the other hand, it is necessary to conduct averaging over time intervals with the length considerably smaller than that of the transient period of the cavitation process. In our case, this time interval is about 50 periods of oscillations. As the average quantities, we used the amplitudes of harmonics calculated at a finite-length realization. For this purpose, we used the spectral analysis of the obtained realizations with the help of the fast Fourier transform. In the nonstationary cavitation regime, a recorded realization of the hydrophone signal was divided into equal intervals with the number of selected points in each of them equal to two to the power m (m is an integer). The fast Fourier transform was applied within each interval, which resulted in the spectrum of a specific time interval. Such a scheme was also applied for the stationary regime. The spectrum was calculated at each time interval of the recorded signal realization, and then it was averaged over the whole realization.

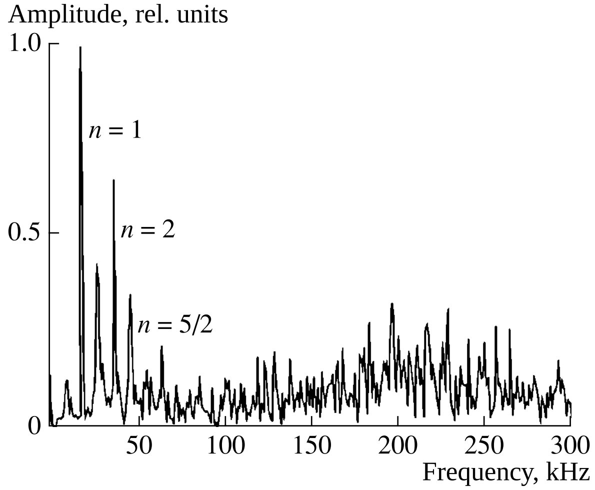

Fig. 3. Spectral distribution of the cavitation noise in water 4 cm from the radiator surface, 18 ms after turning on the ultrasound.

The resulting spectra have a form typical of the cavitation process (Fig. 3). The harmonics of the fundamental frequency (the second, third, etc.) are clearly pronounced in the spectrum. The subharmonic $f/2$ and its multiple frequencies are also present. A cavitation noise characterized by an approximately constant spectral density and extending to tens of megahertz is present in the high-frequency region of the spectrum. Figure 3 shows the spectrum in the frequency range up to 300 kHz. The rise of the spectral amplitude in the frequency range 200–230 kHz is related to the frequency characteristic of the used hydrophone, which has natural resonance at these frequencies. As the cavitation develops further, the relationship of the spectral amplitudes changes and the form of the spectrum becomes more and more similar to the spectrum corresponding to the stationary cavitation.

In the case of cavitation in water, the amplitude of the fundamental harmonic at the beginning of the process is maximal. As one can see from Fig. 4, as cavitation develops, the amplitude of the fundamental harmonic decreases and reaches its value corresponding to the case of stationary cavitation. Near the radiator, the transient period for the stationary value is about 40 ms, and, in this case, the value of the fundamental harmonic amplitude in the stationary regime is only 25% smaller than the initial value. Far from the radiator, outside the cavitation region, the corresponding difference in the values of the fundamental harmonic amplitude is

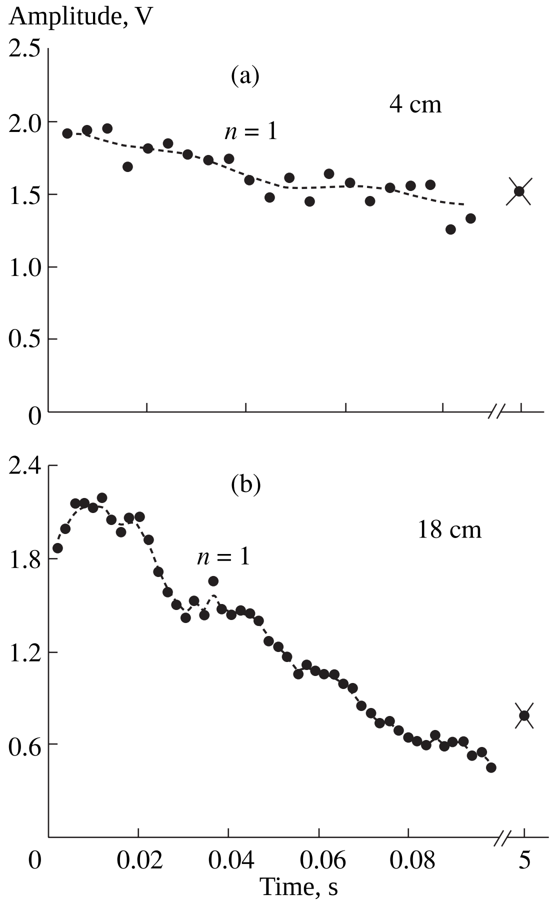

Fig. 4. Time dependence of the amplitude of the first harmonic in water 4 and 18 cm from the radiator surface. The cross indicates the amplitude value in the stationary cavitation regime.

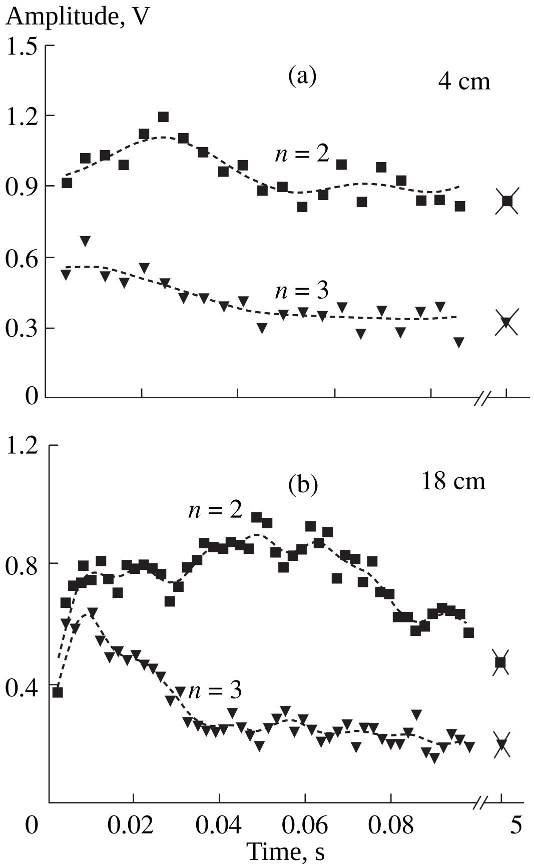

Fig. 5. Time dependences of the amplitudes of the second and third harmonics in water 4 and 18 cm from the radiator surface. The crosses indicate the values of harmonic amplitudes in the stationary cavitation regime.

almost 400% and the transient period for the stationary value is equal to 70 ms. It follows from Fig. 5 that the amplitudes of the harmonics and the subharmonic grow rapidly at the beginning and then decrease slowly, approaching the values characterizing the stationary cavitation. In this case, the characteristic transient periods for the stationary values of harmonics are 40–50 ms. It should be noted that the amplitudes of harmonics within the cavitation region differ little (by 30–60%) from the corresponding stationary values, while outside the cavitation region this difference is large (200–300%).

In transformer oil near the radiator, the amplitude of the fundamental harmonic grows as cavitation develops, while the amplitudes of the higher harmonics and the subharmonic decrease and reach a stationary level (Fig. 6).

Let us consider the results obtained by studying the transient period for stationary cavitation in water. In the course of cavitation development, the acoustic impedance of the medium decreases, since the density and the sound velocity decrease simultaneously. This in turn leads to a decrease in the ultrasonic radiation efficiency. This effect can be detected far from the cavitation region. Near the piston surface, at distances smaller than the wavelength, the motion of particles is directly connected to the motion of the radiator surface. As a consequence, the field near the radiator reaches its stationary value sufficiently fast. However, the amplitude of harmonics far from the radiator depends on the radiation from the whole bubble region, and the number of bubbles increases as the cavitation process develops. Therefore, the harmonic amplitudes grow at the beginning and then become stable, following in such a way the dynamics of the number of cavitation bubbles. However, this mechanism does not quite agree with the results obtained in transformer oil. To correctly explain the phenomenon, it is necessary to perform additional theoretical and experimental studies.

In this connection, we briefly review some results of the theoretical description of the cavitation phenomenon as a whole. Certain aspects of this problem are considered in a book by Akulichev, Alekseev, and Bulanov [10]. It is well known that acoustic cavitation being of

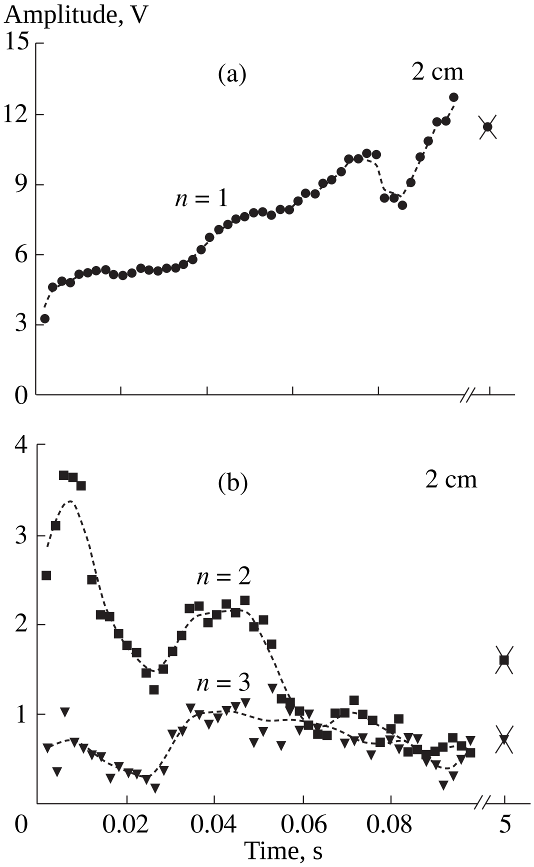

Fig. 6. Time dependences of the (a) first, (b) second, and third harmonics in transformer oil at the distance 2 cm from the radiator surface. The cross indicates the values of harmonic amplitudes in the stationary cavitation regime.

stochastic nature occurs at relatively high intensities of sound and is usually accompanied by many phenomena of mechanical and general physical character. This leads to the necessity to involve a very large number of equations for obtaining a full description of a cavitation region. Certainly, the consideration of separate components of the process or its investigation on one or another space–time scale, the selection of additional conditions, etc., can considerably reduce the total number of control equations. However, in our opinion, the complete set of equations that describes acoustic cavitation must include three blocks of equations at the minimum.

First, the set must include a wave equation, or, more precisely, several equations describing the propagation of a sound wave in a bubble medium. Since the bubbles are distributed randomly in space, in the case of the propagation of an acoustic wave in a randomly inhomogeneous medium, one should discuss only the statistical mean characteristics of the wave field. If the consideration is restricted to the two first moments of the wave field, such characteristics can be the average field and the second-order correlation function of the sound field. The average field $\langle p(\mathbf{r}, t)\rangle$ obeys the equation of a self-consistent field of the Dyson type, and the correlation function $\langle p(\mathbf{r}_1)p^*(\mathbf{r}_2)\rangle$ obeys the equation of the Bethe–Solpeter type. In the latter case, if the problem is formulated less rigorously, it is possible to introduce the ray intensity function $I(\mathbf{r}, \mathbf{n})$ according to the rule

$$\langle p(\mathbf{r}_1)p^*(\mathbf{r}_2)\rangle = \int d\Omega I(\mathbf{r}, \mathbf{n})e^{ik(\mathbf{r}_1-\mathbf{r}_2)\mathbf{n}} \qquad (1)$$

and use a transfer equation for it. Here, $\mathbf{n}$ is the unit vector directed along the vector $\mathbf{r} = (\mathbf{r}_1 + \mathbf{r}_2)/2$, $k = \omega/c$ is the wave number, and Ω is the spatial angle.

In the general case, the equation for the average field, i.e., the first moment, has the form

$$\begin{aligned}\langle p(\mathbf{r}, t)\rangle &= p_0(\mathbf{r}, t)\\ &+ \int G_0(\mathbf{r}, \mathbf{r}_1)M(\mathbf{r}_1, \mathbf{r}_2)\langle p(\mathbf{r}_1, t)\rangle d\mathbf{r}_1 d\mathbf{r}_2.\end{aligned} \qquad (2)$$

Here, $p_0(\mathbf{r}, t)$ and $\langle p(\mathbf{r}, t)\rangle$ are the incident and average fields, $G_0(\mathbf{r}_1, \mathbf{r}_2)$ is the Green function of free space, and $M(\mathbf{r}_1, \mathbf{r}_2)$ is the so-called mass operator. In the theory of multiple scattering of waves, the mass operator is usually taken in the Bourret approximation. In the case of a monodisperse size distribution of bubbles, it can be represented in a rather simple form: $M(\mathbf{r}_1, \mathbf{r}_2) = nf_s\delta(\mathbf{r}_1 - \mathbf{r}_2)$. Here, n is the number of bubbles per unit volume and f_s is the amplitude of sound scattering by a single bubble. In the general case, the number of bubbles n is a function of space and time, and in the case of a monodisperse distribution, it is expressed through the function of the size distribution $g(\mathbf{r}, t)$ in the following way: $n = \int g(\bar{R})d\bar{R}$. Here and below, the overbar means the time averaging, or, more precisely, averaging over the time comparable with the period of the field oscillations. The angular brackets mean averaging over a spatial coordinate. We note that, from here on, we do not mention the indicated dependence on $\mathbf{r}$ and t on larger scales to simplify the notations. As for the scattering amplitude f_s, in many cases it can be formally written in the standard form

$$f_s = \frac{\bar{R}}{\omega_0^2/\omega^2 - 1 - i\delta}, \qquad (3)$$

where ω_0 is the so-called resonance frequency of a single bubble and δ is the loss usually related to the acoustic, viscous, and thermal losses of the oscillation energy of a single bubble. The resonance frequency of a single bubble expressed through its compressibility β is generally represented by the formula $\omega_0^2 = (3/\beta - 2\alpha/\bar{R})\rho^{-1}\bar{R}^{-2}$, where α is the surface tension. In the stationary case of the propagation of an initially undisturbed plane wave, the solution of Eq. (2) usually leads to a renormalization of the wave number with the effective value written in the form

$$k_{\mathrm{eff}}^2 = \frac{\omega^2}{c_l^2} + 4\pi\int\frac{\bar{R}g(\bar{R})d\bar{R}}{\omega_0^2/\omega - 1 - i\delta}, \tag{4}$$

where c_l is the sound velocity in a pure liquid.

One can see already from the relations given above that it is necessary to know the dimensions of cavities, their time distribution, and the time behavior in order to determine the wave parameters of the field in a bubble medium. Normally, liquids already contain some microscopic nuclei in the form of microscopic bubbles. For example, microscopic air bubbles distributed in size according to the power law $g(\bar{R}) = A\bar{R}^{-n}$, where $A \approx 10^{-9}$ and $n \approx 3$–3.5 [11], exist even in settled tap water. These microscopic cavities start to grow when sound is turned on, and the values of their instantaneous radius obeys an equation of the Rayleigh type. For example, one of the modifications of this equation, the Nolting–Napierce equation, has the form

$$\rho\left(R\ddot{R} + \frac{3}{2}\dot{R}^2\right) = \left(p_0 - p_{v0} + \frac{2\alpha}{R_0}\right)\left(\frac{R_0}{R}\right)^{3\gamma} - p_0 + p_v + p_m\sin\omega t - \frac{2\alpha}{R}. \tag{5}$$

This equation describes the time behavior of a single bubble in an incompressible liquid under the effect of monochromatic sound with the amplitude p_m and frequency ω. It is assumed in this case that a bubble with the initial radius R_0 behaves adiabatically ($\gamma = c_p/c_v$) and the saturated vapor pressure inside it is equal to p_v. The static pressure in the liquid is equal to p_0. There is no exact analytic solution to this equation, but many authors have conducted numerical calculations for this equation with different parameters of the problem. The radial oscillations of a bubble at small amplitudes p_m are of harmonic character. However, at moderate and large amplitudes, multiple harmonics and subharmonics arise and are especially noticeable at the stage of bubble collapse. In particular, this can be seen in the plots shown in Fig. 2. If the right-hand side of Eq. (5) is equal to $-\Delta p$, the problem has the characteristic time τ of collapse for a bubble with the radius R_0:

$$\tau = CR_0\sqrt{\frac{\rho}{\Delta p}}, \text{ where } C = \frac{\Gamma(5/6)}{\Gamma(1/3)}\sqrt{\frac{3\pi}{2}} \approx 0.915. \tag{6}$$

This time is used in particular for the evaluation of the collapse time of bubbles in an alternating pressure field. In this case, Δp represents various combinations of the sound field amplitudes.

In the general case, equations of the type of Eq. (5) provide an opportunity to determine not only the instantaneous values of the cavity radii, but also the time behavior of their values averaged over the period of oscillations of the external field. In many cases, a noticeable change in the average size of bubbles occurs within the time that proves to be much longer than the characteristic times $1/\omega$ or τ. For example, in the case of a rectified gas diffusion, the characteristic transient period before reaching the stationary regime at moderate sound intensities can constitute several tens of minutes. In the case of vapor bubbles, the time required for reaching the asymptotic size also turns out to be long compared to the basic period of sound.

The third block of equations describing the development of a cavitation region in time and space is a kinetic equation. Like the previous equations, it can be written for both the instantaneous values of the function of bubble distribution in size $g(\mathbf{r}, R, t)$ and for the time-average values. We present here the kinetic equation for a bubble medium in the most general and somewhat formalized form:

$$\frac{\partial g}{\partial t} + \mathbf{v}\frac{\partial g}{\partial \mathbf{r}} + \frac{\partial}{\partial R}g\dot{R} = \mathrm{St}\,g. \tag{7}$$

The second term on the left-hand side of this equation is connected with the change of the function $g(\mathbf{r}, R, t)$ due to the progressive motion of the gravity center of a bubble. As is well known, a bubble in a sound field can perform not only radial oscillations, but also oscillations characterized by the center of its gravity oscillating with velocity $\mathbf{v}$ and frequency ω. Moreover, the center of a bubble can move in space in a certain direction under the action of constant forces like the buoyancy force or constant forces of the type of radiation pressure, etc. The third term on the left-hand side of Eq. (7) is connected with the natural change of the bubble radius in time under the effect of sound. As for the collision integral $\mathrm{St}\,g$ on the right-hand side of the equation, it is connected with the processes of scattering, as well as coalescence and splitting of bubbles. Here, we give the part of the collision integral that leads to a change in the average radius of bubbles on account of the processes of their coalescence and splitting:

$$\mathrm{St}\,g = \frac{1}{2}\int_0^{\bar{R}} d\bar{R}_1\sigma g(\bar{R}_1)g(\bar{R}_2)|\mathbf{V}_1 - \mathbf{V}_2|\left(\frac{\bar{R}}{\bar{R}_2}\right)^2 - \int_0^{\infty} d\bar{R}'\sigma g(\bar{R})g(\bar{R}')|\mathbf{V} - \mathbf{V}'| + Q(\bar{R}, \mathbf{r}, t). \tag{8}$$

Here, σ is the capture cross-section (of scattering) and $|\mathbf{V}_1 - \mathbf{V}_2|$ is the relative forward speed of colliding bubbles.

The first term on the right-hand side of Eq. (8) describes the increase in the number of bubbles with radius $\bar{R}$ on account of collision and coalescence of two bubbles with smaller radii $\bar{R}_1$ and $\bar{R}_2$ under the condition that they combine into a single cavity. It is assumed that two merging bubbles produce a new bubble with the radius $\bar{R}$ in such way that the condition of retaining their total volume is satisfied:

$$\frac{4\pi}{3}\bar{R}_1^3 + \frac{4\pi}{3}\bar{R}_2^3 = \frac{4\pi}{3}\bar{R}^3. \tag{9}$$

The second term on the right-hand side of Eq. (8) describes the decrease in the number of bubbles with the radius $\bar{R}$ due to their collision with other bubbles and their further merging into a cavity with a size different from $\bar{R}$. The last term on the right-hand side of the collision integral (Eq. (8)) characterizes the sources and sinks of phase inclusions with the radius $\bar{R}$ due to various mechanisms. For example, it is well known that, when a bubble reaches a certain size, at a corresponding velocity of radial fluctuations, a spherical instability of the bubble occurs. Under the condition $\bar{R} > R_{\text{cr}}$, an exponential growth is observed in the second harmonic of the cavity surface oscillations, the limiting critical radius being determined by the expression

$$R_{\text{cr}} = \sqrt{\frac{24\alpha(3+\delta)\bar{R}}{5\rho\omega^2|\delta R|}}, \tag{10}$$

where $|\delta R|$ is the amplitude of bubble oscillations. Finally, this leads to the destruction of the bubble surface and to bubble splitting. As a result, not one but several smaller bubbles are produced. In this case, the source function Q can be written in the form

$$Q = \sum_i N_i g_0(\bar{R}_i)\delta(\bar{R} - \bar{R}_i) - g(\bar{R})\delta(\bar{R} - \bar{R}_{\text{cr}}). \tag{11}$$

Here, N_i is the number of small bubbles with the radius $\bar{R}_i$, which are produced in the process of the cavity splitting, and $g_0(\bar{R}_i)$ is the function describing their size distribution.

Remember that bubbles in a liquid under the effect of sound perform not only radial oscillations but also translational motion. The forces of radiation pressure arise between oscillating bubbles. These forces lead to the interaction of bubbles. In the case of two bubbles oscillating at a small distance from each other, the forces have the character of attraction and are analogous to the Bjerknes forces. In the case of a bubble located at the point $\mathbf{r}_1$, the attractive force from the side of the second bubble oscillating at the point $\mathbf{r}_2$ has the form

$$\mathbf{F}_{\text{in}} = 4\pi\rho\bar{R}_1^2\bar{R}_2^2\overline{\dot{R}_1\dot{R}_2}\frac{(\mathbf{r}_2 - \mathbf{r}_1)}{|\mathbf{r}_2 - \mathbf{r}_1|^3}. \tag{12}$$

The velocities of radial oscillations of the surfaces of the bubbles $\dot{R}_1$ and $\dot{R}_2$ are determined as the result of solving Eq. (5).

Both primary and secondary forces of radiation pressure lead to the translationl motion of the gravity centers of bubbles, and the scattering of bubbles by each other results from their interaction. Finally, this leads to an additional term in the collision integral, which takes into account the redistribution of the bubble momentum. We will not present here this term, which is to some extent analogous to Eq. (8). For approximate calculations, we can use the so-called τ-approximation in which both summands of the collision integral on the right-hand side of the kinetic equation (7) are replaced by their simple estimates:

$$\text{St}\, g \approx \frac{g - g_0}{\tau_1} + \frac{g - g_0}{\tau_2} = \frac{\delta g}{\tau_0}. \tag{13}$$

Here, g_0 is the stationary function of bubble size distribution, τ_1 is analogous to the mean free time of particles in an ideal gas, and τ_2 is the characteristic time of bubble coalescence. The times τ_1 and τ_2 are usually long compared to other characteristic times of the problem ($2\pi/\omega$, the transient period of oscillations, etc.), and the kinetic equation can often be treated as a homogeneous one, i.e., without the right-hand side. If coalescence and the flare regime of cavitation are absent, when the average value of the forward speed of bubbles is almost zero, Eq. (7) can be reduced to the following simple form:

$$\frac{\partial g}{\partial t} + \frac{\partial}{\partial R} g\dot{R} = 0. \tag{14}$$

It follows in particular from Eq. (14) that, in the stationary case, the distribution function for average values reaches its minimum at the maximal velocities of surface oscillations. It should be noted that, in the case of acoustic cavitation with the average radius varying in time, the velocity $\dot{\bar{R}}$ reaches the highest values for resonance bubbles. This means that the distribution function must have a minimum at the resonance bubble size [12].

As we have already mentioned above, in the case of nonlinear oscillations of bubbles, new frequencies arise due to the excitation of harmonics and subharmonics, which are described in the framework of the nonlinear equation (5). However, a sharp expansion of the range of discrete frequencies also occurs as a result of bubble interaction. The formation of zones analogous to those formed in solids occurs in the vicinity of each frequency. For example, it is easy to show that the interaction of two bubbles with the resonance frequencies ω_{01} and ω_{02} due to the Bjerknes-type forces (Eq. (12)) leads to splitting and shifting of their eigenfrequencies according to the law

$$\omega_{1,2}^2 = \frac{\omega_{01}^2 + \omega_{02}^2 \pm \sqrt{(\omega_{01}^2 - \omega_{02}^2)^2 + 4\varepsilon_1\varepsilon_2\omega_{01}^2\omega_{02}^2}}{2(1 - \varepsilon_1\varepsilon_2)}. \tag{15}$$

Here, the coupling coefficients ε_1 and ε_2 are equal to $\varepsilon_{1,2} = \bar{R}_{1,2}\exp(ikL)/L$, where $L = |\mathbf{r}_1 - \mathbf{r}_2|$. In the case of n bubbles, each eigenfrequency is split into a region consisting of n different but closely spaced frequencies.

In closing our brief and schematic mathematical description of a cavitation region, we note the specific features of the stationary regime that occur in the case of cavitation. As one can see from the above consideration and from Eqs. (1)–(15), each block of equations can be characterized by a whole set of its own characteristic times. Single times of each set can widely differ from each other and differ from the characteristic times of other blocks of equations by several orders of magnitude. For example, in the case of wave equations, such times as the period of oscillations, the characteristic time of the development of the nonlinear regime, and the characteristic time of rescattering can be several orders of magnitude smaller than the times τ_1 and τ_2 mentioned above, which determine the time of the variation of the function describing the bubble size distribution. In this case, such quasi-equilibrium situations can take place as, e.g., in the cases of rectified gas diffusion or directional thermal diffusion, when the system rapidly reaches its stationary state in some individual parameters. Then, a relatively slow adiabatic change of these parameters occurs, and, within some new characteristic time determined by other parameters of the problem, the existence of a new stationary regime becomes possible. In some cases, the existence of several such quasi-stationary states is possible. Regretfully, at the moment we do not know or cannot calculate some of the coefficients involved in Eqs. (1)–(15). For example, we have no idea how to determine the exact values of the coefficient N_i and the number i in Eq. (11), which determine the avalanche character of bubble multiplication. We note that, according to [4, 8], the factor of bubble multiplication during the cavitation time can reach a value of the order of 10^5. However, we know neither the capture cross-section nor the probability of bubble coalescence. Therefore, we cannot even approximately estimate the time within which the number of multiplying bubbles becomes stabilized at a given pressure level. Thus, to correctly interpret the results obtained in the first part of this paper, it is necessary to conduct additional theoretical and experimental studies.

ACKNOWLEDGMENTS

This work was supported in part by the program Universities of Russia (project no. 1-5286) and the Russian Foundation for Basic Research (project no. 00-02-17055).

REFERENCES

1. M. Kameda and Y. Matsumoto, J. Acoust. Soc. Am. **106**, 3156 (1999).
2. Z. C. Feng and L. G. Leal, Annu. Rev. Fluid Mech. **29**, 201 (1997).
3. R. G. Holt and L. A. Crum, J. Acoust. Soc. Am. **91**, 1924 (1992).
4. L. D. Rozenberg, in *Physics and Technology of High-Intensity Ultrasound. Intense Ultrasonic Fields*, Ed. by L. D. Rozenberg (Nauka, Moscow, 1968), pp. 221–266.
5. C. E. Bvennen, *Cavitation and Bubble Dynamics* (Oxford Univ. Press, Oxford, 1995).
6. R. Mettin, S. Luther, C.-D. Ohl, and W. Lauterborn, Ultrason. Sonochem., No. 6, 25 (1999).
7. *Chemistry and Ultrasound*, Ed. by T. Mason (Elsevier, UK, 1990; Mir, Moscow, 1993).
8. M. G. Sirotyuk, in *Physics and Technology of High-Intensity Ultrasound. Intense Ultrasonic Fields*, Ed. by L. D. Rozenberg (Nauka, Moscow, 1968), pp. 167–220.
9. V. A. Akulichev, Akust. Zh. **14**, 337 (1968) [Sov. Phys. Acoust. **14**, 284 (1968)].
10. V. A. Akulichev, V. N. Alekseev, and V. A. Bulanov, *Periodic Phase Transformations in Liquids* (Nauka, Moscow, 1986).
11. L. R. Gavrilov, in *Physical Foundations of Ultrasonic Technology*, Ed. by L. D. Rozenberg (Nauka, Moscow, 1970), pp. 395–426.
12. V. N. Alekseev and V. P. Yushin, Akust. Zh. **32**, 748 (1986) [Sov. Phys. Acoust. **32**, 469 (1986)].

Translated by M. Lyamshev

Acoustical Physics, Vol. 47, No. 4, 2001, pp. 384–391. Translated from Akusticheskiĭ Zhurnal, Vol. 47, No. 4, 2001, pp. 451–459.
Original Russian Text Copyright © 2001 by Borodina, Petukhov.

Specific Features of the Space–Time Structure of Acoustic Signals in Multimode Waveguides

E. L. Borodina and Yu. V. Petukhov

Institute of Applied Physics, Russian Academy of Sciences,
ul. Ul'yanova 46, Nizhni Novgorod, 603600 Russia
e-mail: petukhov@hydro.appl.sci.nnov.ru

Received February 16, 2000

Abstract—The effect of the diffraction focusing of an acoustic field on the space–time intensity distribution of narrow-band pulsed signals in multimode oceanic waveguides is analytically and numerically studied. The laws governing this effect and its specific features are illustrated by the results of calculations based on the standard ray approximation and the mode theory for the acoustic field in an isovelocity waveguide. *© 2001 MAIK "Nauka/Interperiodica".*

It is well known [1] that the propagation of pulsed acoustic signals in an oceanic waveguide is accompanied by the formation of a space–time structure characterized by a certain pattern of the lines of maximal field intensity $J(t, r_0, z)$ at a fixed distance $r = r_0$ in the propagation time–depth plane $(t - z)$. For each waveguide, the pattern of such lines, which is called the $t - z$ diagram [2, 3], determines the dependence of the travel time t of the pulsed signals on the reception depth z. Each line of the $t - z$ diagram connects the arrival times of the pulsed signals of a similar type and actually describes the form of the corresponding wave front in the waveguide cross-section [1–3].

First proposed long ago [2] for describing the ray structure of a field of pulsed signals at different depths, now, the $t - z$ diagrams find wide application in solving urgent problems of ocean tomography [4, 5]. This fact accounts for the attention given to the experimental and theoretical studies of the laws that govern the formation of the space–time distribution of the pulsed signal intensity in oceanic waveguides [1, 4, 5]. One of the most important directions of these studies is the theoretical description of the diffraction effects arising in the formation of $J(t, r_0, z)$, where the diffraction effects are understood as all possible deviations of $J(t, r_0, z)$ from the $t - z$ diagrams calculated in the geometrical acoustics approximation [4–6]. However, in such a formulation, the question about the adequacy of the description of the space–time structure of the field $J(t, r_0, z)$ with the use of the ray-calculated $t - z$ diagrams deals with a rather fundamental problem on the limits of applicability and on the correctness of the geometrical acoustics approximation for describing the acoustic fields in oceanic waveguides [3, 7].

In this paper, without considering the whole diversity of the conventionally considered diffraction effects [3, 7], we will concentrate on the effect of the diffraction focusing of acoustic fields [8–10] on the space–time distribution of the pulsed signal intensities $J(t, r, z)$ in the oceanic waveguides. The reason is that, in contrast to other effects [3, 7], this effect occurs in both refractive [8, 9] and isovelocity waveguides [10, 11] and is most pronounced in the case of the multimode propagation of cw acoustic signals; on the other hand, it was not considered in the scientific literature except in two papers [12, 13] where, however, some physically unjustified conclusions had been made. As an illustrative example, we consider the behavior of the field $J(t, r, z)$ in an isovelocity waveguide for which the numerical calculations with the use of both the ray approximation and the mode theory are considerably simplified; this allows a direct comparison of the results following from these two approximations.

Let us first dwell very briefly on the description of the basic effects arising in the diffraction focusing of the acoustic fields generated by a cw point source in waveguides [8–11]. As shown in [8, 14], the interference pattern of the acoustic field along the track in an oceanic waveguide is rearranged with the minimal $R_{\min}$ and maximal $R_{\max}$ spatial periods. This rearrangement manifests itself as a partial repetition of the characteristic features observed at $0 \le r \ll R_{\min}$ in the spatial (in the depth z and the horizontal distance r) distribution of the sound field intensity. This repetition leads to the diffraction focusing of the field in the corresponding intervals of distances [8, 14]

$$mR_{\min} \le r \le mR_{\max} \quad (m = 1, 2\ldots). \tag{1}$$

In expression (1), the characteristic spatial periods are determined by the following expressions [8–10, 14]:

$$\begin{aligned} R_{\min} &= \min\{R_g(l, l+1;\ l+1, l+2)\}, \\ R_{\max} &= \max\{R_g(l, l+1;\ l+1, l+2)\}, \end{aligned} \tag{2}$$

where the quantity

$$\begin{aligned} &R_g(l, l+1;\, l+1, l+2) \\ &= R_{l,\,l+1}R_{l+1,\,l+2}/\left|R_{l,\,l+1} - R_{l+1,\,l+2}\right| \end{aligned} \tag{3}$$

corresponds to the period of the rearrangement of the interference structure formed by a pair of adjacent modes with the characteristic interference periods

$$\begin{aligned} R_{l,\,l+1} &= 2\pi/(k_l - k_{l+1}), \\ R_{l+1,\,l+2} &= 2\pi/(k_{l+1} - k_{l+2}). \end{aligned} \tag{4}$$

The frequency dependence of the horizontal wave number k_l of the lth mode in Eq. (4) is determined by the dispersion equation corresponding to the specific waveguide.

Thus, here as in [8–10, 14], by analogy with the diffraction imaging of periodic structures in optics [15], the diffraction focusing of the acoustic field in a waveguide means the formation of zones of enhanced insonification. In this case, in contrast to refractive focusing [3, 7] where the dependence of the spatial period on the wavelength is determined by only a small diffraction correction to the ray approximation, the spatial period of the focusing significantly depends on the wavelength λ [8–10, 14, 16].

The term diffraction focusing and the manifestation of the corresponding effect can be explained on the basis of the simplest model of an isovelocity waveguide with a water layer of a depth H and with a rigid bottom. In this case, the field of the point source is equivalent to the field of a one-dimensional luminous lattice consisting of real and imaginary sources [3, 7]. The aperture of such a linear lattice is infinitely large, and, therefore, the Fraunhofer zone is at infinity. The latter means that the receiver is always in the Fresnel zone of such an aperture. As a consequence, a periodic focusing of its radiation should appear [15]. By analogy with the diffraction of waves transmitted through a diffraction lattice [15], the period of this focusing should be proportional to the quantity H^2/λ [10, 11, 16]. This statement has been analytically proved in [17] by using the representation of the field as the superposition of imaginary sources [3]. It was shown that, for multimode signal propagation, where $\lambda/H \ll 1$, the diffraction focusing of a cw radiation in an ideal waveguide occurs with the spatial period $4H^2/\lambda$, which coincides with the period $R_{\max}$ obtained from the mode theory (Eq. (2)) [10].

In an arbitrary plane-layered waveguide, the diffraction focusing of a cw acoustic radiation will occur with the spatial period $R_{\max}$ given by Eq. (2); therefore, the less the difference

$$\Delta R = R_{\max} - R_{\min} \tag{5}$$

between the maximal and minimal periods (2) (i.e., for $\Delta R/R_{\min} \ll 1$), the stronger the diffraction focusing. However, when $R_{\min}$ and $R_{\max}$ given by Eqs. (2) differ greatly but the condition $\Delta R/R_{\min} \approx 1$ is valid, the diffraction focusing can, nevertheless, occur for certain groups of the energy modes with relatively small changes in the quantity R_g given by Eq. (3) [8, 9]. It is clear that the greater the number of modes $L_m = l_b - l_s$ in every such group $l_s \le l \le l_b$, the more pronounced the diffraction focusing of the field in the corresponding intervals of horizontal distances:

$$mR_s \le r \le mR_b, \tag{6}$$

where

$$\begin{aligned} R_s &= \min\{R_g(l, l+1;\, l+1, l+2)\}, \\ R_b &= \max\{R_g(l, l+1;\, l+1, l+2)\}, \end{aligned} \quad (l_s \le l \le l_b) \tag{7}$$

and l_s and l_b correspond to the boundary values of the mode numbers characterizing the specific group of modes.

As is clear from expressions (1)–(7), the diffraction focusing of the cw acoustic radiation is caused by the constructive interference of adjacent pairs of constructively interfering modes. Therefore, a noticeable manifestation of this effect in the propagation of pulsed signals is possible only in certain conditions that are necessary for the realization of the constructive interference of the corresponding modal pulses.

In order to determine the conditions necessary for the appearance of diffraction focusing of the pulsed signals, we consider the multimode propagation of a rather narrow-band pressure pulse in an arbitrary plane-layered waveguide. In contrast to [18, 19], for the description of the temporal form of the initial pressure pulse $P_s(t)$, we will use the function

$$P_s(t) = \int_0^\infty S(\omega)e^{-i\omega t}d\omega + \text{c.c.} = p_0 e^{-t^2/T^2}\cos(\omega_0 t), \tag{8}$$

whose spectrum $S(\omega)$ depends on the cyclic frequency ω as

$$S(\omega) = \frac{p_0}{2\sqrt{\pi}\Omega}\left\{e^{-(\omega-\omega_0)^2/\Omega^2} + e^{-(\omega+\omega_0)^2/\Omega^2}\right\}.$$

Here, $\omega_0 \gg 1/T$ is the carrier frequency of the pulse whose effective length is $\Delta t = 2T$ and $\Omega = 2/T$ is the frequency characterizing the half-width of the spectrum; the symbol c.c. in Eq. (8) designates a complex conjugate term; and p_0 is the perturbation amplitude of the pressure generated by the point source in free space on the spherical surface of the radius R_0.

Using the mode representation for the sound field in the waveguide, the expression for the impulse pressure wave $P'(t, z, r)$ can be written as [7, 18]

$$P'(t, r, z) = R_0\left\{\int_0^\infty S(\omega)p(r, z)e^{-i\omega t}d\omega + \text{c.c.}\right\}, \tag{9}$$

$$p(r, z) = \pi i \sum_{l=1}^{L(\omega)} \psi_l(z_s)\psi_l(z)H_0^{(1)}(k_l r). \tag{10}$$

Here, the quantity $p(r, z)$ together with the exponential factor in Eq. (9) determines the field of the cw radiation formed by all $L(\omega)$ propagating modes and $\psi_l(z)$ are the orthonormalized eigenfunctions of the waveguide, which satisfy the standard boundary conditions at its surface $z = 0$ and at the bottom $z = H$. In the far zone of the point source $k_l r \gg 1$, which allows one to use only the main term of the asymptotics of the Hankel function $H_0^1(k_l r)$ [3], Eq. (10) can be reduced to a form convenient for the subsequent analysis:

$$p(r, z) = \frac{1}{\sqrt{r}} \sum_{l=1}^{L(\omega)} A_l(\omega, z, z_s) e^{i(k_l r + \pi/4)}, \tag{11}$$

$$A_l(\omega, z, z_s) = \sqrt{\frac{2\pi}{k_l}} \psi_l(z_s) \psi_l(z). \tag{12}$$

Furthermore, by analogy with [18, 19], we neglect the dependence of the mode amplitude $A_l(\omega, z, z_s)$ on the radiation frequency in a narrow range $\omega_0 - \Omega \le \omega \le \omega_0 + \Omega$ of its variation and expand the horizontal wave number of the lth mode in a power series in $(\omega - \omega_0)$ retaining the terms of no higher than the second order of smallness:

$$k_l = k_l(\omega_0) + \frac{(\omega - \omega_0)}{v_l(\omega_0)} - \left(\frac{d v_l}{d\omega}\right)\Bigg|_{\omega = \omega_0} \frac{(\omega - \omega_0)^2}{2 v_l^2(\omega_0)}, \tag{13}$$

where $v_l = d\omega/dk_l$ is the group velocity of the mode. Performing the integration in Eq. (9) with the use of Eqs. (11)–(13), we determine the approximate expression for the temporal dependence of the pressure perturbation in the waveguide:

$$P'(t, r, z) \approx p_0 R_0 \sum_{l=1}^{L} \Pi_l(t, r, z), \tag{14}$$

$$\begin{gathered} \Pi_l(t, r, z) = A_l(\omega_0, z, z_s) \frac{p_l}{\sqrt{r}} e^{-\tau_l^2/T_l^2} \\ \times \cos\left[k_l(\omega_0) r - \omega_0 t + \frac{\pi}{4} - \Theta_l + a_l \frac{\tau_l^2}{T_l^2}\right], \end{gathered} \tag{15}$$

where

$$p_l = (1 + a_l^2)^{-1/4}, \quad a_l = \frac{r}{r_l} \operatorname{sgn}\left\{\left(\frac{d v_l}{d\omega}\right)\Bigg|_{\omega = \omega_0}\right\},$$

$$r_l = T^2 v_l^2(\omega_0)/2\left(\left|\frac{d v_l}{d\omega}\right|\right)\Bigg|_{\omega = \omega_0},$$

$$\tau_l = \frac{r}{v_l(\omega_0)} - t, \quad T_l = T\sqrt{1 + a_l^2}, \quad \Theta_l = \arctan(a_l).$$

Using expressions for the space–time dependence of the pressure perturbation in the modal pulse $\Pi_l(t, r, z)$ given by Eq. (15), we can derive some conclusions which are of interest for the formulation of the conditions necessary for the manifestation of the diffraction focusing of the field in the total pulsed response $P'(t, r, z)$ given by Eq. (14). According to Eq. (15), as the distance increases, the intramode dispersion first leads to an increase in the effective duration of each modal pulse, $\Delta t_l = 2T_l$, and second to an additional decrease in its amplitude as compared to the cylindrical decay law $r^{-1/2}$, the additional decrease being characterized by the factor p_l.

Thus, in contrast to the intermode dispersion leading to a divergence of modal pulses, the intramode dispersion promotes the appearance of the effect of diffraction focusing of the sound field (Eq. (14)) because of the increase in Δt_l. In this connection, we can state that, for a group of modes with the numbers $l_s \le l \le l_b$ (Eqs. (6) and (7)), which is of interest for us, the diffraction focusing will be noticeable if the divergence in time of the centers ($\tau_l = 0$) of the respective modal pulses does not exceed half of the minimal effective duration of one of the pulses:

$$r\left(\frac{1}{v_s} - \frac{1}{v_b}\right) \le T\sqrt{1 + \left(\frac{r}{r_b}\right)^2}, \tag{16}$$

where

$$v_s = \min\{v_l(\omega_0)\}, \quad v_b = \max\{v_l(\omega_0)\},$$
$$r_b = \max\{r_l(\omega_0)\} \quad (l_s \le l \le l_b).$$

Using expressions (6) and (16), we obtain the condition

$$m \frac{R_b}{r_b} \left\{\frac{(v_s - v_b)^2 r_b^2}{v_s^2 v_b^2 T^2} - 1\right\}^{1/2} \le 1 \quad (m = 1, 2 \ldots), \tag{17}$$

which must be satisfied for the manifestation of the diffraction focusing of the modal pulses belonging to the corresponding group of modes with the numbers $l_s \le l \le l_b$ in a plane-layered waveguide.

On the other hand, the intramode dispersion, which was ignored in [20, 21], prevents the manifestation of the diffraction focusing because of the additional decrease (characterized by p_l) in the amplitude of each modal pulse (see Eq. (15)). However, this fact does not play any fundamental role, since it affects only the relative (with respect to the energy sum of modal pulses) magnitude of the effect, which is mainly determined by the dependence of the mode amplitudes (12) on their number. In addition, the intramode dispersion can negatively affect the diffraction focusing of the sound field because of the additional change in the phase of each modal pulse, this change being characterized by the quantity

$$\varphi_l = -\Theta_l + a_l \left(\frac{\tau_l}{T_l}\right)^2. \tag{18}$$

It should be noted that the presence of the second term in Eq. (18) leads to a linear (in time) frequency modulation in each modal pulse. In this case, the carrier frequency of the modal pulse

$$\omega_l = \omega_0 + \frac{a_l}{1+a_l^2}\frac{\tau_l}{T^2} \tag{19}$$

increases to the left of its center ($\tau_l = 0$) and decreases to the right of it when $(dv_l/d\omega)|_{\omega=\omega_0} > 0$; in the case $(dv_l/d\omega)|_{\omega=\omega_0} < 0$, the situation is reversed. As is seen from Eq. (19), the maximal difference of ω_l from ω_0 is reached at the characteristic distances $r = r_l$ (at $a_l = 1$); beginning from this, we obtain $\omega_l \longrightarrow \omega_0$ as $r \longrightarrow \infty$.

Thus, in order to determine the possibility of the manifestation of the diffraction focusing of the sound field in the case of the propagation of narrow-band pulsed signals in multimode plane-layered oceanic waveguides, it is necessary to carry out the corresponding analysis of the dependences of R_g, A_l, v_l, $dv_l/d\omega$, and r_l on the mode number l at the carrier frequency ω_0, which allows one to determine the mode groups for which condition (17) is satisfied in a given interval of horizontal distances.

It is evident from the foregoing that, in deriving condition (17), we ignored the dependence of the mode amplitude on the radiation frequency in the corresponding range $\omega_0 - \Omega < \omega < \omega_0 + \Omega$. With the use of analytical calculations without specifying the type of the waveguide, the effect of the frequency dependence of the mode amplitudes on the propagation of modal pulses can be studied in the framework of the WKB approximation for the mode representation of the sound field [18, 22]. It can be easily shown that the inclusion of this effect will lead to the appearance of corrections that depend on the depths of the source z_s and receiver z but do not depend on the horizontal distance r to the travel time of the modal pulse r/v_l and to the quantity a_l characterizing the changes in the pulse duration Δt_l and in its phase φ_l. It is evident that, on the whole, such corrections do not change the pattern of the phenomenon and, therefore, are not taken into account in this study.

Now we quantitatively illustrate the manifestation of the diffraction focusing of the sound field in the space–time structure of the intensity of narrow-band pulsed signals in an isovelocity waveguide represented by a homogeneous water layer of depth H with the sound velocity c_0 and density ρ_0 overlying a homogeneous liquid halfspace with the acoustical characteristics c and ρ. This simple model of the waveguide is chosen, since, in the framework of this model, the main features of the diffraction focusing of cw acoustic signals are well understood [10] and, in addition, numerical evaluations of the sound field in an isovelocity waveguide are considerably simplified not only in the mode representation, but in the ray approximation as well. The latter allows one to demonstrate rather clearly the possibilities for these two theories to describe the diffraction focusing of the sound field.

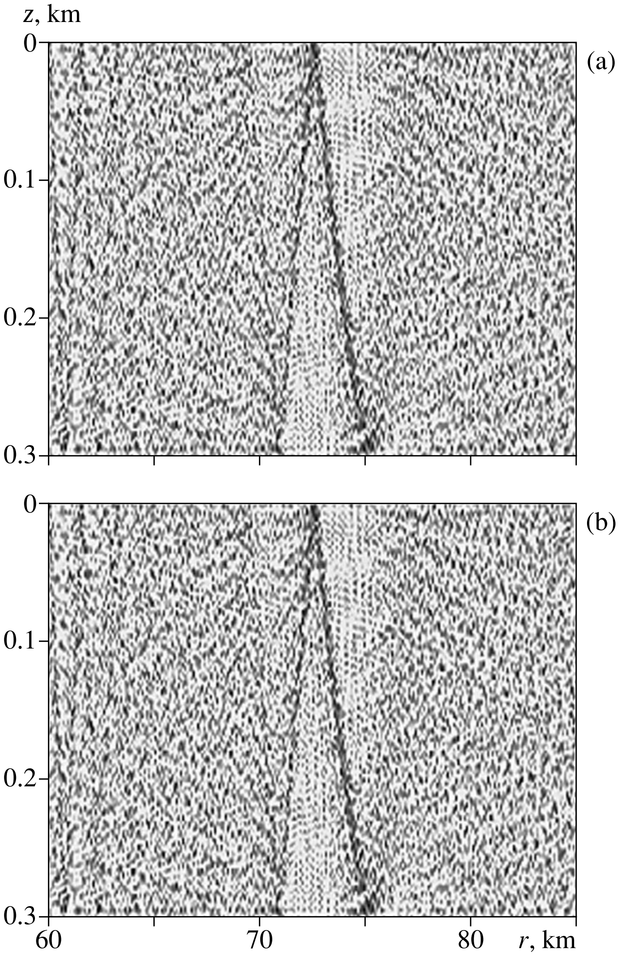

Fig. 1. Spatial distribution of the normalized acoustic field intensity calculated in the first zone of the diffraction focusing: (a) the mode theory for $J_m(r, z)$, Eq. (20), and (b) the ray theory for $J_r(r, z)$, Eq. (21).

With the aim to illustrate the structure of the first zone of the diffraction focusing, which is necessary for further analysis, we first consider the spatial distribution of the acoustic intensity normalized by the corresponding geometric divergence at the specific carrier frequency $\omega = \omega_0$. This distribution is obtained using both mode ($J_m(r, z)$) and ray ($J_r(r, z)$) theories:

$$J_m(r, z) = r|p(r, z)|^2, \tag{20}$$

$$J_r(r, z) = \sqrt{(2H)^2 + r^2}|\bar{p}(r, z)|^2. \tag{21}$$

The quantity $p(r, z)$ in Eq. (20) is determined by Eq. (11), and $\bar{p}(r, z)$ in Eq. (21) by an expression (see [17]) obtained using the representation of the sound field as multiple reflections from the bottom but without allowance for the ray displacement at the total internal reflection [7].

For the numerical calculations of the spatial distribution of the normalized intensity of the sound field by the mode (Eq. (20)) and ray (Eq. (21)) theories, the

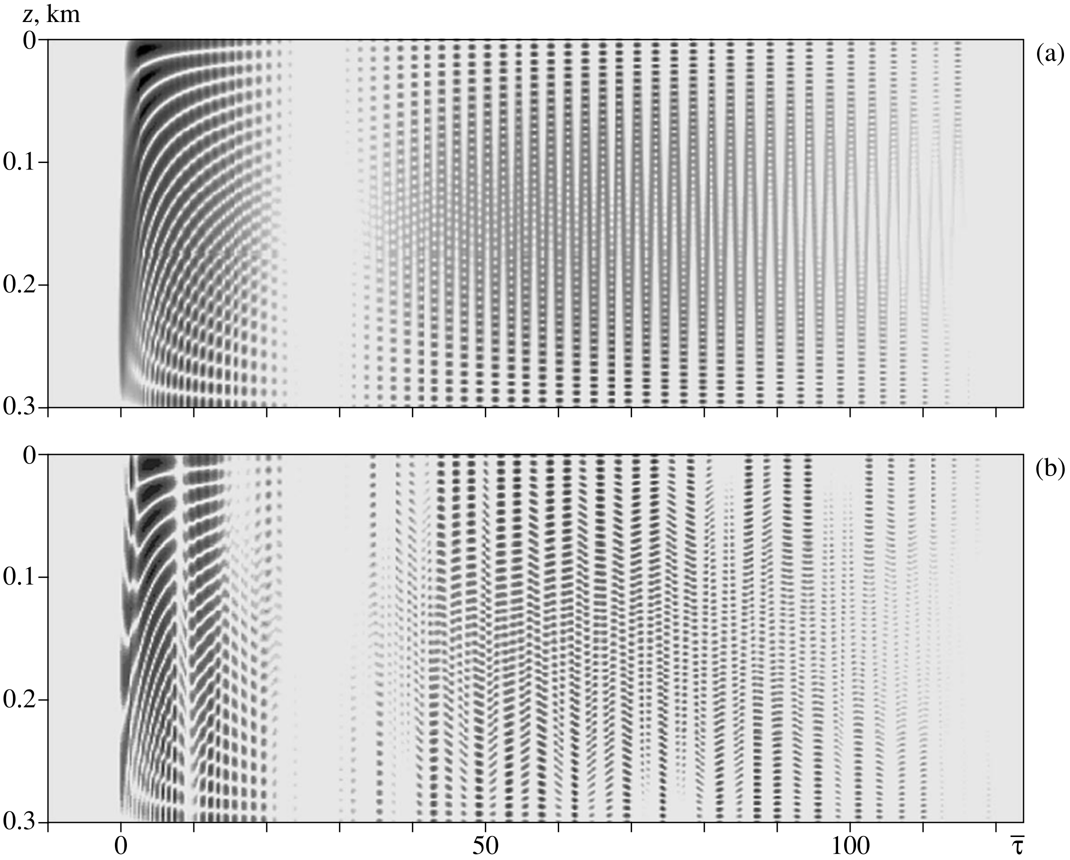

Fig. 2. Space–time distribution of the normalized intensity calculated for pulsed signals at $T = 0.035$ s: (a) the mode theory for $J_m(t, r, z)$, Eq. (22), and (b) the ray theory for $J_r(t, r, z)$, Eq. (23); here $\bar{\tau} = \tau/2T$.

following parameters (as in [10]) were chosen: $f = f_0 = 300$ Hz, $z_s = 9$ m, $H = 300$ m, $c_0 = 1.45$ km/s, $c = 1.7$ km/s, $\rho_0 = 10^3$ kg/m^3, and $\rho = 1.6 \times 10^3$ kg/m^3.

Figure 1 exhibits the results of numerical modeling, which are presented in the $r - z$ plane in the contrast form with the dynamic range 20 dB. As follows from Fig. 1, the intensity distributions $J_m(r, z)$ and $J_r(r, z)$ (Eqs. (20) and (21)) in the first zone of the diffraction focusing almost coincide. In this case, they are characterized by two lines of maximal sound intensity. These lines emerge from a point located near the pressure-release surface and have opposite signs of the slope angles in the $r - z$ plane. A similar agreement of the spatial dependences $J_m(r, z)$ and $J_r(r, z)$ is also observed in other ($m > 1$) zones of the diffraction focusing. This is a consequence of the fact that the field in these zones is mainly formed by the modes of low numbers with shallow grazing angles. These modes correspond to the rays with shallow grazing angles whose displacement at the total internal reflection is small and can be neglected [7]. Owing to the latter fact, the standard ray theory correctly describes the process of the formation of the diffraction focusing zones of the sound field in the isovelocity waveguide.

Using the information on the interference pattern of the sound field at a fixed radiation frequency in the first zone of the diffraction focusing (Fig. 1), we now consider the features of the space–time structure of narrow-band pulsed signals with the same carrier frequency in the first zone.

In solving this problem, numerical calculations of the space–time distribution of the pulsed signal intensity (normalized by the geometric divergence) were carried out using the mode ($J_m(t, r, z)$) and ray ($J_r(t, r, z)$) theories:

$$J_m(t, r, z) = r|P'(t, r, z)|^2/p_0^2R_0^2, \tag{22}$$

$$J_r(t, r, z) = \sqrt{(2H)^2 + r^2}|\Pi(t, r, z)|^2/p_0^2R_0^2. \tag{23}$$

Here, the dependence $P'(t, r, z)$ in Eq. (22) is determined by Eq. (19) and $\Pi(t, r, z)$ in Eq. (23) is determined by an expression (see [17]) where the field is represented in the form of multiple bottom reflections [7]. In deriving this expression in [17], we neglected the displacement of rays, as well as the change in the temporal form of the pulsed signals at the total internal reflection from the bottom. The latter means that, at the total internal reflection of a narrow-band signal with

$\omega_0 T \gg 1$ from the waveguide bottom, we neglect the change in its envelope but take into account the change in its phase.

The numerical calculations of the space–time distribution of the normalized intensity of the pulsed signals were carried out by Eqs. (22) and (23) for $f_0 = 300$ Hz, $z_s = 9$ m, and for two values $\Delta t = 0.07$ and 0.2 s of the effective duration $\Delta t = 2T$ of the initial pressure wave (8). Taking into account the spatial structure of the diffraction focusing zone of the sound field generated by the cw source (see Fig. 1), the value of the horizontal distance ($r = 72.5$ km) was chosen so that the diffraction focusing of the field was noticeable near the free surface of the isovelocity waveguide (see Fig. 1).

The results of the numerical calculations of the dependences $J_m(t, r, z)$ and $J_r(t, r, z)$ are presented in the $\tau - z$ plane in Figs. 2 and 3 in the contrast form with the dynamic range 20 dB; here, $\tau = t - t_0$ is the time measured from the minimal propagation time of pulsed signals t_0. The analysis of these results allows one to make the following conclusions.

First, up to the diffraction focusing zone, the space–time field structure is separated into two characteristic groups, one of which is formed by the modes of relatively small numbers, $l < 34$, with large group velocities and the maximum $A_l(z_s, z = z_s, \omega)$ for $l = 16$. The second group is formed by the modes of relatively large numbers $l > 34$ with smaller values of group velocities and the maximum $A_l(z_s, z = z_s, \omega)$ for $l = 50$. The whole space–time field structure formed by both the first and the second mode groups consists of two systems of crossing lines of maximal intensities. These lines have hyperbolic form and emerge from the points located near the free surface and the bottom, respectively. These intensities correspond to the modal pulses with minimal travel times.

Second, as can be expected, the diffraction focusing of the sound field occurs only for the first group of modes, $1 \le l < 34$, and is characterized by enhanced intensity near the free surface at $r = 72.5$ km. The greater the characteristic duration of the initial pressure pulse, the more pronounced the diffraction focusing; the space–time structure of the field $J(t, r, z)$ in the $\tau - z$ diagram becomes more and more similar to the spatial structure of the field $J(r, z)$ of cw radiation presented in the $r - z$ plane (Fig. 1).

Third, on the background of the above-mentioned hyperbolic lines of maximal values of the sound intensity (typical of the dispersion of modes of a water wave in an isovelocity waveguide, the travel times of these modes decreasing with the increase in the radiation frequency [3, 7]), the structure of the wave fronts typical of such a waveguide is formed. This structure represented in the $\tau - z$ diagram has the form of a bundle whose angle of incidence on the waveguide boundaries increases with time. The corresponding structure of the wave fronts is most pronounced in the $\tau - z$ diagram for the second group of modes. Clearly, as the effective duration of the initial pressure pulse increases, the manifestation of the bundle structure of the wave fronts becomes less pronounced in the $\tau - z$ diagram.

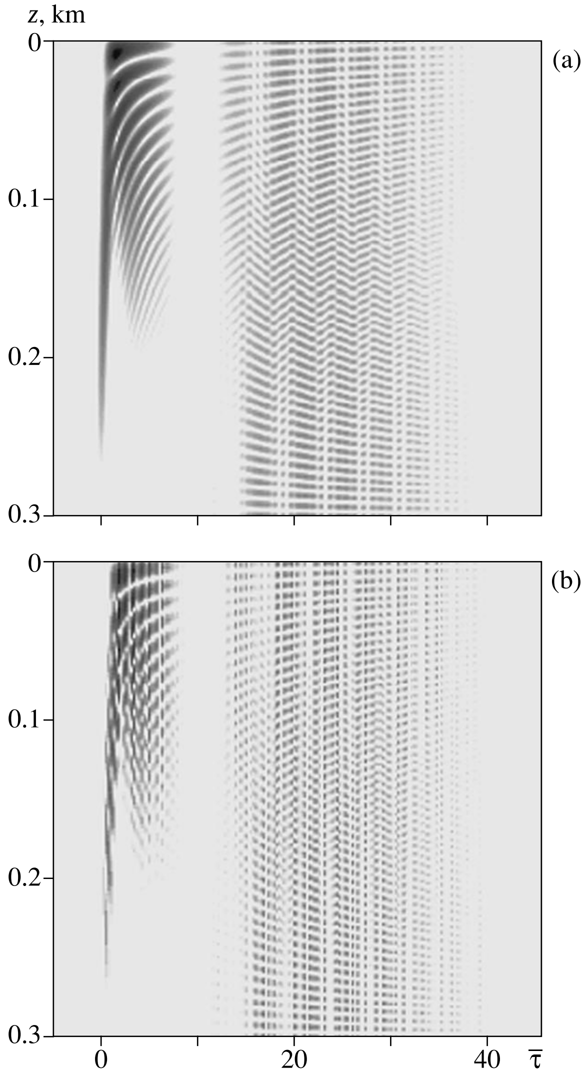

Fig. 3. Space–time distribution of the normalized intensity calculated for pulsed signals at $T = 0.1$ s: (a) the mode theory for $J_m(t, r, z)$, Eq. (22), and (b) the ray theory for $J_r(t, r, z)$, Eq. (23); here $\bar{\tau} = \tau/2T$.

From the above discussion it follows that the diffraction focusing has no relation to the formation of the bundle structure of wave fronts in the $\tau - z$ diagram and, therefore, the opposite statement made in [12, 13] is incorrect. The latter is also confirmed by the results of the numerical calculations of the space–time distribution of the sound intensity (normalized by the geometric divergence) with an incoherent summation of the contributions of individual rays (Fig. 4).

As is seen from Fig. 4, the bundle structure of the wave fronts typical of an isovelocity waveguide is formed even by an incoherent summation of rays, when the diffraction focusing of the field is absent. It means,

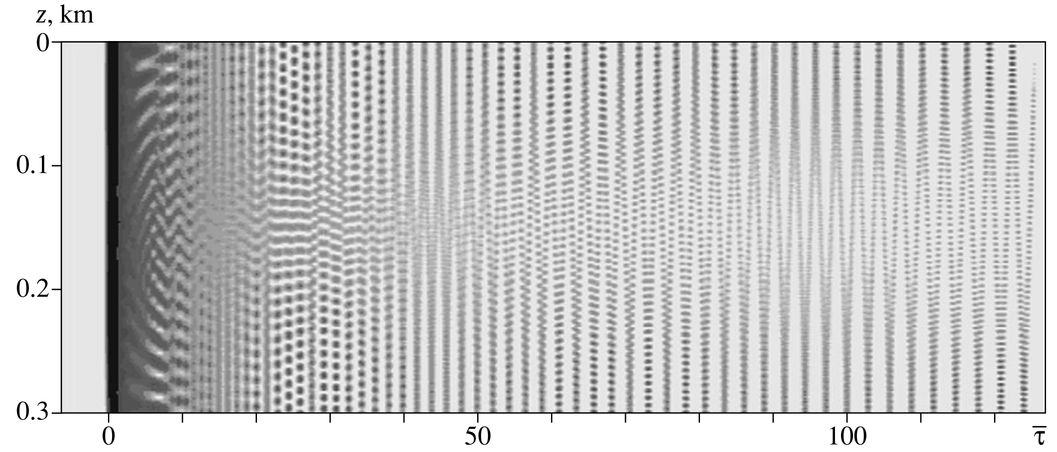

Fig. 4. Space–time distribution of the normalized intensity calculated for pulsed signals at $T = 0.035$ s by the incoherent theory; here, $\bar{\tau} = \tau/2T$.

in turn, that this wave front structure appears in the $\tau - z$ diagram only when the conditions, which are necessary for the formation of rays corresponding to constructively interfering mode groups, are satisfied [3]. Therefore, the corresponding lines in the $\tau - z$ diagram characterize the usual dependences of the travel times of rays, $t(r, z)$, on the reception depth for different multiplicity of their reflection from the surface and bottom of the oceanic waveguide at a fixed horizontal distance. Such dependences are adequately described by the approximate analytical expressions for $t(r, z)$ presented in our previous paper [17].

To conclude with, we analyze the differences in the space–time field structures calculated by using the mode ($J_m(t, r, z)$, Eq. (22)) and the ray ($J_r(t, r, z)$, Eq. (23)) theories.

As follows from the results of calculations of the dependences $J(t, r, z)$ (Figs. 2, 3), errors in the ray approximation are revealed in describing the space–time field structure formed by both the first and the second groups of modes. However, these errors are of the energy type, since they manifest themselves mainly in the magnitude of the sound intensity along the corresponding lines in the $\tau - z$ diagrams. The structure of the wave fronts is adequately described by both theories.

In addition, the ray approximation gives noticeably greater errors in describing the space–time field structure of pulsed signals (Figs. 2, 3) than in describing the spatial interference structure of the field generated by a cw source (Fig. 1). This result is caused by the fact that, in deriving the expression for $J_r(t, r, z)$ (Eq. (23)), we used some additional (as compared to $J_r(r, z)$, Eq. (21)) approximations taken from [17] concerned with the change of the temporal form of the profile of a narrowband pressure pulse at its total internal reflection from the ocean bottom. Therefore, it is natural that, with an increase in the effective duration $\Delta t = 2T$ of the initial pressure pulse, the errors of the ray approximation in describing the space–time field structure decrease down to the minimum attainable as $T \longrightarrow \infty$ (see Figs. 2, 3).

ACKNOWLEDGMENTS

This work was supported by the Russian Foundation for Basic Research, project nos. 98-05-64652 and 00-05-64604.

REFERENCES

1. J. Boyd, B. D. Cornuelle, T. F. Duda, *et al.*, J. Acoust. Soc. Am. **95**, 3118 (1994).
2. V. A. Apanasenko, Akust. Zh. **13**, 128 (1967) [Sov. Phys. Acoust. **13**, 100 (1967)].
3. L. M. Brekhovskikh and Yu. P. Lysanov, *Fundamentals of Ocean Acoustics* (Gidrometeoizdat, Leningrad, 1982; Springer, New York, 1991).
4. A. B. Baggeroer, T. G. Birdsall, J. A. Colosi, *et al.*, J. Acoust. Soc. Am. **105**, 3185 (1999).
5. A. B. Baggeroer, T. G. Birdsall, J. A. Colosi, *et al.*, J. Acoust. Soc. Am. **105**, 3202 (1999).
6. J. L. Spiesberger and F. D. Tappert, J. Acoust. Soc. Am. **99**, 173 (1996).
7. L. M. Brekhovskikh, *Waves in Layered Media* (2nd ed., Nauka, Moscow, 1973; Academic, New York, 1980).
8. Yu. V. Petukhov, Preprint No. 443, NIRFI (Radiophysical Research Inst., Nizhni Novgorod State Univ., 1998); Akust. Zh. **46** (3), 384 (2000) [Acoust. Phys. **46** (3), 327 (2000)].
9. D. I. Abrosimov and Yu. V. Petukhov, Preprint No. 467, IPF RAN (Inst. of Applied Physics, Russian Academy of Sciences, Nizhni Novgorod, 1998); Akust. Zh. **46**, 149 (2000) [Acoust. Phys. **46**, 113 (2000)].
10. D. I. Abrosimov and Yu. V. Petukhov, Preprint No. 466, IPF RAN (Inst. of Applied Physics, Russian Academy of Sciences, Nizhni Novgorod, 1998); Akust. Zh. **46**, 5 (2000) [Acoust. Phys. **46**, 1 (2000)].
11. D. E. Weston, J. Acoust. Soc. Am. **44**, 647 (1968).

12. E. L. Borodina, A. A. Stromkov, and A. I. Khil'ko, in *The Formation of Acoustical Fields in Oceanic Waveguides. Coherence Phenomena*, Ed. by V. A. Zverev (Inst. of Applied Physics, Russian Acad. Sci., Nizhni Novgorod, 1997), pp. 186–212.
13. V. G. Burdukovskaya, V. A. Lazarev, and A. I. Khil'ko, in *Proceedings of the School–Seminar "Acoustics of the Ocean,"* Ed. by L. M. Brekhovskikh (GEOS, Moscow, 1998), pp. 198–202.
14. Yu. V. Petukhov, Akust. Zh. **42**, 688 (1996) [Acoust. Phys. **42**, 606 (1996)].
15. R. F. Edgar, Opt. Acta **16**, 281 (1969).
16. L. A. Rivlin and V. S. Shil'dyaev, Izv. Vyssh. Uchebn. Zaved., Radiofiz. **11**, 572 (1968).
17. E. L. Borodina and Yu. V. Petukhov, Preprint No. 524, IPF RAN (Inst. of Applied Physics, Russian Academy of Sciences, Nizhni Novgorod, 2000).
18. V. A. Polyanskaya, Akust. Zh. **5**, 91 (1959) [Sov. Phys. Acoust. **5**, 91 (1959)].
19. M. G. Brown, F. D. Tappert, and J. Viechnicki, J. Acoust. Soc. Am. **100**, 2093 (1996).
20. K. J. McCann and F. Lee-McCann, J. Acoust. Soc. Am. **89**, 2670 (1991).
21. V. M. Kudryashov, Akust. Zh. **43**, 810 (1997) [Acoust. Phys. **43**, 706 (1997)].
22. N. A. Veshchev, A. I. Vinokurova, and S. Yu. Slavyanov, Akust. Zh. **34**, 1004 (1988) [Sov. Phys. Acoust. **34**, 576 (1988)].

Translated by Yu. Lysanov

Acoustical Physics, Vol. 47, No. 4, 2001, pp. 392–397. Translated from Akusticheskiĭ Zhurnal, Vol. 47, No. 4, 2001, pp. 460–465.
Original Russian Text Copyright © 2001 by Golyamina, Greshilov, Mironov, Rastorguev.

The Use of Distributed Pressure Receivers Based on Elastic Piezoelectric Composite Materials for Measuring the Hydrodynamic Noise Produced by a Near-Wall Turbulence

I. P. Golyamina, E. M. Greshilov, M. A. Mironov, and D. L. Rastorguev

Andreev Acoustics Institute, Russian Academy of Sciences,
ul. Shvernika 4, Moscow, 117036 Russia
e-mail: bvp@akin.ru

Received September 22, 2000

Abstract—Receiving electroacoustic transducers with sensing elements made of an elastic piezoelectric composite material are described. The parameters of a composite material that exhibits a bulk piezoelectric effect are presented. Results obtained by measuring the turbulent noise in a hydrodynamic channel with the use of piezoelectric composite receivers are reported. The results are compared with those of the noise measurements by a miniature piezoceramic receiver and are considered in the light of the known models of near-wall turbulence. *© 2001 MAIK "Nauka/Interperiodica".*

The measurements of wall pressure fluctuations in turbulent boundary layer flows continue to attract the interest of researchers [1]. The main instruments used in such measurements are the pressure receivers represented by electromechanical and electroacoustic transducers. In recent years, elastic piezoelectric materials have found expanding application in solving the problems of electromechanical and electroacoustic transformations. These materials include polyvinylidene fluoride-type (PVDF-type) polymer films, which exhibit a piezoelectric effect after being subjected to mechanical and electric treatment [2], and the so-called piezoelectric composites, which consist of fine-disperse solid piezoelectric particles (usually, a piezoceramic powder) distributed throughout a passive elastic polymer matrix [3]. The properties of piezoelectric composites depend on the properties of the piezoelectric powder; on the concentration, shape, and distribution of its particles; and, to a lesser extent, on the properties of the polymer matrix. The new elastic piezoelectric materials are used for the fabrication of mechanical vibration transducers and sound receivers of various types for various purposes [4, 5]. These materials also are of interest for aerodynamic and hydrodynamic studies: receivers made on their basis can serve for measuring pressure fluctuations in a turbulent flow and for analyzing the noise generated by a flow about an obstacle, as well as for solving other similar problems. The advantages of elastic piezoelectric receivers over the standard piezoceramic ones are primarily related to the possibility of varying their dimensions over wide limits: they can be manufactured as small devices with the dimensions within 1 mm and as distributed devices whose length may exceed 1 m. Such receivers can be in tight contact with a surface of any shape, they can be easily mounted on it and cause no significant distortions of the surrounding acoustic field. In a water environment, their small effect on the medium is additionally provided by their relatively small wave impedance, which is closer to the wave impedance of water than the impedance of conventional active materials (piezoceramics).

Receivers made of a piezoelectric polymer film with dimensions about 1 mm^2 were used by Nitsche *et al.* [6, 7] for measuring wall pressure fluctuations, which occurred in the turbulent boundary layer of an air flow in the initial part of a wind tunnel and in the boundary layer formed in a flow about an airfoil. The cited papers present the rms values and oscillograms of the signal fluctuations caused by a combined effect of pressure fluctuations and tangential stresses; they describe the experimental method used for separating these factors and present the results of its application. However, these studies did not include the spectral measurements, which provide additional information on the structure of the turbulent flow. The study of the spectrum of turbulent pressure fluctuations by not only small-size receivers, but also by distributed receivers that can be brought into coincidence with the flow boundaries is quite promising for solving a number of problems of acoustohydrodynamics.

The effect of the receiver dimensions on the measurements of the wall pressure fluctuations in a turbulent boundary layer was considered in [8–12]. The data presented in these publications testify that the true variable pressure caused by the near-wall turbulence can be measured only by a receiver whose dimensions are

1063-7710/01/4704-0392$21.00 © 2001 MAIK "Nauka/Interperiodica"

small relative to the characteristic scale of the local pressure fluctuations. At high Reynolds numbers, in the frequency range $2\pi f \le 0.1u_d^2/\nu$ (u_d is the dynamic flow velocity and ν is the kinematic viscosity coefficient), the pressure fluctuations are determined by the frozen turbulence model. In this case, to measure the fluctuations without distortions, it is necessary that the size d of the receiver satisfy the condition $d \le u/3f$, where u is the mean flow velocity and f is the frequency. Numerical estimates show that, for a mean velocity of 10 m/s and frequencies below 3000 Hz, the turbulent pressure fluctuations (the pseudosound) are recorded without distortions by receivers whose sizes do not exceed 1 mm. In the frequency range $2\pi f \ge 0.1u_d^2/\nu$ where high-frequency fluctuations are caused by the nonstationary processes of turbulence generation at the boundary of the viscous sublayer, the resolution criterion for small-scale fluctuations is expressed as $d \le 20\text{–}30\nu/u_d$. Then, for $u = 10$ m/s and a limiting frequency of 3000 Hz, the critical size of the receiver is estimated as $d \approx 0.1$ mm. These estimates offer the following conclusion: the greater the length of the receiving element, the weaker its response to the small-scale disturbances and, hence, the smaller the contribution of the pseudosound component to the total received signal and the greater the proportion of the sound component in the resulting spatial spectrum.

Pressure receivers that have a sufficient length and do not distort the shape of the surface contacting the flow can be manufactured on the basis of elastic piezoelectric materials. Conventional piezoceramics is of little use for this purpose. Below, we describe the experiments on the reception of noise generated by the near-wall turbulence in a hydrodynamic channel with the use of a distributed piezoelectric composite receiver; we compare the results with those of the reception by a conventional small-size piezoceramic receiver. The sensing element of the distributed receiver was made of a PKP-83 piezoelectric composite developed as a result of the cooperation of the Acoustics Institute with the Plastmassy Research and Production Association [13, 14]. According to the classification proposed in [3], this material belongs to the composites of the (0–3) type. The active piezoelectric component of this material is lead titanate piezoceramic powder (its volume fraction is 30%), and the passive polymer matrix is polyester-polyurethane resin. The coefficient of the bulk piezoelectric sensitivity of the PKP-83 composite is $g_h = 70$ mV m/N, which is superior to that of conventional types of piezoceramics because of the large anisotropy of the piezoelectric properties of the powder material. The density of the composite is $\rho = 3000$ kg/m^3, which is half the density of piezoceramics, and the elastic modulus is $c_h = 5.5$ GPa, which is an order of magnitude less than the corresponding parameter of piezoceramics. The wave impedance of the composite material is about 4000 kg/m^2/s, so that its acoustic matching with water is better than in the case of piezoceramics by almost a factor of five. The relative permittivity of the composite is fairly low ($\varepsilon = 18$), which is usually considered as a disadvantage. As a rule, the piezoelectric elements are made in the form of plates whose thickness is about 1 mm and area is (160–180) × (40–90) mm^2; the plates are polarized in the thickness direction by a strong electric field. The reversible flexure radius of such piezoelectric composite elements is 70 mm, and their properties do not depend on hydrostatic pressure up to 700 atm.

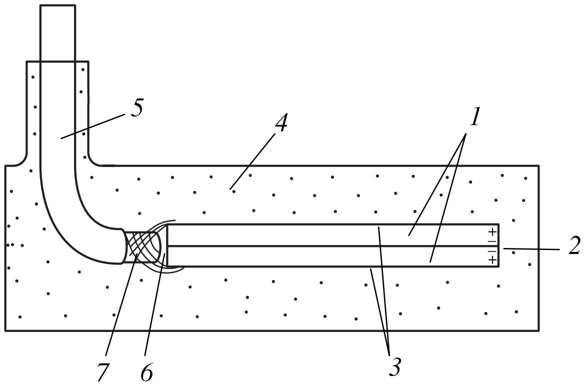

Fig. 1. Structure of a distributed piezoelectric composite receiver: (*1*) piezoelectric plates, (*2*) inner electrode, (*3*) outer electrodes, (*4*) polyurethane coating, (*5*) signal-transmitting cable, (*6*) central wire, and (*7*) screen braiding.

The pressure receiver under study is schematically represented in Fig. 1. Its sensing element consists of two PKP-83 piezoelectric composite plates whose large surfaces, 165 × 40 mm^2 in area, are glued together. The contacting plate surfaces are selected so as to have similar polarization charges. The inner electrode is connected to the central wire of the cable and the outer electrodes are connected to the earthed screen braiding. This structure provides a reduction of electromagnetic interference. The sensing element is covered with a polyurethane layer about 10 mm thick and the cable passes through it. The overall dimensions of the receiver are 230 × 65 × 20 mm^3.

The receiver was calibrated by sound signals in the hydroacoustic tank of the Acoustics Institute. The sensitivity of the receiver proved to be 70–80 μV/Pa in the frequency range from 10 Hz to 3 kHz. With a further increase in frequency, the sensitivity gradually decreased, which can be explained by the high resistivity of the electrodes made of a conducting polymer. The capacitance of the receiver was 2000 pF. The measurements performed in a high-pressure tank showed that the sensitivity and the capacitance remain constant within ±15% when the hydrostatic pressure increases up to 700 atm.

For comparison with the piezoelectric composite pressure receiver, we used a cylindrical hydrophone made of TsTS-19 (lead zirconate titanate) piezoceram-

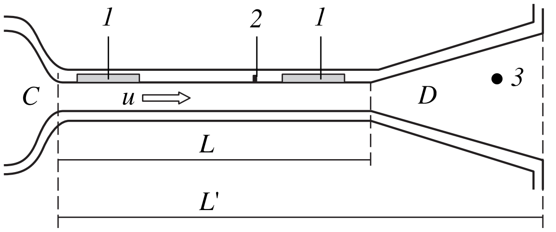

Fig. 2. Schematic representation of the experimental hydrodynamic system: (*L*) working part of the hydrodynamic channel, (*C*) contractor, (*D*) diffuser, (*1*) piezoelectric composite pressure receivers, (*2*) miniature piezoceramic receiver, and (*3*) reference receiver (hydrophone).

ics. The diameter of the hydrophone was 1.5 mm and its sensitivity was 3 μV/Pa.

In the experiments on the reception of noise produced by the near-wall turbulence, we used a hydrodynamic system described in our previous publication [12]. The main working part of this system is the channel shown in Fig. 2. The channel has the form of a rectangular waveguide with length $L = 3$ m, width $b = 7$ cm, and height $h = 2$ cm. The metal walls of the waveguide are 3 to 5 cm thick and have polished inner surfaces. The water flow in the channel issues from an elevated water tank with a volume of 14 m^3 placed at a height of 14 m. This kind of free water discharge due to the pressure drop together with the solidity of the channel walls provides a low level of intrinsic noise and vibration of the channel. Two hydrodynamic parameters of the system were measured in the course of the experiments: the mean velocity u of the channel flow and the tangential stresses τ in the stationary flow region. The value of u was estimated by the water discharge, and the value of τ was estimated by the pressure drop along the working channel, which was measured by a pressure gauge. Both these parameters were determined with an accuracy of 1–2%. Using the value of τ, we calculated the dynamic flow velocity

$$u_d = (\tau/\rho)^{1/2}.$$

From the elevated tank, the water was supplied through a vertical pipe to a damping tank 2 m^3 in volume and, then, to a wide horizontal pipe. The end of this pipe was separated from the working channel by a contractor, which reduced the flow cross-section by a factor of 20 and caused a corresponding increase in the flow velocity. A gradual decrease in the flow cross-section in the contractor provided a low level of turbulence at the inlet to the working channel. At the outlet, the flow velocity gradually decreased as the flow passed through a diffuser smoothly diverging at an angle of 3°. After the diffuser, the water arrived at a damping tank and then through the outlet pipe to a receiving tank. The outlet pipe had a gate valve, which served for varying the flow velocity u in the working channel from 1.5 to 12 m/s.

In the experiments, the receivers intended for detecting hydrodynamic noise were mounted on the upper removable wall of the channel. They were fixed in specially prepared holes so that their receiving surfaces (the plane of the distributed piezoelectric composite receiver and the end of the cylindrical piezoceramic receiver) were flush with the surface around which the water flowed. The reception was performed at two distances 1 from the working channel inlet: $l_1 = 100h$ and $l_2 = 20h$, which corresponded to the terminal and initial parts of the working channel, respectively. We used two identical distributed piezoelectric composite receivers (Fig. 2). The position of the receiver at the longer distance from the inlet corresponded to a fully developed, uniformly turbulent flow (the inner hydrodynamic problem). At the shorter distance from the inlet, the boundary layers belonging to the upper and lower walls did not intersect (the outer hydrodynamic problem). The piezoceramic hydrophone that was compared with the distributed receiver was placed closer to the channel end. Owing to its small dimensions, the piezoceramic receiver could detect the small-scale pseudosound pressure fluctuations. Because of its low sensitivity, the sound component of the hydrodynamic noise, which was weaker than the pseudosound component, affected this receiver to a lesser extent. The sound pressure generated by the turbulent flow along the whole channel was reliably detected by the distributed receiver, which, in principle, could also receive the turbulent fluctuations. In addition to the receivers installed in the working channel, one more receiver was placed in the diffuser. The additional receiver was a standard spherical piezoceramic hydrophone with a diameter of 50 mm and a sensitivity of 100 μV/Pa. The receiver mounted in the diffuser detected the sound pressure almost exclusively, because the flow velocity there was as low as 0.04 of the velocity in the working channel and, hence, the turbulence was very small. The corresponding characteristic frequencies of pseudosound fluctuations were shifted to the infrasound range. Thus, in compliance with its dimensions, this hydrophone detected only the sound waves generated by the turbulence in the working channel. The pressure measured in the diffuser, p_{sp}, was recalculated to the sound component p_{sc} of the pressure in the working channel by the formula

$$p_{sc} = p_{sp}S_d/S_c,$$

where S_d is the cross-sectional area of the diffuser at the hydrophone site and S_c is the cross-sectional area of the working channel. In the setup used in our experiments, the ratio S_d/S_c was equal to 22.

In the previous experiments [12], the frequency dependences of the measured sound pressure were found to exhibit some peaks. The presence of the peaks was explained by the formation of standing waves in the region between two cross-sections with widely different areas (see Fig. 2). In our experimental setup, the distance between these cross-sections was $L' = 6.7$ m, so that one should expect the appearance of resonances at a fundamental frequency of 125 Hz and at its harmonics.

The electric signals from the receivers were supplied to a specially designed multichannel amplifier with a controlled gain coefficient of 10 to 100 and with the intrinsic noise level no higher than 10 μV in the frequency range 0.1–10^4 Hz. The amplifier output was connected to a spectrum analyzer.

In the experiments, we used the receivers described above to determine the spectral characteristics of hydrodynamic noise generated by the near-wall turbulence in the channel.

Figure 3 shows the levels of the output signal of the distributed piezoelectric composite receiver that was fixed in the terminal part of the working channel. The signal was recorded by the spectrum analyzer in 1/3-octave frequency bands at different values of the mean flow velocity. For comparison, the figure also shows the spectrogram obtained with the zero flow velocity in the channel. The data presented in Fig. 3 show that the receiver provides a reliable measurement of the noise produced by the flow about the surface: even at the lowest flow velocity, the signal caused by the near-wall turbulence exceeds the background noise signal by more than 20 dB. The spectrograms exhibit peaks near the frequency 100 Hz and at higher harmonics, which can be explained by the aforementioned resonance of the sound component of noise.

Figure 4 compares the spectrograms of the output signals of the distributed receivers fixed in the terminal ($l_1 = 100h$) and initial ($l_2 = 20h$) parts of the working channel. One can see that the difference in the readings of the two receivers, which is determined by different degrees of turbulence development and, hence, by different levels of pseudosound fluctuations at the receiver sites, manifests itself only in the lowest frequency range. At the frequencies 200 Hz and higher, the readings of the receivers practically coincide. This means that, at sufficiently high frequencies, the distributed receivers are affected by the pseudosound component to a lesser extent than by the sound component, as one would expect according to theoretical predictions.

Figure 5 presents the spectral characteristics of the pressure measured in the working channel by the miniature and distributed receivers and by the hydrophone fixed in the diffuser. The pressure values were calculated from the spectrograms of the output signals of the receivers with allowance for their sensitivity and the gain coefficients of the preamplifiers. The receivers were fixed in the terminal part of the channel at $l_1 = 100h$. At the flow velocity $u = 10$ m/s, the thickness δ of the boundary layer formed in this part of the channel was equal to half the channel height, i.e., $\delta = 1$ cm. The dynamic velocity determined by the value of the tangential stress τ measured at these conditions was $u_d = 0.43$ m/s. Thus, the Reynolds number was

$$\mathrm{Re} = u_d\delta/\nu = 4.3 \times 10^3.$$

This value of Re in the channel corresponds to the formation of a region with a logarithmic velocity profile and with the spectrum of the pseudosound component of pressure fluctuations decreasing with frequency according to the law

$$P(f) \approx f^{-1/2}.$$

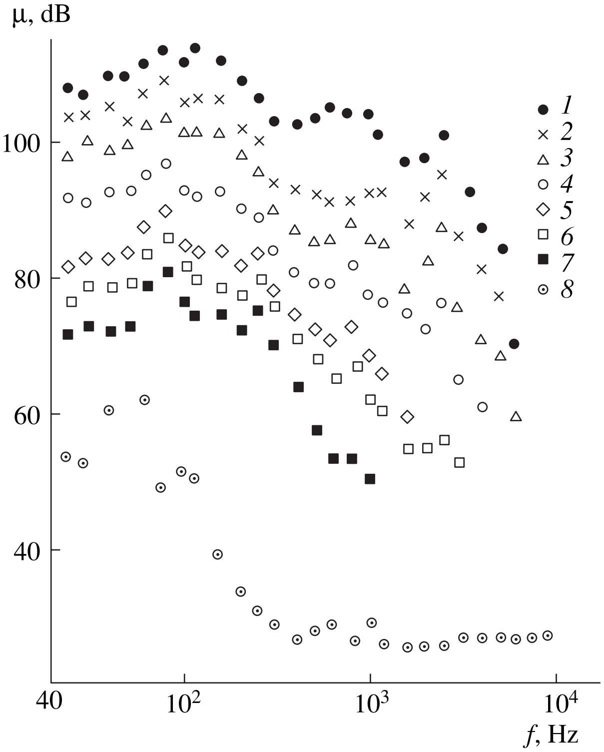

Fig. 3. Spectrogram of the signal levels obtained from the distributed piezoelectric composite receiver at different values of the mean flow velocity: u = (*1*) 10, (*2*) 9, (3) 7, (*4*) 5, (*5*) 3.3, (*6*) 2.5, (*7*) 1.8, and (*8*) 0 m/s.

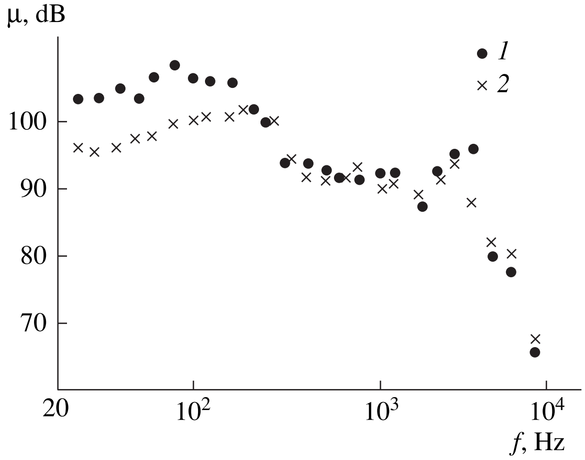

Fig. 4. Spectrogram of the signal levels obtained from the distributed receivers placed in the (*1*) terminal and (*2*) initial parts of the working section at u = 9.5 m/s.

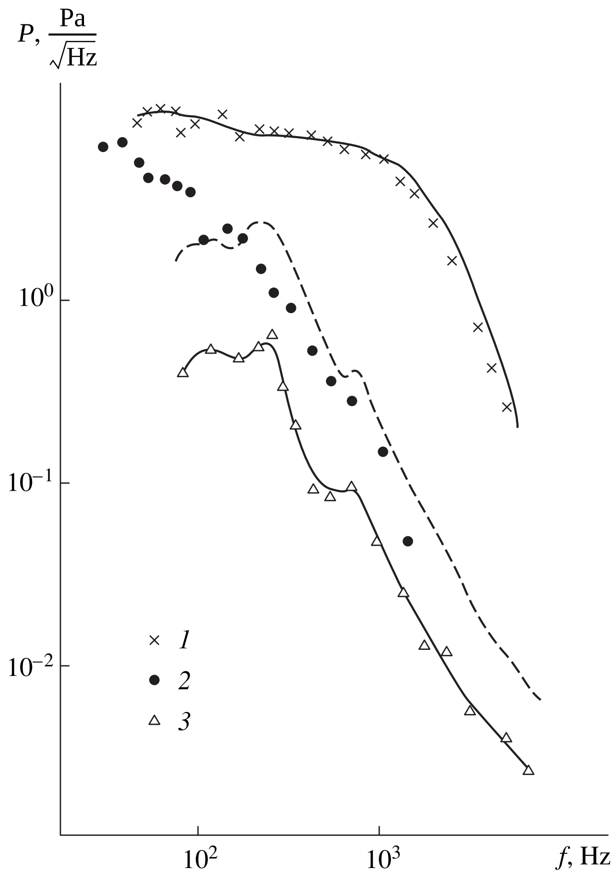

Fig. 5. Pressure spectra recorded by the (*1*) miniature and (*2*) distributed receivers in the channel and (*3*) by the hydrophone in the diffuser at $u = 10$ m/s. The dashed line represents the level of the sound component.

In Fig. 5, this dependence fitted to the experimental value of the spectral component of pressure at a frequency of 1000 Hz is represented by a solid curve. One can see that the pressure fluctuation spectrum measured by the miniature receiver obeys this dependence in the frequency range $5 \times 10^2 < f < 3 \times 10^3$ Hz. In this range where the quasi-frozen turbulence model is applicable, the miniature receiver satisfies the necessary condition $d < u/(3f)$ and adequately measures the pseudosound pressure fluctuations. At higher frequencies at which the fluctuations are determined by the nonstationary processes in the buffer zone and in the viscous sublayer, to obtain the true spectrum of small-scale pseudosound fluctuations with the use of a miniature receiver, it is necessary to introduce some corrections into the receiver signal [9]. The corrected dependence, which was obtained on the basis of our experimental data by correlating them with the results reported in [12], coincides closely with the spectral pressure dependence measured in the experiment. The dashed line in Fig. 5 shows the spectral characteristic of the sound component in the working channel. This characteristic is obtained by recalculating the pressure values measured by the hydrophone in the diffuser. The curve exhibits pronounced resonance peaks corresponding to the first (125 Hz) and second (250 Hz) harmonics and smeared (due to the 1/3-octave filtering) peaks at higher harmonics. The presence of these peaks additionally confirms the assumption [10] that the measured spectrum of turbulent noise is affected by the geometric parameters of the hydrodynamic channel.

To judge the pressure measurement by the distributed piezoelectric composite receiver under study, we compare the spectral characteristic of noise measured by this device with the spectra of the pseudonoise and noise components measured by the miniature receiver in the channel and by the hydrophone in the diffuser, respectively. From Fig. 5, one can see that, in the low-frequency range ($f < 50$ Hz), the distributed receiver detects the pseudosound fluctuations. This fact can be explained by a sufficiently large scale of turbulence in this frequency range compared to the receiver dimensions. At higher frequencies ($50 < f < 100$ Hz), the contribution of the pseudosound fluctuations to the receiver signal decreases, but it still remains significant. The difference observed in the low-frequency range between the readings of the piezoelectric composite receivers at l_1 and l_2 (Fig. 4) is explained by the variation of the Reynolds number along the channel. Earlier [13], it was shown that in the initial part of the channel, the low-frequency pseudosound fluctuations are 5–7 dB lower than in the terminal part. At frequencies above 200 Hz, the piezoelectric composite receiver under study receives almost exclusively the sound component of the turbulent noise in the channel. This is evidenced by the fact that the spectral characteristic of its readings coincides with the spectrum recalculated from the readings of the hydrophone fixed in the diffuser (see Fig. 5). Thus, our experiments confirm the *a priori* evident assumption that a distributed transducer of considerable length is not affected by small-scale pressure fluctuations. The longer the receiver, the lower the frequencies at which it ceases responding to such fluctuations. Based on simple physical considerations, this fact can be explained by the averaging of the effect of small-scale fluctuations over the receiver area. It is also possible that a certain role in the suppression of the effect of fluctuations is played by the relatively thick polyurethane coating of the sensing element.

On the basis of the data obtained from our experiments, we can conclude that the use of distributed piezoelectric composite pressure receivers in underwater acoustics is possible and effective. The experiments confirmed that the receiver under study possesses the main property of distributed hydrophones: the immunity from turbulent pressure fluctuations. This property is primarily of interest for the reception of acoustic signals in the presence of turbulent hydrodynamic noise in the case of a moving receiver or in the presence of a flow around the receiver. It is well known that at high speeds of motion, the level of such a pseudosound noise can reach 120 dB. At the same time, experiments showed that with increasing speed and increasing scale of the fluctuations (i.e., in the lower frequency range), the receiver under study becomes sensitive to pseudosound. Thus, one can conclude that distributed piezoelectric composite receivers can also serve for hydrodynamic studies, e.g., for studying near-wall turbulence. Depending on the relations between the receiver dimensions (which can be easily varied in the course of its fabrication), the flow velocity, and the frequency range, such a receiver can detect the turbulent pressure fluctuations, i.e., the pseudosound, or the sound generated by the flow itself.

Other advantages of the receivers of the type under study, namely, the advantages determined by the nature of their material, are also important. They include high compliance, compatibility with surfaces of complex shapes, shock resistance, and relatively low wave resistance in combination with a sufficiently high sensitivity.

REFERENCES

1. T. A. Brungart, W. E. Holmberg, A. A. Fontaine, *et al.*, J. Acoust. Soc. Am. **108**, 71 (2000).
2. M. Kawai, Jpn. J. Appl. Phys. **8**, 973 (1969).
3. B. E. Newnham, D. P. Skinner, and L. E. Cross, Mater. Res. Bull. **13** (5), 525 (1978).
4. G. Sessler, J. Acoust. Soc. Am. **70**, 1596 (1981).
5. I. P. Golyamina and D. L. Rastorguev, in *Acoustics of the Oceanic Medium* (Nauka, Moscow, 1989), pp. 209–216.
6. W. Nitsche, P. Mirow, and J. Szodruch, Exp. Fluids, No. 7, 111 (1989).
7. W. Nitsche and P. Mirow, J. Fluid Mech. **71**, 136 (1994).
8. L. M. Lyamshev and S. A. Salosina, Akust. Zh. **12**, 261 (1966) [Sov. Phys. Acoust. **12**, 228 (1966)].
9. E. M. Greshilov, Akust. Zh. **31**, 320 (1985) [Sov. Phys. Acoust. **31**, 189 (1985)].
10. S. P. Gravante, A. M. Naguib, C. F. Wark, and M. M. Naguib, AIAA J. **36**, 1808 (1998).
11. *Underwater Acoustics* (Mir, Moscow, 1965).
12. E. M. Greshilov and M. A. Mironov, Akust. Zh. **29**, 460 (1983) [Sov. Phys. Acoust. **29**, 275 (1983)].
13. I. P. Golyamina, G. A. Lushcheĭkin, and D. L. Rastorguev, in *Proceedings of the IV Session of the Russian Acoustical Society* (1995), pp. 35–37.
14. *Piezoelectric Composite Polymer Material*, Technical Conditions TU 6-06-279-92.
15. E. M. Greshilov and T. N. Surgan, Akust. Zh. **18**, 316 (1972) [Sov. Phys. Acoust. **18**, 262 (1972)].

Translated by E. Golyamina

Acoustical Physics, Vol. 47, No. 4, 2001, pp. 398–404. Translated from Akusticheskiĭ Zhurnal, Vol. 47, No. 4, 2001, pp. 466–473.
Original Russian Text Copyright © 2001 by Guzhavina, Gulin.

Experimental Studies of Low-Frequency Reverberation on the Continental Slope in the Northwestern Pacific Ocean

D. V. Guzhavina and É. P. Gulin

Andreev Acoustics Institute, Russian Academy of Sciences, ul. Shvernika 4, Moscow, 117036 Russia

e-mail: bvp@akin.ru

Received December 29, 1999

Abstract—Experimental data obtained on the continental slope near the Kamchatka peninsula for the reverberation at the frequencies 230, 600, and 850 Hz in the cases of coincident and spaced source and receiver of sound are presented. The data include the dependences of the reverberation level on time for both directional and omnidirectional receiving systems, as well as the dependences of the reverberation level on the duration of the probing pulses and on the sea depth at the source site. It is shown that, at the frequency 230 Hz, a substantial contribution to the reverberation is made by the reflection and scattering on the shelf near the coastline and in the region of the "depth drop." At the frequencies 600 and 850 Hz, the predominant mechanism is bottom and surface scattering in the region of the continental slope. © *2001 MAIK "Nauka/Interperiodica".*

In recent years, much attention has been given to the studies of sound reverberation in shallow-water ocean regions, including the coastal zones of the outlying seas and the areas of the continental slope [1–10]. At low frequencies (below 1 kHz), the reverberation is governed by sound scattering from the sea floor and the rough water surface. If the sound signals are received by acoustic systems located within coastal wedge zones (at a shelf), substantial contributions can be made by the local reflections from some areas of the coastal slope and from the signals refracted by the coastal wedge. For such regions, the reverberation characteristics are difficult to predict, because there is no exact solution to the problem of sound propagation in wedge-shaped regions with realistic bottom parameters, which, in addition, are not always known. The existing approximate methods of estimating the reverberation level in the coastal wedge [4, 11] are based on the ray approach and use the effective sea-floor characteristics, which are specified in an empirical way. However, these methods provide no full description of the reverberation for all scattering areas of the bottom and surface. Therefore, the experimental studies of the reverberation in coastal regions with different reliefs and structures of the sea floor are quite important, because nothing but the experiments can confirm or disprove the proposed prognostic model of reverberation. Revealing the empirical features for different characteristics of the shelf and continental-slope reverberation is an unavoidable stage in constructing a computational model that adequately describes the realistic reverberation-forming mechanisms.

In this paper, we consider the results of the experimental studies of the low-frequency reverberation, which were carried out in the mid-1980s in the northwestern Pacific on the continental slope near the Kamchatka peninsula. The main experimental results are concerned with the intensity characteristics of the reverberation. At distances of 25 to 75 km from the coastline (as measured along the shortest path) at sea depths of 200 to 3400 m, pulsed CW signals were transmitted from a research vessel. The signals had the carrier frequencies 230, 600, and 850 Hz and durations 2–30 s. The sound sources, weakly directional in the vertical and omnidirectional in the horizontal, were at a depth of about 100 m. For sound reception, an omnidirectional hydrophone was used that was deployed from the vessel to a depth of 150 m; the horizontal distance from the hydrophone to the vessel was about 100 m in order to decrease the interfering noise. The sound signals were also received by a separate omnidirectional hydrophone of a multielement horizontally elongated antenna array, and by individual beams of this array, which was bottom-moored in the region of the inclined sea floor, at a depth of about 180 m near the depth drop at the boundary between the shelf zone and the continental slope.

The region of the experiment was characterized by an underwater sound channel with a shallow (70–75 m) axis (Fig. 1a). Figure 1b shows the smoothed seafloor relief that illustrates the bottom slopes on the path along the shortest line to the coast. These slopes were about 5° near the coast; they decreased to 0.2°–1° at the shelf at distances up to 20 km (the sea depths h up to 200–250 m), and increased up to 10°–16° in the vicinity of the depth drop (where the depth changed most steeply) at distances of 20–30 km (at h = 300–2000 m). In other directions, in some regions near the depth

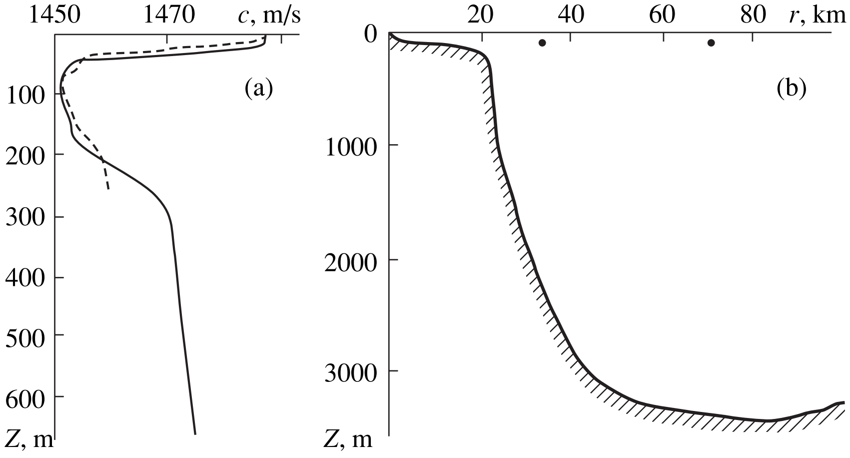

Fig. 1. (a) Vertical distribution $c(z)$ of the sound speed and (b) the bottom profile along the shortest path to the coast for the region of the experiment. The position of the transmitting–receiving system in the continental slope region is indicated.

drop, the slopes reached 25°–30°. Within the distances 30–80 km at h = 2–3.5 km, the slopes decreased from 5° to 0.2°–0.5° and were no higher than several tenths of a degree at 80–150 km from the coast at h = 3–3.5 km. For paths that were perpendicular to the aforementioned one, at the shelf and at the continental slope beyond the region of the depth drop, the bottom slopes did not exceed several degrees in magnitude at distances up to 150 km from the sound sources. According to the synoptic measurements, the wind speed was 3 to 6 m/s during the experiment and the maximal height of surface waves (within a sequence of 10 waves) was 1.5–2 m (for both swell and wind-generated waves).

Figures 2 and 3 illustrate the time decay of the reverberation intensity. Here, reverberation envelopes smoothed over 10 s and averaged over several realizations in the case of the reception by the omnidirectional hydrophone deployed from the transmitting vessel with the duration T_0 = 10 s of the probing pulses are presented. The repetition period of the pulses was 300 s. The time delays t_d measured relative to the initial moment of transmission are represented by the abscissa axes of the plots. On the ordinate axes, the values of the total intensity I_Σ, which is a sum of the reverberation intensity I_r and the interference noise I_n, are shown in decibels relative to 1 Pa^2. At all three frequencies, the 0-dB level corresponds to –85 dB relative to the transmission level (with an accuracy of 1 dB). At the frequency 230 Hz (Fig. 2), for different sea depths h at the transmission points and different distances from the coastline, a rather sharp decrease in the reverberation level is observed in the initial part ($t_d \lesssim 30$ s) of the time dependence with a following considerable increase in the level for higher t_d values corresponding to longer distances from the coastline. At h = 3400 m (Fig. 2a), the reverberation level is lower than that of the noise within the range of delays t_d = 30–60 s. Within the range t_d = 60–150 s, two reverberation maximums are observed at t_d = 70–72 s and t_d = 100–103 s. The first (the lower) maximum being corrected for the value $\bar{c}\,T_0/2$ (where $\bar{c}$ is the mean horizontal sound speed)

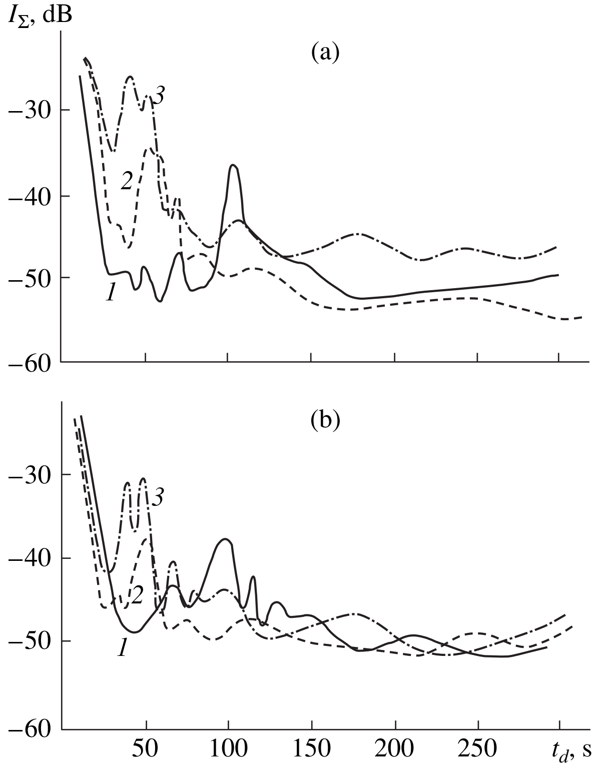

Fig. 2. Examples of smoothed time dependences of the total reverberation and noise intensity I_Σ at the frequency 230 Hz. Two averaged realizations, (a) and (b), are obtained for different distances r_1 from the source to the coast (along the shortest path), different sea depths h at the source site, and different time lags Δt: $r_1 \cong$ (*1*) 71, (*2*) 34, and (*3*) 25 km; h = (*1*) 3400, (*2*) 2000, and (*3*) 250 m; and $\Delta t \cong$ (*1*, *2*) 1 h and (*3*) 10 min. The duration of the probing pulses is T_0 = 10 s.

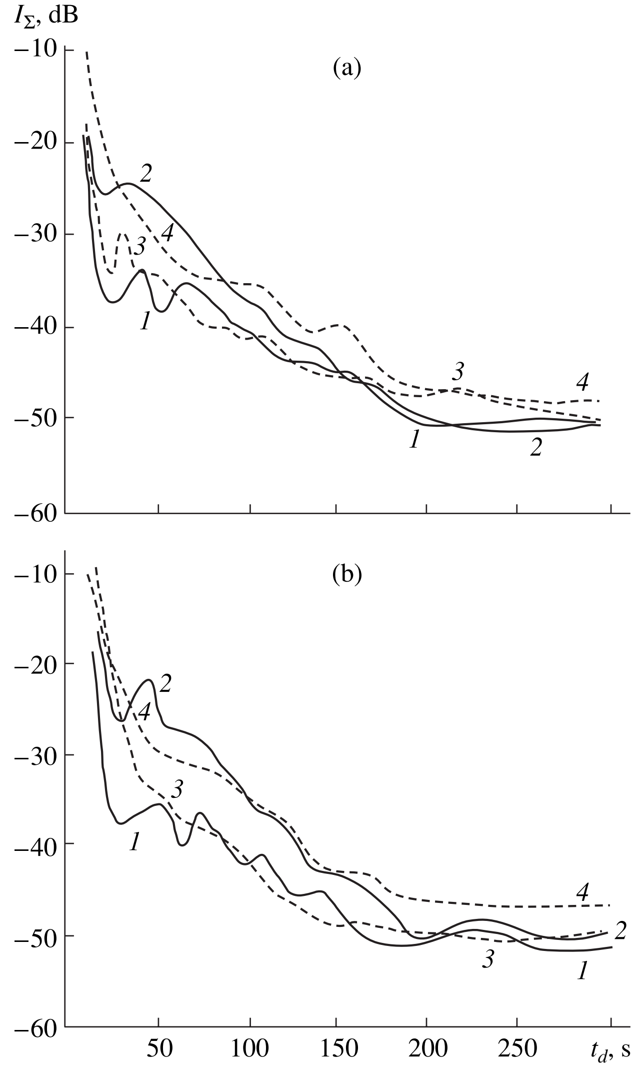

Fig. 3. Examples of smoothed time dependences for the reverberation intensity at the frequencies (*1*, *3*) 600 and (*2*, *4*) 850 Hz, $r_1 \cong$ (*1*, *2*) 71 and (*3*, *4*) 34 km, and $h =$ (*1*, *2*) 3400 and (*3*, *4*) 2000 m for two averaged realizations, (a) and (b), obtained with a time lag of 1 h. $T_0 = 10$ s.

corresponds to a distance of 46–49 km. According to the map of the region at hand, this distance proved to be close to that from the transmitting–receiving system to the region of the depth drop with mean bottom slopes of 20°–25°. The second maximum (with the same correction) corresponds to a distance of 70–72 km, which, up to 1 km, coincides with the minimal distance r_1 to the coastline, as the map indicates. These data show that, for the time delays at hand, the reverberation is mainly determined by the sound reflection and scattering within a narrow coastal zone. The slow decay of the reverberation level, which is observed for the delays exceeding 110–120 s, is governed by the scattering and local reflections in the coastal zone at distances from the coastline that are longer than the minimal one (r_1). Similar conclusions were drawn from analyzing the experimental data [2] obtained in analogous conditions of the continental slope near the Kamchatka peninsula when the low-frequency reverberation was received by a horizontal omnidirectional system and bistatic scattering geometry took place (with spatially separated transmission and reception points).

For different realizations from the sequence of pulses separated by 300 s, the effective width of the second reverberation maximum was estimated. According to these estimates, in view of the coastline shape and the positions of the 20–100-m isobaths, the dimensions of the scattering coastal region proved to be no greater than 15–45 km along the coastline and 4–7 km along the scattering direction. As measured at a level of 6 dB above the noise within the 2.5-Hz filter band, the time of reverberation is 30–40 s, which corresponds to the maximal distances 90–100 km from the coast with a scattering region of 100–110 km along the coastline. At $t_d > 200$–250 s, hardly any traces of the reverberation are observed, and the background noise predominates at a level of –(49–53) dB.

As the distance from the coast decreases according to the profile of the continental slope, the sea depth decreases, the reverberation maximum related to the scattering and reflection from the narrow coastal region is shifted towards lower time delays, and the reverberation intensity corresponding to this maximum increases. At $r_1 = 34$ km and $h = 2000$ m, the maximum corresponds to the delays $t_d = 50$–52 s; at $r_1 \cong 25$ km and $h \cong 250$ m, it corresponds to $t_d \cong 39$–40 s. In view of the aforementioned correction for $\bar{c}\,T_0/2$, these values of t_d correspond to the above values of r_1 with an accuracy of 1 km. In the first case (at $r_1 \cong 34$ km), some realizations exhibit two unstable peaks at $t_d = 34$ and 66–70 s in addition to the main maximum. These additional peaks seem to be caused by local reflections at the shelf and distant bottom regions near the depth drop. The reflection from the depth drop, which, in this case, was at a minimal distance of 9 km, was masked by a high-level near-field reverberation. In the second case (at $r_1 \cong 25$ km and $h \cong 250$ m) when both transmission and reception points were located within the shelf zone, the main maximum was accompanied by two relatively stable peaks at $t_d \cong 51$ and 68 s. According to the map of the region, both additional peaks are caused by the scattering from the areas belonging to the bays. At $h =$ 2000 and 250 m, the effective reverberation time is equal to 70–80 s, which is lower than at $h = 3400$ m. The noise level increases by 4–6 dB when the path runs through the shelf zone. One can also notice that the drift-caused decrease from 500 to 250 m in h, which occurs in the vicinity of the depth drop, is accompanied by an increase in the reverberation level at its maximum while the distance from the coast changes insignificantly.

A somewhat different shape is exhibited by the smoothed time dependences of the reverberation intensity at the frequencies f = 600 and 850 Hz (Fig. 3). At the frequency 600 Hz, the intensity sharply decreases in the initial part of the dependence (at $t_d \lesssim$ 25–30 s). After that, it decays relatively slowly. When h = 3400 m and $r_1 \cong 71$ km, within a range of 30 to 100 s, the reverberation level is considerably (by at least 15 dB) higher than at the frequency f = 230 Hz. On the background of the increased reverberation level, the 230-Hz maximum caused by the reflection from the coast and corresponding to t_d = 100–110 s was not observed. This maximum is also absent at an even shorter distance from the coast ($r_1 \cong 34$ km, h = 2000 m). The contribution of the reflection and scattering from the coast area seems to manifest itself in a slower decay of the reverberation level at t_d > 30 s. Within the 2.5-Hz filter band, the traces of reverberation are pronounced against the noise background up to $t_{d\max} \cong$ 150 and 120 s, at h = 3400 and 2000 m, respectively. The lower values of $t_{d\max}$ at h = 2000 m can be attributed to the somewhat higher level of the interfering noise. At the frequency 850 Hz, the reverberation decay curves seem to be even smoother. In this case, within the range of delays 30–100 s, the reverberation level is 7–15 dB higher than at f = 600 Hz, and the decay is faster. No pronounced increase is observed in the reverberation intensity at the delays that correspond to the reflections from the coast. With the experimentally observed noise level, the duration of the reverberation signal increases up to about 160 s at the frequency 850 Hz.

According to the time dependences $I_\Sigma(t_d)$, different dependences of I_Σ on the distance from the coast r_1 (or on the sea depth h under the vessel carrying the transmitting system) are observed for different values of the time delay t_d at the frequency 230 Hz (Fig. 4). In Fig. 4, the experimental points are conventionally connected by straight lines (a smooth curve is used for $t_d = t_d^{(\max)}$, i.e., for the delays corresponding to the reverberation maximum). For greater time delays (120 to 150 s), the value of I_Σ, on the average, does not depend on h and r_1, while the levels of the reverberation and noise are comparable. For the delays $t_d \cong 100$ s, the maximal reverberation level corresponds to h = 3400 m. The level of I_r is noticeably lower at depths h = 200–2000 m. At small delays ($t_d \cong 30$ s), the level of the near-field reverberation weakly depends on h within a range of 300–3400 m. However, this level increases by 5–6 dB in the shelf zone (at $h \cong 200$ m). An increase in the reverberation level is also observed at the shelf and in the vicinity of the depth drop (h = 200–600 m) for t_d = 70 s. At the maximums corresponding to the reflections from the coast ($t_d = t_d^{(\max)}$), the reverberation intensity increases as the depth h and the distance from the coast decrease, this behavior being quite explainable.

Additional information can be extracted from the dependences of the reverberation intensity on the duration T_0 of the probing pulses (Fig. 5). At the frequency 230 Hz (Fig. 5a), both at small delays (t_d = 30 s, the near-field reverberation) and at large ones (t_d = 120 s), the values of I_Σ, on the average, increase proportionally to T_0 beyond the reverberation maximum. The somewhat higher level of I_Σ observed at T_0 = 2 s can be explained by the fact that the levels of reverberation and noise are comparable in this case. At the reverberation maximum ($t_d \cong 100$ s), the values of $I_\Sigma \cong I_r$ increase proportionally to T_0 within the range of delays 2–10 s. However, at higher T_0 (up to 30 s), the reverberation intensity remains nearly constant. This behavior can be explained by the finite size of the effectively scattering area, which is no greater than the size of the area covered by the pulse with a 10-s duration in the case of back-scattering in the coastal region. Thus, being estimated from the width of the reverberation maximum and from the dependence of the maximal reverberation level on the duration of the probing pulse, the dimensions of the effectively scattering area prove to be nearly the same at the frequency 230 Hz.

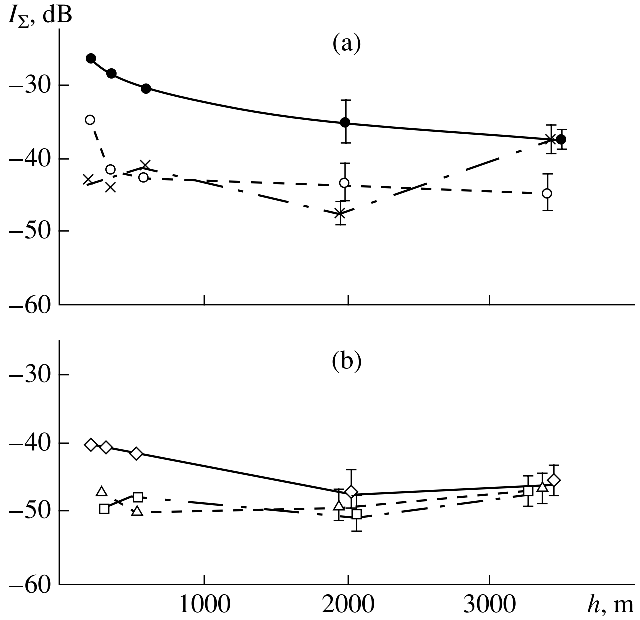

Fig. 4. Dependence of the total intensity I_Σ of reverberation and noise on the sea depth h at the source site at the frequency 230 Hz for different time delays: t_d = (○) 30, (◇) 70, (×) 100, (△) 120, and (□) 150 s; (●) $t_d = t_d^{\max}$.

The reverberation intensity ($I_r \cong I_\Sigma$) increases proportionally to the pulse duration T_0 within the entire range of T_0 (2–30 s) for different time delays at the frequencies 600 and 850 Hz (Fig. 5b). Such a proportionality is evidence of a more uniform distribution of the scatterers responsible for the reverberation at these frequencies.

From the data on the reverberation at the three frequencies, one can approximately estimate the frequency dependence of the reverberation intensity for the continental slope. The frequency dependence is

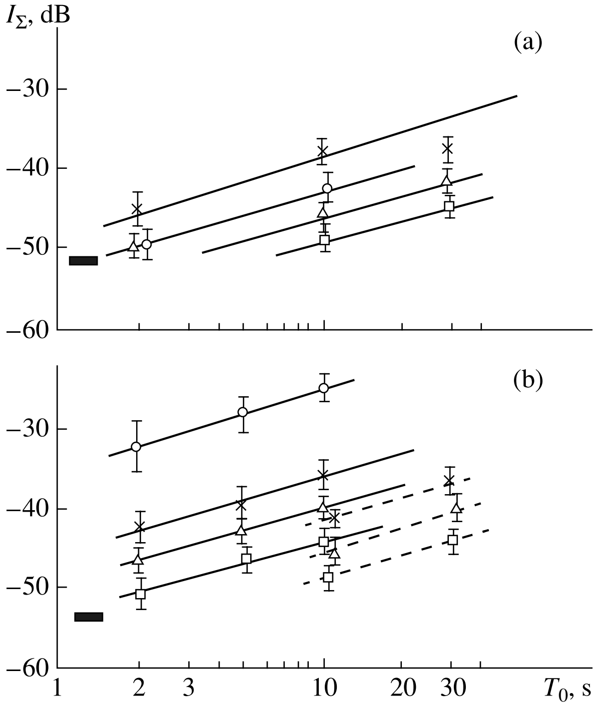

Fig. 5. Dependence of the total intensity I_Σ on the duration of the probing signals at the frequencies (a) 230 Hz and (b) 600 and 850 Hz for $r_1 \cong 71$ km, $h = 3400$ m, and different time delays: t_d = (○) 30, (×) 100, (△) 120, and (□) 150 s. The solid curves show the dependences $I_\Sigma \sim T_0$ for the frequencies (a) 230 and (b) 850 Hz. The dashed curves show the dependence $I_\Sigma \sim T_0$ for the frequency 600 Hz. The levels of the interfering noise are indicated as ▬.

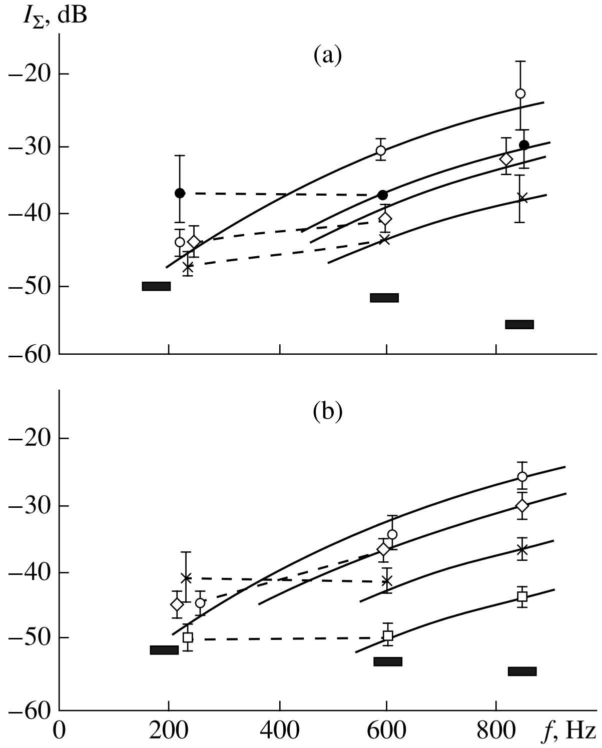

Fig. 6. Frequency dependences of the total intensity I_Σ for $r_1 \cong$ (a) 34 and (b) 71 km, h = (a) 2000 and (b) 3400 m, and for different time delays t_d = (○) 30, (●) 50, (◇) 70, (×) 100, and (□) 150 s. The solid curves show the dependences $I_\Sigma \sim f^4$. $T_0 = 10$ s.

strongly influenced by the nonmonotone time dependence of I_r at the frequency 230 Hz, which leads to different rates of increase in the frequency dependences of I_r at different time delays (Fig. 6). Thus, for the near-field reverberation ($t_d \cong 30$ s), the experimental data agree well with the frequency dependence $I_r \cong I_\Sigma \sim f^4$, which corresponds to the bottom scatterers that are small relative to the wavelength and to the resonant surface scatterers (for a certain form of the spectrum of surface elevations). The same frequency dependence occurs at greater t_d for the frequencies 600 and 850 Hz. At the same time, for the frequency band 230–600 Hz, a weaker frequency dependence is typical, which is related to an increase in the reverberation level at 230 Hz due to reflection and scattering in the coastal zone. For the delays that correspond to the reverberation maximum at 230 Hz, and for even larger delays, the reverberation intensity nearly does not change when the frequency changes from 230 to 600 Hz (the experimental values of I_Σ obtained at these two frequencies are connected by the dashed straight lines). At $t_d = 70$ s and $h = 3400$ m (Fig. 6b), reverberation peaks are observed that are caused by the scattering in the vicinity of the depth drop, and the reverberation intensity considerably increases when the frequency changes from 230 to 600 Hz, though this increase is slower than $I_r \sim f^4$.

To estimate the parameters of the decay law for the reverberation intensity $I_r(t)$ in more detail, we used the least squares method in approximating the dependence $I_r(t)$ by the expression $I_r(t) = I_{r0}(\bar{c}\,t)^{-n} \times 10^{-0.1\beta\bar{c}t}$ where the value of $\bar{c}$ was specified to be 1.47 km/s. At the frequency 230 Hz, the parts of the reverberation envelopes that followed the maximum and corresponded to the reflection from the coast were processed. At the frequencies 600 and 850 Hz, the processing procedure was performed for the delays from 20–30 to 150 s. Prior to processing, the reverberation envelopes were averaged over 5 s. Three modifications of the processing procedure were used. First, the value of β was specified to be equal to the absorption coefficient in sea water according to the formula $\beta = 0.036f^{3/2}$ (dB/km), where f is measured in kilohertz and the exponent n was determined. Second, the values of n were specified for different laws of the spread of the wave front in the course of the sound propagation and for different range dependences of the effective coefficient of sound scattering; in this case, the value of β was determined. Third, with the use of the least squares method, all three parameters (n, β, and I_{r0}) that govern the approximating law were determined.

Processing the 230-Hz data provided unsatisfactory results: the value obtained for n varied within wide limits, from 3 to 8–12, and β took negative values for some realizations. This situation evidences that the chosen approximation is not adequate for the reverberation caused by sound reflection and scattering in the coastal region. If the values of β are chosen to be equal to the absorption coefficients at the frequencies 600 and 850 Hz, the best approximation is obtained with the values n = 1.7–2.8 and 2–3.7, respectively. For the cylindrical and spherical spread laws, the values $n > 1$ and $n > 2$, respectively, can be observed only if the scattering coefficient decreases as the distance increases. On the other hand, the overestimated values of n can be a consequence of underestimated values of β, which ignore the additional attenuation caused by the leakage of the sound energy into the sea floor. At $n = 2$ (the most frequent case in approximating the experimental dependence $I_r(t)$), the values $\beta \cong 0.03$–0.08 dB/km obtained by the least squares method are two to three times higher than the absorption coefficient. These values of β agree well with the experimental estimates of the effective coefficient of spatial sound attenuation in the region at hand. Note that the chosen approximation of $I_r(t)$ with $n = 2$ corresponds to the 3/2 power law (with the exponential factor) for the range dependence of the direct field if the scattering coefficient is range-independent. This approximation also agrees with the cylindrical law of the wave front spread if the scattering coefficient is inversely proportional to range.

The experimental data presented above are obtained with nearly coincident transmission and reception points, i.e., for the case of a monostatic reverberation. Let us now consider the experiment with a widely spaced transmitter and receiver, i.e., with a bistatic geometry of scattering. Figure 7 shows the examples of the reverberation envelopes obtained in this case. The ordinate axis represents the values of I_r in decibels relative to the maximal level for each realization. The abscissa axis shows the time delays that are measured relative to the arrival time $\tilde{t}_d$ of the direct signal. With omnidirectional reception at the frequency 230 Hz (Fig. 7a), the time dependences of the reverberation intensity are similar in their shapes to those obtained with the coincident transmitter and receiver. However, the delay $\tilde{t}_d^{(\max)} \cong 32$–$34$ s of the reverberation maximum formed by the reflection from the coast does not depend on the minimal distance r_1 from the coastline: it is fully determined by the distance $r_2 = \bar{c}\tilde{t}_d^{(\max)}/2$ (for $r_2 < r_1$) from the receiving system to the coast. In receiving with the system whose horizontal directivity pattern (DP) has a main lobe approximately 8° in width, the reverberation level, as measured relative to the level of the direct signal, is significantly (by 15–25 dB for different realizations) lower than that measured with the omnidirectional receiver (Fig. 7a) at the same frequency. The effective reverberation duration also decreases from about 100 s to 40–50 s. These features can be explained by the fact that the strongly scattering area of the coastal zone becomes screened at $\tilde{t}_d \gtrsim 30$ s, and, at $\tilde{t}_d \cong 20$–30 s; the size of the scattering area is reduced by the DP of the receiver. The reverberation level is also lower relative to the noise level because of the horizontal anisotropy of the reverberation, which is much more pronounced than that of the interfering noise.

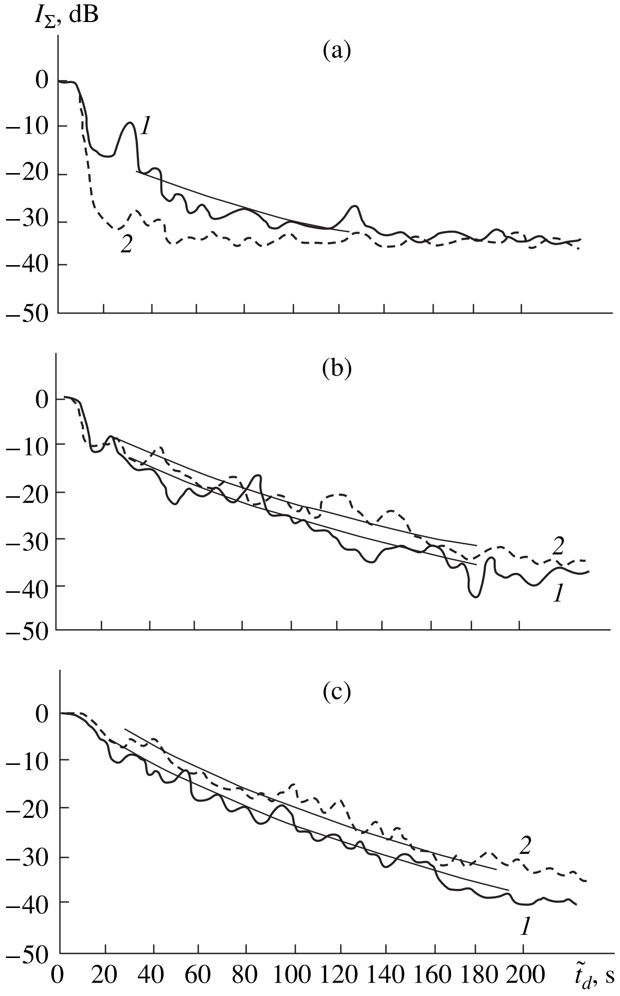

Fig. 7. Examples of time dependences of the total intensity I_Σ of reverberation and noise for spaced transmission and reception points at the frequencies (a) 230, (b) 600, and (c) 850 Hz for (*1*) omnidirectional and (*2*) directional receivers: $r_1 \cong$ (a) 71, (b) 31, and (c) 43 km; h = (a) 3400, (b) 1400, and (c) 2500 m; T_0 = 10 s. The approximating curves are also presented.

At the frequencies 600 and 850 Hz, no pronounced maximums occur in the reverberation envelopes (Figs. 7b, 7c). The use of narrower DPs of the receivers (with the widths 3° and 2° of the main lobes at f = 600 and 850 Hz, respectively) does not lead to a significant decrease in the reverberation level relative to that of the noise. This may be due to a more uniform angular distribution of the reverberation in the horizontal, as compared to the case with the frequency 230 Hz. The normalized reverberation envelopes obtained with the directional reception lie in Figs. 7b, 7c even higher than those obtained with omnidirectional reception. This behavior can be attributed to the deviation of the axis of the array DP from the direction to the source of radiation. The decay rate of the reverberation nearly does not depend on the distance r_1 from the sound sources to the coast and on the sea depth h under the transmitting vessel within the ranges $r_1 = 28–72$ km and $h = 1400–3400$ m. The estimates were obtained by the least squares method for the approximating expression differing from that used in the monostatic case in replacing $(\bar{c}\, t_d)^{-n}$ by $[\bar{c}\tilde{t}_d\,(\bar{c}\tilde{t}_d + 2D)]^{-n/2}$, where D is the distance between the source and the receiving array. For both omnidirectional and directional reception, the estimates agree well with the experimental data if the following values of the parameters are specified: $n = 2$, $\beta = 0.04–0.05$ dB/km at $f = 600$ Hz and $\beta = 0.06–0.07$ dB/km at $f = 850$ Hz.

Thus, the experimental data presented above reveal a number of features in the low-frequency reverberation at the continental slope of the northwestern Pacific. At the frequency 230 Hz, a substantial contribution to the reverberation is made by the sound reflection and scattering within a narrow layer of the coastal zone. At the frequencies 600 and 850 Hz, the scattering on the bottom and the surface predominates in both shallow-water and deep-water regions of the continental slope. The data obtained can be used to develop computational models that describe the intensity characteristics of the low-frequency reverberation on a continental slope and in a shelf zone. The data can also be used for estimating the interfering noise due to the reverberation, which influences the sonar systems operating in such regions.

ACKNOWLEDGMENTS

We are grateful to V.A. Akulichev, L.F. Bondar’, K.I. Malyshev, V.I. Moiseenkov, and Yu.I. Morgunov for assistance in preparing and performing the experimental studies.

REFERENCES

1. V. S. Averbakh, L. F. Bondar’, V. N. Golubev, *et al.*, Akust. Zh. **36**, 1119 (1990) [Sov. Phys. Acoust. **36**, 625 (1990)].
2. I. B. Andreeva and V. N. Lupovskiĭ, Akust. Zh. **39**, 564 (1993) [Acoust. Phys. **39**, 297 (1993)].
3. M. Yu. Andreev, Akust. Zh. **39** (4), 751 (1993) [Acoust. Phys. **39** (4), 395 (1993)].
4. D. I. Abrosimov, V. S. Averbakh, E. I. Bolonicheva, *et al.*, Akust. Zh. **41**, 364 (1995) [Acoust. Phys. **41**, 315 (1995)].
5. R. A. Vadov, D. V. Guzhavina, and S. I. Dvornikov, Akust. Zh. **43**, 409 (1997) [Acoust. Phys. **43**, 350 (1997)].
6. R. Yu. Popov and E. V. Simakina, Akust. Zh. **40**, 655 (1994) [Acoust. Phys. **40**, 580 (1994)].
7. Shishido Masaaki, J. Acoust. Soc. Jpn. **53**, 552 (1997).
8. K. L. Williams and D. R. Jackson, J. Acoust. Soc. Am. **103**, 169 (1998).
9. D. H. Berman, J. Acoust. Soc. Am. **105**, 672 (1999).
10. V. M. Kudryashov, Akust. Zh. **45**, 363 (1999) [Acoust. Phys. **45**, 320 (1999)].
11. I. B. Andreeva and V. N. Goncharov, in *Problems of the Ocean Acoustics* (Nauka, Moscow, 1984), pp. 69–77.

Translated by E. Kopyl

Acoustical Physics, Vol. 47, No. 4, 2001, pp. 405–414. Translated from Akusticheskiĭ Zhurnal, Vol. 47, No. 4, 2001, pp. 474–484.
Original Russian Text Copyright © 2001 by Gurbatov, Demin, Pasmanik.

Parametric Generation of Low-Frequency Sound in the Propagation of High-Intensity Modulated Noise

S. N. Gurbatov, I. Yu. Demin, and G. V. Pasmanik
Lobachevskiĭ State University, Nizhni Novgorod, pr. Gagarina 23, Nizhni Novgorod, 603600 Russia
e-mail: gurb@rf.unn.runnet.ru

Received July 17, 2000

Abstract—With the use of the one-dimensional Burgers equation, the evolution of a high-intensity noise with periodically modulated intensity is analyzed. The nonlinearity is shown to lead to partial suppression of the amplitude modulation and to the generation of a regular low-frequency component. The probability distributions and the power spectra of the field are studied. *© 2001 MAIK “Nauka/Interperiodica”.*

For high-intensity sound fields, the superposition principle is known to be violated, and the harmonics of the initial disturbance affect each other. Because of the absence of dispersion, the synchronism conditions are met for any arbitrary triplet of interacting collinear waves. Therefore, at high Reynolds numbers, the number of interacting harmonics grows in an avalanche-like manner [1, 2]. The higher the frequency of the new harmonic combination, the more efficient its generation. Hence, at the initial stage of the wave propagation, the generation of the highest harmonics predominates, which leads to the formation of discontinuities at which energy dissipates. In the case of a monochromatic disturbance, the wave transforms to a sequence of sawtooth pulses whose amplitudes do not depend on the initial amplitude and are proportional to the wave period. An arbitrary periodic wave acquires the same universal shape. However, if the spectrum of the initial signal contains nonmultiple frequencies, the nonlinear interaction will lead to both sum and difference combination frequencies. In spite of the fact that the generation efficiency is lower for the low-frequency difference components than for the high-frequency sum components, the low-frequency components attenuate slower, and, hence, they predominate in the asymptotic behavior of the sound field at long times.

For the propagation of a modulated high-frequency sound, the generation of the low-frequency components is much studied [2–4], because this process is what forms the basis for parametric sound emission. In the evolution of high-intensity, quasi-monochromatic, amplitude-modulated signals, the nonlinear effects are more pronounced in the high-amplitude parts of the wave. As a result, at the stage of developed discontinuities, the amplitude modulation proves to be totally suppressed. Since the generation efficiency for the low-frequency component is proportional to the derivative of the intensity of the high-frequency wave, nonlinear attenuation leads to saturation in the generation process for the low-frequency components at the stage of developed discontinuities. The interaction between the low- and high-frequency waves results in the coalescence of discontinuities in the pump wave and the high-frequency wave finally vanishes [5].

The objective of this paper is to analytically and numerically study the evolution of high-intensity sound signals that are harmonically modulated and have a noiselike carrier. This carrier is supposed to be of two widely different scales, the mean initial field being equal to zero. In this case, unlike the case with quasi-harmonic signals, the nonlinearity leads to a partial suppression of the amplitude modulation. The nonlinear processes also result in the generation of a nonzero mean sound field that characterizes the large-scale components of the wave. By asymptotically solving the Burgers equation at high Reynolds numbers, in view of the theory of random outliers, we analyze the properties of the mean field and the power spectrum of the wave.

The propagation of high-intensity plane sound waves is known to follow the Burgers equation. Here, we use this equation in its classical form [1]

$$\frac{\partial v}{\partial t} + v\frac{\partial v}{\partial x} = \nu\frac{\partial^2 v}{\partial x^2}, \tag{1}$$

where $v = v(x, t)$ is the velocity field and ν is the viscosity of the medium. Equation (1) is to be solved with the following initial condition:

$$v(x, 0) = v_0(x) = -\frac{d\psi_0(x)}{dx}, \tag{2}$$

where ψ_0 is the potential. For the problem of evolution of the sound signal, the initial condition $v_0(x)$ corresponds to the field at the sound source, x is analogous to time, and the variable t in Eq. (1) is proportional to the distance from the starting point.

We consider the case of infinitely high Reynolds numbers when $\nu \longrightarrow 0$ and the solution of the Burgers equation takes the form

$$v(x,t) = \frac{x - y(x,t)}{t}, \tag{3}$$

where $y(x, t)$ is the coordinate y at which the function

$$\phi(x,y,t) = \psi_0(y) - \frac{(x-y)^2}{2t} \tag{4}$$

reaches its global maximum at fixed x and t. This solution is the limiting Hopf and Cole solution for $\nu \longrightarrow 0$. At the same time, it can be treated as a generalized solution to Eq. (1) with $\nu = 0$ and with the conservation conditions at discontinuities. The aforementioned solution is known as the Oleinik–Lax construction [6], which is valid for both plane waves and one-dimensional waves of nonplane geometric properties. Here, the variable t plays the role of a normalized coordinate. For instance, if the waves are spherical, $t = \sigma_0 \ln r/r_0$, where r_0 denotes the radius of the spherical sound source.

In this paper, we consider the evolution of modulated signals whose initial potential can be represented as

$$\psi_0(x) = M(x)F(x), \tag{5}$$

where $F(x)$ is the potential of the carrier signal with the characteristic spatial scale l_0, and $M(x)$ is the modulating function with the spatial scale $L_0 \gg l_0$. When $L_0 \gg l_0$, Eq. (2) can be used to obtain the following form of the initial velocity field:

$$\begin{gathered} v_0(x) = m(x)f(x), \\ m(x) \approx M(x), \quad f(x) \approx -F'(x). \end{gathered} \tag{6}$$

We assume that the carrier signal $f(x)$ is a stationary Gaussian noise with zero mean value, $\langle f(x)\rangle = 0$, and with the initial intensity spectrum

$$E_0(k) = \frac{1}{2\pi}\int \langle f(x)f(0)\rangle e^{ikx}dx = \alpha^2 k^n b_0(k). \tag{7}$$

Here, $b_0(k)$ is a nonnegative function rapidly decreasing at $k > k_*$, and the value of the exponent n meets the condition $n \geq 2$, which is typical of sound signals.

Let us briefly describe the evolution of the stationary noise at high Reynolds numbers. The behavior of a random field that obeys Eq. (1) is usually called the Burgers turbulence. In the limit of infinitely low viscosity ($\nu \longrightarrow 0$), the continuous initial field $v_0(x) = f(x)$ transforms to a sequence of sawtooth pulses that have identical slopes $\frac{\partial v(x,t)}{\partial x} = \frac{1}{t}$ and random positions of discontinuities. Because of the coalescence of discontinuities, their number decreases, and, hence, the characteristic spatial scale of the field $l(t)$ increases. To statistically analyze the random field $v(x, t)$, it is advantageous to use solutions (3) and (4), which reduce the Burgers equation to the problem of finding the coordinate of an absolute maximum of the function $\phi(x, y, t)$. The statistical properties of the coordinate of the absolute maximum, $y(x, t)$, and, hence, those of the field $v(x, t)$, Eq. (3), can be studied by using the theory of outliers in random processes [7, 8]. The evolution of the field essentially depends on the behavior of the power spectrum $E_0(k)$ (Eq. (7)) of the stationary noise in the region of small wave numbers and also on the statistics of the initial field when $n \geq 2$ [7, 9–12]. For sound fields, the situation when $n \geq 2$ is most typical: there are no large-scale components at low frequencies. Because of multiple coalescence of discontinuities, at long times, all statistical characteristics of the Burgers turbulence become automodelling and are governed by a single scale $l(t)$, i.e., by the integral scale of turbulence [7]. If the statistics of the initial field is Gaussian, the integral scale $l(t)$ evolves according to the expression

$$l(t) = (t\sigma_\psi)^{1/2}\ln^{-1/4}\left(\frac{t\sigma_v^2}{2\pi\sigma_\psi}\right) \simeq l_0\left(\frac{t}{t_{nnl}}\right)^{1/2}. \tag{8}$$

Here, σ_v^2 and σ_ψ^2 are the variances for the velocity field and its potential, respectively; l_0 is the initial integral scale; and t_{nnl} is the characteristic time for the nonlinear effects in the noise:

$$\begin{gathered} \sigma_v^2 = \langle v_0^2\rangle, \quad \sigma_\psi^2 = \langle \psi_0^2\rangle, \\ l_0 = \frac{\sigma_\psi}{\sigma_v}, \quad t_{nnl} = \frac{l_0}{\sigma_v}. \end{gathered} \tag{9}$$

At the stage of developed discontinuities, the spectrum of the turbulence has the automodelling character:

$$E(k,t) = \frac{l^3(t)}{t^2}\tilde{E}(kl(t)) \tag{10}$$

with universal asymptotic forms $E(k, t) \sim t^{-3/2}k^{-2}$ and $E(k, t) \sim t^{1/2}k^2$ at high and low frequencies, respectively. The spectral maximum is displaced toward low frequencies $\sim l^{-1}(t)$. The coalescence of the discontinuities and the increase in the characteristic scale $l(t)$ lead to a slower attenuation of turbulence in comparison with the periodic signal:

$$\begin{aligned} \bar{E}(t) &= \langle v^2\rangle \\ &= \frac{l^2(t)}{t^2} = \frac{\sigma^\psi}{t}\ln^{-1/2}\left(\frac{t\sigma_v^2}{2\pi\sigma_\psi}\right) \simeq \sigma_v^2\left(\frac{t_{nnl}}{t}\right). \end{aligned} \tag{11}$$

Next, we consider the evolution of the modulated noise, Eqs. (5) and (6), for which we have $\langle v_0(x)\rangle = \langle \psi_0(x)\rangle = 0$ as well. If $L_0 \gg l_0$, the variances $\sigma_{M,v}^2(x)$ and $\sigma_{M,\psi}^2(x)$ of the velocity and the potential are respectively equal to

$$\sigma_{M,v}^2(x) = M^2(x)\sigma_v^2, \quad \sigma_{M,\psi}^2(x) = M^2(x)\sigma_\psi^2. \tag{12}$$

At the initial stage ($t < t_{nnl}$), when the formation of the discontinuities can be neglected, the Riemann equation is applicable to the evolution of the initial field of the modulated noise. In this case, the probability density $W_v(v; x, t)$ has the following form (see [7], Chap. 4.1):

$$W_v(v; x, t) = \frac{\partial}{\partial v}\int_{-\infty}^{v} W_0(z; x - vt)dz = \frac{\partial}{\partial v}F_0(v; x - vt), \quad (13)$$

where $W_0(z; x)$ and $F_0(v; x)$ are the probability density and the integral distribution function for the initial velocity field $v_0(x)$, respectively.

Let us assume that the initial field $v_0(x)$ has the variance $\sigma^2_{M,\,v}(x) = \sigma^2_v M^2(x)$, and its distribution function $W_0(v; x)$ can be represented as

$$W_0(v; x) = \tilde{W}_0\left(\frac{v}{\sigma_{M,\,v}(x)}\right)\frac{1}{\sigma_{M,\,v}(x)}, \quad (14)$$

where $\tilde{W}_0(\xi)$ is a dimensionless function with zero mean value $\langle\xi\rangle = 0$, and unity variance $\langle\xi^2\rangle = 1$. Then, from Eq. (13), we find the probability density for the Riemann wave:

$$W_v(v; x, t) = \tilde{W}_0\left(\frac{v}{\sigma_v M(x - vt)}\right) \times \frac{1}{\sigma_v M(x - vt)}\left(1 + vt\frac{M'_x(x - vt)}{M(x - vt)}\right). \quad (15)$$

Equation (15) shows that, as a result of nonlinear evolution, the probability density of the nonstationary Riemann wave is distorted, this evolution being governed by nothing but the single-point probability distribution of the initial field and the shape of the modulating function. Note that, for a stationary signal with $M(x) = \text{const}$, we have a well-known result: the probability density is conserved for the Riemann wave [7].

Let us consider the generation of the regular component, i.e., the mean field

$$\langle v(x, t)\rangle = \int_{-\infty}^{+\infty} vW_v(v; x, t)dv. \quad (16)$$

By substituting Eq. (15) into Eq. (16) and changing to a new integration variable, $\xi = v/\sigma_v M(x - vt)$, we obtain

$$\langle v(x, t)\rangle = \int_{-\infty}^{+\infty} \xi\sigma_v M(x - v(\xi, x, t)t)W_0(\xi)d\xi, \quad (17)$$

where $v(\xi, x, t)$ is the solution to the equation $\xi = v/\sigma_v M(x - vt)$. At the initial stage ($t < t_{nnl}$), when the displacement of the wave profile is much smaller than the characteristic scale L_0 of the envelope, we can specify $\xi = v/\sigma_v M(x)$. Then, from Eq. (17), we obtain

$$\langle v(x, t)\rangle = -\frac{1}{2}\sigma_v^2 t\frac{d}{dx}M^2(x), \quad (18)$$

i.e., the mean field increases linearly with time and the field profile is proportional to the derivative of the squared envelope.

When $t > t_{nnl}$, both the nonlinear attenuation of the carrier and the increase in the internal scale of the field, which is caused by the coalescence of discontinuities, become significant. For a nonstationary noise, energy density $\bar{E}(x, t)$ and the scale $l(x, t)$ depend on the x coordinate. If $l(x, t)$ is much greater than the initial scale l_0 but much smaller than the modulation scale, one can use the quasi-static approximation. Then, we can assume that the integral scale $l(x, t)$ of the carrier and the energy density $\bar{E}(x, t)$ obey Eqs. (8) and (11) and are slowly varying functions of the x coordinate:

$$l_M(x, t) = M^{1/2}(x)l_0\left(\frac{t}{t_{nnl}}\right)^{1/2}\ln^{-1/4}\left(\frac{M(x)t}{2\pi t_{nnl}}\right). \quad (19)$$

$$\bar{E}(x, t) = \frac{l_M^2(t, x)}{t^2} = M(x)\sigma_v^2\left(\frac{t}{t_{nnl}}\right)^{-1}\ln^{-1/2}\left(\frac{M(x)t}{2\pi t_{nnl}}\right). \quad (20)$$

It follows from Eq. (20) that nonlinear attenuation leads to partial suppression of the amplitude modulation for the wave with the noise carrier, $\bar{E}(x, t) \sim M(x)$, while at the input of the process, we have $\bar{E}(x, 0) \sim M^2(x)$. The partial conservation of the modulation can be explained by the fact that even at $t \gg t_{nnl}$, the noise energy depends on the initial energy $\bar{E}(x, t) \sim \sigma_v M(x)l_0/t$. Note that for a quasi-harmonic signal, $\bar{E}(x, t) \sim l_0^2/t^2$, which does not depend on the amplitude of the input signal.

We neglect the nonlinear distortions of the large-scale component, which now coincides with the mean field $v_l(x, t) = \langle v(x, t)\rangle$, and use the Burgers equation (1). Then, in the quasi-static approximation, we obtain the following expression for v_l:

$$\frac{\partial v_l(x, t)}{\partial t} = -\frac{1}{2}\frac{\partial}{\partial x}\bar{E}(x, t). \quad (21)$$

At the initial stage ($t < t_{nnl}$), when the attenuation can be neglected and $\bar{E}(x, t) \sim M^2(x)$, Eq. (21) is reduced to Eq. (18). For a quasi-harmonic signal, the generation terminates at $t \gg t_{nnl}$, because the energy density becomes independent of the coordinate. However, for the noise signal, the generation of the mean field (the large-scale component) persists at the stage of developed discontinuities.

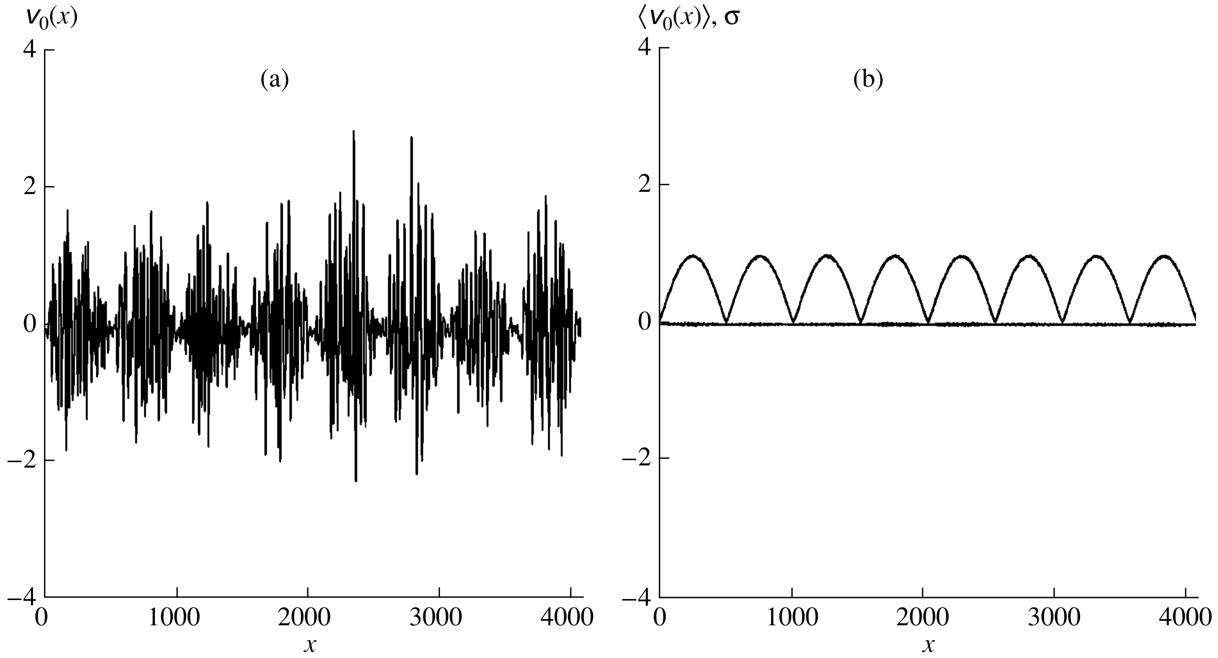

Fig. 1. (a) Profile of the initial velocity field $v_0(x)$, (b) its mean value $\langle v_0(x)\rangle = 0$ and variance $\sigma_{M,\,v} = \sigma_v M(x)$, $\sigma_v = 1$ (statistical averaging over 10000 realizations of the noise carrier).

To analyze the statistical characteristics of the field $v(x, t)$ at the stage of developed discontinuities, we use the asymptotic solution in the form of Eqs. (3) and (4). In our recent paper [13], we used this procedure to consider the evolution of pulsed noise signals. With modulated signals, let us now assume that the modulating function $M(x)$ is periodic with a period $L_0 = 2\pi/k_0$ and has a single maximum in a period at $x = 0$, where the approximation $M(x) = 1 - x^2/2L_*^2 + \ldots$ is valid. In numerical calculations, we specify $M(x) = |\sin k_0x/2|$. Figure 1 shows a realization of the initial field $v_0(x) = M(x)f(x)$ (Eq. (6)), where $f(x)$ is a stationary Gaussian noise with zero mean value $\sigma_v = 1$ (Eq. (7)), and with the averaged parameters $\langle v_0(x)\rangle$ and $\sigma_{M,\,v}$. Because mathematically the problem of evolution of a periodically modulated signal is close to that of evolution of a noise pulse, here we follow the cited paper [13] and present only the key points of the derivation procedure for the probability characteristics of the field $v(x, t)$.

Let us consider the statistical characteristics of the field at the stage of developed discontinuities when the integral scale $l_M(x, t)$ (Eq. (19)) of the field is much greater than the initial scale l_0; i.e., for times when the discontinuities in the noise carrier multiply coalesce. For the asymptotic solution given by Eqs. (3) and (4), this situation corresponds to times at which the parabola in Eq. (4) is a smooth function on the scale of the noise carrier. In this case, a large number of local maximums of the initial potential $\phi(x, y, t)$ “pretend” being the absolute maximum of the function $\psi_0(y)$, and, to analyze the statistics, one can use the limiting theorems of the theory of large outliers [7, 8].

Let us introduce the probability $P(H, y, y + \Delta y)\Delta H$ that the function $\phi(x, y, t)$ has the absolute maximum within the interval $(y, y + \Delta y)$, the value of this maximum falling within the interval $(H, H + \Delta H)$. This probability is expressed through the integral distribution function:

$$Q(H;\,\Delta y) = \mathrm{Prob}(\phi(x, y, t) < H, y \in (y, y + \Delta y)), \tag{22}$$

$$P(H;\,\Delta y) = \frac{\partial Q(H;\,\Delta y)}{\partial H}. \tag{23}$$

The probability that the coordinate of the absolute maximum lies within the interval Δy and its value H lies within $(H, H + \Delta H)$ is equal to the probability that the value H lies within $(H, H + \Delta H)$ in the interval Δy and, in the remaining intervals $\overline{\Delta y}$, the value of the absolute maximum is less than H. Let us choose the interval Δy so that $l_0 \ll \Delta y \ll l_M(x, t)$. Then, we can consider the absolute maximums to be independent in the intervals Δy and $\overline{\Delta y}$ and we obtain

$$P_{\max}(H, y)\Delta H\Delta y = (P(H;\,\Delta y)\Delta H)Q(H;\,\overline{\Delta y}). \tag{24}$$

The first factor in Eq. (24) stands for the probability that the value of the absolute maximum falls within $(H, H + \Delta H)$ on the interval $(y, y + \Delta y)$. The second factor means the probability that the value of the absolute maximum is lower than H outside the interval $(y, y + \Delta y)$.

According to definition (22), $Q(H; \overline{\Delta y})$ is the probability that $\phi(x, y, t)$ never crosses the level H within $(y, y + \Delta y)$. For times when the parabola is a slow function on the scale $\phi_0(y)$ ($l_M(x, t) \gg l_0$), only sufficiently high-valued local maximum $H \gg \sigma_\psi M(x)$ can be the absolute maximum of $\phi(x, y, t)$. Hence, the statistics of crossings of the level H obeys the Poisson law. Now, the integral distribution function of the absolute maximum H coincides with the probability that there are no crossings of the level H within the interval (Δy). This function has the form [7, 13]

$$Q(H; \Delta y) = e^{-\langle N(H;\, \Delta y)\rangle}, \tag{25}$$

where $\langle N(H; \Delta y)\rangle$ is the mean number of crossings of the level H from below to above for the function $\phi(x, y, t)$ within the interval (Δy).

If $L_0 \gg l_0$ and $l_M(x, t) \gg l_0$, the parabola and the envelope $M(x)$ are slowly varying functions on the scale of $\phi_0(y)$, and the mean number of crossings can be expressed as [7, 13]

$$\langle N(H; y, y + \Delta y)\rangle$$
$$\simeq \frac{1}{2\pi l_0} \int\limits_{y}^{y+\Delta y} dy \exp\left\{-\frac{H^2 + H\dfrac{(x-y)^2}{2t}}{2\sigma_\psi^2 M^2(y)}\right\}. \tag{26}$$

This expression is obtained in view of the fact that the probability distribution lies in a narrow interval ΔH at $H \gg \sigma_\psi M(x)$ [13]. From Eqs. (24)–(26), we can derive an expression for the combined probability of the value and coordinate of the absolute maximum:

$$P_{\max}(H, y)\Delta y = -\frac{\partial}{\partial H}\langle N(H; \Delta y)\rangle Q_\infty(H), \tag{27}$$

$$Q_\infty(H) = e^{-N_\infty(H)}, \quad P_\infty(H) = \frac{\partial Q_\infty(H)}{\partial H}. \tag{28}$$

Here, $N_\infty(H)$ is the mean number of crossings of the level H for the function $\phi(x, y, t)$ in an infinite interval:

$$N_\infty(H) = \frac{1}{2\pi l_0}\int\limits_{-\infty}^{+\infty} dy \exp\left\{-\frac{H^2 + H\dfrac{(x-y)^2}{2t}}{2\sigma_\psi^2 M^2(y)}\right\}. \tag{29}$$

By integrating Eq. (27) with respect to H, we obtain the following expression for the probability that the coordinate of the absolute maximum falls within $(y, y + \Delta y)$:

$$P_{\max}(y)\Delta y = \int\limits_0^\infty \langle N(H; \Delta y)\rangle P_\infty(H) dH. \tag{30}$$

When $M(x) = 1$, Eqs. (28)–(30) describe the probability characteristics for stationary noise [7], and the value H of the absolute maximum in Eq. (28) is limited by a narrow domain $\Delta H \ll \sigma_\psi$ at $H = \sigma_\psi\left(\ln\dfrac{t}{2\pi t_{nnl}}\right)^{1/2} \gg \sigma_\psi$. In this case, for the coordinate of the absolute maximum given by Eq. (30), the probability distribution is Gaussian with the mean value $\langle y\rangle = x$ and variance $\langle y^2\rangle = l^2(t)$ (Eq. (8)).

For a modulated noise, one can distinguish three characteristic stages of field evolution. At the quasi-static stage ($t \ll t_{nnl}(L_0^2/l_0^2)$), the field is a sequence of random pulses with the integral scale $l_M(x, t)$ (Eq. (19)), which is much smaller than the modulation scale L_0. At this stage, the regular low-frequency component is generated, but its amplitude is lower than the characteristic amplitude of the noise. At $l_M(x, t) \simeq L_0$, the regular low-frequency components predominate, and the field is represented by a sequence of triangular pulses with the period L_0 and with weakly fluctuating positions of the zeros and of the discontinuity coordinates. Since the discontinuities move, they coalesce, and, for sufficiently long times, the characteristic distance between the discontinuities far exceeds L_0. In this case, the coherent components again become much smaller than the zeroth component. The evolution of the modulated random field, its mean value, and its variance are presented in Figs. 2 and 3 for the characteristic times.

Let us use the solutions (28)–(30) to consider the field properties at the aforementioned stages of evolution. In view of the fact that $(x - y)/t \sim l_M(t)$ and $H \gg (x - y)^2/2t$ [7] in these expressions, the integral in Eq. (30) has its peak values at the points $y(x, t) = y_{\max}$, which satisfy the transcendental equation

$$\frac{y_{\max} - x}{t} - H\frac{M'(y_{\max})}{M(y_{\max})} = 0. \tag{31}$$

At the quasi-static stage (when t is sufficiently small), Eq. (31) has a single root, and by using the perturbation method, we obtain

$$y_{\max} \approx x + tH\frac{M'(x)}{M(x)}. \tag{32}$$

For the mean number of crossings in an infinite interval, we obtain the expression

$$N_\infty(H)$$
$$= \left(\frac{\sigma_\psi M(x)}{H}\frac{t\sigma_\psi M(x)}{2\pi l_0^2}\right)^{1/2}\exp\left\{-\frac{H^2}{2\sigma_\psi^2 M^2(x)}\right\}. \tag{33}$$

By substituting Eq. (33) into Eq. (28), we obtain that, at $t\,M(x)/2\pi t_{nnl} \gg 1$ ($l_M(x, t) \gg l_0$), the probability distribution $P_\infty(H)$ is located within the narrow vicinity ΔH of $H_0 \gg \sigma_\psi M(x)$. If we represent H in the form

$$H = H_0 + \frac{\sigma_{M,\psi}^2}{H_0}z, \tag{34}$$

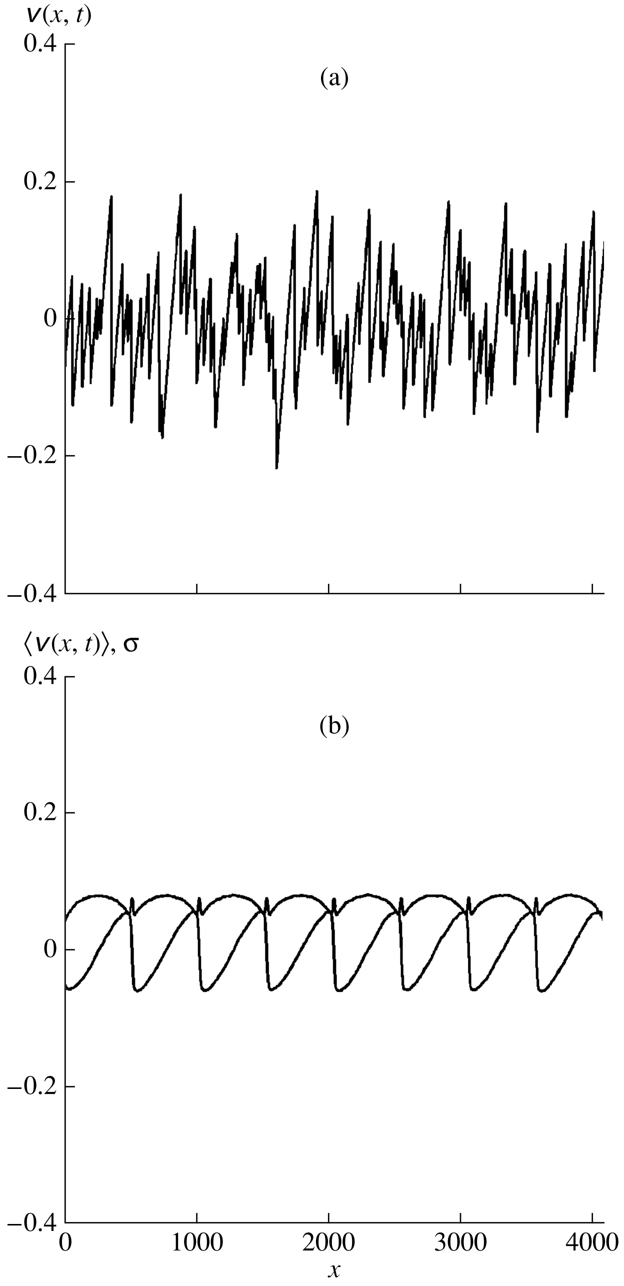

Fig. 2. (a) Profile of the velocity field $v(x, t)$ at $t = t_{\max}$, (b) its mean value $\langle v(x, t)\rangle$ and variance.

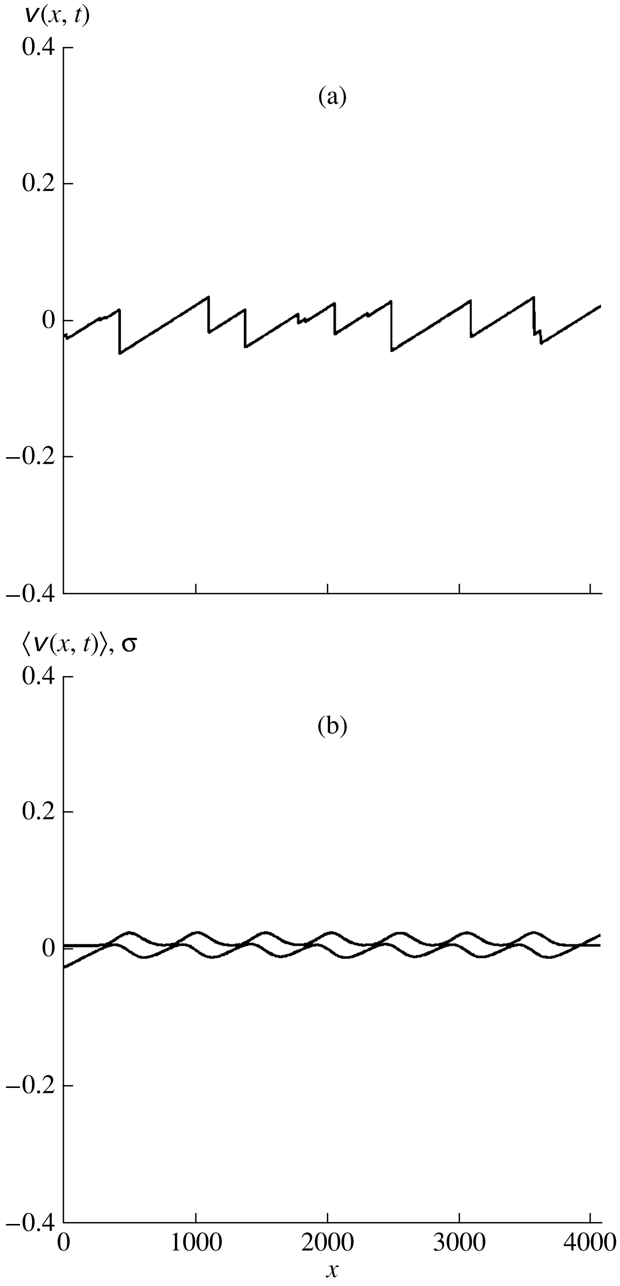

Fig. 3. (a) Profile of the velocity field $v(x, t)$ at $t = 2t_{nnl}(L_0/l_0)^2$, (b) its mean value $\langle v(x, t)\rangle$ and variance.

where H_0 is the solution to the transcendental equation

$$N_\infty(H_0) = 1; \quad H_0 \approx \sigma_\psi M(x)\left(\ln\frac{tM(x)}{2\pi t_{nnl}}\right)^{1/2}, \qquad (35)$$

we conclude that z is double-exponentially distributed:

$$P(z) = e^{-z}e^{-e^{-z}}, \quad Q(z) = e^{-e^{-z}}. \qquad (36)$$

By substituting these expressions into Eq. (30), we obtain a Gaussian distribution for the y coordinate of the absolute maximum with the variance $l_M(x, t)$ (Eq. (19)) and the mean value $\langle y\rangle = y_{\max}$ (Eq. (32)), where $H = H_0$ (Eq. (35)) should be specified. It follows from solution (3) that the distribution of the velocity field is also Gaussian with the variance given by Eq. (20) and the mean value

$$\langle v(x, t)\rangle = v_l(x, t) = -M'(x)\sigma_\psi\left(\ln\frac{M(x)t}{2\pi t_{nnl}}\right)^{1/2}. \qquad (37)$$

Thus, for the noise signal, the low-frequency components are also generated at the stage of developed discontinuities. The amplitude $v_l(x, t)$ (Eq. (37))

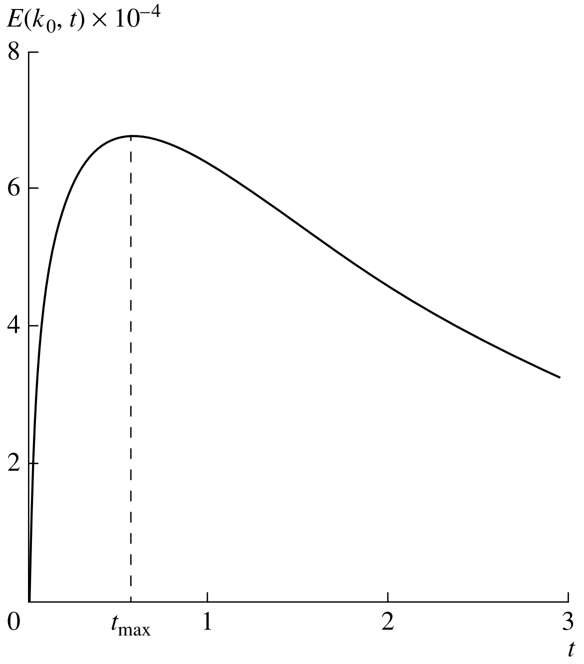

Fig. 4. Time dependence of the amplitude of the spectral component that corresponds to the modulation frequency (in the numerical experiment, $k_0 = 8$). The amplitude reaches its maximum at $t_{\max} \simeq 6t_{nnl}$.

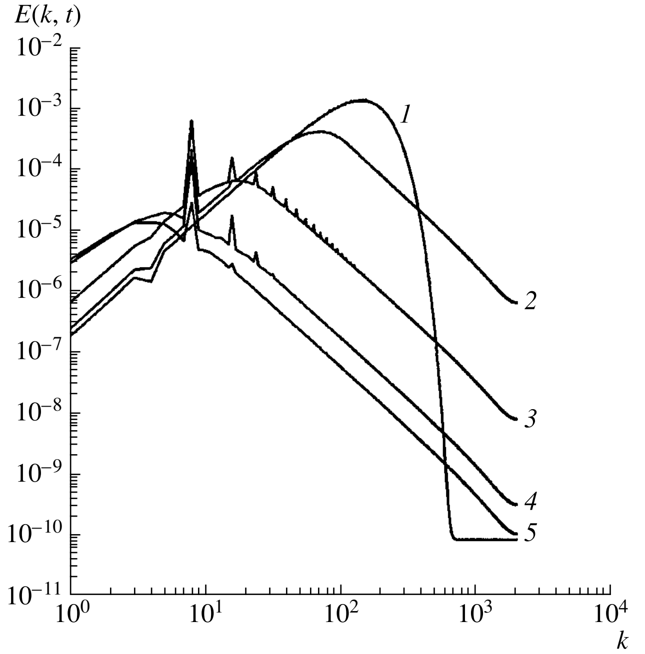

Fig. 5. Evolution of the power spectrum $E(k, t)$ of the high-intensity modulated noise with time: t = (*1*) 0, (*2*) $3t_{nnl}$, (*3*) $t_{\max}$, (*4*) $t_{nnl}(L_0/l_0)^2$, and (*5*) $2t_{nnl}(L_0/l_0)^2$.

reaches its maximal values at the times $t_{\max}$ when the velocity is of the same order of magnitude as the amplitude of the carrier. For the stage of developed discontinuities, it is equivalent to the condition that the integral scale $l_M(x, t)$ of the carrier and the scale L_0 of the envelope become of the same order of magnitude, and hence, $t \simeq t_{nnl}(L_0/l_0)^2$.

Now let us consider the evolution of the large-scale component. As time increases, the integral scale $l_M(x, t)$ of the carrier becomes larger, and the intrinsic structure of the signal fully vanishes at $t \simeq t_{nnl}(L_0/l_0)^2$. The zero values of the field $v(x, t)$ lie in the vicinity of the maximums of the envelope $M(x)$, $y_n = kL_0$. To find the probability distribution for the velocity field $v(x, t)$, we start by calculating the mean number of crossings of the level H for the process $\phi(x, y, t)$. According to Eq. (31), the extremum value of the integrand in Eq. (29) is located near the points $y_n = kL_0$. By using the method of steepest descent to estimate the integral in the vicinity of these points, we represent the mean number of crossings in an infinite interval as follows:

$$N_\infty(H) = \exp\left[-\frac{H^2}{2\sigma_\psi^2}\right]\left(\frac{L_*^2}{2\pi l_0^2}\frac{\sigma_\psi^2}{H^2}\right)^{1/2}\bar{n}, \qquad (38)$$

$$\bar{n} = \sum_n \exp\left[-\frac{H(x-y_n)^2}{2\sigma_\psi^2 t}\right]. \qquad (39)$$

Here, $\bar{n} = \bar{n}(x, \sigma_\psi t/H)$ is the effective number of maximums of $M(x)$ that contribute to the total number $N_\infty(H)$ of crossings. As at the quasi-static stage, the probability distribution $P_\infty(H)$ (Eq. (28)) lies within the narrow vicinity ΔH of $H_0 \gg \sigma_\psi$, and the integral distribution has the double-exponential form of Eq. (36), where H and z are related by Eq. (34) and H_0 is the solution to the equation $N_\infty(H_0) = 1$.

By using the fact that the probability distribution $P_\infty(H)$ lies within the narrow vicinity of H_0 and the integral distribution has the double-exponential form (Eq. (36)), we arrive at the following expression for probability distribution of the coordinate y (Eq. (30)) of the absolute maximum (which determines the field $v(x, t)$ given by Eq. (3) in a single-valued manner):

$$P(y; x, t) = \sum_n P_n(x, t)\frac{1}{\sqrt{2\pi l_*^2}}\exp\left[-\frac{(y-y_n)^2}{2l_*^2}\right], \qquad (40)$$
$$l_* = L_*\frac{\sigma_\psi}{H_0},$$

$$P_n(x, t) = \frac{1}{\bar{n}}\exp\left[-\frac{(x-y_n)^2}{2l^2(t)}\right], \quad l^2(t) = \frac{\sigma_\psi^2 t}{H_0}. \qquad (41)$$

Thus, a conclusion can be drawn that the zero values of the field $v(x, t)$ fall into a narrow interval of l_* ($H_0 \gg \sigma_\psi$) in the vicinities of maximums y_n of the envelope, P_n

in Eq. (40) being the probability that, for the field at the point x, the zero value lies within the nth period, i.e., at the point $y_n = nL_0$. In view of definition (39) for $\bar{n}$, we obtain for the mean field $v_l(x, t) = \langle v(x, t)\rangle$:

$$\langle v(x, t)\rangle = \frac{x - \langle y\rangle}{t} = \sum_n \frac{(x - y_n)}{t} P_n = -\frac{\sigma_\psi^2}{H_0}\frac{1}{\bar{n}}\frac{\partial\bar{n}}{\partial x}. \quad (42)$$

Since the modulating function $M(x)$ and, hence, all statistical characteristics of the field are periodic functions of x, it is sufficient for us to analyze the field evolution within a single period, $x \in (-L_0/2, L_0/2)$.

According to Eqs. (40) and (41), the field behavior is governed by the ratio of the characteristic scale $l(t) \simeq l_0(t/t_{nnl})^{1/2}$ to the modulation period L_0. If this parameter is not too large, the only summand P_n is significant within the kth period. Therefore, the field $v(x, t)$ is quasi-periodic with the period L_0:

$$v(x, t) \simeq \frac{x - \tilde{y}_n}{t}, \quad x_n < x < x_{n+1}, \quad (43)$$

the zero points $\tilde{y}_n$ being located in the vicinities of the maximums $y_n = kL_0$ of the envelope $M(x)$ and having Gaussian distributions with variances $l_* \simeq L_*\left(\ln\frac{L_*^2}{2\pi l_0^2}\right)^{-1/2}$. For the energy density, the same expression as for the sawtooth periodic wave is valid: $\bar{E} \simeq L_0^2/12t^2$. As in the case of the sawtooth periodic wave, the mean field has a universal structure of the form $v_l = (x - y_n)/t$. At the interval boundaries, when $x \simeq \frac{L_0}{2} + kL_0$, only two summands predominate in Eqs. (39) and (42), and

$$\bar{n} \simeq \exp\left[-\frac{L_0^2}{8l^2(t)}\right] 2\cosh\frac{L_0(x - L_0/2)}{2l^2(t)}. \quad (44)$$

With the use of Eq. (42), we obtain for the mean field

$$\langle v\rangle = \frac{L_0}{2t}\tanh\frac{L_0(x - L_0/2)}{2l^2(t)}, \quad (45)$$

where $l(t)$ is determined by Eq. (41), and $H_0 \simeq \sigma_\psi\left(\ln\frac{L_*^2}{2\pi l_0^2}\right)^{1/2}$. Thus, the fluctuations of the discontinuity positions lead to the same structure of the mean field as for the field of the sawtooth wave in a medium with a finite viscosity.

The random character of the motion of discontinuities in the sawtooth wave causes them to coalesce, and the quasi-periodic structure proves to be destroyed at $l(t) \gg L_0$. In this case, the characteristic scale of the field is

$$l^2(t) = \frac{\sigma_\psi^2 t}{H_0}; \quad H_0 \simeq \left(\ln\frac{\sigma_\psi t}{l_0^2}\frac{L_*^2}{L_0^2}\right)^{1/2}, \quad (46)$$

which far exceeds the modulation period L_0. The field energy $\bar{E}$ is governed by Eq. (11), $\bar{E} \simeq l^2(t)/t^2$, and it attenuates proportionally to $1/t$ with some logarithmic corrections, i.e., in the same way as for the stationary noise (11).

To find the attenuation of the mean field, it is advantageous to convert Eq. (39) to summation over the spatial frequencies with the use of the Poisson summation formula [15]:

$$\bar{n} = \sqrt{\frac{2\pi\sigma_\psi^2 t}{L_0^2 H_0}}\sum_{m=0}^{\infty}\exp\left[-\frac{m^2}{2}\left(\frac{(2\pi)^2\sigma_\psi^2 t}{L_0^2 H_0}\right)\right]\cos\frac{2\pi m x}{L_0}. \quad (47)$$

Then, from Eq. (42), we obtain for the mean field

$$\langle v\rangle = \frac{k_0 l(t)}{t}\exp\left[-\frac{1}{2}k_0^2 l^2(t)\right]\sin k_0 x, \quad (48)$$

and the mean field attenuates exponentially in time, which means decay of the quasi-harmonic structure.

The evolution of the spectrum of modulated noise can be considered as follows. Because of the statistical nonuniformity of the process $v(x, t)$, the power spectrum $E(k, t)$ should be sought by introducing the correlation function of the second kind, which is determined by averaging the correlation function $\langle v(x + \rho, t)v_0(x)\rangle$ over the period L_0 [14]. By virtue of the condition $l_0 \ll L_0$, we have $E(k, 0) = \overline{M^2(x)}^{L_0} E_0(k)$ for the spectrum of the input signal $v_0(x)$ (Eq. (6)), where $(\overline{M^2(x)}^{L_0})$ means the corresponding quantity averaged over the period of the modulating function. Thus, the spectrum of the input signal without modulation coincides with the spectrum of the carrier. The generation of the regular component creates discrete components in the signal spectrum at frequencies that are multiples of the modulation frequency $k = mk_0$, $k_0 = 2\pi/L_0$. Figure 4 illustrates the time evolution of the spectral component that corresponds to the modulation frequency $k = k_0$. At the initial stage, the amplitudes of these harmonics are governed by the spectrum of the derivative of the squared modulating function $M(x)$ from Eq. (18), and they increase linearly with time. At the quasi-static stage, the harmonic amplitudes are determined by the spectrum of the modulating function from Eq. (37) and have a logarithmic time dependence. At the stage of developed discontinuities, when the quasi-static approximation is valid and the integral scale $l_M(x, t)$ (Eq. (19)) of the carrier is much smaller than the modulation period L_0, a local spectrum $E(k; x, t)$ can be introduced that is locally automodelling and follows Eq. (10), where the integral scale $l(t) = l_M(x, t)$ is a slowly varying function of the coordinate. In this case, the power spectrum of the field is obtained by averaging the local automodelling spectrum over the modulation period: $E(k, t) = \overline{E(k; x, t)}^{L_0}$. The power spectrum of the modulated wave can be shown to have universal asymptotic forms, just as the spectrum of the uniform noise at high and low spatial frequencies: $E(k) \sim k^{-2}\overline{M^{1/2}(x)}^{L_0}t^{-3/2}$ and $E(k) \sim k^2\overline{M^{5/2}(x)}^{L_0}t^{1/2}$, respectively.

Let us consider the spectrum at the evolution stage when the intrinsic signal structure is fully degenerate because of the coalescence of the discontinuities in the carrier, and the field is quasi-periodic (Eq. (43)). The coordinates x_n of discontinuities in Eq. (44) are determined by the condition of coincidence for the global maximums of $\phi(x, y, t)$ at two points: $\phi(x_n, \tilde{y}_n, t) = \phi(x_n, \tilde{y}_{n+1}, t)$. At this stage, the coordinates of the global maximum $\tilde{y}_n$ are equal to those of the maximum in the potential within the nth period, $\tilde{y}_n = y_n = nL_0 + \Delta y_n$, where Δy_n is the offset of the zero point of the sawtooth wave from the maximum position nL_0, and, according to Eq. (42), $\Delta y_n \ll L_0$.

Let H_n be the value of the absolute maximum within the nth period. This value can be represented as

$$H_n = H_0 + \frac{\sigma_\psi^2}{H_0}z_n, \quad H_0 = \sigma_\psi\left(\ln\frac{L_*^2}{2\pi l_0}\right)^{1/2}, \tag{49}$$

where the values of z_n are independent for different periods and are double-exponentially distributed in their probabilities (Eq. 36). For the coordinate of the discontinuity x_n, we now have

$$x_n = nL_0 + \Delta x_n = \frac{\Delta y_{n-1} - \Delta y_n}{2} + \Delta V_n t, \tag{50}$$

$$\Delta V_n = \frac{H_n - H_{n+1}}{y_{n+1} - y_n} \simeq \frac{z_n - z_{n+1}}{L_0}\frac{\sigma_\psi^2}{H_0}. \tag{51}$$

To find the spectrum, let us consider the derivative $V'_x(x, t) = u(x, t)$ of the velocity field, which is a set of delta-functions:

$$u(x, t) = \frac{1}{t} - \sum_n \frac{\eta_n}{t}\delta(x - x_n), \tag{52}$$

where $\eta_n = y_{n+1} - y_n = L_0 + (\Delta y_{n+1} - \Delta y_n) \simeq L_0$ is the distance between two zero points of the sawtooth wave. For the Fourier transform of Eq. (52), we obtain

$$\begin{aligned} C_u(k) &= \frac{1}{2\pi}\int_{-\infty}^{+\infty} u(x, t)e^{ikx}dx \\ &= \frac{1}{t}\left[\delta(k) - \frac{1}{2\pi}\sum_{n=-\infty}^{+\infty}\eta_n e^{ikx_n}\right]. \end{aligned} \tag{53}$$

In view of evident relations between the power spectra of the derivative and the process itself, we arrive at the following expression for the power spectrum of the field [15]:

$$E_V(k, t) = \frac{1}{k^2t^2}\left[\frac{1}{k_0}\sum_{r=-\infty}^{\infty}H_r(k, t) - \delta(k)\right], \tag{54}$$

$$H_r(k, t) = \langle e^{ik(x_{n+r} - x_n)}\rangle, \tag{55}$$

where the coordinates of discontinuities are determined by Eqs. (50) and (51). In Eq. (53), we neglected the amplitude fluctuations in the quasi-periodic wave, which are caused by the fluctuations of zero points y_n of the sawtooth wave. We also neglect the fluctuations Δy_n of the zero points in Eq. (50) determining the discontinuity coordinates x_n. Then, according to Eqs. (50) and (51), the power spectrum is uniquely determined by the characteristic function of the dimensionless potential z_n (Eq. (53)), which has the double-exponential probability distribution (Eq. (36)):

$$\begin{aligned} \theta_z(\kappa) &= \langle e^{i\kappa z}\rangle = \Gamma(1 + i\kappa), \\ |\Gamma(1 + i\kappa)|^2 &= \frac{\pi y}{\sinh\pi y}, \end{aligned} \tag{56}$$

where $\Gamma(z)$ is the gamma function.

With the use of the Poisson summation formula, we extract the discrete part of the spectrum from Eq. (54)

$$\begin{aligned} &E^d(k, t) \\ &= \sum_{n=-\infty,\, n\neq 0}^{+\infty}\frac{1}{(k_0nt)^2}\frac{(nk_0^2l^2(t))^2}{\sinh^2(nk_0^2l^2(t))}\delta(k - nk_0) \end{aligned} \tag{57}$$

as well as its continuous part

$$\begin{aligned} E^c(k, t) = \frac{1}{k^2t^2k_0}\Bigg[1 - \left|\theta_z\left(\frac{kl^2(t)}{L_0}\right)\right|(1 + 2\cos kL_0) \\ + 2Re\left(e^{ikL_0}\theta_z\left(\frac{2kl^2(t)}{L_0}\right)\theta_z^{*2}\left(\frac{kl^2(t)}{L_0}\right)\right)\Bigg]. \end{aligned} \tag{58}$$

Here, the quantity $l(t)$ given by Eq. (41) characterizes the displacement of the discontinuity. According to Eq. (57), the discrete part of the spectrum is equal to the spectrum of the sawtooth wave in a medium with a finite viscosity. In this situation, the coherent structure is destroyed because of the random movements of the discontinuities. The continuous part of the spectrum has universal asymptotic forms both at low frequencies, $E^c \sim k^2$, and at high frequencies, $E^c \sim k^{-2}$.

At long times $l(x, t) \gg L_0$, the quasi-periodic structure totally decays. The characteristic scale $l(t)$ of the field starts to be much higher than the modulation period. The field spectrum becomes automodelling and obeys Eq. (10), where the integral scale of turbulence is given by Eq. (47). The evolution of the spectrum is illustrated by Fig. 5 for the initial disturbance at hand.

To conclude with, let us discuss the main features of the evolution of modulated signals with noise and quasi-harmonic carriers in a nondispersive medium with an infinitely small viscosity. For quasi-harmonic signals, the combined effect of the nonlinearity and dissipation leads to a full suppression of the modulation amplitude at the stage of developed discontinuities. At this stage, the generation of the difference-frequency wave terminates. For long time intervals, the shape and amplitude of this wave remains unchanged, because the characteristic time of the nonlinear interaction is much longer for the difference-frequency waves than for the high-frequency ones. The long-time asymptotic behavior of the waves depends on the frequency content of the initial signal. If the spectrum of the initial disturbance consists of two multiple frequencies, $k_1 = n\kappa$ and $k_2 = m\kappa$ ($|n - m| \ll n, m$), the nonlinear interaction causes the wave of the difference frequency $k = |n - m|\kappa$ to transform to a saw-tooth wave whose discontinuities, however, will have a nonzero velocity. As a result of the coalescence of discontinuities, the quasi-periodic structure (with the period $L = 2\pi/k$) will be destroyed, and, asymptotically, the wave will be transformed to the sawtooth structure with the period $L_{\max} = 2\pi/\kappa$.

For waves with a noise carrier, only partial suppression of the modulation amplitude takes place, and, hence, the generation of the difference-frequency waves persists at the stage of developed discontinuities. Because of the coalescence of the discontinuities of the carrier, the field transforms to a quasi-periodic structure with a period equal to that of modulation and with weakly fluctuating positions of the zero points and discontinuities. Since the discontinuities move, they coalesce, and, asymptotically, the field becomes noisy in its nature.

To numerically model the evolution of the modulated noise, we used the asymptotic solution (3), (4) to the Burgers equation, this solution being equivalent to the Legendre transform. Since the function $y(x, t)$ is nondecreasing, one can construct a fast algorithm for numerically solving the problem with $O(N\log_2 N)$ steps required for determining the coordinates of the absolute maximum (here, N is the number of points at which the initial disturbance is determined [16]). In numerical experiments, the fast Legendre transform allowed us to average over 10000 realizations of the initial random disturbance.

ACKNOWLEDGMENTS

This work was supported by the Russian Foundation for Basic Research (project no. 99-02-18354), INTAS (project no. 97-11134), the Competition Center for Basic Natural Sciences (project no. 97-8.1-79), and the Universities of Russia program.

REFERENCES

1. J. M. Burgers, *The Nonlinear Diffusion Equation* (Reidel, Dordrecht, 1974).
2. O. V. Rudenko and S. I. Soluyan, *Theoretical Foundations of Nonlinear Acoustics* (Nauka, Moscow, 1975; Consultants Bureau, New York, 1977).
3. B. K. Novikov, O. V. Rudenko, and V. I. Timoshenko, *Nonlinear Underwater Acoustics* (Sudostroenie, Leningrad, 1981; Acoustical Society of America, New York, 1987).
4. V. Gusev, J. Acoust. Soc. Am. **107**, 3047 (2000).
5. S. N. Gurbatov and C. M. Hedberg, Acustica-Acta Acust. **84**, 414 (1998).
6. R. Courant, *Partielle Differentialgleichungen* (Gottingen, 1932; Mir, Moscow, 1964) (unpublished lecture notes).
7. S. N. Gurbatov, A. N. Malakhov, and A. I. Saichev, *Nonlinear Random Waves in Nondispersion Media* (Nauka, Moscow, 1990), p. 215.
8. M. R. Leadbetter, G. Lindgren, and H. Rootzen, *Extremes and Related Properties of Random Sequences and Processes* (Springer, New York, 1983), p. 340.
9. S. A. Molchanov, D. Surgailis, and W. A. Woyczynski, Commun. Math. Phys. **168**, 209 (1995).
10. S. N. Gurbatov, S. I. Simdyankin, E. Aurell, *et al.*, J. Fluid. Mech. **344**, 339 (1997).
11. S. N. Gurbatov, Phys. Rev. E **61** (3), 2595 (2000).
12. W. A. Woyczynski, *Burgers-KPZ Turbulence. Gottingen Lectures* (Springer, Berlin, 1998), p. 358.
13. S. N. Gurbatov, B. O. Enflo, and G. V. Pasmanik, Acustica-Acta Acust. **85**, 181 (1999).
14. A. N. Malakhov, *Fluctuations in Self-Oscillatory Systems* (Nauka, Moscow, 1968).
15. B. R. Levin, *Theoretical Foundations of Statistical Radio Engineering* (Sov. Radio, Moscow, 1974), Book 1, p. 551.
16. A. Noullez and M. Vergassola, J. Sci. Comput. **9**, 259 (1994).

Translated by E. Kopyl

Acoustical Physics, Vol. 47, No. 4, 2001, pp. 415–418. Translated from Akusticheskiĭ Zhurnal, Vol. 47, No. 4, 2001, pp. 485–488.
Original Russian Text Copyright © 2001 by Dvoesherstov, Petrov, Cherednik, Chirimanov.

Thermal Stabilization of SAW Devices by Metal Films

M. Yu. Dvoesherstov, S. G. Petrov, V. I. Cherednik, and A. P. Chirimanov
Lobachevskiĭ State University, Nizhni Novgorod, pr. Gagarina 23, Nizhni Novgorod, 603600 Russia
e-mail: obolensk@rf.unn.runnet.ru

Received March 23, 2000

Abstract—The characteristics of surface acoustic waves (SAW) propagating in a structure that consists of a metal layer overlying an YX-cut quartz crystal are numerically analyzed for a wide range of operating temperatures. It is shown that the presence of a metal film of a certain thickness on the surface of an YX-cut quartz crystal considerably improves the thermal stability of the characteristics of SAW propagating in such a structure. *© 2001 MAIK "Nauka/Interperiodica".*

Piezoelectric quartz crystals represent one of the most popular materials used in the SAW technology. These crystals have been extensively studied both theoretically and experimentally and exhibit a high thermal stability of their properties [1]. It was found that some cuts of quartz crystals and some directions in them are characterized by a zero first-order temperature coefficient of delay ($\mathrm{TCD}^{(1)}$) of SAW (e.g., the ST,X-cut of the quartz crystal) or by a close-to-zero value of this coefficient (e.g., the AT,X-cut of the quartz crystal [2]). One of the main technical characteristics in the SAW technology is the sensitivity of the thermally stable direction of the crystal to changes in the external temperature. However, in the aforementioned cuts of the quartz crystal, the thermal stability of SAW is observed in only a narrow interval of operating temperatures near room temperature (t_0 = 25°C). The second-order temperature coefficient of delay ($\mathrm{TCD}^{(2)}$) of SAW propagating in these crystal cuts is relatively high: $\mathrm{TCD}^{(2)} \approx 32 \times 10^{-9}$ 1/°C^2 for the ST,X-cut and $\mathrm{TCD}^{(2)} \approx 28.4 \times 10^{-9}$ 1/°C^2 for the AT,X-cut.

This paper presents a theoretical study of the SAW characteristics in a structure consisting of a metal layer overlying an YX-cut quartz substrate in a wide range of operating temperatures t.

As a result of numerical calculations, we determined the materials of the film and the values of the film thickness for which a thermal stabilization of SAW is achieved in a wide temperature range. For example, in the structure consisting of an aluminum film with thickness $h = 0.061\lambda$ (λ is the SAW wavelength) and an YX-cut quartz crystal, the relative variation of the SAW delay time $\Delta\tau/\tau_0$ [3] in the temperature interval from –60 to +60°C was 2.5 times smaller than in the well-known ST,X-cut quartz.

Let us first discuss the conditions for which we perform the numerical analysis of the properties of SAW in a film–substrate system. In the presence of an isotropic metal film of a finite thickness on the surface of a piezoelectric crystal, we will consider the problem on the SAW propagation in the structure that consists of an isotropic layer overlying a piezoelectric substrate. In this case, we use the system of equations of the theory of elasticity in combination with the electrostatic equation [4]:

$$\rho^{(m)}\frac{\partial^2 u_i^{(m)}}{\partial\tau^2} = \frac{\partial T_{ij}^{(m)}}{\partial x_j}; \quad \operatorname{div} D^{(m)} = 0. \qquad (1)$$

Here, T_{ij} is the elastic stress tensor, u_i represents the mechanical displacements, D is the electric displacement vector, $\rho^{(m)}$ represents the densities of the film and substrate materials, τ is time, and x_j are the coordinates. The subscripts are $i, j = 1, 2, 3$; the superscript takes the values m = 1 and 2 to indicate the film and substrate materials, respectively.

Using the method described in [4, 5], we developed an algorithm and a program for the numerical calculation of the main characteristics (the velocity V_l, the displacement amplitudes u_i, etc.) of SAW propagating in a structure formed by a metal film and a YX-cut quartz substrate; we carried out numerical analysis of the temperature characteristics ($\mathrm{TCD}_l^{(1)}$, $\mathrm{TCD}_l^{(2)}$, and $\Delta\tau/\tau_0$) of SAW propagating in these structures for a wide range of operating temperatures. In our calculations, we took into account the following factors: the temperature dependences of the quartz material constants C_{ijkl}, e_{ijk}, and ε_{ij}; the thermal expansion of the crystal [2]; the temperature dependences of the crystal density ρ and the density of the layer material ρ_l; the temperature dependences of the Lamé elastic constants of the isotropic layer; the thermal expansion of the film; the variation of the film thickness h with temperature [3]; and the presence of the initial thermal internal stresses in the layered structure due to the difference between the

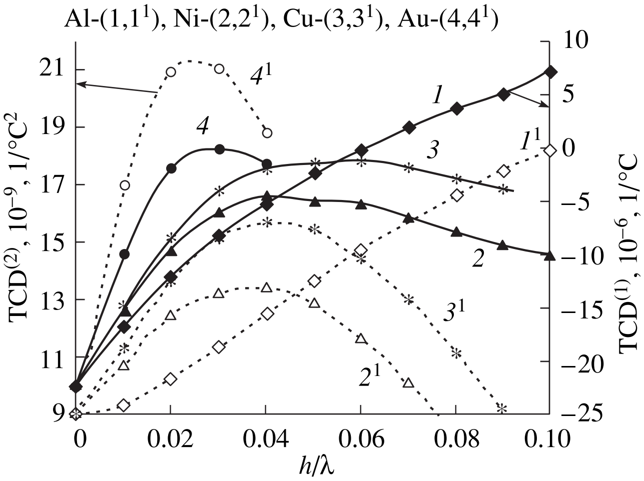

Fig. 1. Dependences of the coefficients $\mathrm{TCD}_l^{(1)}$ (solid curves) and $\mathrm{TCD}_l^{(2)}$ (dotted curves) of SAW on the relative layer thickness for different metal films on the surface of a YX-cut quartz crystal: (*1*, *1*^{1}) Al, (*2*, *2*^{1}) Ni, (*3*, *3*^{1}) Cu, and (*4*, *4*^{1}) Au.

coefficients of thermal expansion of the film and substrate materials [6, 7].

The temperature coefficients of delay, $\mathrm{TCD}_l^{(1)}$ and $\mathrm{TCD}_l^{(2)}$, of SAW propagating in the layered structure can be calculated by the formulas [2, 8]

$$\mathrm{TCD}_l^{(1)} = \frac{1}{\tau_0(t_0)}\frac{d\tau_l}{dt}\bigg|_{t_0} = \alpha_{11}^{(1)} - \mathrm{TCV}_l^{(1)}, \tag{2}$$

$$\mathrm{TCD}_l^{(2)} = \frac{1}{2}\frac{1}{\tau(t_0)}\frac{d^2\tau_l}{dt^2}, \tag{3}$$

where τ_l and τ_0 are the SAW delay times in the layered structure at the operating and room temperatures, respectively; $\mathrm{TCV}_l^{(1)}$ is the temperature coefficient of velocity for SAW propagating in the layered structure [2]; and $\alpha_{11}^{(1)}$ is the coefficient of thermal expansion of the crystal in the direction of wave propagation.

If the film thickness h is much smaller than the substrate thickness H, we can assume that, as the operating temperature t varies, the substrate length varies in one or another direction and the film length also varies. This process should be accompanied by a variation of the film thickness h [3].

To calculate the dependence of the SAW delay time τ_l on the temperature t in the layered structure, we can use the Taylor series expansion of τ_l near the room temperature t_0:

$$\tau_l(t) = \tau_0(t_0) + \frac{d\tau_l}{dt}\bigg|_{t_0}(t-t_0) + \frac{1}{2}\frac{d^2\tau_l}{dt^2}\bigg|_{t_0}(t-t_0)^2 + \dots. \tag{4}$$

If we neglect the higher orders in Eq. (4), we can represent the relative variation of the SAW delay time $\Delta\tau/\tau_0 = (\tau_l - \tau_0)/\tau_0$ in the form

$$\frac{\tau_l - \tau_0}{\tau_0} = \mathrm{TCD}_l^{(1)}(t-t_0) + \mathrm{TCD}_l^{(2)}(t-t_0)^2. \tag{5}$$

As one can see from Eqs. (2)–(5), to calculate the temperature characteristics of SAW in the layered structure, it is necessary first to solve the system of equations (1) from which one can determine the velocity V_l of SAW in the layered structure for different values of the film thickness and for different operating temperatures t.

According to [8], YX-cut quartz exhibits no thermal stability of the SAW characteristics. For example, at room temperature, the first-order temperature coefficients of delay of SAW take the following values: $\mathrm{TDC}^{(1)} = -22 \times 10^{-6}$ 1/°C 1 for a free surface and $\mathrm{TCD}_m^{(1)} = -22.3 \times 10^{-6}$ 1/°C for a coated (i.e., covered with an infinitely thin metal film whose mass is negligibly small) surface. A metal film of finite thickness h (with a finite mass) covering the surface of an YX-cut quartz crystal can noticeably change the SAW velocity (making it smaller or greater, depending on the temperature characteristics of the film and substrate materials), and at some value of the thickness h, it can improve the temperature characteristics of SAW propagating in the structure.

Figure 1 shows the calculated dependences of $\mathrm{TCD}_l^{(1)}$ and $\mathrm{TCD}_l^{(2)}$ of SAW on the ratio h/λ for different film materials: aluminum (Al), gold (Au), copper (Cu), and nickel (Ni) at room temperature. One can see that, when the surface of a YX-cut quartz crystal is covered with an aluminum layer of thickness $h = 0.061\lambda$, the value of $\mathrm{TCD}_l^{(1)}$ becomes zero (curve *1*). The corresponding value of $\mathrm{TCD}_l^{(2)}$ is 14.8×10^{-9} 1/°C^2 (curve *1*^{1}). A nickel layer (curve *2*) of thickness $h/\lambda = 0.045$ reduces the absolute value of $\mathrm{TCD}^{(1)}$ to -4.5×10^{-6} 1/°C but does not compensate it totally (i.e., to zero); the corresponding value of $\mathrm{TCD}_l^{(2)}$ is 13×10^{-9} 1/°C^2 (curve *2*^{1}). A copper layer (curve *3*) with $h/\lambda = 0.05$ provides an almost total compensation of $\mathrm{TCD}^{(1)}$; in this case, $\mathrm{TCD}_l^{(2)} = 15.5 \times 10^{-9}$ 1/°C^2 (curve *3*^{1}). A gold layer provides a compensation of $\mathrm{TCD}^{(1)}$ at $h/\lambda = 0.028$

(curve *4*); in this case, $\mathrm{TCD}_l^{(2)} = 21 \times 10^{-9}$ 1/°C^2 (curve 4^1).

It can be shown that, for a free surface of an YX-cut quartz crystal, the calculated dependence of the relative variation of the delay time $\Delta\tau/\tau_0$ given by Eq. (5) on the temperature t (within the interval –60 to +60°C) is linear, and the value of the relative variation of the delay time varies over wide limits. For example, at t = –60°C, we have $\Delta\tau/\tau_0 = 1942 \times 10^{-6}$ and, at t = +60°C, $\Delta\tau/\tau_0 = -767 \times 10^{-6}$.

Figure 2 presents the calculated temperature dependences of the relative variation of the delay time $\Delta\tau/\tau_0$ of SAW and the temperature dependences of $\mathrm{TCD}_l^{(1)}$ (t varies from –60 to +60°C) for different materials of the film covering the surface of the YX-cut quartz crystal. All dotted lines in the figure represent $\mathrm{TCD}_l^{(1)}$, and all solid lines represent $\Delta\tau/\tau_0$ of SAW. From Fig. 2, one can see that the aluminum film (h/λ = 0.061) provides a thermal stabilization of the YX-cut quartz crystal ($\mathrm{TCD}_l^{(1)} = 0$) at room temperature (curve 1^1). In addition, in such a structure, the range of variation of the quantity $\Delta\tau/\tau_0$ (curve *1*) within the temperature interval from –60 to +60°C is much smaller (at t = –60°C, we have $\Delta\tau/\tau_0 = 81 \times 10^{-6}$ and, at t = +60°C, $\Delta\tau/\tau_0 = 21 \times 10^{-6}$) than in the case of a free surface of YX-cut quartz. From Fig. 2 it also follows that gold films with h/λ = 0.028 (curves *2*, 2^1), nickel films with h/λ = 0.045 (curves *4*, 4^1), and copper films with h/λ = 0.05 (curves *3*, 3^1), when deposited on the surface of an YX-cut quartz crystal, also provide a thermal stabilization of SAW in the crystal and reduce the value of $\Delta\tau/\tau_0$ of SAW in a wide temperature range from –60 to +60°C.

In contrast to a free YX-cut quartz crystal, the presence of a metal film of a certain thickness on its surface leads to a thermal stabilization of the characteristics of SAW propagating in the resulting layered structure. For example, in the structure consisting of an aluminum film with h/λ = 0.061 and a YX-cut quartz substrate, we obtain $\mathrm{TCD}_l^{(1)} = 0.03 \times 10^{-6}$, 1/°C and $\mathrm{TCD}_l^{(2)} = 14.87 \times 10^{-9}$ 1/°C^2. The corresponding values of other parameters are as follows: velocity V_l = 3.162 km/s, power flux angle [9] pfa = 0°, anisotropy coefficient γ = 0.62, and electromechanical coupling coefficient [9] K^2 = 0.185%.

When the crystal surface is loaded with a film of a finite thickness, not only the temperature characteristics but also the velocity of SAW propagating in this structure undergo some changes. It is of interest to consider the changes that occur in the SAW velocity when the surface of the YX-cut quartz crystal is covered with a metal film of finite thickness.

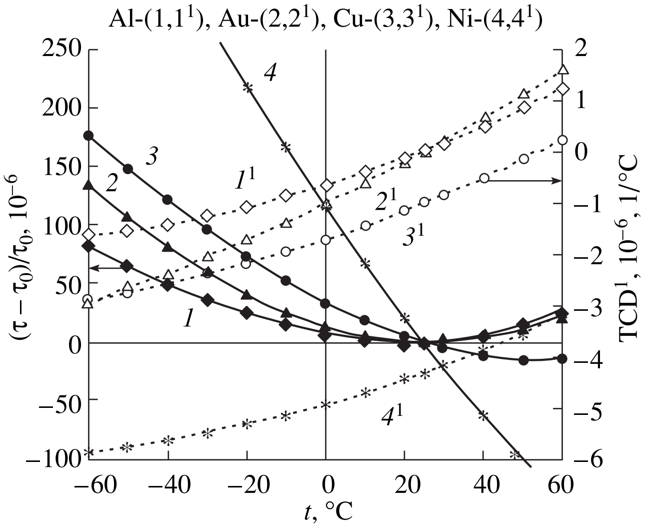

Fig. 2. Temperature dependences of the relative variation of the delay time $\Delta\tau/\tau_0$ (solid curves) and the coefficient $\mathrm{TCD}_l^{(1)}$ (dotted curves) of SAW for different films deposited on the surface of a YX-cut quartz crystal: (*1*, 1^1) Al film with h/λ = 0.061, (*2*, 2^1) Au with h/λ = 0.028, (*3*, 3^1) Cu with h/λ = 0.05, and (*4*, 4^1) Ni with h/λ = 0.045.

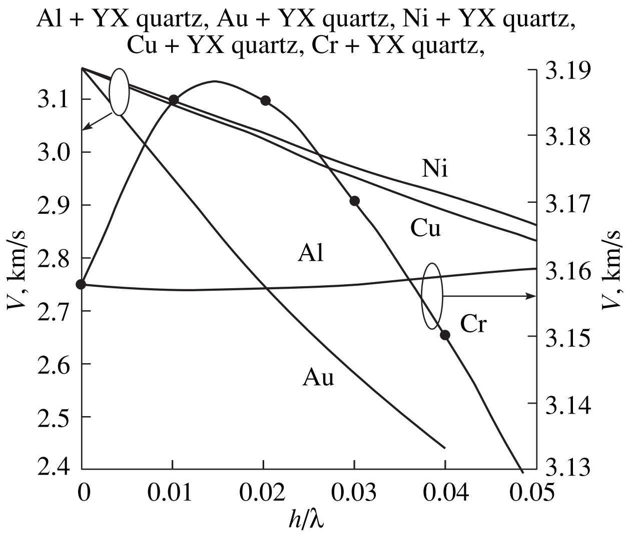

Fig. 3. Dependences of the SAW velocity on the relative layer thickness in the structures: Al film + YX-cut SiO_2; Au film + YX-cut SiO_2; Ni film + YX-cut SiO_2; Cu film + YX-cut SiO_2; and Cr film + YX-cut SiO_2.

Figure 3 presents the dependences of the SAW velocity on the ratio h/λ in the structures: Al film + YX-cut quartz, Au film + YX-cut quartz, Ni film + YX-cut quartz, Cu film + YX-cut quartz, and Cr film + YX-cut quartz. One can see that, unlike Al and Cr films, the copper (Cu), nickel (Ni), and, especially, gold (Au) films effectively reduce the velocity of SAW in the film–crystal structure. For example, in the presence of a gold film whose thickness is equal to 0.01λ, the SAW velocity in the structure decreases from 3.1605 to 2.945 km/s. This result is explained by the fact that the velocity of the slow shear bulk wave in gold is much lower than the velocity of the shear bulk wave in YX-cut quartz. We note that, if the velocity of the shear bulk wave in the film material is much higher than in the substrate, only one surface acoustic wave can exist in the layered structure. The existence of this wave is possible only in a limited range of values of h/λ [4]. When the velocity of the shear bulk wave in the layer material is close to that in the substrate material, the dependence of the SAW velocity in the layered structure on the ratio h/λ can exhibit an anomalous behavior, i.e., local maximums and minimums [10]. This effect is observed in the case of chromium film (see Fig. 3).

The crystal cut and the direction of the SAW propagation are usually described by three Eulerian angles (ϕ, θ, Ψ) [4]. Numerical calculations showed that a thermal stabilization of SAW by thin metal films is possible not only for YX-cut quartz (with the Eulerian angles (0°, 90°, 0°)), but also for other orientations of the quartz crystal, namely, the orientations with the second Eulerian angle θ falling either within the interval 10°–40° or 90°–120° (while the two other angles are $\phi = \Psi = 0°$).

Thus, our numerical experiment shows how a thin metal (Al, Au, Cu, or Ni) film covering the surface of an YX-cut quartz crystal affects the main characteristics of SAW. For different metal films covering the surface of a YX-cut quartz crystal, we determined the thickness values with which it is possible to considerably improve the thermal stability of SAW propagating in such structures in a wide temperature range.

REFERENCES

1. Y. Shimizu and Y. Yamamoto, in *Proceedings of IEEE Ultrasonic Symposium* (1980), p. 420.
2. *Acoustic Surface Waves*, Ed. by A. A. Oliner (Springer, New York, 1978; Mir, Moscow, 1981).
3. Y. Shimizu, A. Terazaki, and T. Sakaue, in *Proceedings of IEEE Ultrasonic Symposium* (1976), p. 519.
4. *Surface Wave Filters: Design, Construction and Use*, Ed. by H. Mathews (Wiley, New York, 1977; Radio i Svyaz’, Moscow, 1981).
5. M. Yu. Dvoesherstov, V. I. Cherednick, A. P. Chirimanov, and S. G. Petrov, Proc. SPIE–Int. Soc. Opt. Eng. **3900**, 283 (1999).
6. I. Ya. Ashbel’, M. Yu. Dvoesherstov, and S. G. Petrov, Akust. Zh. **36**, 360 (1990) [Sov. Phys. Acoust. **36**, 196 (1990)].
7. K. Yamanouchi, K. Kotani, H. Odagawa, and Y. Cho, in *Proceedings of IEEE Ultrasonic Symposium* (1999), p. 283.
8. D. Williams and F. Cho, in *Proceedings of IEEE Ultrasonic Symposium* (1979), p. 627.
9. A. J. Slobodnik, Jr., IEEE Trans. Sonics Ultrason. **SU-20** (4), 315 (1973).
10. I. Ya. Ashbel’, M. Yu. Dvoesherstov, and S. G. Petrov, Zh. Tekh. Fiz. **61** (6), 155 (1991) [Sov. Phys. Tech. Phys. **36** (6), 677 (1991)].

Translated by E. Golyamina

Acoustical Physics, Vol. 47, No. 4, 2001, pp. 419–423. Translated from Akusticheskiĭ Zhurnal, Vol. 47, No. 4, 2001, pp. 489–493.
Original Russian Text Copyright © 2001 by Zverev, Korotin, Tsiberev.

High-Resolution Interference Acoustic Location

V. A. Zverev, P. I. Korotin, and A. V. Tsiberev
Institute of Applied Physics, Russian Academy of Sciences,
ul. Ul'yanova 46, Nizhni Novgorod, 603600 Russia
e-mail: zverev@hydro.appl.sci-nnov.ru

Received March 20, 2000

Abstract—A method of forward-scattering location on the basis of resolving the arrival times of direct and scattered signals is proposed. The method is specific in that it allows one to use a long sinusoidal probing signal. The required time resolution of the signals produced by moving targets is achieved by processing the spectrum of the received echo signals so as to broaden its effective bandwidth. The method is tested in both numerical and full-scale acoustic experiments. For the first time, the forward-scattering location is implemented with the use of long probing pulses in a narrow frequency band. *© 2001 MAIK “Nauka/Interperiodica”.*

The maximal signal scattered by a target is known to come from the direction that coincides with the propagation direction of the probing signal. The target location that uses such signals is named the forward-scattering location (FSL). In addition to the maximal value of the scattered signal, FSL is advantageous in that there is no influence of the absorption on the relation between the direct and diffracted signals. That is why the FSL methods that use continuous probing signals were developed and implemented. With such methods, the target to be located is detected by its motion in the field of the continuous insonification. This procedure is performed by inverse aperture synthesis in the acoustic dark field [1–4]. The aforementioned methods are not always feasible for reasons that cannot be eliminated with continuous insonification of the target. First, a continuos probing signal creates a high-level reverberation background, which makes detecting the target difficult or impossible. Second, the need in the aperture synthesis to detect the target imposes stringent constraints on the stability of its motion.

The aforementioned restrictions can be circumvented by using pulsed probing signals with resolving the targets in the arrival times of the signals scattered by them. However, the use of a pulsed signal in the FSL scheme is accompanied by technical difficulties. To separate the scattered signal from the direct one propagating in nearly the same direction, a high time resolution is required. For this purpose, one needs a much broader frequency band than with continuous insonification.

It was found [5] that a high spatial resolution can be achieved by using a sinusoidal probing pulse. The effective frequency band of the signal reception can be increased by combined processing of the received and probing signals [5]. The method has a high efficiency if the probing signal is exactly known. This situation is typical of mathematical modeling rather than in practice. A high uncertainty can be introduced by the frequency response of the transmitting circuit. In this paper, we propose a method of increasing the effective bandwidth of signal reception without relying on a known form of the probing signal.

To make the reception bandwidth broader, we propose to process the echo signals in combination with one of them, rather than with the probing signal. In contrast to the procedure considered in [5], the proposed method leads to a pure interference location. With this technique, an interval of delays is determined between the selected (reference) signal and all other signals rather than the absolute delay between the received signal and the transmitted one. In the FSL case, the direct signal is most intense and is optimal as the reference signal. Thus, the interference location allows one to detect the weak scattered signal and to measure its delay relative to the direct signal. Another advantage of the proposed time selection of signals in the FSL consists in the possibility to detect the signals from moving targets. In contrast to the case of aperture synthesis, the target becomes visible when it moves along an arbitrary trajectory and, in the general case, nonuniformly.

The essence of the method is illustrated by the numerical calculations in the mathematical modeling of the problem. The results of computations are compared with those of the experiment in an anechoic acoustic chamber.

Let us consider the basic theoretical concepts of the method. The geometric difference in the path lengths of the scattered and direct signals is determined from the layout of the FSL, which is shown in Fig. 1. Let the distance between the sound source and the receiving microphone be D and the scatterer be at the distance d from the line (SR) connecting the source and the receiver. Then, for the scattered and direct signals, the difference in their path lengths is

$$\Delta = 2\sqrt{\left(\frac{D}{2}\right)^2 + d^2} - D \approx 2\frac{d^2}{D}. \qquad (1)$$

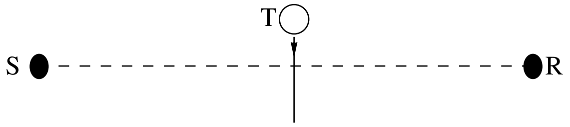

Fig. 1. Layout of the experiment at the forward-scattering location: S is the source, T is the scatterer, and R is the receiving microphone. The dashed line (S–R) connects the source and the receiver. The solid line indicates the scatterer trajectory used in the numerical calculations and in the experiment.

Note that, if the value of $\frac{d}{D}$ is small, it is equal to the angle at which the signal diffracted by the scatterer is received, this angle being measured from the propagation direction of the direct signal. The lower this angle, the higher the intensity of the scattered signal. That is why one should try to observe the scatterer at the lowest possible ratio $\frac{d}{D}$. In this case, one can separate signals with a low difference in the arrival times. Let d and D involved in Eq. (1) have the values that are required to successfully implement the FSL technique. Then, the time interval between the arrivals of the direct and scattered signals will be

$$\tau = \frac{\Delta}{c}, \tag{2}$$

where c is the propagation velocity of the waves and Δ is given by Eq. (1). A universal relation between the time resolution and the required frequency band Ω has the form

$$\Omega = \frac{2\pi}{\tau}. \tag{3}$$

Relation (3) is a consequence of the features of Fourier-conjugated functions and cannot be overridden or violated. The only way to achieve the required time resolution seems to have a sound source and a medium that can transmit the frequency band Ω with no significant attenuation. However, this is not quite true. In view of the nonlinearity of the problem, the high-intensity probing signal can have a strongly nonuniform transmitted spectrum, this nonuniformity being compensated at the signal reception [5].

If the direct signal is received along with the identical one delayed by τ in time, the spectrum of the sum of these signals as a function of frequency ω will be

$$S(\omega) = S_0(\omega)[1 + a\exp(i\omega\tau)], \tag{4}$$

where $S_0(\omega)$ is the complex spectrum of the probing signal, which can be essentially nonuniform, and a is the ratio of the scattered signal to the direct one.

To effectively broaden the frequency band involved in the signal processing, the spectrum $S(\omega)$ of the received signal should be transformed according to the following formula [5]:

$$SP(\omega) = \frac{S(\omega)}{SR(\omega)}, \tag{5}$$

where $SR(\omega)$ is the spectrum of the reference signal. Procedure (5) changes the signal spectrum $S(\omega)$ in such a manner that it becomes smoother. The best reference signal is one whose spectrum coincides with $S_0(\omega)$ (correct to a constant delay). The question is how to obtain this signal. In mathematical modeling, there is no such question, because $S_0(\omega)$ is the product of two functions: the spectrum of the electric signal applied to the transmitting circuit (it can be known) and the frequency response of the transmitting circuit itself, which is not known with the required accuracy within the entire frequency band.

For the reference signal, we propose to use the signal received at a certain moment of time. To show that such choice is sufficient, we imagine that the denominator of Eq. (5) contains the FSL signal received at the moment when the scatterer was at a position between the source and the receiver, precisely on the line connecting them. The spectrum of the signal received at the moment of such an eclipse of the source by the scatterer is obtained from Eq. (4) with $\tau = 0$: it is just the desired

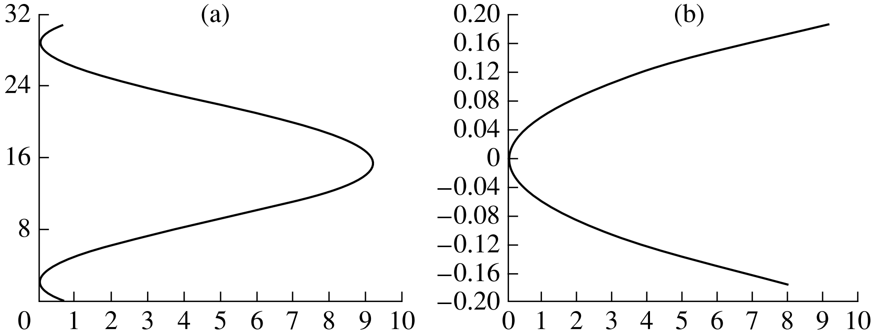

Fig. 2. Results of calculations: (a) the geometric difference in the path lengths (in centimeters, along the horizontal axis) as a function of the scatterer position (in ordinal numbers of the pulses) for the trajectory shown in Fig. 1; (b) the angle (in radians) of scatterer deviation from the source–receiver line.

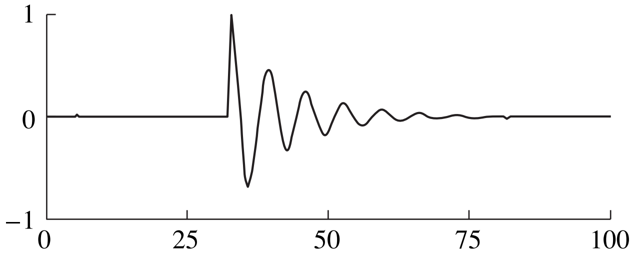

Fig. 3. Form of the probing pulse used in the numerical experiment. The horizontal axis shows the time recalculated to the path length (in centimeters) with the use of Eq. (2).

spectrum $S_0(\omega)$ that is appropriate to serve as the spectrum of the reference signal in Eq. (5).

More generally, the denominator of Eq. (5) involves the spectrum of a signal received at an arbitrary moment of time. Let the delay τ of the scattered signal in Eq. (2) be a function of time t. In addition, let the delay be a slowly varying function, so that the change in τ does not exceed $2\pi/\Omega$ (the interval of the delay resolution) within the pulse length. Then, one can substitute $\tau(t)$ into Eq. (2). Taking Eq. (2) at $t = t_1$ as the reference signal, we represent Eq. (5) in the form

$$SP(\omega, t) = \frac{S_0(\omega)[1 + a\exp[i\omega\tau(t)]]}{S_0(\omega)[1 + a\exp[i\omega\tau(t_1)]]}. \qquad (6)$$

As a rule, $|a| \ll 1$, and Eq. (6) can be simplified:

$$SP(\omega, t) = 1 + a\exp[i\omega\tau(t)] - a\exp[i\omega\tau(t_1)]. \quad (7)$$

The current spectrum of function (7) will include two harmonic components with a time resolution of $2\pi/\Omega$; one of these components remains constant and the other moves relative to the first component according to the motion of the scatterer.

The numerical simulation was carried out in accordance with [5]. The direct and scattered signals, along with noise, were modeled. The delayed scattered signal was the result of diffraction by an inhomogeneity, which moved along the trajectory shown in Fig. 1. The motion of the scatterer followed a harmonic law. This law corresponds to the experiments and, besides, confirms that the possibility for the signal to be detected weakly depends on the character of the motion. Figure 2b illustrates the change in the scattering angle as a function of the delay shown in Fig. 2a.

Figure 3 presents the form of the numerically modeled probing pulse. As in [5], the signal is combined with noise whose level is 40 dB lower than the signal maximum. Figure 4 illustrates the results of the numerical experiment. Figures 4a and 4b correspond to different methods of signal processing. In Fig. 4a, the processing method is the same as in [5]. As the reference signal, we used the function $S_0(\omega)$, which was known in the mathematical modeling of the problem. Figure 4b shows the result of processing with the use of one of the realizations of the echo signal as the reference signal. The selected time moment corresponded to zero delay. This moment is indicated by the white horizontal bar in Fig. 4b. Here, the noise is doubled in comparison with Fig. 4a. The added noise corresponds to a fixed time and, therefore, is fully correlated along the vertical axis. The signal-to-noise ratio is 20 dB in Fig. 4a. This ratio means that the scattered signal is always specified to be 20 dB lower than the probing signal. The method of signal processing, which is illustrated by Fig. 4a, is characterized by the maximal noise immunity. With other processing procedures, the noise immunity is 5–7 dB lower.

Let us consider the results of the physical experiment performed in a damped unechoic chamber. In the experiment, we used an electrodynamic loudspeaker

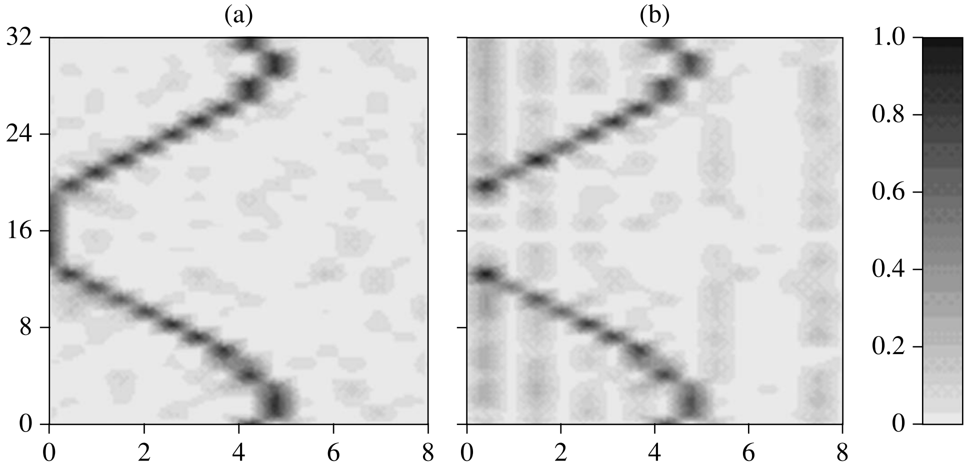

Fig. 4. Numerically modeled FSL. In the horizontal: time recalculated to the difference in the path lengths (in centimeters) with the use of Eq. (2). In the vertical: time in ordinal numbers of the pulses. The signal processing is performed according to (a) [5] and (b) the proposed method.

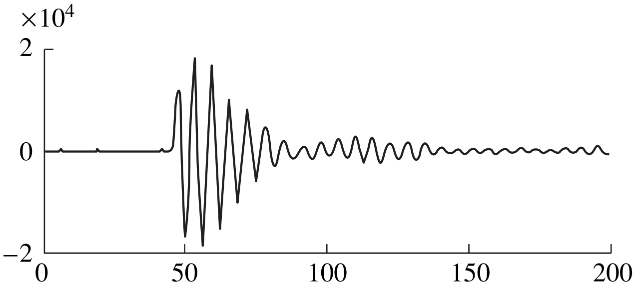

Fig. 5. Form of the probing pulse used in the acoustic experiment. In the horizontal: time recalculated to the path length (in centimeters) with the use of Eq. (2).

fed by an electric pulse of constant amplitude with a duration of 1 ms and a carrying frequency of 5.3 kHz. The receiving microphone was 3 m away from the transmitter. Figure 5 shows the form of the pulse received by the microphone. The loudspeaker had a rather intricate frequency response, which is evidenced by the long tail of the received signal. A sphere of 10 cm in radius served as the scatterer. The scatterer was suspended on a thread of about 2 m in length. In the course of the experiment, the scatterer swung freely with an amplitude of about 30 cm by crossing the source–receiver line in its periodic motion.

As one would expect, the scatterer is well seen when it is in the vicinity of the source–receiver line. One can increase the signal-to-noise ratio at the expense of the time resolution. To do so, one can omit the noisy parts of the spectrum. For the changes in the processing procedure not to affect the possibility to compare the modeling and experimental results, the modeling procedure was repeated in accordance with the processing technique used in the experiment. For this purpose, the same frequencies were eliminated from the modeled spectrum. The results are shown in Fig. 6. Figure 6a illustrates the mathematical calculations, and Fig. 6b presents the processed experimental data. From Fig. 6, we eliminated the signal that corresponds to the spectrum of the second term on the right-hand side of Eq. (7). The selection was performed in view of the difference in the signal signs: the negative components of the spectrum were eliminated. Such a selection is useful, because Fig. 6 was obtained by using a sum of two echo signals as the reference signal. As a result, the signal-to-noise ratio is lower in Fig. 6, though there are no light bars that correspond to the probing signals used in the denominator of Eq. (6).

According to the data presented in the figures, the theory and experiment are in good agreement. The differences consist in that the experimental signal decays as the scatterer moves away from the source–receiver line, whereas the modeled signal does not exhibit such a decay. The main advantage of the FSL is the use of the maximal scattering. This advantage is evident from the experimental data. One can also notice that the time dependences of the echo signals become widely different in Figs. 6a and 6b when the scatterer approaches the source–receiver line. This difference is a consequence of the fact that a point scatterer was implied in modeling, while a signal diffracted by a sphere of finite radius was observed in the experiment.

The diffraction phenomena observed in the acoustic FSL experiments confirm the possibility to experimentally solve the diffraction problem in the case of forward scattering, which was solved theoretically in [6]. The use of pulsed probing signals in the FSL considerably extends the possibilities for the experimental studies of the sound diffraction by weakly scattering bod-

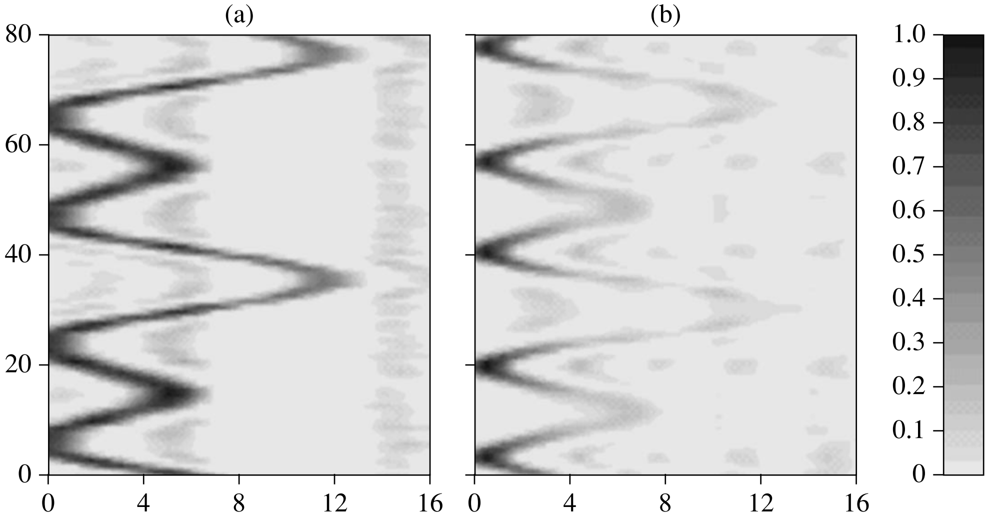

Fig. 6. Results of the calculation and the experiment for the sum of two echo signals used as the reference signal. The axes are the same as in Fig. 4.

ies, which was previously analyzed mainly theoretically (see, e.g., [7]).

ACKNOWLEDGMENTS

We are grateful to B.M. Salin for the support of this work and useful discussions.

The work was supported by the Russian Foundation for Basic Research, project nos. 96-00-15-96741, 99-02-16401, and 97-02-17555.

REFERENCES

1. V. A. Zverev, Akust. Zh. **40**, 401 (1994) [Acoust. Phys. **40**, 360 (1994)].
2. V. A. Zverev, A. L. Matveev, and V. V. Mityugov, Akust. Zh. **41**, 591 (1995) [Acoust. Phys. **41**, 518 (1995)].
3. V. A. Zverev, Akust. Zh. **46**, 75 (2000) [Acoust. Phys. **46**, 62 (2000)].
4. V. A. Zverev, P. I. Korotin, A. L. Matveev, *et al.*, Akust. Zh. **46**, 650 (2000) [Acoust. Phys. **46**, 569 (2000)].
5. V. A. Zverev, Izv. Vyssh. Uchebn. Zaved., Radiofiz. **43**, 406 (2000).
6. C. Feuillade and C. S. Clay, J. Acoust. Soc. Am. **106**, 553 (1999).
7. K. Chandra and C. Thomson, J. Acoust. Soc. Am. **92**, 1047 (1992).

Translated by E. Kopyl

Acoustical Physics, Vol. 47, No. 4, 2001, pp. 424–429. Translated from Akusticheskiĭ Zhurnal, Vol. 47, No. 4, 2001, pp. 494–500.
Original Russian Text Copyright © 2001 by Katsnel'son, Pereselkov, Petnikov, Sabinin, Serebryanyĭ.

Acoustic Effects Caused by High-Intensity Internal Waves in a Shelf Zone

B. G. Katsnel'son*, S. A. Pereselkov*, V. G. Petnikov,**
K. D. Sabinin*, and A. N. Serebryanyĭ*****
**Voronezh State University, Universitetskaya pl. 1, Voronezh, 394693 Russia*
e-mail: katz@mph.vsu.ru
***Wave Research Center, General Physics Institute, Russian Academy of Sciences,*
ul. Vavilova 38, Moscow, 117333 Russia
e-mail: petnikov@kapella.gpi.ru
****Andreev Acoustics Institute, Russian Academy of Sciences,*
ul. Shvernika 4, Moscow, 117333 Russia
e-mail: bvp@akin.ru

Received April 27, 2000

Abstract—The sound field fluctuations caused by high-intensity, solitonlike, quasi-plane internal waves crossing a fixed acoustic path at different angles are numerically modeled for natural conditions of the shelf zone of the Sea of Japan. The horizontal refraction of sound is considered for the case of an acoustic path parallel to the internal wave front. *© 2001 MAIK "Nauka/Interperiodica".*

Internal waves are an important factor of vertical mixing in the ocean. They also strongly affect sound propagation. The effects of internal waves are most pronounced in the regions of ocean shelves, seamounts, and the continental slope, where internal waves are enhanced and can reach very high amplitudes [1]. In the shelf zone, the tidal energy is regularly transferred by the tidal internal waves from the continental slope towards the coast. While passing over the shelf, the internal tides undergo a nonlinear transformation giving rise to trains of short high-intensity waves. Similarly to the tidal wave, these short waves travel towards the coast until they reach the coastal zone where further energy transfer to even shorter waves and turbulence takes place [2]. It is not uncommon that in the shelf zones of open seas and oceans the amplitudes of the internal waves are as high as 10 m or more. The size of the train along its propagation direction depends on the number of waves forming the train and vary from several hundreds of meters to several kilometers. The crests of the internal waves that propagate over a shelf are usually parallel to the isobaths and follow the mean features of the seafloor profile. Sometimes, the crests remain nearly straight for many kilometers or even tens of kilometers. Near the shelf edge, the crests often have the shape of arches that are convex in the propagation direction, which indicates the local character of the internal wave sources.

Thus, the internal waves that are generated over the shelf and near its edge cause pronounced deformations of the pycnocline, which extend over large sea areas. Such a medium cannot be treated as a plane-layered one for sound propagation. A number of researchers (see, e.g., [3, 4]) studied sound propagation in such a medium in terms of the geographical features of the region. However, these studies almost completely neglect the effects of the orientation of the sound propagation path relative to the propagation direction of internal waves. This dependence is the subject of our paper.

To illustrate the aforementioned effects in numerical experiments, we used the data that were obtained in a special-purpose experimental study of internal waves, which was carried out on the shelf of the Sea of Japan in August and September, 1983 [5]. Figure 1 shows the average hydroacoustic parameters for the experimental site. These parameters were calculated from the directly measured vertical profiles of the water temperature and salinity. The internal waves were measured from a vessel that went on linear tacks at a constant speed with a towed distributed temperature sensor [6] deployed in the temperature discontinuity layer. The sensor covered the depths 12 to 23 m. The data obtained in this way characterize the spatial variability of the thermocline depths over the shelf and allow reliable detection of the thermocline disturbances caused by the train of internal waves. Each towing act consisted of several (at least two) passages in opposite directions across the isobaths of the continental slope through the shelf from a point near the coast to a point beyond the continental slope. One tack covered an area 30–40 km in length. The main direction of towing coincided with the

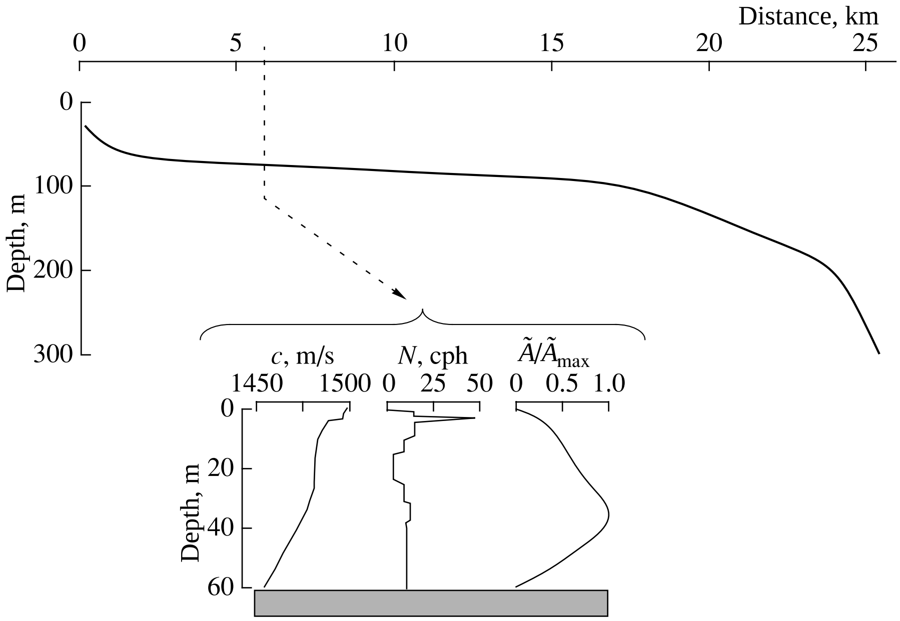

Fig. 1. Hydroacoustic parameters of the experimental site. The plot at the bottom shows the vertical profiles of the sound speed c, the buoyancy frequency N, and the normalized vertical displacements $\tilde{A}/\tilde{A}_{max}$ for the first gravity mode of the internal wave at a distance of 6 km from the coastline.

mean direction of the trains of high-intensity internal waves that arrived at the coastal zone from the open sea. This arrival direction was determined from the measurements performed with a spatial array of distributed temperature sensors in the previous summer season [7]. The temperature profile was measured at a speed of about 3 m/s, which is an order of magnitude higher than the propagation velocity of the internal waves. In towing, a train of high-intensity internal waves was detected at a distance of about 6 km from the coastline, at depths of 50–60 m. The train moved towards the coast with a velocity of about 0.2 m/s. With these experimental data, we calculated the time dependences for the vertical displacements of water particles under the effect of internal waves along the path 5 km in length at a depth of 33.5 m (see Fig. 4a). In the calculations, we used the average vertical profiles of temperature and density in the region along with the depth distribution of the internal wave amplitude $\tilde{A}(z)/\tilde{A}_{max}$, which was calculated with the computer code developed by Goncharov [8] (see Fig. 1). It was assumed that the first gravity mode predominates in the internal-wave field, as is typical of shallow-water regions. Figure 4a shows that the train itself is preceded by a smooth rise of the thermocline followed by its sharp sink, the latter, in fact, being the leading edge of the train. The wave of maximal peak-to-peak amplitude (the second one in the train, 7 m) is indicated by arrows in the figure. This wave exhibits a sharp foot and a smooth crest. Such features are typical of nonlinear waves propagating in the subsurface thermocline and characteristic of internal waves on the shelf [9].

Let us now consider the acoustic effects that can be observed in the presence of the recorded internal waves. In particular, let us analyze the sound field generated by a fixed bottom-moored sound source with a frequency of 250 Hz. Let the field be received at a fixed observation point located 5 km from the source (i.e., we consider the sound field on a fixed propagation path). For a plane-layered medium (both in shallow- and deep-water cases), the sound field is known to consist of a sum of waveguide modes that are depth dependent and have constant amplitudes along the path (the amplitudes exponentially decay in the presence of sound absorption). In accordence with the cylindrical symmetry of the problem, the wave fronts and curves of constant amplitude are circles in the horizontal plane. Internal waves cause some perturbation in the planar structure of the plane-layered medium, which, however, are assumed to be sufficiently weak for the field to be represented as a sum of modes. Let the disturbance (in the depth or sound speed profile) depend on the distance from the sound source, and the dependence on the transverse coordinate (with respect to the propagation path) be neglected. Then, in terms of the normal-wave description, the amplitudes of local modes (or reference modes, which are the solutions to the waveguide problem for each cross-section of the waveguide) will vary with distance (independently of the absorption), this variation being interpreted as the interaction (or transformation) of the modes. The problem of finding the weighting factors for the modes that travelled through the irregular part of the waveguide is well known and methods have been developed to solve it. In particular, for a sufficiently narrow spatial spectrum of the train (and a sufficient duration of the internal-wave realization), the so-called resonant effects were revealed: only individual pairs of modes interact, their interaction depending on the sound frequency. These effects manifest themselves in the resonant absorption of sound generated by broadband sources [10, 11]. At the same time, the wave fronts remain parallel in the horizontal plane. Now, let the disturbance depend on nothing but the transverse coordinate. In this case, the sound field in the waveguide can be represented as a sum of modes, each mode propagating over it own horizontal ray (or a set of rays), and no transformation of modes is observed. In this case, the wave fronts are not parallel in the horizontal plane: the cylindrical symmetry of the problem is violated. If the disturbance is arbitrary, both factors affect the structure of the sound field.

Apart from the practical importance of monitoring internal waves on a shelf by acoustic methods, the observation of the perturbations caused in the structure of the sound-speed field by the trains of internal solitons in a shallow sea allows one to consider the two aforementioned cases in an explicit form and, thereby, to experimentally solve one of the fundamental problems of shallow-water acoustics. Namely, such a study can be performed by using an acoustic path that is parallel or perpendicular to the fronts of internal waves.

Let us represent the oceanic medium as a three-dimensional underwater waveguide in the *XYZ* coordinate system. The waveguide consists of a water layer of density $\rho_w(z)$ and the squared refractive index $n^2(z) + \mu(x, y, z, t)$, where $n^2(z)$ corresponds to the mean equilibrium stratification of the layer (the corresponding sound speed profile is $c(z)$) and $\mu(x, y, z, t)$ characterizes the changes in the acoustic properties of the layer under the effect of the train of internal waves. The water layer is bounded by the pressure-release surface at $z = 0$ and a homogeneous absorbing halfspace at $z = H$, i.e., by the sea floor with the density ρ_1 and the squared refractive index $n_1^2(1 + i\alpha)$, where $n_1 = c(H)/c_1$ and the factor α determines the absorptive properties of the bottom. In numerical calculations, we specified $H = 60$ m, $\rho_1 = 2$ g/cm^3, $c_1 = 1750$ m/s, and $\alpha = 0.02$.

According to [12], the quantity $\mu(x, y, z, t)$ is determined by the parameters of the train:

$$\mu(x, y, z, t) = -\frac{2\delta c(x, y, z, t)}{c(z)} = -2QN^2(z)\zeta(x, y, z, t). \quad (1)$$

Here, δc is the sound speed variation caused by the displacement of the constant-density interface, $N(z) = \left(\frac{g}{\rho}\frac{d\rho}{dz}\right)^{1/2}$ is the buoyancy frequency determined by the mean density stratification of the water layer, ρ is the water density, g is the acceleration of gravity, $Q \approx 2.4$ s^2/m is a constant determined by the physical properties of water, and ζ is the vertical displacement of the water layers. The latter quantity can be represented as

$$\zeta(x, y, z, t) = \Phi(z)\zeta(\mathbf{r} - \mathbf{u}t), \quad (2)$$

where $\mathbf{u}$ is the horizontal velocity of the soliton, which in general depends on the coordinates (this dependence, in particular, can be responsible for a distortion of the wave front); $\mathbf{r}$ is the radius vector of the point (x, y) in the horizontal plane; and $\Phi(z) \equiv \tilde{A}(z)/\tilde{A}_{\max}$ (see Fig. 1).

According to Eqs. (1) and (2), the disturbance strongly depends on the propagation direction of the internal wave. Here, two limiting cases exist: the internal waves cross the fixed acoustic path at right angles or they propagate along the path. Let us consider these cases separately. Let the aforementioned train of internal waves propagate along the *Y* axis and cross the fixed path that coincides with the *X* axis. Because the path is short, the disturbance depends only on the transverse coordinate (*X*). (Within a distance of 5 km, the wave front can be treated as a planar one.) In this case, to describe the sound field in the waveguide, one can use the theory of horizontal rays and vertical modes [13]. Then, the complex amplitude of the sound field can be represented as

$$P(\mathbf{r}, z) = \sum_n \sum_m A_{nm}(\mathbf{r})\psi_m(\mathbf{r}, z)\exp[i\theta_{nm}(\mathbf{r})]. \quad (3)$$

Here, $A_{nm}(x, y)$ is the amplitude and $\theta_{nm}(x, y)$ is the phase shift (eikonal) for the *m*th acoustic mode $\psi_m(x, y, z)$, which depends on the horizontal coordinates in a parametric manner. Let us introduce the notation $\xi_m = q_m + i\frac{\gamma_m}{2}$ for the eigenvalues of the Sturm problem in the given cross-section of the waveguide (they are complex because of sound absorption). Note that, in general, several horizontal rays corresponding to a single mode can arrive at the reception point. These rays have different trajectories and, hence, different amplitudes and phase shifts. That is why the summation in Eq. (3) is performed over the vertical modes (the subscript m) and over the horizontal rays (the subscript n).

For the amplitude and the eikonal, one can obtain ordinary equations of geometric acoustics:

$$(\nabla_r \theta_{nm})^2 = q_m^2, \qquad (4)$$

$$2\nabla_r A_{nm} \nabla_r \theta_{nm} + A_{nm} \nabla_r^2 \theta_{nm} + q_m \gamma_m A_{nm} = 0. \qquad (5)$$

For the case of internal solitons, their solutions can be constructed by applying the theory of perturbations to the effective refraction index [14]. Let us consider the ray pattern for the case when the fixed path is crossed by the aforementioned train of internal waves at right angle. We assume that, along the path, the water particles oscillate synchronously (see Fig. 2a). Figure 3 illustrates the calculated sets of horizontal ray trajectories corresponding to the first and second vertical acoustic modes. The calculations are performed for the situations when the crest (region I in Figs. 2a, 4a) and foot (region II) of the soliton are present on the path. The source (i.e., the origin of rays for each ray set) was assumed to be at the point $x = 0$, $y = 0$. As Fig. 3 shows, the large-amplitude internal waves lead to the focusing or defocusing of sound waves in the horizontal plane, depending on whether the maximum or minimum of the internal-wave field is present on the path at the moment. Note that focusing or defocusing takes place for all vertical modes simultaneously, which enhances the fluctuations of the sound field at the receiver.

In view of the focusing and defocusing effects, let us calculate the temporal fluctuations of the sound field intensity for the case at hand, when the train of internal waves crosses the fixed path. To be more accurate, we use the parabolic equation in the horizontal plane with vertical waveguide modes [15]. According to this method, the received sound field can be represented as

$$P(\mathbf{r}, z) = \sum_{m=0}^{M} F_m(x, y) \psi_m(\mathbf{r}; z) \exp[i q_m^{(0)} x], \qquad (6)$$

where $F_m(x, y)$ is the smoothly varying amplitude ($\partial F_m/\partial x \ll q_m^{(0)} F_m$) and $q_m^{(0)}$ is the real part of the eigenvalue for the waveguide without internal waves. Then, for the function $F_m(x, y)$, the following equation is valid:

$$\frac{\partial F_m}{\partial x} = \frac{i}{2q_m^{(0)}} \frac{\partial^2 F_m}{\partial y^2} + \frac{i q_m^{(0)}}{2} (n_q^2(x, y) - 1) F_m, \qquad (7)$$

where $n_q(x, y) = q_m(x, y)/q_m^{(0)}$. Because the characteristic time scale of the variations of the refractive index (1) due to the internal wave motion is much greater than the time of the sound propagation along the path, the quasi-static approximation can be used to calculate the time dependence $|P(\mathbf{r}, z, t)|$ for the received sound field. In this calculation, the eigenfunctions and eigenvalues can be assumed to depend on time in a parametric way.

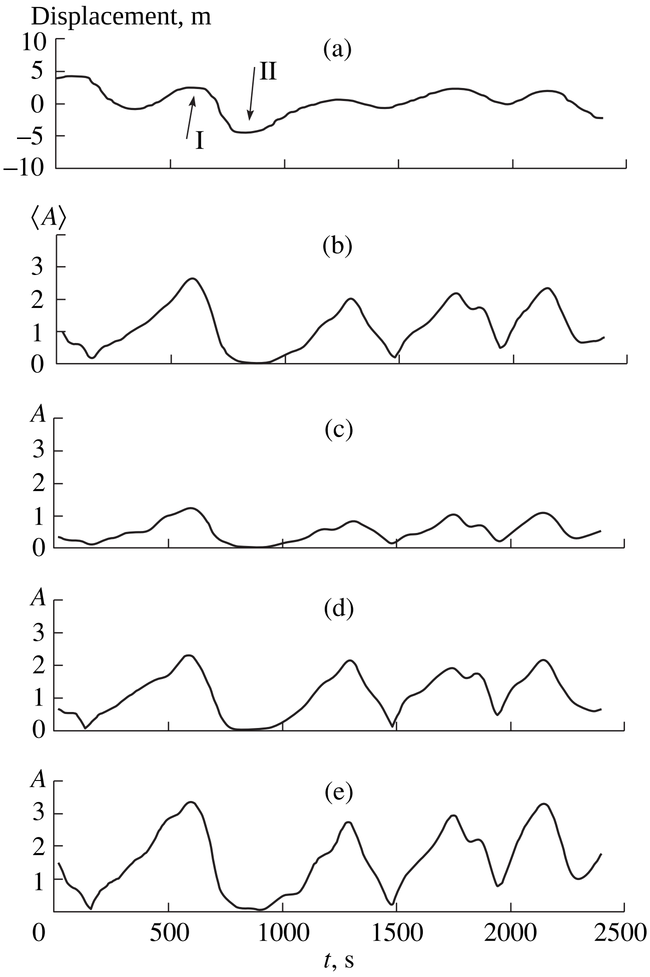

Fig. 2. (a) Time dependence $\zeta(t)$ of the vertical displacements of water particles at 33.5 m depth on the fixed path crossed at right angles by the internal waves. The arrows indicate the maximal displacements caused by the passage of the soliton. (b) Time dependence of the average relative amplitude $\langle A \rangle$ of the sound field. (c–e) Time dependences of the relative amplitude A of the sound field at the reception depths 5, 30, and 55 m, respectively.

Figures 2c–2e show the dependences of the relative amplitudes A ($A = |P(t)|/\overline{\langle |P(t)| \rangle}$) of the sound field calculated for different depths of reception. Here and below, the angular brackets stand for averaging over the reception depths and the overbar indicates the time averaging. According to Fig. 2, the internal waves perpendicularly crossing the fixed path at an angle of 90° lead to intense variations of the sound field. The spectrum of these variations is shown in Fig. 5 as a solid curve. The variations are caused both by the changes in the interference pattern in the waveguide and by the aforementioned focusing and defocusing effects. The variations remain considerable even if the sound field is averaged in the vertical. In Fig. 2b, the averaging result

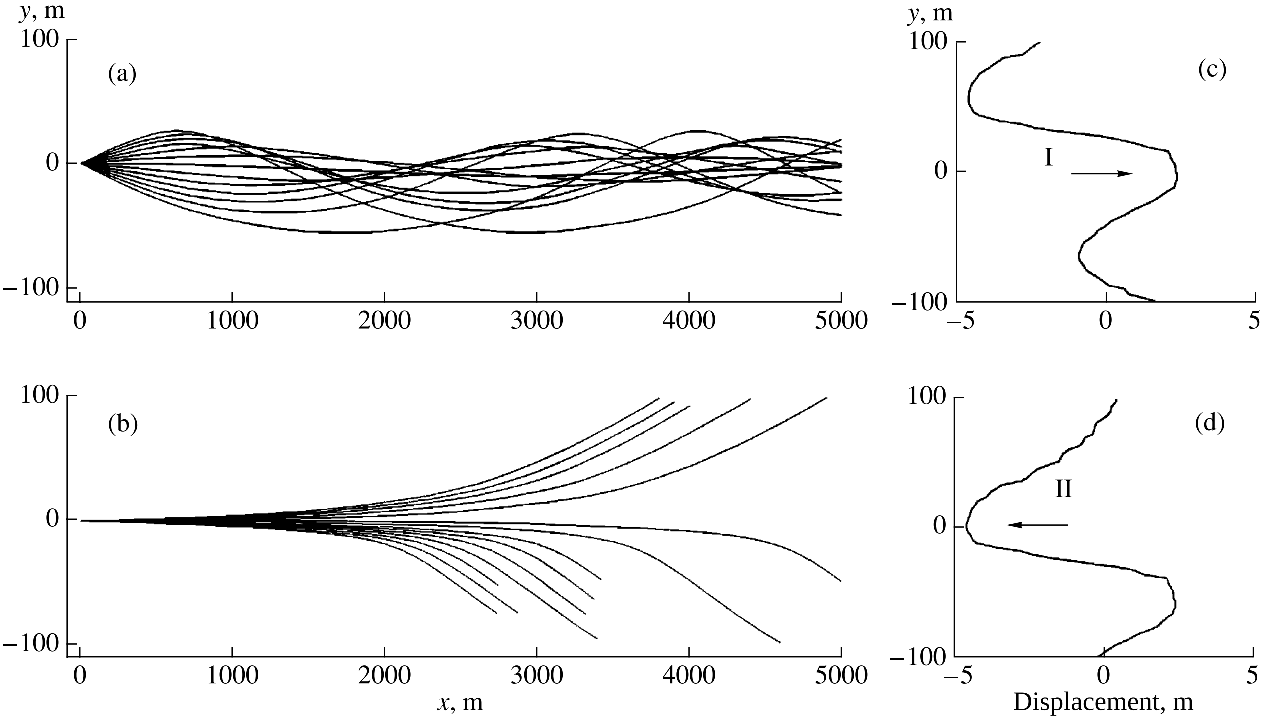

Fig. 3. (a, b) Calculated sound-ray trajectories corresponding to focusing and defocusing in the horizontal plane, respectively. (c, d) Vertical displacements of water particles across the fixed path, which cause the focusing and defocusing effects.

($\langle A\rangle = \langle|P(t)|\rangle/\overline{\langle|P(t)|\rangle}$) is shown for eleven horizons of reception, from 5 to 55 m with a step of 5 m.

Now consider the second situation when the train of internal waves moves along the path with the velocity 0.2 m/s; in other words, the path is assumed to be nearly perpendicular to the coastline. For this situation, Fig. 4a shows the vertical displacements of water particles along the path at a fixed moment of time. In this case, the disturbance depends on the distance from the source. At the same time, the dependence on the transverse coordinate can be neglected. The amplitudes of the local modes change in distance, which testifies to the interaction (transformation) of the modes. The aforementioned horizontal refraction is absent, and the wave train remains parallel to itself in the horizontal plane.

Figures 4c–4e show the calculated variations of the sound field amplitude A for the case of the train moving along the path. In our situation with a relatively short path and a relatively broad spatial spectrum of the soliton train, a simultaneous interaction of many modes takes place. Mathematically, the calculation consists in solving the system of a large number of ordinary differential equations that describe the interaction of the modes. It is advantageous to use the well-known method of a parabolic equation (in the vertical plane) [16] in this case. Such a calculation was performed. The spectrum of the variations is shown in Fig. 5. Figure 4b presents the depth-averaged amplitude. As previously, averaging was performed over eleven horizons. Note that this time, averaging leads to a nearly total smoothing of the sound field variations.

By comparing the calculations carried out for the two limiting cases of longitudinal and transverse propagation of the internal waves, we arrive at two main conclusions.

First, the amplitude variations are much higher in the transverse propagation than in the longitudinal one.

Second, the spectrum of the variations is much broader for the transverse propagation than for the longitudinal one. In other words, high-intensity internal waves crossing a fixed path at right angles cause high-frequency variations of the sound field, which are absent when the internal waves propagate along the path.

Note that similar conclusions were obtained from the numerical experiments [17] for the train of internal waves measured on the New York shelf. However, additional enhancement of the variations because of horizontal focusing was not considered in the cited publication.

To conclude, we emphasize once again that, in the shelf zones, the internal waves strongly affect the low-frequency sound field, and the magnitude of this effect depends on both the amplitude of internal waves and the direction of their propagation. The greater the angle

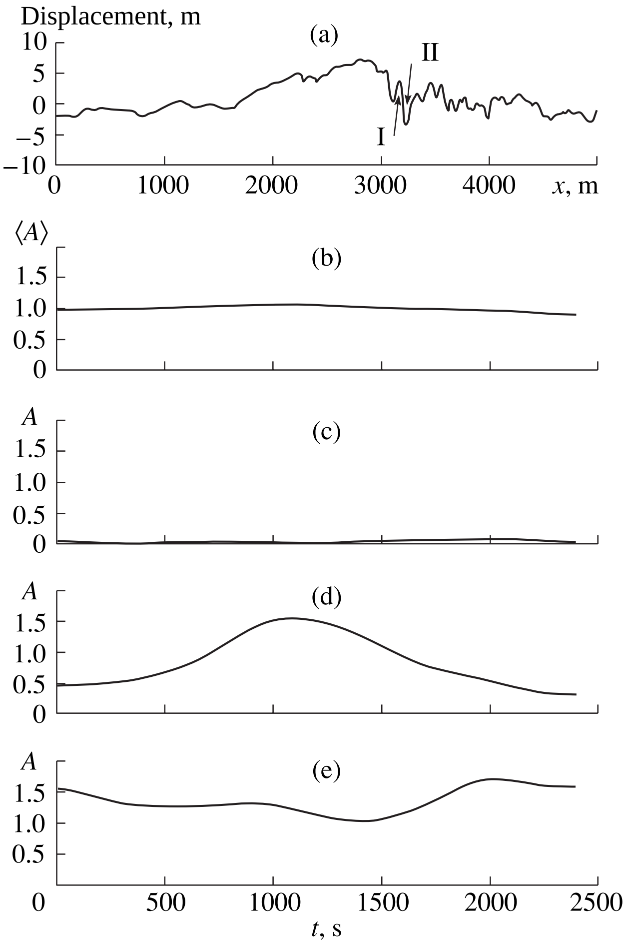

Fig. 4. (a) Vertical displacements $\zeta(x)$ of water particles along a fixed path in the case of the longitudinal propagation of internal waves. The arrows indicate the maximal displacements caused by passage of the solitons. (b) Time dependence of the average relative amplitude $\langle A\rangle$ of the sound field. (c–e) Time dependences of the relative amplitude A of the sound field at the reception depths 5, 30, and 55 m, respectively.

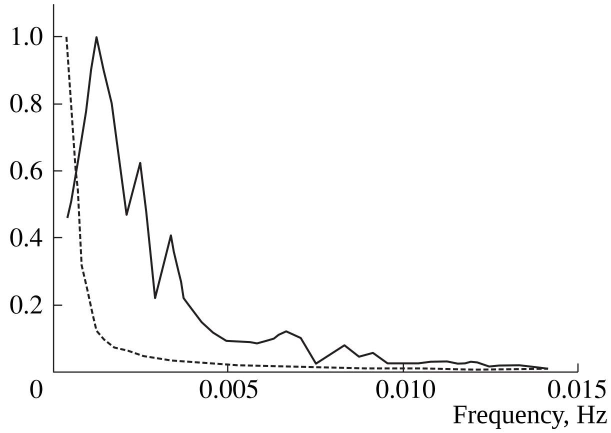

Fig. 5. Spectra $\langle S(f)\rangle$ of the sound field amplitude variations in the case of transverse (the solid curve) and longitudinal (the dashed curve) propagation of internal waves.

between the propagation directions of the internal and sound waves, the greater the amplitude variations of the sound field.

ACKNOWLEDGMENTS

This work was supported by the Russian Foundation for Basic Research, project nos. 98-05-64804, 00-05-64752, and 99-02-17671.

REFERENCES

1. A. N. Serebryany, in *Proceedings of International Symposium "Ocean Cities 95"* (Monaco, 1995), p. 376.
2. A. N. Serebryanyĭ, in *Atlas of Temporal Variations of Natural, Anthropogenic, and Social Processes* (Nauchnyĭ Mir, Moscow, 1998), Vol. 2, pp. 297–302.
3. J. R. Apel, M. Badie, C. S. Chiu, *et al.*, IEEE J. Ocean Eng. **22**, 465 (1997).
4. D. Tielbuerger, S. Finette, and S. Wolf, J. Acoust. Soc. Am. **101**, 789 (1997).
5. A. N. Serebryanyĭ, Okeanologiya (Moscow) **27** (2), 225 (1987).
6. K. V. Konyaev and K. D. Sabinin, *Waves within the Ocean* (Gidrometioizdat, St. Petersburg, 1992).
7. A. N. Serebryanyĭ, Okeanologiya (Moscow) **25** (2), 744 (1985).
8. V. V. Goncharov, in *Tsunami and Internal Waves* (MGI AN USSR, Sevastopol, 1976), pp. 87–96.
9. A. N. Serebryanyĭ, Izv. Akad. Nauk SSSR, Fiz. Atmos. Okeana **26**, 285 (1990).
10. Ji-Xun Zhou and Xue-Zhen Zhang, J. Acoust. Soc. Am. **90**, 2042 (1991).
11. B. G. Katsnel'son and S. A. Pereselkov, Akust. Zh. **44**, 786 (1998) [Acoust. Phys. **44**, 684 (1998)].
12. *Sound Transmission through a Fluctuating Ocean*, Ed. by S. Flatte (Cambridge Univ. Press, Cambridge, UK, 1979; Mir, Moscow, 1982).
13. R. Burridge, in *Wave Propagation and Underwater Acoustics*, Ed. by J. B. Keller and J. S. Papadakis (Springer, New York, 1977; Mir, Moscow, 1979).
14. B. G. Katsnel'son and S. A. Pereselkov, Akust. Zh. **46**, 779 (2000) [Acoust. Phys. **46**, 684 (2000)].
15. M. D. Collins, J. Acoust. Soc. Am. **94**, 2269 (1993).
16. F. D. Tappert, in *Wave Propagation and Underwater Acoustics*, Ed. by J. B. Keller and J. S. Papadakis (Springer, New York, 1977; Mir, Moscow, 1979).
17. V. G. Petnikov, B. G. Katsnelson, S. A. Pereselkov, and K. D. Sabinin, in *Proceedings of International Conference on Shallow-Water Acoustics* (Beijing, 1997), p. 289.

Translated by E. Kopyl

Acoustical Physics, Vol. 47, No. 4, 2001, pp. 430–437. Translated from Akusticheskiĭ Zhurnal, Vol. 47, No. 4, 2001, pp. 501–508.
Original Russian Text Copyright © 2001 by Kozhevnikov.

Effect of an Ultrasonic Field on the Structure of a Cholesteric Liquid Crystal

E. N. Kozhevnikov
Samara State University, ul Ak. Pavlova 1, Samara, 443011 Russia
e-mail: kozhev@ssu.samara.ru

Received July 25, 2000

Abstract—A spatially modulated structure arising in a layer of a cholesteric liquid crystal under the effect of an ultrasonic wave is studied theoretically. The structure is described on the basis of the equations of fluid dynamics for cholesteric liquid crystals. The equations are represented in terms of the angular variables. An anisotropic term caused by the relaxation of the orientational order parameter is introduced into the stress expressions. The results of calculations are compared with experimental data. © *2001 MAIK "Nauka/Interperiodica".*

Liquid crystals exhibit a variety of dissipative structures that may arise under external actions, including the case of periodic deformation of a crystal in oscillating flows, viscous waves, and sound fields. Nematic crystals with a simple structure have been thoroughly investigated both experimentally and theoretically [1–5]. The effect of sound on the structure of cholesteric liquid crystals is less well understood. Experimental studies [1, 6, 7] show that, when an ultrasonic wave is incident on a layer of a cholesteric liquid crystal with planar orientation of molecules, periodic distortions of the cholesteric structure in the form of domains are observed. The effect is of a threshold character. The form of the resulting structure depends on the initial geometry of the liquid-crystal sample, and its spatial period decreases beyond the threshold of the effect.

An attempt to theoretically describe the appearance of a spatially modulated structure in a layer of a cholesteric liquid crystal in the case of the normal incidence of an ultrasonic wave on it is made in [8]. The description is based on the equations of fluid dynamics for cholesteric liquid crystals. In this study, a cholesteric liquid crystal is treated as a twisted nematic crystal and the stresses are represented in the Leslie–Eriksen form. The perturbation method provides an opportunity to separate the stationary distortions of the structure and is used to determine the threshold of their appearance. It is assumed that the pitch of the cholesteric helix is much smaller than the thickness of the layer of the cholesteric liquid crystal, and the role of the preliminary tension of the layer is analyzed. The calculation predicts the appearance of a domain structure in the layer of a cholesteric liquid crystal under the effect of ultrasound. At the same time, detailed comparison [7] revealed a significant quantitative disagreement between the calculations and the experimental data. This disagreement shows that, in terms of the classical fluid dynamics for cholesteric liquid crystals, it is impossible to adequately describe the domain structure formed in the case of the compression of a cholesteric layer at ultrasonic frequencies.

In this paper, the effect of ultrasound on a layer of a cholesteric liquid crystal is treated from another point of view. The relaxation processes leading to an anisotropy of the dynamic elasticity are taken into account in this study. The general pattern of the domain formation is analogous to that described in [8]: in a sound field, the random distortions of the cholesteric structure that are periodic along the liquid crystal layer lead to oscillating vortex flows and structure distortions, which have the same spatial period. The convective interaction of vortices and oscillating rotation angles of molecules with the sound field leads to stationary moments and flows increasing the structure distortion. In the case of a sufficiently intense effect of sound, the destabilizing moments start to exceed the Frank elastic moments, and a domain structure arises in the layer. In contrast to [8], this paper takes into account the relaxation of the orientational order parameter in the sound field, which leads to an anisotropy of the dynamic modulus of elasticity of the medium and changes the character of the liquid motion. The convection of the azimuth rotation of molecules in the cholesteric planes and the change in the helix pitch in the case of layer tension in a sound wave are taken into account in the equations of rotation.

Following [8], we represent the equations of motion and the equations of molecule rotation in the form

$$\rho\dot{\mathbf{v}} = -\nabla p + \nabla\hat{\sigma} + \mathbf{F},$$
$$\gamma_1\mathbf{N} + \gamma_2[\hat{V}\cdot\mathbf{n} - (\mathbf{n}\cdot\hat{V}\cdot\mathbf{n})\mathbf{n}] - \nabla_i\frac{\partial g}{\partial\nabla_i\mathbf{n}} + \frac{\partial g}{\partial\mathbf{n}} = 0, \tag{1}$$

where ρ is the density, $\mathbf{v}$ is the velocity, $\mathbf{n}$ is the director, $\mathbf{N} = \dot{\mathbf{n}} - \frac{1}{2}(\operatorname{rot}\mathbf{v}\times\mathbf{n})$ is the rate of the director rotation with respect to the surrounding medium, $\hat{V}$ is the strain

1063-7710/01/4704-0430$21.00 © 2001 MAIK "Nauka/Interperiodica"

rate tensor, p is the pressure, g is the density of the Frank elastic energy, and $\hat{\sigma}$ is the stress tensor.

In the stress tensor, we take into account the anisotropic term $\delta\hat{\sigma}^{(a)}$ due to the relaxation processes in a liquid crystal in a sound wave. We use the results of [9] to derive the expression for $\delta\hat{\sigma}^{(a)}$ (the cited paper is devoted to the study of the anisotropy of the acoustic properties of a nematic crystal). According to [9], the anisotropic part of the stress tensor $\delta\hat{\sigma}^{(a)}$ in a sound wave with frequency ω can be presented in the form

$$\delta\sigma_{ij}^{(a)} = (\Delta E u_{\alpha\alpha} + \mu_3 v_{\alpha\alpha}) n_i n_j,$$

where $\Delta E = DE\dfrac{(\omega\tau)^2}{1 + (\omega\tau)^2}$, $\mu_3 = DE\dfrac{\tau}{1 + (\omega\tau)^2}$, $2DE = (E_\parallel - E_\perp)\big|_{\omega = 0}^{\omega = \infty}$ is the dispersion jump of anisotropy of the elastic modulus of the nematic medium in the case of its compression along ($E_\parallel$) perpendicular to ($E_\perp$) the crystal axis, μ_3 is the bulk viscosity coefficient, and τ is the relaxation time of the orientational order parameter.

Taking into account the anisotropy of the crystal elasticity, we represent the stress $\hat{\sigma}$ in the form

$$\sigma_{ij} = n_i n_j(\Delta \mathrm{E} u_{\alpha\alpha} + \mu_3 v_{\alpha\alpha}) + \alpha_1 v_{\alpha\beta} n_\alpha n_\beta n_i n_j$$
$$+ \alpha_2 N_i n_j + \alpha_3 N_j n_j + \alpha_4 v_{ij} + \alpha_5 v_{ik} n_k n_j + \alpha_6 v_{jk} n_k n_i,$$

where α_i are the Leslie viscosity coefficients. By analogy with nematic crystals, we assume that the viscosity coefficient α_3 is small and take it equal to zero. Then, we obtain $\gamma_1 = -\gamma_2 = \gamma$.

The distorted structure of a cholesteric liquid crystal is characterized by an additional free energy, i.e., the Frank elastic energy G. In the two-constant approximation, the energy G has the form [10]

$$G = \int_V g dV$$
$$= \frac{1}{2}K\int_V \{(\operatorname{div}\mathbf{n})^2 + \lambda(\mathbf{n}\operatorname{rot}\mathbf{n} + q_0)^2 + (\mathbf{n}\times\operatorname{rot}\mathbf{n})^2\} dV,$$

where $K = K_{11} = K_{33}$ are the Frank elastic constants, $\lambda = K_{22}/K$, $q_0 = 2\pi/P_0$, and P_0 is the pitch of the cholesteric helix.

The force $\mathbf{F}$ involved in the equation of motion arises in a distorted cholesteric structure and is determined by the variation of the density of the Frank elastic energy g with respect to the displacements $\mathbf{u}$:

$$\mathbf{F} = -\frac{\partial g}{\partial \mathbf{u}} + \nabla_i \frac{\partial g}{\partial \nabla_i \mathbf{u}} - \Delta\frac{\partial g}{\partial \Delta \mathbf{u}}. \tag{2}$$

In the unperturbed state, the director lies in the cholesteric planes and rotates uniformly in passing from one plane to another with the period P_0. We set the structure distortions by the angles θ and φ that determine the deviations of molecules from the unperturbed cholesteric plane and (in the plane) from the initial orientation, respectively. A uniform rotation through the angle φ shifts the cholesteric layers along the crystal axis by the distance φ/q_0, and a nonuniform rotation of molecules along the layer leads to its distortion.

In the approximation quadratic in θ and φ, the Frank elastic energy has the form

$$G = \frac{1}{2}K\int_V \{(\nabla_\perp\varphi)^2 + \lambda(\nabla_\parallel\varphi)^2 + (\nabla\theta)^2 + q_0^2\theta^2$$
$$+ 4q_0\theta(\mathbf{n}\nabla)\varphi + (\lambda - 1)(n_1\nabla_2\theta - n_2\nabla_1\theta)^2\} dV,$$

where $\mathbf{n}$ is the director in the unperturbed structure of the cholesteric liquid crystal with the components n_1 and n_2 in the cholesteric plane, and $\nabla_\parallel$ and $\nabla_\perp(\nabla_1, \nabla_2)$ are the gradients along and perpendicular to the axis of the cholesteric circuit, respectively.

Let us take into account the possible tension of the layer along the axis of the cholesteric crystal in the expressions for energy. The layer tension occurs in particular in the case of nonparallel boundaries near the Grangin lines and in a layer with paired disclinations where the number of cholesteric layers changes. The tension of the cholesteric structure does not affect the form of hydrodynamic equations (1) but changes the Frank elastic energy. We obtain a new expression for the latter by maintaining the third powers of the variables in the energy expansion in angles. This leads to the appearance of the term $K\tilde{\varphi}_{,z}(\nabla_\perp\varphi)^2/2q_0$, where $\tilde{\varphi} = -q_0 z\delta'_z + \varphi$ is the total angle of molecule rotation, which is a result of the rotation of molecules through the angle φ and their displacement due to the layer tension, and δ'_z is the tensile strain. Eliminating the third powers of the angles φ and θ, we obtain the following expression for G:

$$G = \frac{1}{2}K\int_V \{(\nabla_\perp\varphi)^2(1 - \delta'_z) + \lambda(\nabla_\parallel\varphi)^2 + (\nabla\theta)^2 \tag{3}$$
$$+ q_0^2\theta^2 + 4q_0\theta(\mathbf{n}\nabla)\varphi + (\lambda - 1)[n_1\nabla_2\theta - n_2\nabla_1\theta]^2\} dV.$$

The minimum of the elastic energy for the perturbations of the angles θ and φ that are periodic along the layer leads to the possibility of the formation of domains of a square grid type at the critical tensile strain δ_0. The strain δ_0, the structure wave number k_0, and the domain size d_0 at the threshold of the effect are determined by the expressions

$$k_0 = \frac{2\pi}{\sqrt{P_0 h}}\left(\frac{2\lambda}{3 + \lambda}\right)^{1/4}, \quad \delta_0 = \frac{P_0}{4h}\sqrt{2\lambda(3 + \lambda)},$$
$$d_0 = \frac{\pi\sqrt{2}}{k_0} = \sqrt{hP_0}\left(\frac{3 + \lambda}{8\lambda}\right)^{1/4}. \tag{4}$$

Let us consider the normal incidence of an ultrasonic wave with the frequency ω and the amplitude of particle velocity v_0 upon a layer of a cholesteric liquid crystal of thickness h. We restrict ourselves to the frequencies ω at which the viscous wavelength is smaller and the sound wavelength is larger than the thickness of the layer. The last inequality provides an opportunity to replace the effect of sound by the average over the layer in determining the threshold of the effect.

Describing the effect, we select the following geometry. The z axis is directed along the normal to the layer with the lower boundary of the layer corresponding to the coordinate $z = 0$. The x and y axes lie in the plane of the lower boundary of the layer. The unperturbed cholesteric layers are parallel to the xy plane. We assume that

$$n_1 = n_x, \quad n_2 = n_y, \quad \nabla_1 = \partial_x, \quad \nabla_2 = \partial_y.$$

The inequality $\eta\omega/\rho c^2 \ll 1$ is valid at ultrasonic frequencies. It provides the opportunity to eliminate the acoustic modes from the equation of motion Eqs. (1) by applying a double rot operation. In the equations, we keep the quadratic terms proportional to the product of the rotation angles of molecules θ and φ by the velocities and take into account the change of the wave number q_0 due to the tension of the medium in the sound field. Performing the necessary transformations, we arrive at the following equations of rotation:

$$\gamma_1\Big[\varphi_{,t} + q_0 v_z - q_0 u_{zz} v_z - \frac{1}{2}(\mathrm{rot}\, v)_z$$

$$+ n_x n_y(v_{xx} - v_{yy}) + (n_x^2 - n_y^2) v_{xy}\Big] - \Gamma_\varphi = 0, \qquad (5)$$

$$\gamma_1(\dot{\theta} - n_\alpha v_{z,\alpha} - \theta v_{zz}) - \Gamma_\theta = 0.$$

Here, Γ_θ and Γ_φ are the elastic moments corresponding to the angles θ and φ that are determined through free energy (3) by the Euler equations

$$\Gamma_\varphi = \nabla\frac{\partial g}{\partial\nabla\varphi} - \frac{\partial g}{\partial\varphi}$$

$$= K[(1 - \delta_z')\Delta_\perp\varphi + \lambda\varphi_{,zz} + 2q_0 n_\alpha\theta_{,\alpha}],$$

$$\Gamma_\theta = \nabla\frac{\partial g}{\partial\nabla\theta} - \frac{\partial g}{\partial\theta} = K[\Delta\theta - q_0^2\theta - 2q_0 n_\alpha\varphi_{,\alpha}$$

$$+ (\lambda - 1)(n_x^2\theta_{,yy} + n_y^2\theta_{,xx} - 2n_x n_y\theta_{,xy})].$$

Here and below, the index α takes the values $\alpha = x, y$, and $\Delta_\perp = \partial_x^2 + \partial_y^2$.

In order to obtain an expression for the force F according to Eq. (2), it is necessary to proceed to the material angular variables θ_m and φ_m in the expression for the Frank elastic energy and to exclude the molecule rotations connected with rotation of the medium as a whole. This transition is performed by substituting the angles θ and φ in the form

$$\theta = \theta_m - n_\alpha u_{z,\alpha},$$

$$\varphi = \varphi_m - q_0 u_z - \frac{1}{2}(u_{x,y} - u_{y,x})$$

into Eq. (3).

Now, we fix the variables θ_m and φ_m in the elastic energy and substitute the latter in Eq. (2). Then, we obtain

$$F_z = -q_0\Gamma_\varphi + n_\alpha\Gamma_{\theta,\alpha},$$

$$F_{x,y} - F_{y,x} = \frac{1}{2}\Delta_\perp\Gamma_\varphi, \quad F_{\alpha,\alpha} = 0.$$

Expressing Γ_θ and Γ_φ from Eqs. (5) through viscous moments, we arrive at the set of equations of motion

$$(\rho\partial_t\Delta - \eta\hat{D}_1) v_z = -\gamma\Delta_\perp n_\alpha\dot{\theta}_{,\alpha}$$

$$+ [\Delta \mathrm{E} u_{zz}\Delta_\perp + (\mu_3 + \alpha_5) v_{zz}\Delta_\perp] n_\alpha\theta_\alpha + [\mathrm{rot}\,\mathrm{rot}\,\mathbf{g}]_z$$

$$- \alpha_6\partial_z^2(v_{zz} n_\alpha\theta_{,\alpha}) - \gamma\Delta_\perp\{q_0[\varphi_{,t} + q_0 v_z - \mathbf{\Omega}_z$$

$$+ n_x n_y(v_{xx} - v_{yy}) + (n_x^2 - n_y^2) v_{xy}$$

$$- n_\beta\partial_\beta(\dot{\theta} - n_\alpha v_{z,\alpha} - \theta v_{zz})\}, \quad \beta = x, y;$$

$$\left[\rho\partial_t - \left(\eta + \frac{1}{4}\alpha_5\right)\Delta_\perp - \eta\partial_z^2\right]\mathbf{\Omega}_z$$

$$- \frac{1}{4}(n_x^2 - n_y^2)\Big\{\alpha_5(\partial_x^2 - \partial_y^2)\mathbf{\Omega}_z - \alpha_6(v_{xy,z^2} + v_{zz,xy}) \qquad (6)$$

$$+ \frac{\alpha_6}{2}((3\partial_x^2 + \partial_y^2) v_{x,y} + (3\partial_y^2 + \partial_x^2) v_{y,x})\Big\}$$

$$+ \alpha_5 n_x n_y\partial_x\partial_y\mathbf{\Omega}_z$$

$$= -\frac{1}{2}\gamma\Big\{\Delta_\perp\dot{\varphi}_m + n_x n_y\Big[\partial_x\partial_y\dot{\varphi}_m + \frac{1}{2}\Delta_\perp(v_{xx} - v_{yy})\Big]$$

$$+ \frac{1}{2}(n_x^2 - n_y^2)\Delta_\perp v_{xy}\Big\} - \frac{1}{2}\alpha_6\partial_z[v_{zz}(n_y\theta_{,x} - n_y\theta_{,y})]$$

$$+ \partial_z(\mathrm{rot}\,\mathbf{g})_z, \quad \mathrm{div}\,\mathbf{v} = 0,$$

where $\mathbf{g} = \rho[(\mathbf{v}\nabla)\mathbf{v} + \mathbf{v}(\nabla\mathbf{v})]$ is the convective force, $\dot{\varphi}_m = \varphi_{,t} + q_0 v_z - \mathbf{\Omega}_z$ is the material rate of rotation of molecules φ_m about the z axis, $\mathbf{\Omega}_z = \frac{1}{2}(\mathrm{rot}\,\mathbf{v})_z = \frac{1}{2}(v_{y,x} - v_{x,y})$ is the z component of the angular velocity of the medium rotation, and $\hat{D}_1$ is the differentiating operator

$$\hat{D}_1 = \frac{2\alpha_4 + \alpha_5 + 2\gamma}{4\eta}\Delta_\perp^2$$

$$+ \frac{\alpha_4 + \alpha_5/2 + 3/8\alpha_1}{\eta}\Delta_\perp\partial_z^2 + \partial_z^4,$$

$$\eta = \frac{1}{2}(\alpha_4 + \alpha_6/2).$$

Next, we linearize the set of Eqs. (5) and (6) with respect to the angular variables and the velocity perturbations $\delta\mathbf{v}$ by considering the velocity of the medium motion and the medium compression in an incident sound wave as the coefficients depending on time and coordinates. We represent θ, φ, and $\delta\mathbf{v}$ as the sums of the stationary and oscillating at the sound frequency terms:

$$\theta = \theta_2 + \theta', \quad \varphi = \varphi_2 + \varphi', \quad \delta\mathbf{v} = \mathbf{v}_2 + \mathbf{v}',$$

where the subscript 2 indicates the stationary part and the prime indicates the oscillating one. We separate the equations for stationary and nonstationary variables from the set of Eqs. (5) and (6). Let us consider the structure distortions with the minimal free energy, when the angle θ is given in the form $\theta = n_\alpha\tau_\alpha$, where τ_α and φ vary slowly along the crystal axis. We also assume the velocity perturbations to change slowly with the functions. We average all terms in equations for φ and $\mathbf{v}$ over the helix pitch P_0 and eliminate the elastic moments, which are small in comparison to the viscous ones, from the equation for oscillating variables.

Analyzing the effect, we restrict ourselves to the total reflection of sound from the boundary $z = h$ and assume the boundary to be rigid. In this case, the sound field in the layer is determined by the standing wave

$$v_z = 2v_0 \sin\omega t \sin[\omega(z-h)/c],$$

where c is the sound velocity.

Formulating the equations of motion, we take into account the relation

$$\frac{\left|\overline{\langle(v\nabla)\theta'\rangle}\right|}{\left|\overline{\langle\theta' v_{zz}\rangle}\right|} \sim \frac{\langle\sin^2 k_s h\rangle}{\langle\cos^2 k_s h\rangle} \sim (k_s h)^2 \ll 1,$$

which allows us to eliminate the terms containing the convection θ from the equations of fluid dynamics (the angular brackets here mean averaging over the layer thickness, and the overbar means averaging over the period of acoustic oscillations).

Performing the necessary transformations, we obtain the following self-consistent set of equations for θ', φ, v'_z, Ω'_z, θ_2, φ_2, $v_{2,z}$, and Ω_{2z}:

$$\begin{gathered}
\theta'_{,t} - n_\alpha v'_{z,\alpha} - \theta_2 v_{zz} = 0, \\
\varphi_{,t} + q_0(v'_z + v_z) - \Omega'_z = 0, \\
(\rho\partial_t\Delta - \eta\hat{D}_1)v'_z = [(\Delta\mathrm{E}u_{zz} + (\mu_3+\alpha_6)v_{zz})]\Delta_\perp \\
\times\langle n_\alpha\theta_{2,\alpha}\rangle - \alpha_6\partial_z^2(v_{zz}\langle n_\alpha\theta_{2,\alpha}\rangle), \\
\left[\rho\partial_t - \left(\eta + \frac{1}{4}\alpha_5\right)\Delta_\perp - \eta\partial_z^2\right]\Omega'_z \\
= -\frac{1}{2}\alpha_6\partial_z(v_{zz}\langle n_x\theta_{2,y} - n_y\theta_{2,x}\rangle), \\
\gamma[\overline{\varphi'_{,z}(v'_z + v_z)} - q_0\overline{u_{zz}v'_z} + q_0 v_{2z} - \Omega_{2,z}] \\
-K[(1-\delta'_z)\Delta_\perp\varphi_2 + \lambda\varphi_{2,zz} + 2q_0\langle n_\alpha\theta_{2,\alpha}\rangle] = 0, \\
\gamma(n_\alpha v_{2z,\alpha} + \overline{\theta' v_{zz}}) + K\{\Delta\theta_2 - q_0^2\theta_2 - 2q_0 n_\alpha\varphi_{2,\alpha} \\
+ (\lambda-1)(n_x^2\theta_{2,yy} + n_y^2\theta_{2,xx} - 2n_x n_y\theta_{2,xy})\} = 0, \\
\hat{D}_0 v_{2z} = -\Delta_\perp\overline{(\Delta\mathrm{E}u_{zz} + (\mu_3+\alpha_6)v_{zz})\langle n_\alpha\theta'_{,\alpha}\rangle} \\
-\overline{\langle(\mathrm{rot}\,\mathrm{rot}\,\mathbf{g})_z\rangle} + \alpha_6\overline{\partial_z^2(v_{zz}\langle n_\alpha\theta'_{,\alpha}\rangle)} \\
+ \gamma\Delta_\perp q_0(q_0 v_{2z} - \Omega_{2z}), \\
\left[\left(\eta + \frac{1}{4}\alpha_5\right)\Delta_\perp + \eta\partial_z^2\right]\Omega_{2z} = \overline{\partial_z(\mathrm{rot}\,g)_z} \\
+ \frac{1}{2}\gamma\Delta_\perp(q_0 v_{2,z} - \Omega_{2z}) + \frac{1}{2}\alpha_6\overline{\partial_z(v_{zz}\langle n_x\theta'_{,y} - n_y\theta'_{,x}\rangle)}, \\
\operatorname{div}\mathbf{v}_2 = 0.
\end{gathered} \tag{7}$$

Here, $\hat{D}_0$ is the differentiating operator:

$$\hat{D}_0 = \frac{\alpha_4 + \alpha_5/2}{\eta}\Delta_\perp^2 + \frac{\alpha_4 + \alpha_5/2}{\eta}\Delta_\perp\partial_z^2 + \partial_z^4.$$

In Eqs. (7) and the following, the velocity v_z and its derivatives with respect to z refer to the sound wave in the layer and the angular brackets mean averaging over the helix pitch.

We assume stationary perturbations to be zero at the boundaries:

$$\varphi_2|_{z=0,h} = \theta_2|_{z=0,h} = 0; \quad v_{2z}|_{z=0,h} = 0$$

and determine the oscillating variables v'_z and θ' as a particular solution to the corresponding inhomogeneous equations. In this case, we ignore the effects in the boundary layers with thicknesses smaller than the viscous wavelength. The condition for the existence of a nonzero solution to Eqs. (7) corresponds to the threshold of the domain formation.

In order to estimate the threshold of the effect, we represent stationary perturbations as depending on the x and y coordinates and consistent with the zero boundary conditions

$$\varphi_2, \theta_2, v_{2z} \sim \exp(ik_x x + ik_y y)\sin(k_z z),$$

where k_x and k_y are the wave numbers determining the form of the domain structure and $k_z = 2\pi/h$; in this case, $\partial_\alpha = ik_\alpha$ and $\Delta_\perp = -k_x^2 - k_y^2 = -k^2$.

We assume that the following inequalities are valid:

$$k_z < k < q_0, \tag{8}$$

and consider the formation of the structure of the square grid type. In the case of such a structure, the terms

$$\langle n_x\theta'_{,y} - n_y\theta'_{,x}\rangle, \quad \langle n_x\theta_{2,y} - n_y\theta_{2,x}\rangle, \quad \text{and} \quad (\mathrm{rot}\,g)_z$$

averaged over the helix pitch vanish, and as a consequence, the rate of the medium rotation also vanishes; $\Omega'_z = 0$.

From the next to last equation of Eqs. (7), we obtain a relation for the rate of stationary rotation of molecules with respect to the cholesteric liquid:

$$\Omega_{2z} - q_0 v_{2z} = -Aq_0 v_{2z}, \tag{9}$$

where $A = (4\eta + \alpha_5)/(2\gamma + 4\eta + \alpha_5)$.

If the conditions given by inequalities (8) are valid, the sound field in the cholesteric layer leads to the following oscillations of the velocity v'_z and the angles θ' and φ':

$$v'_z = \frac{k^2}{2B}\tau_{2\alpha,\alpha}\{[\eta|D_1|\Delta\mathrm{E} + |\Delta|\rho(\mu_3 + \alpha_6)\omega^2]u_{zz}$$
$$+ [\eta(\mu_3 + \alpha_6)|D_1| - |\Delta|\rho\Delta\mathrm{E}]v_{zz}\},$$

$$\theta' = \frac{k^2}{2B}n_\beta\tau_{2\alpha,\alpha\beta}\{[\eta(\mu_3 + \alpha_6)|D_1| - |\Delta|\rho\Delta\mathrm{E}]u_{zz}$$
$$- [\eta|D_1|\Delta\mathrm{E} + |\Delta|\rho(\mu_3 + \alpha_6)\omega^2]\omega^{-2}v_{zz}\},$$

$$\varphi' = -q_0(u'_z + u_z).$$

Here, we used the notations

$$B = \eta^2[|D_1|^2 + 4\sigma^4|\Delta|^2], \quad \sigma = \sqrt{\rho\omega/2\eta},$$

$$|D_1| = \frac{2\alpha_4 + \alpha_5 + \gamma}{4\eta}k^4 + \frac{\alpha_4 + \alpha_5/2 + 3/8\alpha_1}{\eta}k^2k_z^2 + k_z^4,$$

$$|\Delta| = k^2 + k_z^2.$$

The parameter σ has the meaning of the wave number of the viscous wave propagating along the z axis.

The averaged terms in the stationary equations of the set of Eqs. (7) are equal to

$$\begin{gathered}\gamma\overline{\varphi'_{,z}(v'_z + v_z)} = -q_0\overline{v'_z u_{zz}} = -Lm_0^2 q_0\tau_{\alpha,\alpha},\\ \gamma\overline{\theta' v_{zz}} = -Lm_0^2 n_\beta\tau_{\alpha,\alpha\beta},\\ \overline{[\Delta\mathrm{E}u_{zz} + (\mu_3 + \alpha_6)v_{zz}]\langle n_\alpha\theta'_{,\alpha}\rangle} = Mq_0^2 m_0^2\tau_{\alpha\alpha},\\ \overline{\langle(\mathrm{rot\,rot}\,\mathbf{g})_z\rangle} = -\rho\Delta_\perp\overline{(v'_z v_{zz})} = Nq_0^2k^2m_0^2\tau_{\alpha,\alpha},\end{gathered} \tag{10}$$

where

$$L = \frac{4\gamma k^2}{B}(\eta|D_1|\Delta\mathrm{E} + |\Delta|\rho(\mu_3 + \alpha_6)\omega^2),$$

$$M = \frac{k^6}{2q_0^2B}\mathrm{DE}\Delta\mathrm{E}\left\{1 + 2\left(\frac{\alpha_6}{\mu_{3,0}}\right) + \left(\frac{\alpha_6}{\mu_{3,0}}\right)^2(1 + \omega^2\tau^2)\right\},$$

$$N = \frac{2\rho k^2\omega^2}{Bq_0^2}[\rho k^2\Delta\mathrm{E} - \eta(\mu_3 + \alpha_6)|D_1|]$$

$m_0 = v_0/c$ is the Mach number in the sound wave incident on the layer of a cholesteric liquid crystal, and $\mu_{3,0} = \mathrm{DE}\tau$ is the viscosity coefficient μ_3 at low frequencies ($\omega\tau \ll 1$).

Substituting the averaged products from Eqs. (10) into stationary Eqs. (7) and using Eq. (9), we arrive at the self-consistent system of equations for φ_2, θ_2, and $v_{2,z}$ with the coefficients containing the external action m_0^2:

$$\begin{cases}\gamma Aq_0v_{2z} - Lm_0^2q_0\tau_{\alpha,\alpha}\\ \quad + K\{[k^2(1 - \delta'_z) + \lambda k_z^2]\varphi - q_0\tau_{\alpha,\alpha}\} = 0\\ \gamma Ak^2v_{2z} - Lm_0^2k^2\tau_{\alpha,\alpha}\\ \quad + K\left[\left(2q_0^2 + \frac{3 + \lambda}{4}k^2\right)\tau_{\alpha,\alpha} - 2q_0k^2\varphi\right] = 0\\ \gamma Av_{2z} - (M + N)m_0^2\tau_{\alpha,\alpha} = 0.\end{cases} \tag{11}$$

To determine the value of m_0 at which perturbations with the wave number k start to increase, we equate the determinant of the system of Eqs. (11) to zero. As a result, we obtain

$$m_0(\omega, k) = \left\{\frac{K_{33}}{4k^2}[(3 + \lambda)(1 - \delta'_z)k^4 + 8\lambda k_z^2q^2 - 8k^2q^2\delta'_z + \lambda(3 + \lambda)(1 - \delta'_z)k_z^2k^2] \times [(L - M - N)(2q^2 + k^2 + \lambda k_z^2)]^{-1}\right\}^{1/2}.$$

The wave number k at the effect threshold and the threshold value of $m_{0,\mathrm{th}}$ are determined by the minimization of $m_0(\omega, k)$ with respect to k.

The final expression for m_0 as a function of the crystal parameters and the cell geometry is cumbersome. We present a simplified expression for m_0, which was obtained by taking into account the inequality

$$\frac{|N + M|}{L} \ll 1 \tag{12}$$

and inequalities (8). Their validity for the typical parameters of a crystal, the helix pitch, the layer thickness, and the frequencies considered below is proved by direct testing.

If inequalities (8) and (12) hold, the expression for $m_0(\omega, k)$ can be reduced to the form

$$m_0(\omega, k) = \sqrt{\frac{\eta K_{33}k_0^4(3 + \lambda)}{32\gamma\mathrm{DE}q^2}}F(\omega, k). \tag{13}$$

The function $F(\omega, \xi)$ determines the dependences of m_0 on frequency through the dimensionless parameter

$\Omega = 4\sigma^4/k_0^4$ and on the wave number k through the ratio $\xi = k/k_0$:

$$F(\omega, k) = \left\{\frac{(\xi^4 + 1 - 2\xi^2\delta)(\xi^4 + \Omega)}{\xi^4 + a\xi^2}\frac{a^2 + \Omega}{\Omega}\right\}^{1/2}.$$

Here, $a = \rho/(\eta\tau k_0^2)$, the parameter δ determines the ratio of the layer tension to the critical δ_0 at which the structure of a cholesteric liquid crystal becomes unstable in the absence of external action: $\delta = \delta'_z/\delta_0$.

The analysis of Eqs. (7) shows that the convection of perturbations of the angle φ' and the layer tension in a sound wave, as well as the stationary moments $\gamma\overline{\theta' v_{zz}}$, destabilize the structure of a cholesteric liquid crystal, whereas the flows v_{2z} stabilize it. The main action turns out to be related to the convection of both φ' and tension. The angular moments produced by these mechanisms are a factor of $q_0/k_z \gg 1$ greater than the moments caused by the gradients of the velocities of stationary flows, and only they are taken into account in the derivation of Eq. (13).

The wave number of the domain structure at the effect threshold k_{th} and the period $d = \pi\sqrt{2}/k_{\text{th}}$ are determined by the minimization of the function $F(\omega, k)$ with respect to the wave number k. The equation for k_{th} obtained by differentiating the function $F(\omega, k)$ does not have a solution in a closed form. Therefore, we restrict ourselves to the analytical representation of the results for high and low frequencies.

In the case of high frequencies, when $\Omega \gg 1$, the size of domains is estimated by the formula

$$d \approx d_0\sqrt{\frac{a + 2\delta}{1 + \sqrt{1 + a^2 + 2a\delta}}}, \qquad (14)$$

where d_0 is the domain size in the case of a static tension of the layer (Eqs. (4)). For the real values of the parameter $a \gg 1$ ($a \approx 6$ for the parameters of the crystal and the layer thickness considered below), the domain size approaches the value of d_0. The function $F(\omega, k_{\text{th}})$ at high frequencies is approximated by the formula

$$F(\omega, k_{\text{th}}) \approx \left\{2\frac{\sqrt{1 + a^2 + 2a\delta}(1 - a\delta - 2\delta^2) + 1 + a^2 + 2a\delta}{(1 + \sqrt{1 + a^2 + 2a\delta})(1 + a^2 + 2a\delta + \delta)} \times (a^2 + \Omega)\right\}^{1/2} \sim \omega^{1/2}.$$

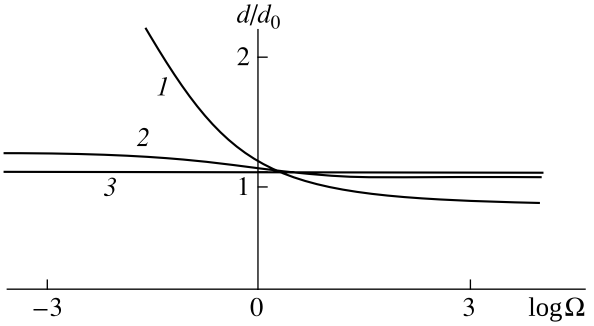

Fig. 1. Dependence of the reduced domain size d/d_0 on the parameter $\Omega = 4\sigma^4/k_0^4$ for different values of tension in the layer: δ = (*1*) 0.2; (*2*) 0.5; and (*3*) 0.9.

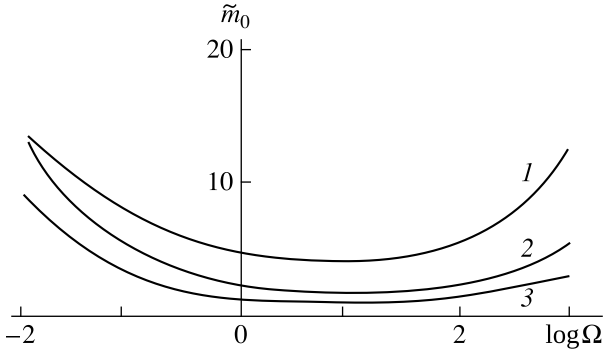

Fig. 2. Dependence of the reduced threshold $\tilde{m}_{0,\,\text{th}}$ on the parameter $\Omega = 4\sigma^4/k_0^4$ for different values of tension in the layer: δ = (*1*) 0.2; (*2*) 0.5; and (*3*) 0.9.

At low frequencies, when $\Omega \ll 1$, the domain size and the function $F(\omega, k)$ are approximated by simple relations

$$\frac{d}{d_0} \approx \frac{1}{\sqrt{2\Omega}} \sim \omega^{-1/2},$$

$$F(\omega, k_{\text{th}}) \approx \sqrt{\frac{2a}{\sqrt{\Omega}}} \sim \omega^{-1/2}.$$

The dependences of the reduced domain size d/d_0 and the reduced Mach number $\tilde{m}_0 = m_0/\sqrt{\eta K_{33}k_0^4(3 + \lambda)/32\gamma \mathrm{DE} q_0^2}$ on Ω for $a = 1$ and different values of the layer tension δ, which are calculated with the help of Eq. (13), are given in Figs. 1 and 2. One can see from Fig. 1 that, in the case of large values of Ω, the domain size does not depend on frequency for any δ and is determined by Eq. (14). On the curve $\tilde{m}_0(\Omega)$ (Fig. 2), it is possible to separate the frequency range where the threshold of the effect weakly depends on frequency.

Let us compare the theoretical results with the experimental studies of the effect of ultrasound on the

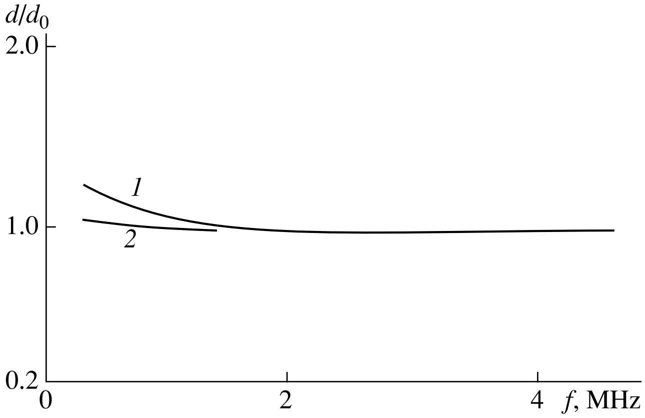

Fig. 3. Dependence of the reduced domain size d/d_0 on the frequency f for different values of tension: δ = (*1*) 0.5 and (*2*) 0.9. The layer thickness and the helix pitch are h = 22 μm and P_0 = 4.3 μm.

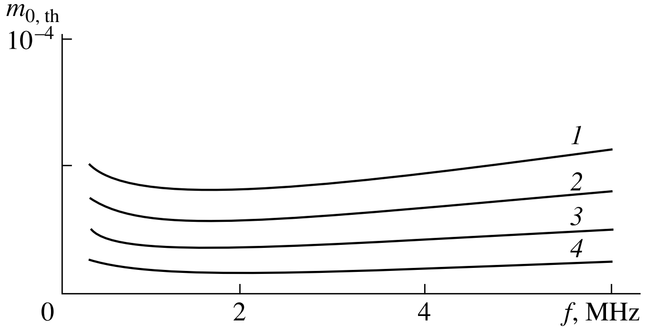

Fig. 4. Dependence of the threshold amplitude $m_{0,\,\mathrm{th}}$ on the frequency f for different values of tension: δ = (*1*) 0; (*2*) 0.5; (*3*) 0.7; and (*4*) 0.9. The layer thickness and the helix pitch are h = 22 μm and P_0 = 4.3 μm.

structure of cholesteric liquid crystals in the frequency range 0.3–3.6 MHz [1, 7]. The formation of the domain structure of the type of a square grid with the sides parallel and perpendicular to the lines of rubbing of the boundary surface was indicated there. The grid appears only in single parts of the cholesteric layer. The domain dimensions are proportional to $(P_0h)^{1/2}$. The threshold velocity amplitude $v_{0,\,\mathrm{th}}$ and the size of domains almost do not depend on frequency. The value of $v_{0,\,\mathrm{th}}$ weakly depends on the layer thickness h. The threshold intensity of a sound wave incident upon the layer of a cholesteric liquid crystal is about $I_{\mathrm{th}} \sim 10^{-5}$–$10^{-4}$ W/m^2. The experimental pattern of the effect of ultrasound on a cholesteric layer qualitatively corresponds to the theory developed for a stretched structure. In the experiment, stretched regions are apparently bound by disclinations.

We conducted numerical analysis of the solution for the parameters of a cholesteric liquid crystal equal to typical values for nematic crystals: $K_{33} \approx 0.5 \times 10^{-11}$ N, $\alpha_4 \approx \gamma_1 \approx 0.1$ Pa, $\alpha_6 \approx 0$, $\rho \approx 10^3$ kg m^{-3}, the sound velocity $c = 1.5 \times 10^3$ m/s [10], DE = 10^7 N/m^2, and $\tau = 3 \times 10^{-8}$ s [11, 12]. We determine the value of λ by comparing the theoretical expression for the domain size with experimental data. The experimental size of the domain structure arising in a layer of a cholesteric liquid crystal with thickness h = 22 μm and the helix pitch P_0 = 4.3 μm under a static tension is given in [7]: $d_0 \approx 18.5$ μm. Setting the theoretical size d_0 given by the last formula of Eqs. (6) equal to the experimental one, we determine the ratio of the elastic moduli: $\lambda = K_{22}/K_{33} \approx 2.8 \times 10^{-2}$. This value of λ is used for numerical calculations. The critical tension at the same values of h, P_0, and λ is equal to $\delta_0 \approx 0.02$.

It is impossible to conduct numerical comparison of the theoretical results with experimental data without using free parameters, because we have to assume that in the experiment the tension δ is undetermined. Indeed, the domain size d_0 in the case of a stretched cholesteric layer and the critical tension δ_0 are determined from the form of the Frank energy and related to the crystal parameters by Eqs. (4). The value of d_0 given in [7] provided an opportunity to simultaneously determine the parameter λ and the critical tension $\delta_0 \approx 0.02$. At the same time, the static tension $\delta_z' = 0.046$ given in [7] exceeds the value of δ_0 more twice and disagrees with the value of d_0. Therefore, we conduct the numerical calculation of m_0 and d for different values of tension and indicate the values of δ at which the theoretical results agree with the experimental data.

The theoretical size of the domains and the effect threshold for the layer thickness h = 22 μm and the helix pitch P_0 = 4 μm in the frequency range from 0.3 to 6 MHz are given in Figs. 3 and 4, which present the frequency dependences of d/d_0 and $m_{0,\,\mathrm{th}}$ for different values of the tension parameter. In the indicated frequency range, the calculations for all values of δ show a weak dependence on frequency for both the size of the domain structure and the threshold of the effect, which agrees with the experimental results. The domain size $d = d_0$ coincides with the domain size given in [1, 7] for a fully developed structure. In the case of the theoretical sound intensity at the effect threshold $I_{\mathrm{th}} = \rho c^3 m_{0,\,\mathrm{th}}^2$, we obtain the order of magnitude given in [7], $I_{\mathrm{th}} \sim 10^{-5}$ W/m^2, for the relative values of tension $\delta \approx 0.7$–0.8.

In closing, we present the estimates obtained for the parameters of a cholesteric liquid crystal layer and the sound frequencies considered above:

$$\frac{k_{\mathrm{th}}}{q} \approx 0.16, \quad \frac{k_z}{k_{\mathrm{th}}} \approx 0.5, \quad \frac{|N+M|}{L} \sim 10^{-2},$$

which testify to the validity of inequalities (4) and (12) and the legitimacy of using Eq. (13) in numerical calculations.

ACKNOWLEDGMENTS

This work was supported by the Russian Foundation for Basic Research, project no. 00-02-17732.

REFERENCES

1. O. A. Kapustina, Mol. Cryst. Liq. Cryst. **112**, 1 (1984).
2. A. P. Kapustin and O. A. Kapustina, *Acoustics of Liquid Crystals* (Nauka, Moscow, 1986).
3. H. Mailer, K. L. Likins, T. R. Taylor, and J. L. Fergason, Appl. Phys. Lett. **18**, 105 (1971).
4. *Pattern Formation in Liquid Crystals*, Ed. by A. Buka and L. Kramer (Springer, New York, 1996).
5. A. P. Krekhov and L. Kramer, J. Phys. (Paris) **4**, 677 (1994).
6. I. N. Gurova, O. A. Kapustina, V. N. Lupanov, and G. S. Chilaya, in *IV International Conference of Socialistic Countries on Liquid Crystals* (Tbilisi, 1981), Vol. 2, p. 74.
7. I. N. Gurova and O. A. Kapustina, Akust. Zh. **43**, 338 (1997) [Acoust. Phys. **43**, 290 (1997)].
8. E. N. Kozhevnikov, Zh. Éksp. Teor. Fiz. **92** (4), 1306 (1987) [Sov. Phys. JETP **65**, 731 (1987)].
9. E. N. Kozhevnikov, Akust. Zh. **36**, 458 (1990) [Sov. Phys. Acoust. **36**, 255 (1990)].
10. M. J. Stephen and J. P. Straley, Rev. Mod. Phys. **46**, 617 (1974).
11. C. A. Castro, A. Hikata, and C. Elbaum, Phys. Rev. A **17**, 353 (1978).
12. G. C. Bacri, J. Phys. (Paris) **35**, 601 (1974).

Translated by M. Lyamshev

Acoustical Physics, Vol. 47, No. 4, 2001, pp. 438–447. Translated from Akusticheskiĭ Zhurnal, Vol. 47, No. 4, 2001, pp. 509–519.
Original Russian Text Copyright © 2001 by Nazarov.

Dissipative Acoustic Nonlinearity of Polycrystalline Zinc

V. E. Nazarov
Institute of Applied Physics, Russian Academy of Sciences,
ul. Ul'yanova 46, Nizhni Novgorod, 603600 Russia
e-mail: nazarov@hydro.appl.sci-nnov.ru

Received April 14, 2000

Abstract—Results of experimental studies of nonlinear acoustic effects, namely, the attenuation of a weak ultrasonic pulse under the action of an intense low-frequency pumping wave and the limitation of the ultrasonic pulse amplitude in rod-type resonators made of unannealed and annealed polycrystalline zinc, are presented. The measurements are performed for the first four longitudinal modes of the rods with the frequency of the ultrasonic pulses varying from 40 kHz to 1 MHz. An analytical description of this effect is presented in the framework of the phenomenological equation of state allowing for dissipative nonlinearity. A modification of the Granato–Lucke dislocation theory that explains the experimentally observed amplitude and frequency dependences of the coefficient of nonlinear attenuation of ultrasonic pulses is proposed. Estimates for the parameters of the modified model are obtained from the comparison of theoretical and experimental data. *© 2001 MAIK "Nauka/Interperiodica".*

The acoustic properties of polycrystals are determined mainly by dislocations, i.e., linear defects of the crystal lattice of a solid [1–4]. Their motion and interaction with point defects (impurity atoms) lead to the phenomenon of dislocation internal friction. In order to explain it, Granato and Lucke proposed a dislocation theory of absorption [1–4]. The basic ideas and conclusions of this theory, which are used in this paper, are briefly described below.

In the Granato–Lucke theory, it is assumed that a polycrystal contains a dislocation network. Each dislocation is represented in the form of a string of length L_N determined by the network intersection points. In the absence of stress, the string is also fixed by impurity atoms in addition to the intersection points of the network. The distance between the impurity atoms is L_C ($L_C \ll L_N$). The application of a shear stress τ leads to an elastic shear strain γ_0 and also to a dislocation strain γ_d related to the dislocation displacement in a polycrystal.

In the case of a small dynamic stress, the dislocation loops L_C being fixed by the impurity atoms oscillate and the friction force proportional to the velocity of the dislocation loop motion is applied to them. The displacement $\xi = \xi(y, t)$ of a dislocation loop under the stress τ is determined by the equation of transverse oscillations of a string

$$A\xi_{tt} + B\xi_t - C\xi_{yy} = b\tau \qquad (1)$$

with the zero boundary conditions $\xi(0, t) = \xi(L_C, t) = 0$, where $A = \pi\rho b^2$ is the effective mass of the unit length of a dislocation; $C = 2Gb^2/(1 - \nu)$ is its effective tension; B is the friction force per unit length and unit velocity of a dislocation; G, ν, and ρ are the shear modulus, Poisson ratio, and crystal density, respectively; b is the magnitude of the Burgers vector; and y is the coordinate along the dislocation line. (It should be noted that, in contrast to the coefficients A and C, the coefficient B responsible for the damping properties of a dislocation is not determined. It is assumed in the model that this coefficient is constant and can be determined experimentally. From the results of measurements of ultrasonic wave attenuation, it was found that the values of the coefficient B for many metals lie within the range 5×10^{-6}–8×10^{-5} Pa s [2–5].)

The oscillation of dislocations leads to absorption and velocity dispersion of elastic waves. In the case of polycrystals containing dislocation loops of equal length L_C, the attenuation factor $\alpha(\omega)$ and the phase velocity $C_\perp(\omega)$ of a shear wave with the frequency ω are determined by the expressions

$$\alpha(\omega) = \frac{4C_\perp^2\Lambda}{\pi^3 C_\perp(\omega)}\frac{\omega^2 d}{(\Omega_C^2 - \omega^2)^2 + (\omega d)^2}, \qquad (2)$$

$$C_\perp(\omega) = C_\perp\left[1 - \frac{4C_\perp^2\Lambda}{\pi^3}\frac{\Omega_C^2 - \omega^2}{(\Omega_C^2 - \omega^2)^2 + (\omega d)^2}\right], \qquad (3)$$

where $\Omega_C = (\pi/L_C)(C/A)^{1/2} = [2/(1 - \nu)]^{1/2}(C_\perp/L_C)$ is the resonance frequency of the principal mode of a dislocation loop with the length L_C, $C_\perp = (G/\rho)^{1/2}$ is the shear wave velocity for an ideal crystal, $d = B/A$, and Λ is the total length of a moving dislocation line in a unit volume of the polycrystal or the dislocation density. In the case of copper or zinc ($b \cong 3 \times 10^{-10}$ m) at $L_C = 10^{-7}$ m, the resonance frequency Ω_C of a dislocation loop is sufficiently high and reaches a value of about 3.9×10^{10} Hz. In this case, the damping parameter d lies within the range 2.5×10^9–4×10^{10} Hz [1–5].

1063-7710/01/4704-0438$21.00 © 2001 MAIK "Nauka/Interperiodica"

Under relatively high stresses, the dislocations behave as follows. When the stress increases (the loading stage) and exceeds a certain threshold, the dislocation loops separate from the impurity atoms and their length increases from L_C to L_N. This leads to a sharp increase in the dislocation strain at constant stress. At the unloading stage, i.e., when the stress decreases, the presence of impurity atoms does not affect the dislocation motion, and the loops with length L_N return to the initial state and become fixed to the impurity atoms. A similar motion of dislocations occurs during the next half-period, so that, in the case of a high stress, an elastic hysteresis takes place in the dependence $\tau = \tau(\gamma, \gamma_t)$ (γ_t is the strain rate).

The dislocation-caused internal friction manifests itself not only for shear waves but for longitudinal waves as well. In this case, the conclusions of the dislocation theory remain valid in passing from the shear stress τ and strain γ to the longitudinal stress σ and strain ε through the replacement of τ and γ_d by $R\sigma$ and ε_d/R, respectively; here, R is the orientation factor taking into account the misfit between the applied and acting stresses in the plane of the dislocation glide ($R \cong 0.2$ for polycrystals [5]).

The Granato–Lucke theory adequately explains the effect of both amplitude-independent and amplitude-dependent internal friction in many (but not all) polycrystals. For example, it was discovered [7–11] that some metals (annealed copper, zinc, and lead) and rocks (granite and marble) have also dissipative nonlinearity in addition to hysteretic nonlinearity. In this connection, for the development of the dislocation theory it is necessary to conduct detailed experimental studies of nonlinear effects in such polycrystals in which other effects not described in the framework of the Granato–Lucke theory take place along with the conventionally studied manifestations of internal friction [1–4, 6]. In this sense, the study of the interaction and self-action of acoustic waves with various frequencies and amplitudes is promising.

This paper continues our previous papers [7–13] and presents the results of an experimental study and an analytical description of the effects of interaction and self-action of longitudinal acoustic waves in rod-type resonators made of polycrystalline zinc (99.95% Zn). Two rods with square cross-sections with 8 mm sides and length $L = 35$ cm were used in the experiments. The rods were cut from the same zinc plate. The first rod (1) was the reference one and the second rod (2) was annealed for 50 h at a temperature of 350°C. A metallographic analysis showed that the structure of unannealed zinc contained grains about 50 μm in size and the annealing caused an increase in the grain size by a factor of ten and greater [8]. The following nonlinear effects were studied in the experiments described here:

(i) the attenuation of a weak ultrasonic pulse in the field of an intense low-frequency pumping wave (the sound attenuation by sound);

(ii) the limitation of the ultrasonic pulse amplitude.

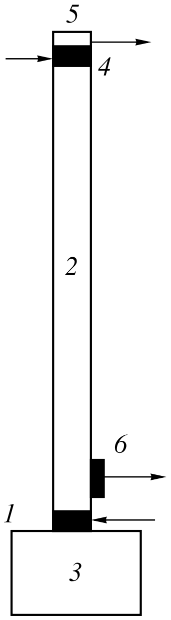

Fig. 1. Schematic diagram of the experiment.

A block scheme of the experimental setup is given in Fig. 1. A piezoceramic pumping radiator (*1*) exciting a resonator (*2*) was glued to a massive metal load (*3*) in such way that the boundary condition at one end of the rod was close to the condition at an absolutely rigid boundary. A piezoceramic radiator (*4*) for the generation of ultrasonic pulses and an accelerometer (*5*) for measuring the pumping wave amplitude were glued to the other end. Their total mass was sufficiently small, and this boundary was close to an acoustically soft one. An accelerometer (*6*) that was sensitive to the longitudinal (along the rod) component of acceleration was glued to the lateral side of the rod, near the pumping radiator (for receiving and measuring the amplitude of ultrasonic pulses transmitted through the rod). The pumping radiator excited low-frequency resonance oscillations in the rods at the frequencies of the first four longitudinal modes: $F_1 \cong 2750$, $F_2 \cong 8250$, $F_3 \cong 13350$, and $F_4 \cong 18850$ Hz.

Let us consider the results of studying the nonlinear sound attenuation by sound. In this series of experiments, the radiator (*1*) excited a low-frequency pumping wave (at the frequency of one of the first four longitudinal modes) in the rods and another radiator (*4*) simultaneously excited a weak ultrasonic pulse. The pulse was detected by the accelerometer (*6*) after its transmission through the rod, and the signal was fed to a spectrum analyzer where the measurement of its amplitude was performed. The frequency f of ultrasonic pulses varied within the range from 40 kHz to 1 MHz, and their duration was about 400 μs.

With an increase in the strain amplitude ε_m of the pumping wave in the resonator, a decrease in the amplitude U_2 of the received ultrasonic pulse was observed in

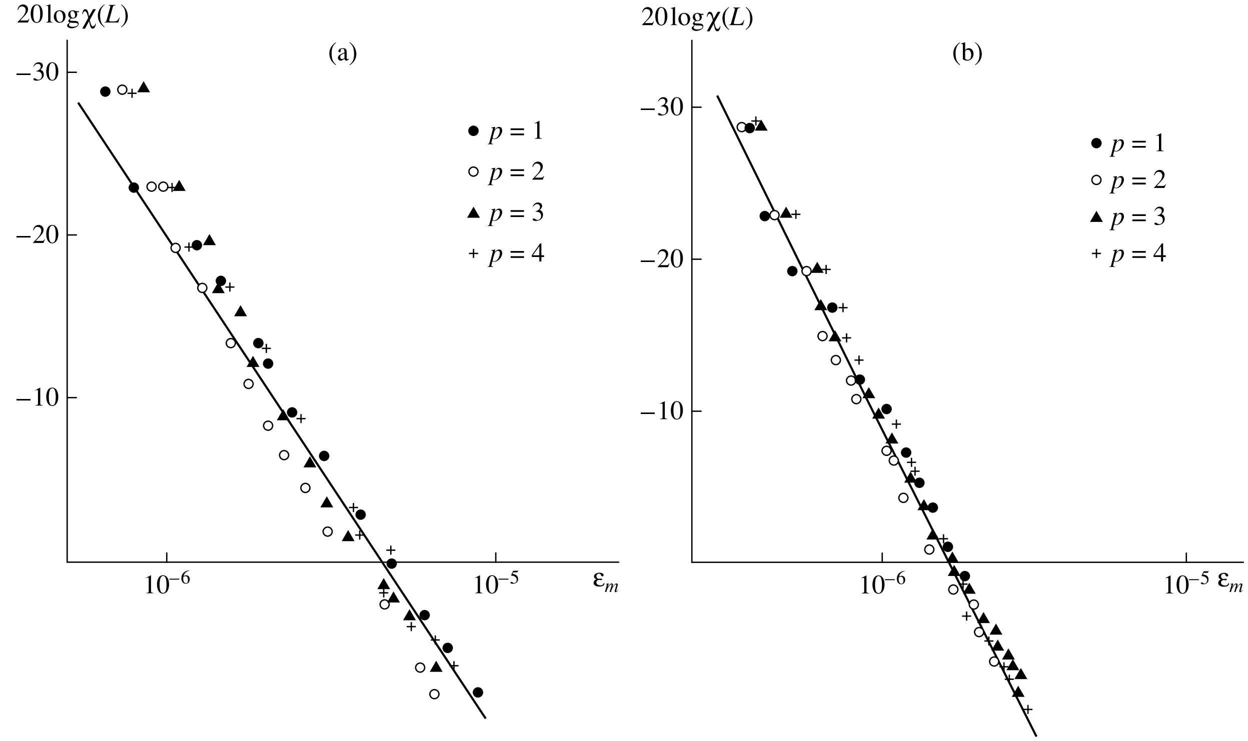

Fig. 2. Dependence of the nonlinear attenuation coefficient of an ultrasonic pulse on the strain amplitude ε_m of the pumping wave at different excitation frequencies F_p of resonators made of (a) unannealed and (b) annealed zinc. The straight lines correspond to the dependences (a) $\chi(L) \sim \varepsilon_m^{3/2}$ and (b) $\chi(L) \sim \varepsilon_m^2$.

addition to the effects described in [10]. Figure 2 shows the dependences of the coefficients $\chi(L) = \ln[U_0/U_2]$ of the nonlinear attenuation of ultrasonic pulses (U_0 is the pulse amplitude without pumping) on the strain amplitude ε_m of the pumping wave at various excitation frequencies F_p of the resonators made of unannealed and annealed zinc (p is the number of a longitudinal mode). (Figures 2a and 2b present the results of measuring the nonlinear attenuation of ultrasonic pulses with the frequencies f_1 = 237 kHz for unannealed zinc and f_2 = 312 kHz for annealed zinc.) It follows from Fig. 2 that the coefficient of nonlinear attenuation of ultrasonic pulses for both rods is a power function of the strain amplitude ε_m of the pumping wave and does not depend on its frequency F_p. In the case of unannealed zinc, we have

$$\chi(L) \sim \varepsilon_m^{3/2} \tag{4}$$

and for annealed zinc, we have

$$\chi(L) \sim \varepsilon_m^2. \tag{5}$$

Similar amplitude dependences of the coefficients of nonlinear attenuation were observed for the pulses with other frequencies f (in the range indicated above).

Figure 3 presents the dependences of the coefficients of nonlinear attenuation of ultrasonic pulses on the frequency f for unannealed and annealed zinc at a constant amplitude ε_m of the resonator excitation for the first mode (p = 1). From these figures, it is possible to derive the following approximate dependences of the coefficients $\chi(L)$ of nonlinear attenuation of ultrasonic pulses on the frequency f

for unannealed zinc

$$\begin{aligned} \chi(L) &\sim f \quad \text{at} \quad f \le 250 \text{ kHz}, \\ \chi(L) &\sim \text{const} \quad \text{at} \quad f \ge 250 \text{ kHz}, \end{aligned} \tag{6}$$

and for annealed zinc (in the frequency range from 90 to 900 kHz)

$$\chi(L) \sim f^n, \tag{7}$$

where $n \approx 0.5$.

The effect of sound attenuation by sound is inertialess; i.e., the pulse amplitude variation occurs simultaneously with the variation of the strain amplitude of the pumping wave. Therefore, this effect cannot be explained by thermal (inertial) processes connected with the increase in the attenuation coefficient of sound due to the rod temperature increase caused by the pumping wave absorption. The sound attenuation by sound in zinc cannot be explained by the interaction of acoustic waves at hysteretic nonlinearity as well, since, according to the results of the first series of experiments [10], this should lead to the dependence of the nonlinear attenuation coefficient of ultrasonic pulses on the pumping wave frequency. This effect could be explained in the framework of the Granato–Lucke dislocation theory, when a modulation of the function of the dislocation distribution in length occurs under the effect of an intense pumping wave because of the periodic separation of the dislocation loops from the impurity atoms. As the strain amplitude of the pumping wave grows, the time-average length of the loops increases and their average resonance frequency decreases. In this case, as follows from Eq. (2) (at $\omega \ll \Omega_C$), the average attenuation coefficient of a high-frequency wave also increases and its dependence on the amplitude ε_m must correspond to the amplitude dependence of the hysteresis loss determined by the pumping wave attenuation (see Fig. 4 in [10]). However, there is no such correspondence: the saturation of the hysteresis loss occurs at large amplitudes, and the sound attenuation by sound increases monotonically. (This is especially clear from the comparison of Fig. 2 with Fig. 5 from [9], where the amplitude-dependent internal friction of lead was studied.)

It was demonstrated earlier [7–9, 11–13] that, in order to explain the nonlinear attenuation of a weak ultrasonic pulse under the action of an intense low-frequency pumping wave (which was observed in some metals and rocks), it was necessary to assume that similar polycrystals have a dissipative nonlinearity leading to the dependence of the attenuation coefficient of the wave on its strain amplitude. In the cited publications [7–9], the sound attenuation by sound was described within the framework of the following phenomenological equation of state:

$$\sigma(\varepsilon, \varepsilon_t) = E\varepsilon + \beta\rho(1 + g|\varepsilon|^S)\varepsilon_t, \quad (8)$$

where E is Young's modulus and the constants s and g are determined by matching the analytical and experimental dependences of $\chi(L)$ on ε_m.

The selection of the nonlinear term $\rho\beta g|\varepsilon|^S\varepsilon_t$ in Eq. (8) is determined by the fact that the coefficient of nonlinear attenuation of a weak ultrasonic pulse does not depend on its amplitude and is a power function of the strain amplitude of the pumping wave (but not of the strain rate amplitude of this wave, since it does not depend on the wave frequency). Substituting Eq. (8) into the equation of motion $\rho U_{tt} = \sigma_x(\varepsilon, \varepsilon_t)$ ($\varepsilon = U_x$ and U is the displacement), we obtain a wave equation with nonlinear dissipation for the strain ε:

$$\varepsilon_{tt} - C_0^2\varepsilon_{xx} = \beta\varepsilon_{xxt} + \beta g(|\varepsilon|^S\varepsilon_t)_{xx}, \quad (9)$$

where $C_0 = (E/\rho)^{1/2}$ is the longitudinal wave velocity in the rod ($C_0 \cong 3.85 \times 10^5$ cm/s).

This equation describes the nonlinear attenuation of a weak ultrasonic pulse in the field of an intense low-frequency wave and determines the experimentally established dependences of the nonlinear attenuation coefficient $\chi(L)$ on the strain amplitude ε_m of the pumping wave. Thus, substituting

$$\begin{gathered}\varepsilon(x, t) = \varepsilon_1(x, t) + \varepsilon_2(x, t),\\ \varepsilon_1(x, t) = \varepsilon_m \cos K_p x \sin\Omega_p t,\\ K_p = \Omega_p/C_0, \quad \Omega_p = 2\pi F_p, \quad (10)\\ \varepsilon_2(x, t) = (1/2)\varepsilon_2(x)\exp[j(\omega t - kx)] + \text{c.c.},\\ \omega = 2\pi f\end{gathered}$$

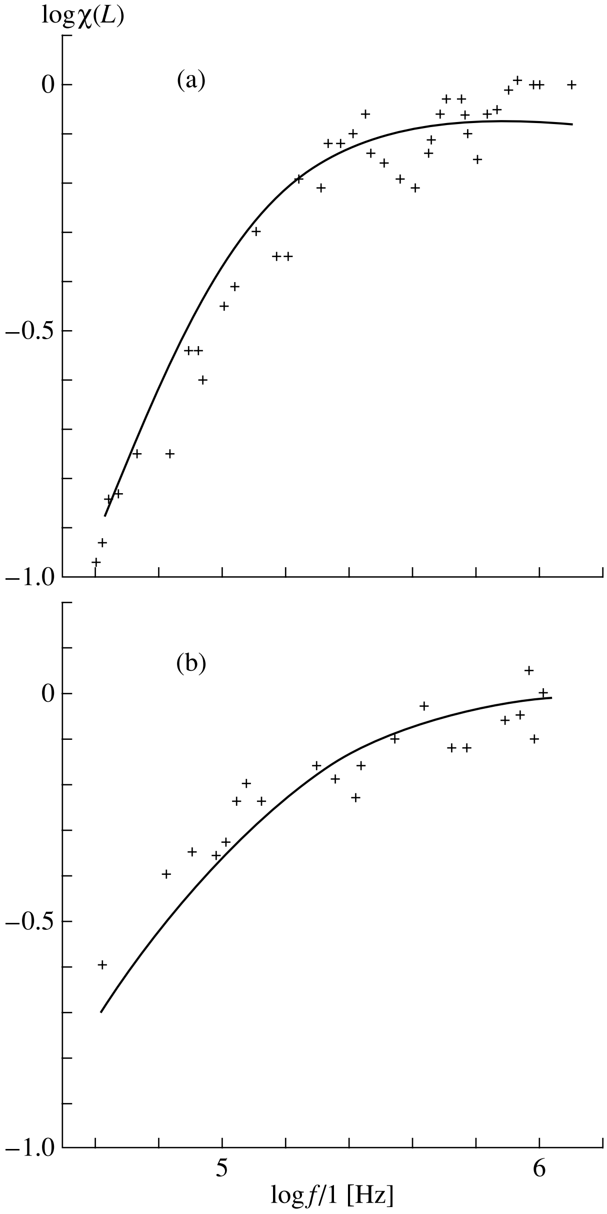

Fig. 3. Dependences of the nonlinear attenuation coefficient of an ultrasonic pulse on the frequency f (a) for unannealed zinc at $\varepsilon_m \cong 7.6 \times 10^{-6}$ and (b) for annealed zinc at $\varepsilon_m \cong 1.5 \times 10^{-7}$. The dots represent the experimental data and the lines represent the calculation by Eq. (28).

into Eq. (9) and taking into account that $K_pL = \pi(p - 1/2)$, $\omega = C_0k \gg \Omega_p$, $|\varepsilon_1(x, t)| \gg |\varepsilon_2(x, t)|$, and $\varepsilon_{2x} \ll k\varepsilon_2$, we obtain an equation for the pulse amplitude $\varepsilon_2(x)$:

$$d\varepsilon_2/dx = -\delta[1 + ga_0\varepsilon_m^S|\cos K_px|^S]\varepsilon_2, \tag{11}$$

where $\delta = \beta\omega^2/2C_0^3$, $a_0 = \pi^{-1}\int_0^\pi|\sin\theta|^S d\theta = \pi^{-1/2}\frac{\Gamma[(s+1)/2]}{\Gamma[(s+2)/2]}$, $\theta = \Omega_pt$, and $s > -1$.

The linear attenuation of a pulse at the frequency $f_1 = 237$ kHz in unannealed zinc and at the frequency $f_2 = 312$ kHz in annealed zinc was $\delta_1L \cong 0.35$ and $\delta_2L \cong 0.45$. This corresponds to $\beta_1 \cong 5 \times 10^2$ cm^2/s and $\beta_2 \cong 3.8 \times 10^2$ cm^2/s.

From Eq. (11), we determine the expression for the nonlinear attenuation coefficient $\chi(L)$ of an ultrasonic pulse:

$$\chi(L) = \frac{g\beta\omega^2L}{2\pi C_0^3}\left(\frac{\Gamma[(s+1)/2]}{\Gamma[(s+2)/2]}\right)^2\varepsilon_m^S. \tag{12}$$

It follows from this expression that, at $s = 3/2$ in the case of unannealed zinc and at $s = 2$ in the case of annealed zinc, the analytical dependences of $\chi(L)$ on ε_m coincide with the experimental ones [Eqs. (5) and (6)]. However Eq. (12) gives a quadratic dependence of $\chi(L)$ on the frequency ω of the pulse, and this does not correspond to the experimental results. In this connection, Eq. (8) must be modified in such a way that not only the amplitude but also the frequency dependences determined experimentally be adequately described by the analytical dependences.

Here, we modify the Granato–Lucke dislocation theory to describe the experimentally established amplitude and frequency dependences characterizing the nonlinear sound attenuation by sound. We also assume that, in the process of separation of the dislocation loops from impurity atoms, the lengths l of dislocations are characterized by the distribution function $N = N(l)$ depending on the pumping wave strain. If the amplitude ε_m increases, the change in the distribution function must correspond to the change in the hysteresis loss determined from the pumping wave attenuation. It is presumed that, at small amplitudes ε_m, the hysteresis loss is absent and the function $N(l)$ is equal to the initial one determined by the impurity atoms. As the strain amplitude increases, the growth and saturation of the hysteresis loss is observed and $N(l)$ must transform from the initial distribution function to a terminal one that does not depend on the medium deformation and is determined by the dislocation network. Since the sound attenuation by sound is also observed after the saturation of the hysteresis loss, we can assume that, at a large amplitude of the pumping wave, $N(l)$ does not depend on the deformation and corresponds to the distribution function determined by the dislocation network. (It is assumed in the Granato–Lucke theory that, after the separation from the impurity atoms, the lengths of all dislocations are identical and equal to L_N.)

According to Eq. (8), we assume that the dislocations have a dissipative nonlinearity, i.e., the coefficient B of the dislocation damping is not constant but depends on the dislocation displacement ξ:

$$B(\xi) = B_0(1 + \mu|\xi/b|^S), \tag{13}$$

where B_0 is the damping coefficient at small dislocation oscillations and μ is the dimensionless coefficient of dissipative nonlinearity. In this case, the dislocation motion is described by the nonlinear equation

$$A\xi_{tt} + B_0(1 + \mu|\xi/b|^S)\xi_t - C\xi_{yy} = b\tau. \tag{14}$$

Deriving the equation of state for a polycrystal containing a large number of dislocations, we determine its strain γ under the action of the stress τ as the sum of the elastic strain $\gamma_0 = \tau/G$ and the dislocation strain γ_d [1–4]:

$$\gamma = \gamma_0 + \gamma_d,$$
$$\gamma_d = b\int_0^\infty\bar{\xi}(t)lN(l)dl, \quad \bar{\xi}(t) = l^{-1}\int_0^l\xi(y, t)dy. \tag{15}$$

It is impossible to obtain an exact analytical solution to Eq. (14), and, therefore, we will use an approximation by assuming (as in the Granato–Lucke theory) that the dislocation oscillations at the principal mode predominate, i.e.,

$$\xi(y, t) \cong \zeta(t)\sin\frac{\pi y}{l}. \tag{16}$$

Solving Eq. (14) by the perturbation method, i.e., by substituting $\zeta(t) = \zeta_0(t) + \zeta_1(t)$, $(|\zeta_0| \gg |\zeta_1|)$ into Eqs. (14) and (16), we obtain the equations for the zeroth ζ_0 (at $\mu = 0$) and first ζ_1 approximations:

$$\zeta_{0tt} + d_0\zeta_{0t} + \Omega^2\zeta_0 = (4b/\pi A)\tau, \tag{17}$$

$$\zeta_{1tt} + d_0\zeta_{1t} + \Omega^2\zeta_1 = -\eta d_0|\zeta_0|^S\zeta_{0t}, \tag{18}$$

where $d_0 = B_0/A$, $\eta = \frac{2\mu}{\pi^{1/2}b^S}\frac{\Gamma[(s+3)/2]}{\Gamma[(s+4)/2]}$, and $\Omega(l) = (\pi/l)(C/A)^{1/2} = [2/(1-\nu)]^{1/2}(C_\perp/l)$ is the resonance frequency of the principal oscillation mode of a dislocation after its separation from the impurity atoms. From Eqs. (17) and (18), we obtain

$$\zeta_0(t) = \frac{8b}{\pi\lambda A}\int_{-\infty}^t\tau(t_1)\exp\left(\frac{d_0}{2}(t_1 - t)\right)\sin\left(\frac{\lambda}{2}(t - t_1)\right)dt_1, \tag{19}$$

$$\zeta_1(t) = -\frac{2\eta d_0}{\lambda} \times \int_{-\infty}^t D[\zeta_0(t_1)]\zeta_{0t}(t_1)\exp\left(\frac{d_0}{2}(t_1 - t)\right)\sin\left(\frac{\lambda}{2}(t - t_1)\right)dt_1, \tag{20}$$

where $\lambda^2 = 4\Omega^2 - d_0^2$ and $D[\zeta_0(t)] = |\zeta_0(t)|^S$.

Substituting Eqs. (19) and (20) into Eqs. (15) and (16) and changing from shear stress τ and strain γ to the longitudinal stress σ and strain ε in the rod [1, 2], we obtain (for a small concentration of dislocations) the equation of state for a polycrystal in the form $\sigma = \sigma(\varepsilon)$:

$$\sigma(\varepsilon) = E\left[\varepsilon - \frac{16C_0^2R^2}{\pi^2\lambda}\int_0^{\infty}\int_{-\infty}^{t}\varepsilon(t_1)\exp\left(\frac{d_0}{2}(t_1-t)\right)\right.$$
$$\left.\times\sin\left(\frac{\lambda}{2}(t-t_1)\right)dt_1 lN(l)dl\right] - \frac{16\eta d_0 C_0^2R^2}{\pi^3\lambda^2}E$$
$$\times\int_0^{\infty}\int_{-\infty}^{t}\int_{-\infty}^{t_1}D[\zeta_0(t_1)]\varepsilon(t_2)\exp\left(\frac{d_0}{2}(t_2-t)\right) \quad (21)$$
$$\times\left[d_0\sin\left(\frac{\lambda}{2}(t_1-t_2)\right) - \lambda\cos\left(\frac{\lambda}{2}(t_1-t_2)\right)\right]$$
$$\times\sin\left(\frac{\lambda}{2}(t-t_1)\right)dt_1dt_2 lN(l)dl,$$

where

$$D[\zeta_0(t)] = \left(\frac{8C_\perp^2}{\pi^2 b\lambda R}\right)^S$$
$$\times\left|\int_{-\infty}^{t}\varepsilon(t_1)\exp\left(\frac{d_0}{2}(t_1-t)\right)\sin\left(\frac{\lambda}{2}(t-t_1)\right)dt_1\right|^S. \quad (22)$$

Substituting Eq. (21) in the equation of motion, we obtain a nonlinear wave equation

$$\varepsilon_{tt} - C_0^2\varepsilon_{xx} = -\frac{16C_0^4R^2}{\pi^3\lambda}\int_0^{\infty}\int_{-\infty}^{t}\varepsilon_{xx}(t_1)\exp\left(\frac{d_0}{2}(t_1-t)\right)$$
$$\times\sin\left(\frac{\lambda}{2}(t-t_1)\right)dt_1 lN(l)dl - \frac{16\eta d_0C_0^4R^2}{\pi^3\lambda^2}$$
$$\times\int_0^{\infty}\int_{-\infty}^{t}\int_{-\infty}^{t_1}[D[\zeta_0(t_1)]\varepsilon(t_2)]_{xx}\exp\left(\frac{d_0}{2}(t_2-t)\right) \quad (23)$$
$$\times\left[d_0\sin\left(\frac{\lambda}{2}(t_1-t_2)\right) - \lambda\cos\left(\frac{\lambda}{2}(t_1-t_2)\right)\right]$$
$$\times\sin\left(\frac{\lambda}{2}(t-t_1)\right)dt_1dt_2 lN(l)dl.$$

This equation describes the nonlinear sound attenuation by sound, as well as Eq. (9), but in contrast to the latter, Eq. (23) can give (depending on the damping parameter and the dislocation distribution function) another (different from quadratic) dependence of the nonlinear attenuation coefficient on the frequency of the ultrasonic pulse. Let us demonstrate this by calculations.

Substituting Eq. (10) into Eqs. (22) and (23), we obtain an expression for $D[\zeta_0(t)]$ and an equation for the complex amplitude $\varepsilon_2(x)$ of an ultrasonic pulse

$$D[\zeta_0(t)] = \left(\frac{8C_\perp^2}{\pi^2 bR}\right)^S\frac{\varepsilon_m^S|\cos K_px|^S|\cos(\Omega_pt-\Psi)|^S}{((\Omega^2-\Omega_p^2)^2+d_0^2\Omega_p^2)^{S/2}}, \quad (24)$$

$$\frac{\varepsilon_{2x}}{\varepsilon_2} = -4j\frac{C_0R^2\omega}{\pi^3}\int_0^{\infty}\frac{lN(l)dl}{\Omega^2-\omega^2+jd_0\omega}$$
$$-4c\eta d_0\varepsilon_m^S|\cos K_px|^S\frac{C_0R^2\omega^2}{\pi^3} \quad (25)$$
$$\times\int_0^{\infty}\frac{((\Omega^2-\Omega_p^2)^2+d_0^2\Omega_p^2)^{-S/2}}{(\Omega^2-\omega^2+jd_0\omega)^2}lN(l)dl,$$

where

$$\Psi = \arctan\left(\frac{d_0\Omega_p}{\Omega^2-\Omega_p^2}\right),$$

$$c = \pi^{-1/2}\frac{\Gamma[(s+1)/2]}{\Gamma[(s+2)/2]}\left(\frac{8C_\perp^2}{\pi^2bR}\right)^S.$$

Assuming in Eq. (25) that $\varepsilon_2(x) = a(x)\exp j\psi(x)$, we obtain the equations for the amplitude $a(x)$ and phase $\psi(x)$ of a pulse (for $\Omega_p \ll \Omega$ and $d_0\Omega_p \ll \Omega^2$):

$$\frac{a_x}{a} = -4\frac{C_0R^2d_0}{\pi^3}\omega^2\int_0^{\infty}\frac{lN(l)dl}{(\Omega^2-\omega^2)^2+d_0^2\omega^2}$$
$$-4c\eta\varepsilon_m^S|\cos K_px|^S\frac{C_0R^2d_0}{\pi^3}\omega^2 \quad (26)$$
$$\times\int_0^{\infty}\frac{[(\Omega^2-\omega^2)^2-d_0^2\omega^2]lN(l)dl}{\Omega^{2S}((\Omega^2-\omega^2)^2+d_0^2\omega^2)^2},$$

$$\psi_x = -4\frac{C_0R^2}{\pi^3}\omega\int_0^{\infty}\frac{(\Omega^2-\omega^2)lN(l)dl}{(\Omega^2-\omega^2)^2+d_0^2\omega^2}$$
$$+8c\eta\varepsilon_m^S|\cos K_px|^S\frac{C_0R^2d_0^2}{\pi^3}\omega^3 \quad (27)$$
$$\times\int_0^{\infty}\frac{(\Omega^2-\omega^2)lN(l)dl}{\Omega^{2S}((\Omega^2-\omega^2)^2+d_0^2\omega^2)^2}.$$

In the absence of the pumping wave, the first terms on the right-hand sides of Eqs. (26) and (27) are responsible for the attenuation and the change in the propagation velocity of a weak elastic wave in a polycrystal with dislocations whose distribution function is determined by the impurity atoms. (At $\varepsilon_m = 0$, these equations yield Eqs. (2) and (3) for the attenuation coefficient and the correction to the phase velocity of a small-amplitude wave.) In the case of relatively small amplitudes ε_m (before saturation of the hysteresis loss), the distribution function depends on the pumping wave strain, and the first terms on the right-hand sides of Eqs. (26) and (27) also contribute to the nonlinear attenuation and the variation of the propagation velocity of the pulse. In the range of amplitudes ε_m, which corresponds to the saturation of the hysteresis loss, the distribution function is determined by the dislocation network and does not depend on the strain, and, therefore, these terms can be ignored in describing the nonlinear attenuation and the variation of the pulse velocity (for relatively large ε_m). Thus, the nonlinear attenuation and the variation of the propagation velocity of an ultrasonic pulse are mainly determined by the second terms on the right-hand sides of Eqs. (26) and (27). From Eq. (27), we determine the coefficient of nonlinear attenuation of an ultrasonic pulse:

$$\chi(L) = Q_S L \varepsilon_m^S \omega^2 \times \int_0^\infty \frac{(\Omega^2 - \omega^2)^2 - d_0^2\omega^2}{\Omega^{2S}((\Omega^2 - \omega^2)^2 + d_0^2\omega^2)^2} l N(l)\,dl, \tag{28}$$

where

$$Q_S = \frac{8\mu C_0 R^2 d_0}{\pi^{9/2}}\left(\frac{8C_\perp^2}{\pi^2 b^2 R}\right)^S \frac{s+1}{s+2}\left(\frac{\Gamma[(s+1)/2]}{\Gamma[(s+2)/2]}\right)^3. \tag{29}$$

It follows from Eq. (28) that, at equal lengths of dislocations ($N(l)dl = (\Lambda/L_N)\delta(l - L_N)dl$, $\Omega_N = [2/1 - \nu]^{1/2}(C_\perp/L_N)$, the sign of the nonlinear attenuation coefficient of an ultrasonic pulse depends on the frequency ω: $\chi(l) > 0$ in the ranges $0 < \omega < \Omega_1 = (-d_0 + [d_0^2 + 4\Omega_N^2]^{1/2})/2$ and $\omega > \Omega_2 = (d_0 + [d_0^2 + 4\Omega_N^2]^{1/2})/2$, and $\chi(l) < 0$ in the range $\Omega_1 < \omega < \Omega_2$; i.e., generally speaking, not only the sound attenuation but also the amplification of sound by sound can be observed in polycrystals. One can also see from Eq. (28) that, at low frequencies ($\omega \ll \Omega^* = \Omega_0^2/d_0$, Ω_0 is the minimal resonance frequency of dislocations), we have $\chi(L) \sim \omega^2$, whereas at high frequencies ($\omega \gg \Omega_2$) – $\chi(L) \sim \omega^{-2}$. Therefore, the intermediate dependences of $\chi(L)$ on ω can be observed in the intermediate frequency range. Their specific form is determined by the damping parameter and the dislocation distribution function. Figure 3 shows the dependences of the nonlinear attenuation coefficient of a pulse on the frequency f with the parameters $d_0 = 5 \times 10^9$ Hz, $\nu = 0.25$, $C_\perp = 2.4 \times 10^3$ m/s, and $R = 0.2$ for the cases

(a) $s = 3/2$, $\varepsilon_m = 7.6 \times 10^{-6}$, $N(l) = \dfrac{5\Lambda l^{-7}}{l_1^{-5} - l_2^{-5}}$,

$l_1 \le l \le l_2$, $l_1 = 7 \times 10^{-7}$ m, and $l_2 = 7 \times 10^{-5}$ m;

(b) $s = 2$, $\varepsilon_m = 1.5 \times 10^{-7}$, $N(l) = \dfrac{6\Lambda l^{-8}}{l_1^{-6} - l_2^{-6}}$,

$l_1 \le l \le l_2$, $l_1 = 9 \times 10^{-7}$ m, and $l_2 = 5 \times 10^{-5}$ m.

One can see from Fig. 3 that, in the case of such a choice of the damping parameter d_0 and the distribution functions $N = N(l)$ for unannealed and annealed zinc, the analytical dependences of $\chi(L)$ on ω are close to the experimental ones. Therefore, it is possible to introduce the effective parameter of dissipative nonlinearity $g = g_{\text{eff}}(\omega)$ into the equation of state, Eq. (8), in order to describe the dissipative nonlinearity of the polycrystal. This parameter is determined from the comparison of Eqs. (12) and (28):

$$g_{\text{eff}}(\omega) = M(s)\int_0^\infty \frac{(\Omega^2 - \omega^2)^2 - d_0^2\omega^2}{\Omega^{2S}((\Omega^2 - \omega^2)^2 + d_0^2\omega^2)^2} l N(l)\,dl, \tag{30}$$

where

$$M(s) = \frac{16\mu d_0 R^2 C_0^4}{\pi^{7/2}\beta}\left(\frac{8C_\perp^2}{\pi^2 b^2 R}\right)^S \frac{s+1}{s+2}\frac{\Gamma[(s+1)/2]}{\Gamma[(s+2)/2]}. \tag{31}$$

From Eq. (30) it follows that $g_{\text{eff}}(\omega) \cong \text{const} > 0$ at low frequencies ($\omega \ll \Omega^* = \Omega_0^2/d_0$) and, when the frequency ω grows, the parameter $g_{\text{eff}}(\omega)$ decreases.

Now after the experimental and analytical dependences of the coefficient $\chi(L)$ on the amplitude ε_m and the frequency ω are matched, we can try to determine the free parameter of the equation of state (21). In this case, it is the product of the coefficient of dissipative nonlinearity μ of a dislocation by the dislocation density Λ. Substituting the measured data into Eqs. (29) and (30), we obtain $\mu\Lambda \cong 2 \times 10^{10}$ m^{-2} for unannealed zinc and $\mu\Lambda \cong 10^{10}$ m^{-2} for annealed zinc. If we assume that in unannealed zinc, $\Lambda \approx 10^{14}$ m^{-2}, and in annealed zinc $\Lambda \approx 10^{10}$ m^{-2}, we obtain the following values of the coefficients of dissipative nonlinearity of dislocations: $\mu_1 \approx 2 \times 10^{-4}$ and $\mu_2 \approx 1$, respectively. Finally, we determine the values of the effective parameter of dissipative nonlinearity from Eqs. (30) and (31):

$g_{\text{eff}}(\omega_1) \cong 8.4 \times 10^8$ for unannealed zinc and

$g_{\text{eff}}(\omega_2) \cong 2.6 \times 10^{12}$ for annealed zinc.

Let us consider the nonlinear limitation of the amplitude of ultrasonic pulses. The equations of state (8) and (21) and the wave equations (9) and (23) corresponding to them describe not only the action of an intense pumping wave on the attenuation of a weak ultrasonic pulse, but also the action of an intense pulse on itself. Such an effect, called self-action, is also caused by the dissipative nonlinearity and manifests itself in the dependence of the coefficient of wave attenuation on its amplitude, which can lead to a nonlinear limitation of the wave amplitude or to self-saturation of the medium. In this connection, experiments on the self-action of ultrasonic pulses were conducted using the same unannealed and annealed zinc rods in order to verify additionally and independently the validity of Eqs. (9) and (23). In these experiments, a pumping radiator (*1*) excited ultrasonic pulses with the carrier frequency f about 100 kHz and the duration 500 μs in a rod (*2*). The pulses were received at the opposite end of the rod by a piezoelectric accelerometer (*5*). The relative values of the following quantities were measured with the help of an oscilloscope: the amplitude V_1 of the voltage at the radiator, which was proportional to the amplitude of the displacement of one end of the rod ($x = 0$), and the amplitude V_2 of the voltage at the accelerometer, which was proportional to the amplitude of the displacement of the other end of the rod ($x = L$). Preliminary testing of the radiator–receiver system demonstrated its linearity. The check experiments with a glass rod also showed no deviations from the dependence $V_2 \sim V_1$.

Figure 4 presents the dependences of the amplitude V_2 on the amplitude V_1 for rods made of unannealed and annealed zinc. One can see from this figure that the dependence $V_2 \sim V_2(V_1)$ is nonlinear, and the amplitude V_2 of the pulse transmitted through the rod grows slower than the initial amplitude V_1; i.e., the effect of a nonlinear limitation of the pulse amplitude is observed. Let us first describe this effect in the framework of the phenomenological equation of state (8) and the wave equation (9) following from it. Assuming in Eq. (9)

$$\varepsilon_2(x, t) = \varepsilon_2(x)\cos[\omega t - kx + \psi(x)] \qquad (32)$$

and taking $\omega = C_0 k$, $\varepsilon_{2x} \ll k\varepsilon_2$, and $\psi_x \ll k$, we obtain an equation for the strain amplitude of the acoustic wave

$$\varepsilon_{2x} = -\delta\varepsilon_2[1 + g a_1 \varepsilon_2^S], \quad \psi(x) = 0, \qquad (33)$$

where

$$a_1 = \pi^{-1}\int_0^{\pi} |\cos\vartheta|^S \sin^2\vartheta d\vartheta$$

$$= \frac{1}{\pi^{1/2}(s+2)} \frac{\Gamma[(s+1)/2]}{\Gamma[(s+2)/2]}, \quad \vartheta = \omega t - kx.$$

The solution to this equation has the form

$$\varepsilon_2(x) = \frac{\varepsilon_0 \exp(-\delta x)}{(1 + g a_1 \varepsilon_0^S[1 - \exp(-s\delta x)])^{1/S}}, \qquad (34)$$

where $\varepsilon_0 = \varepsilon_2(x = 0)$ is the initial wave amplitude.

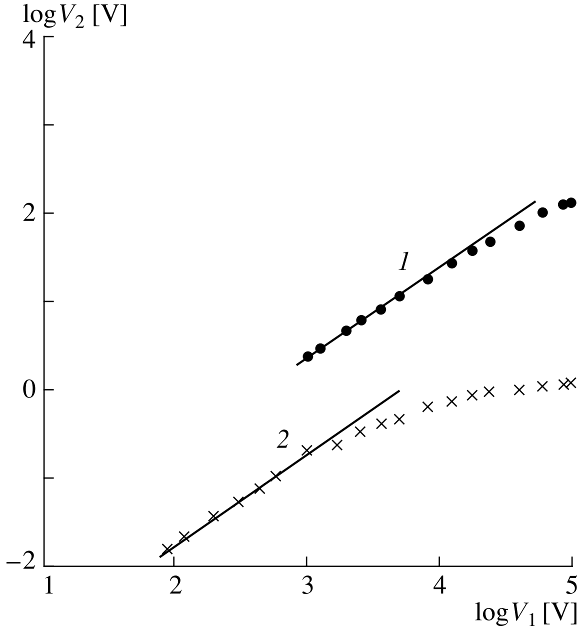

Fig. 4. Dependences of the amplitude of the accelerometer signal V_2 on the amplitude of the radiator oscillations V_1 for the rods made of (*1*) unannealed and (*2*) annealed zinc. The straight lines correspond to the dependence $V_2 \sim V_1$.

By comparing the analytical expression (34) with the experimental data, it is basically possible to determine the parameters s and g of the dissipative nonlinearity of the equations of state for unannealed and annealed zinc. However, since the measurements were relative, it is possible to determine only the exponent s. It follows from Eq. (34) that, for small amplitudes $\varepsilon_{0,1}$ and for $g > 0$, $s > 0$, when $g a_1 \varepsilon_{0,1}^S \ll 1$, the wave attenuates according to the law

$$\varepsilon_{2,1}(x) = \varepsilon_{0,1}\exp(-\delta x). \qquad (35)$$

Let us divide Eqs. (34) and (35) by one another and introduce the notations $Z = g a_1 \varepsilon_{0,1}[1 - \exp(-s\delta L)]$, $P = \varepsilon(L)/\varepsilon_{2,1}(L)$, and $W = \varepsilon_0/\varepsilon_{0,1}$. Then, we obtain (for $ZW^S \ll 1$):

$$\ln[\ln W/P] = \ln[Z/s] + s\ln W. \qquad (36)$$

Using the experimental data (Fig. 4), we plot the dependence of $\ln[\ln W/P]$ on $\ln W$ (Fig. 5). From this figure, it follows that $s \cong 3/2$ for unannealed zinc and $s \cong 2$ for annealed zinc.

Thus, the results of the experiments on the nonlinear limitation of the amplitude of ultrasonic pulses testify that the exponents of the dissipative acoustic nonlinearity of unannealed and annealed zinc coincide with those obtained from the experiments on the sound attenuation in water.

Now, let us describe the processes of the self-action of ultrasonic pulses within the framework of the wave equation (23) obtained from the modified Granato–Lucke dislocation theory. Substituting Eq. (33) into Eq. (23) and performing simple calculations, we obtain

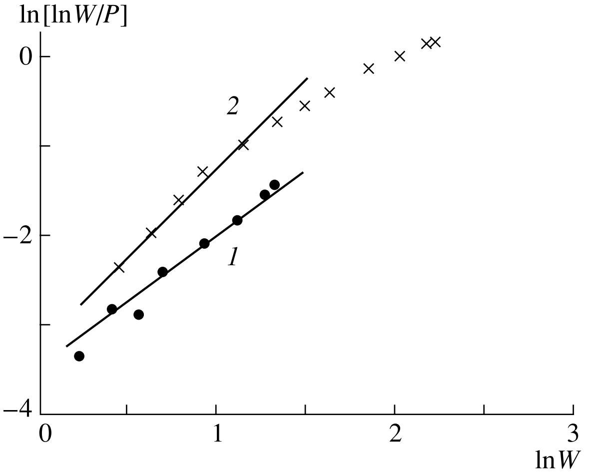

Fig. 5. Dependences of ln[ln*W*/*P*] on ln*W* for (*1*) unannealed and (*2*) annealed zinc. The straight lines correspond to the exponent values s = (*1*) 3/2 and (*2*) 2.

an expression for $D[\zeta_0(t)]$ and the equations for the amplitude and phase of an ultrasonic pulse:

$$D[\zeta_0(t)] = \left(\frac{8C_\perp^2}{\pi^2 bR}\right)^S \frac{\varepsilon_2^S|\cos[\omega t - kx + \psi(x) - \Psi]|^S}{2^S((\Omega^2-\omega^2)^2 + d_0^2\omega^2)^{S/2}}, \quad (37)$$

$$\begin{aligned}\varepsilon_{2x} &= -4\frac{C_0R^2d_0}{\pi^3}\varepsilon_2\omega^2\int_0^\infty \frac{lN(l)dl}{(\Omega^2-\omega^2)^2+d_0^2\omega^2} \\ &- P(s)\varepsilon_2^{S+1}\omega^2\int_0^\infty \frac{(\Omega^2-\omega^2)lN(l)dl}{((\Omega^2-\omega^2)^2+d_0^2\omega^2)^{(S+3)/2}},\end{aligned} \quad (38)$$

$$\begin{aligned}\psi_x &= -4\frac{C_0R^2}{\pi^3}\omega\int_0^\infty \frac{(\Omega^2-\omega^2)lN(l)dl}{(\Omega^2-\omega^2)^2+d_0^2\omega^2} \\ &+ P(s)\varepsilon_2^S d_0\omega^3\int_0^\infty \frac{lN(l)dl}{((\Omega^2-\omega^2)^2+d_0^2\omega^2)^{(S+3)/2}},\end{aligned} \quad (39)$$

where

$$\Psi = \arctan\left(\frac{d_0\omega}{\Omega^2-\omega^2}\right),$$

$$P(s) = 8\frac{\mu C_0R^2d_0}{\pi^4}\frac{s+1}{(s+2)^2}\left(\frac{\Gamma[(s+1)/2]}{\Gamma[(s+2)/2]}\right)^2\left(\frac{4C_\perp^2}{\pi^2b^2R}\right)^S.$$

The first terms on the right-hand sides of Eqs. (38) and (39) (as in Eqs. (26) and (27)) are responsible for the linear attenuation and the variation of the propagation velocity of ultrasonic pulses and the second terms describe their nonlinear absorption and velocity variation. However, in this case, in contrast to the sound attenuation by sound, the dislocation distribution function is determined apparently by the impurity atoms rather than by the dislocation network. This is connected with the fact that as the frequency of an acoustic wave grows, the hysteresis loss caused by the separation of the dislocation loops from the impurity atoms decreases [9, 10]; i.e., no separation of dislocations occurs at ultrasonic frequencies. Comparing Eqs. (33) and (38), it is seen that they have the same structure, and, therefore, the solutions to these equations coincide. It follows also from Eq. (38) that, at equal lengths of dislocation loops, the sign of the nonlinear term depends on the frequency of the ultrasonic pulse and, hence, for $\omega < \Omega$, the nonlinear limitation of the pulse amplitude must be observed, whereas for $\omega > \Omega$, the self-saturation of the polycrystal should be expected. In the experiment, the frequency of ultrasonic pulses was relatively low, and the effect of the nonlinear amplitude limitation was observed.

Thus, in this paper, we presented the results of experimental studies of the following nonlinear acoustic effects: sound attenuation by sound and amplitude limitation of an ultrasonic pulse in unannealed and annealed polycrystalline zinc. The analytical description of these effects was conducted in the framework of a phenomenological equation of state, which contains the dissipative acoustic nonlinearity. A modification of the Granato–Lucke dislocation theory was suggested on the basis of this equation. The modified theory explains the amplitude and frequency dependences observed in the experiment for the nonlinear attenuation coefficient of ultrasonic pulses. The basic issues of this modification are the following assumptions:

(i) the dislocations possess a dissipative nonlinearity;

(ii) the function of the dislocation distribution in length becomes sufficiently wide after the separation of dislocations from the impurity atoms.

The first assumption provides the amplitude dependences of the coefficient of nonlinear attenuation of an ultrasonic pulse under the action of an intense low-frequency pumping wave, which agree with the experimental data, while the second assumption provides the corresponding frequency dependences. The comparison of the experimental data with the analytical calculations showed that the annealing of zinc leads to changes in the parameter and the exponent of the dissipative nonlinearity of a dislocation, as well as in the dislocation distribution function. This is evidence of the fact that the dissipative acoustic nonlinearity is a structure-sensitive characteristic of zinc (and also of some other metals and rocks), which allows one to expect that the effects of nonlinear sound attenuation by sound and the self-action of acoustic pulses can be used for an acoustic diagnostics of the dislocation structure of polycrystals.

ACKNOWLEDGMENTS

This work was supported by the Russian Foundation for Basic Research (project no. 01-05-64417) and the Interdepartmental Research Center (project no. 1369).

REFERENCES

1. A. Granato and K. Lucke, J. Appl. Phys. **27** (6), 583 (1956).
2. *Ultrasonic Methods for Studying Dislocations*, Ed. by L. G. Merkulov (Inostrannaya Literatura, Moscow, 1963).
3. A. Granato and K. Lucke, in *Physical Acoustics: Principles and Methods*, Ed. by W. P. Mason (Academic, New York, 1965; Mir, Moscow, 1969), Vol. 4A, pp. 226–276.
4. R. Truell, C. Elbaum, and B. B. Chick, *Ultrasonic Methods in Solid State Physics* (Academic Press, New York, 1969; Mir, Moscow, 1972).
5. *Internal Friction and Defects in Metals*, Ed. by V. S. Postnikov (Metallurgiya, Moscow, 1965).
6. J. Wang, Q. E. Fang, and Z. G. Zhu, Phys. Status Solidi A **169** (43), 43 (1998).
7. V. E. Nazarov, Akust. Zh. **37**, 1177 (1991) [Sov. Phys. Acoust. **37**, 616 (1991)].
8. V. E. Nazarov and A. V. Kolpakov, J. Acoust. Soc. Am. **107**, 1915 (2000).
9. V. E. Nazarov, Fiz. Met. Metalloved. **88** (4), 82 (1999).
10. V. E. Nazarov, Akust. Zh. **46**, 228 (2000) [Acoust. Phys. **46**, 186 (2000)].
11. S. V. Zimenkov and V. E. Nazarov, Izv. Akad. Nauk SSSR, Fiz. Zemli, No. 1, 13 (1991).
12. V. E. Nazarov and S. V. Zimenkov, Acoust. Lett. **16**, 218 (1993).
13. V. E. Nazarov, Acoust. Lett. **17**, 145 (1994).

Translated by M. Lyamshev

Acoustical Physics, Vol. 47, No. 4, 2001, pp. 448–451. Translated from Akusticheskiĭ Zhurnal, Vol. 47, No. 4, 2001, pp. 520–524.
Original Russian Text Copyright © 2001 by Nosov, Postnov.

Measurement of the Acoustic Parameters of the Ocean Bottom Using Multiply Scattered Sound Pulses

A. V. Nosov and G. A. Postnov
Shirshov Institute of Oceanology, Russian Academy of Sciences,
Nakhimovskiĭ pr. 36, Moscow, 117851 Russia
e-mail: nosoff@chip.sio.rssi.ru

Received April 4, 2000

Abstract—A multibeam echo sounder of a new generation has been developed at the Shirshov Institute of Oceanology on the basis of a transmitting device and a receiving multielement array installed on the *Akademik Ioffe* research vessel. This development makes it possible to measure the angular spectrum of bottom-scattered acoustic signals. The analysis of the spectrum records obtained in the North Atlantic during the vessel motion demonstrates a possibility to use triply-scattered signals (bottom–surface–bottom) for the determination of the coefficient of sound reflection in the case of an oblique incidence on the bottom, whereas similar measurements with a conventional technique require the utilization of horizontally separated transmitter and receiver. The results of calculating the reflection coefficient from the experimental data are presented. *© 2001 MAIK “Nauka/Interperiodica”.*

The coefficient of sound reflection $V_b(\theta')$ and the scattering coefficient $m_b(\theta', \theta)$ belong to the acoustic parameters of the ocean bottom. Here, θ' is the angle of incidence of a plane wave at the bottom and θ is the scattering angle. In the general case, the measurement of these parameters needs spatially separated transmitters and receivers of sound, which is a serious engineering problem [1, 2]. The purpose of this study is to demonstrate that the utilization of triply-scattered acoustic signals (bottom–surface–bottom) considerably facilitates the measurement of these parameters.

Let us consider the case of a combined transmitter–receiver located near the surface. In the case of the utilization of a pulsed sounding signal, the leading edge of a triply-scattered signal is most informative for parameter evaluation. The shortest propagation path of a triply-scattered pulse is shown in Fig. 1a: it corresponds to a double reflection, from the bottom and the surface, and a scattering from the bottom. In the case of a flat (on the average) bottom at depth H and a homogeneous medium, the propagation time of a signal along this path is $t_A = (3/\cos\theta' + 1/\cos\theta)H/c$, $\theta' = \arctan\left(\frac{1}{3}\tan\theta\right)$, where c is the sound velocity in water. The intensities of single- and triply-scattered signals $I^{(1)}$ and $I_A^{(3)}$ are described by the formulas given in [3]. If one uses the transmission arrays that are directional in the vertical plane, it is possible to show that

$$|V_b|^2 = 3\frac{I_A^{(3)}}{I^{(1)}}\frac{G_t(\theta-\theta_M)}{G_t(\theta'-\theta_M)}\frac{m_b(\theta,\theta)}{m_b(\theta',\theta)}\left(\frac{\cos\theta}{\cos\theta'}\right)^3 \times |V_s(\theta')|^{-2}\exp(\beta(ct_A - 2H/\cos\theta)). \quad (1)$$

Here, G_t is the amplification factor of the transmitting array; V_b and V_s are the reflection coefficients of the bottom and the surface, respectively; β is the attenuation coefficient of sound in water; and θ_M is the orientation of the maximum of the array directivity pattern. An expression for the absolute value of the coefficient of reflection from a rough surface can be obtained by solving a model problem on the determination of the total intensity of sound scattered in the specular direction from a rough surface that is on the average flat and absolutely soft.

An unknown function $m_b(\theta', \theta)$ is involved in Eq. (1). Making certain assumptions on the character of scattering from the bottom, one can try to determine such an approximation of the angular dependence of the scattering coefficient, within which the quantity $\frac{m_b(\theta,\theta)}{m_b(\theta',\theta)}$ depends only on the angles θ and θ', or on the parame-

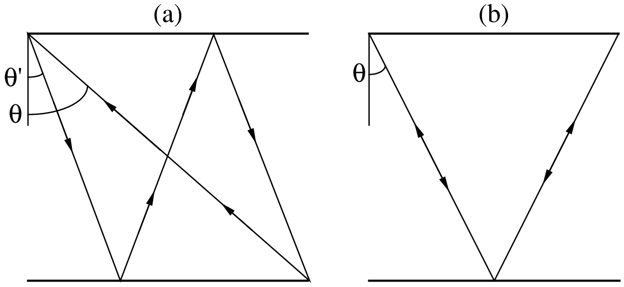

Fig. 1. Sound propagation paths in the case of triple scattering from the surface and bottom of the ocean.

ters that can be evaluated from the data of the same measurements. Let us consider two limiting cases.

(1) Scattering occurs only from the rough surface of the bottom, and the sound transmitted into the bottom thickness attenuates. This model is probably suitable for the bottom consisting of basement rock. If it is possible to use the Kirchhoff approximation, then we have

$$\frac{m_b(\theta, \theta)}{m_b(\theta', \theta)} = \left(\frac{\cos((\theta' + \theta)/2)}{\cos\theta}\right)^4 \times \exp\left[\frac{1}{2\delta^2}\left(\tan\frac{\theta' - \theta}{2} - \tan\theta\right)\right], \tag{2}$$

where δ is the rms inclination of the bottom surface that can be evaluated according to the width $\Delta\theta$ of the function $I^{(1)}(\theta)$ at the level 0.5 of the maximum. It is known that $\Delta\theta \approx 3\delta$.

(2) Scattering occurs from the inhomogeneities of the bottom bulk. According to [4], in the case of shallow-water oceanic regions the experimental frequency–angle dependences of the backscattered field are described well by the model of anisotropic bulk inhomogeneities. Using the formulas obtained in [4] and assuming that $kl\sin\theta \gg 1$, where k is the wave number and l is the horizontal dimension of the bottom inhomogeneities, we obtain

$$\frac{m_b(\theta, \theta)}{m_b(\theta', \theta)} = \frac{1}{16}\left(1 + \frac{\cos\theta}{\cos\theta'}\right)\left(1 + \frac{\sin\theta'}{\sin\theta}\right)^3. \tag{3}$$

Calculating the reflection coefficient of the bottom by Eq. (1), it is natural to use the first maximum of the scattered signal intensity at the receiving array output $I(t)$ as $I^{(1)}$. The problem of selecting the delay time t at which $I_A^{(3)}$ must be measured is more difficult, because at $t = t_A$, we have $I_A^{(3)} = 0$. If the reflection from the bottom and surface is close to coherent, it is possible to use the estimate $t = t_A + \tau$, where $\tau = \tau_0$. It can be readily demonstrated that τ_0 is determined by the delay at the edge of the boundary of the first Fresnel zone in the plane of the ray incidence, and it has the form $\tau_0 = \frac{r_F}{2c}\left(\frac{r_F\cos\theta}{4H} + \sin\theta\right)$, where $r_F = \left(\frac{2cH}{f\cos^3\theta}\right)^{1/2}$ is the length of the first Fresnel zone and f is the frequency. In practice, the response maximum $I(t > t_A)$ can be attained at $\tau > \tau_0$ because of the scattering. On the other hand, in the case of a small deviation of the bottom surface from the horizontal plane, t_A changes. Therefore, we suggest that the first maximum of the function $I(t)$ in the vicinity of t_A be used as $I_A^{(3)}$ in the calculations by Eq. (1).

It is doubtful that a triply scattered signal can be used effectively to evaluate the bottom parameters at a delay exceeding that corresponding to the first maximum of $I(t)$, because it propagates along many paths. An exception is the situation when the reflection from the bottom is close to coherent or the bottom scattering indicatrix is sufficiently narrow. One can expect in this case that the signal propagating along the path B shown in Fig. 1b noticeably exceeds the background signal. The possibility to evaluate the angular dependence V using the signal propagation along the aforementioned path was first demonstrated in our previous paper [5]. In the geometry described above, the maximal intensity of the scattered signal is observed at $t = t_B$, where $t_B = 4H/(c\cos\theta)$ and is described by the expression

$$I_B^{(3)} = I_0\frac{r_0^2}{16H^4}\cos^4\theta G_r(\theta)G_t(\theta - \theta_M) \times S m_s(\theta, \theta)|V_b(\theta)|^4\exp(-4\beta H/\cos\theta), \tag{4}$$

where I_0 is the radiation intensity of an isotropic sound source at the distance r_0, S is the bottom area from which a scattered signal is received, and G_r is the amplification factor of the receiving array.

Since the expression for the coefficient of the backscattering from the surface m_s as the function of the wind speed v is known, Eq. (4) can be used for the independent evaluation of the coefficient of reflection from the bottom in the angular sector $\{0, \delta_s\}$ where m_s is not too small. Here, δ_s is the rms inclination of the sea surface. In the case of the Neumann–Pierson wave spectrum, we have $\delta_s \approx 0.04v^{1/2}$ (δ_s is in radians and v is in meters per second). The comparison of Eqs. (1) and (4) in the indicated angular sector allows one to verify the validity of the model selected for evaluating $|V_s(\theta')|^2$, or (if, for example, it is possible to reliably estimate the bottom reflection coefficient from granulometric data) to estimate $m_b(\theta', \theta)$. It is necessary to note that for small θ, we obtain $t_B \longrightarrow t_A$ and $I^{(3)} \approx I_A^{(3)} + I_B^{(3)}$.

From the aforesaid, we can state that it is possible to obtain approximate estimates of the angular dependence of the coefficient of sound reflection from the bottom by using standard of specialized equipment of a ship, including the case of ship motion. An *a priori* evaluation of the error in the determination of the reflection coefficient by the suggested method is difficult even in the case of a bottom that is on the average flat, and this can apparently be done only by a comparison with known measurement techniques or with the estimates obtained from granulometric measurements of the bottom structure.

Here, we present only some qualitative considerations.

(i) It is necessary to use pencil-beam arrays with a low level of sidelobes. The maximal directivity is determined by the condition that the far wave field not extend beyond the depth in the region of measurements.

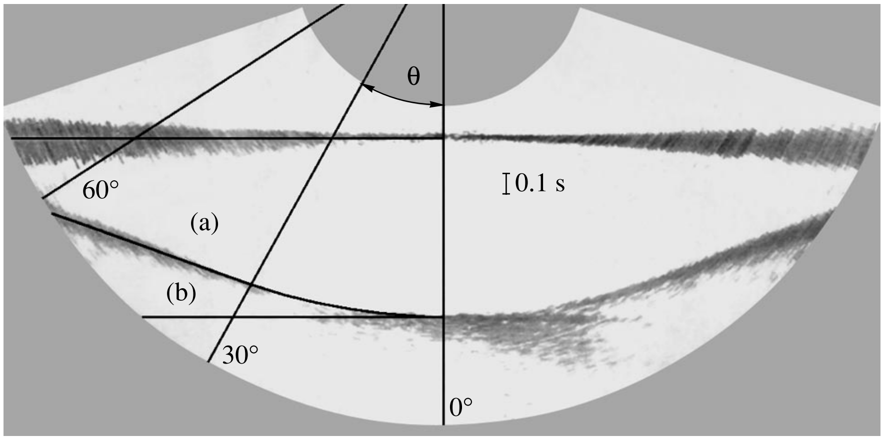

Fig. 2. Average intensity of the scattered signals of a multibeam echo sounder as a function of time and incidence angle.

(ii) Tone-pulsed signals (linear FM pulsed signals at low frequencies) must be used. Their duration and off-duty factor are determined by the penetration depth of the signal into the bottom and by the maximal angle θ at which the suggested method works. At this time, there are not enough data for estimating this angle.

(iii) At large values of the Rayleigh parameter for the bottom and surface, the function determined according to Eq. (1) has the meaning of the effective reflection coefficient [1], whose difference from the reflection coefficient depends on the width of the array directivity pattern and on the signal length.

Considering the standard ship equipment, sonars with rotating antennas and multibeam echo sounders, which provide the output and recording of received signals, are suitable for the indicated measurements.

The calculations of the coefficient of reflection from the bottom were performed according to the data of measurements of the bottom-scattered signals of a multibeam echo sounder carried by the *Akademik Ioffe* research vessel. The echo sounder was redesigned by the employees of the Laboratory of Scattering and Reflection of Sound of the Shirshov Institute of Oceanology, Russian Academy of Sciences. The receiving and transmitting arrays of the echo sounder consisted of 3 × 57 and 3 × 35 elements, respectively. The arrays were directed perpendicularly to each other in the horizontal plane. The operational frequency was 15 kHz, $\theta_M = 30°$, and the resolution in the tilt angle was $\Omega = 0.7°$. The measurements were conducted in the North Atlantic in the process of the ship's movement with a speed of 8 knots. The depth in the region of measurements was 500 m and the bottom was on average flat. According to the available data [6], sand sediments prevail in the region of measurements. Figure 2 shows the intensity (averaged over 30 realizations) of a received signal in the polar coordinate system where the arrival time of a signal (measured from the moment of the emission of the probing pulse) is plotted along the radius, and the angle θ is measured from the vertical downward direction. The degree of darkening is proportional to the intensity. The calculated curve $t_A(\theta)$ is given in the left part of the figure. One can see that the upper boundary of triply scattered signals closely coincides with this curve. At the same time, in a certain interval of angles, one can see triply scattered signals with the delay times described by the formula $t = t_B$. The size of this interval coincides with the estimate for obtained δ_s with the wind speed recorded during the measurements.

The curve $|V_b(\theta)|$ calculated by Eq. (4) is shown by a solid line in Fig. 3. In this case, we used the measured values of the intensity $I_B^{(3)} = \langle I(t = t_B)\rangle$, where $\langle\rangle$ meant averaging over 30 sequential probing pulses, the area of the scattering bottom region was taken as $S = 4\Delta\Omega(H/\cos\theta)^2$ (Δ is the width of the directivity pattern of the transmitting array in the horizontal plane), and an empirical estimate of β was used. The shading indicates the region corresponding to the absolute values of the reflection coefficients calculated by Eqs. (1) and (4) for single probing pulses. The calculation according to Eq. (1) was conducted for several versions of $|V_s(\theta)|$, including $|V_s(\theta)| = 1$ and $|V_s(\theta)| = V_s^e$, where V_s^e is the effective coefficient of reflection from the surface. A formula for this coefficient is given in [1], and the scattering coefficient is determined in the Kirchhoff approximation. However, the closest coincidence with the results of calculation according to Eq. (4) was attained using the sum of the coherent coefficient of reflection and the coefficient of scattering of a plane incident wave in the specular direction (under the assumption of a normal distribution of the surface

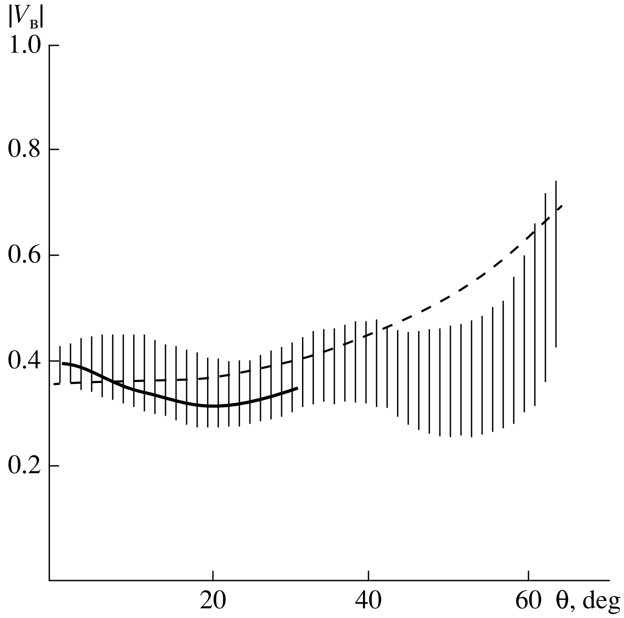

Fig. 3. Angular dependence of the measured absolute value of the effective reflection coefficient of the ocean bottom. Shading corresponds to the calculation by Eq. (1), the solid line represents the calculation by Eq. (4), and the dashed line represents the calculation for a plane boundary between water and a liquid layer whose parameters are taken from [6].

roughness and a Gaussian correlation coefficient). According to [7], we have

$$|V_s^e|^2 = \exp(-(2k\sigma\cos\theta')^2) \times\left[1+\frac{(2kL\cos\theta')^2}{8\pi}\left(\mathrm{Ei}(2k\sigma\cos\theta')^2) - C - 2\ln(2k\sigma\cos\theta')\right)\right]. \qquad (5)$$

Here, σ is the rms deviation of the surface from a plane, L is the interval of the spatial correlation of roughness, C is the Euler constant, and Ei is the integral exponent. The values of σ and L can be calculated through the selected spectrum of wind waves, which is usually approximated by a function of the wind speed v. For example, for the Neumann–Pierson spectrum, we obtain $\sigma \approx 0.0018v^{2.5}$ and $L \approx 0.044v^2$ (δ and L are expressed in meters and v is expresses in meters per second).

The same Fig. 3 shows for comparison the dashed curve that is calculated according to the well known formula for a plane boundary of two liquid layers with the following parameters: the sound velocity in the lower layer is equal to 1670 m/s, the density ratio of the lower and upper layers is equal to 1.92, and the losses in the lower layer are 0.5 dB/(m kHz). One can see that the curves are quite close to each other. The limiting value of the incidence angle for which it is possible to obtain an estimate for the reflection coefficient is determined by the recording time window selected in the experiment, and it can be apparently increased in specially arranged measurements.

The evaluation of the precision and applicability limits of the suggested method needs a large amount of measurements in various regions of the ocean. In practice, currently it is possible to conduct them only in the process of the ship motion. Apparently, the comparison of the results obtained in this way with the data of the model calculations taking into account the granulometric data is the most adequate approach, because in this case, the estimate of the reflection coefficient is averaged over the bottom region far exceeding the region studied by a standard measurement procedure. Certainly, this does not eliminate the necessity of comparative measurements in stationary monitored conditions.

ACKNOWLEDGMENTS

We are grateful to V.N. Kuznetsov, S.A. Dremuchev, and V.V. Yuritsyn, who redesigned the receiving unit of the multibeam echo sounder installed at the *Akademik Ioffe* research ship.

The work was supported in part by the Russian Foundation for Basic Research, project no. 98-05-64779.

REFERENCES

1. V. I. Volovov, *Sound Reflection from the Ocean Bottom* (Nauka, Moscow, 1993).
2. K. Williams and D. Jackson, J. Acoust. Soc. Am. **103**, 169 (1998).
3. I. G. Malyukova and Yu. N. Ryabukha, Vopr. Sudostr., Ser. Akust., No. 14, 106 (1980).
4. Yu. P. Lysanov and A. V. Bunchuk, in *Acoustic Waves in the Ocean*, Ed. by L. M. Brekhovskikh and I. B. Andreeva (Nauka, Moscow, 1987), pp. 151–161.
5. A. V. Nosov and G. A. Postnov, in *Acoustics of the Ocean* (GEOS, Moscow, 2000), pp. 98–101.
6. A. V. Il'in, V. V. Orlenok, and I. I. Shurko, Vopr. Sudostr., Ser. Akust., No. 14, 68 (1980).
7. E. V. Chaevskiĭ, Izv. Vyssh. Uchebn. Zaved., Radiofiz. **9**, 400 (1966).

Translated by M. Lyamshev

Acoustical Physics, Vol. 47, No. 4, 2001, pp. 452–460. Translated from Akusticheskiĭ Zhurnal, Vol. 47, No. 4, 2001, pp. 525–533.
Original English Text Copyright © 2001 by Rudenko, Hedberg, Enflo.

Nonlinear Standing Waves in a Layer Excited by the Periodic Motion of its Boundary[1]

O. V. Rudenko*, C. M. Hedberg, B. O. Enflo*****
**Moscow State University, Vorob'evy gory, Moscow, 119899 Russia*
e-mail: rudenko@acs366b. phys.msu.su
***University of Karlskrona/Ronneby, 37179 Karlskrona, Sweden*
****Royal Institute of Technology, S-10044 Stockholm, Sweden*

Received August 24, 2000

Abstract—A new analytical approach is developed for the description of standing waves caused by arbitrary periodic vibration of a boundary. The approach is based on the nonlinear evolution equation written for an auxiliary function. This equation offers the possibility to study not only the steady-state acoustic field, but also its evolution in time. One can take into account the dissipative properties of the medium and the difference between one of the resonant frequencies and the fundamental frequency of the driving motion of the wall. An exact non-steady-state solution is derived corresponding to the sawtooth-like periodic vibration of the boundary. The maximal "amplitude" values of the particle velocity and the energy of a standing wave are calculated. The temporal profiles of standing waves at different points of the layer are presented. A new possibility of pumping a high acoustic energy into a resonator is indicated for the case of a special type of the wall motion having the form of an "inverse saw." Theoretically, such a vibration leads to an "explosive instability" and an unlimited growth of the standing wave. For a harmonic excitation, the exact non-steady-state solution is derived as well. The standing wave profiles are described by Mathieu functions, and the energy characteristics by their eigenvalues. *© 2001 MAIK "Nauka/Interperiodica".*

INTRODUCTION

Standing waves are of great interest for nonlinear science and its applications [1, 2]. Theoretical and experimental studies have been made during the last few decades (see, for example, [3–6]). Scientific interest is stimulated by the possibility to accumulate considerable energy in a high-Q resonant system and to form conditions for the observation of well-defined nonlinear phenomena even with a weak driving source. In such a system, the linear losses are weak and the nonlinear absorption plays the role of a limiting factor.

The Q-factor shows how many times the amplitude of the stationary wave is higher than the amplitude of vibration of the boundary. Because of nonlinear absorption, the Q-factor of a given resonator depends on this amplitude. As a stationary regime is approached, the amplitude of a standing wave increases and nonlinear effects become more and more important. The wave profiles, the Q-factor, and all other characteristics of the wave field now depend on time.

However, the non-steady-state nonlinear vibrations in cavities have been studied much less than the stationary ones. The main objective of this work is to develop an analysis of the transient processes in a one-dimensional layer and to derive the corresponding analytical results.

SIMPLIFIED EVOLUTION EQUATION

It is evident that in a linear one-dimensional system, a standing wave can be composed of two plane waves propagating in opposite directions. This idea has been generalized for a nonlinear standing wave between rigid immovable walls [7] where the vibration in the layer is described as the sum of two Riemann or Burgers travelling waves. These waves can be distorted significantly by a nonlinear self-action, which results in the formation of a sawtooth-like profile in place of the initial harmonic one with no contribution made by the cross-interaction of the initial harmonic waves. In other words, each wave is distorted by itself during the propagation, but no energy exchange occurs between them. A similar approach has been used [8] to describe the nonlinear field between two parallel rigid planes; in this case, the nonlinear Brillouin modes are formed by two strongly distorted waves intersecting at equal angles the axis of a waveguide. Despite the existing works, this idea is not well proven and needs to be considered in more detail.

The explanation given below is valid when any nonlinear equation describing nondispersive waves in a quadratic nonlinear medium is used. Here, to be specific, a model one-dimensional equation is analysed [9]:

$$\frac{\partial^2 p}{\partial x^2} - \frac{1}{c^2}\frac{\partial^2 p}{\partial t^2} = -\frac{\varepsilon}{c^4\rho}\frac{\partial^2 p^2}{\partial t^2}. \tag{1}$$

---

[1] This article was submitted by the authors in English.

Here, p is the acoustic pressure, c and ρ are the sound velocity and the density of the medium, and ε is the nonlinearity. Equation (1) can govern the Riemann waves propagating in opposite directions, as well as the interaction between them. The solution is sought for by a successive approximation method:

$$p = p^{(1)} + p^{(2)} + \dots . \tag{2}$$

Let the first-approximation solution be a sum of two waves:

$$\begin{aligned} p^{(1)} &= B_1 \cos(\omega_1 t - k_1 x + \varphi_1) \\ &+ B_2 \cos(\omega_2 t + k_2 x + \varphi_2), \quad k_{1,2} = \omega_{1,2}/c. \end{aligned} \tag{3}$$

The second approximation is derived from the inhomogeneous linear equation

$$\begin{aligned} &\frac{\partial^2 p^{(2)}}{\partial x^2} - \frac{1}{c^2}\frac{\partial^2 p^{(2)}}{\partial t^2} \\ &= F(2\omega_1) + F(2\omega_2) + F(\omega_1 + \omega_2) + F(\omega_1 - \omega_2), \end{aligned} \tag{4}$$

the right-hand side of which is calculated on the base of the first-approximation solution (3)

$$\begin{aligned} F(2\omega_{1,2}) &= \frac{2\varepsilon}{c^4\rho}\omega_{1,2}^2 B_{1,2}^2 \\ &\times \cos[2(\omega_{1,2} t \mp k_{1,2} x + \varphi_{1,2})], \\ F(\omega_1 \pm \omega_2) &= \frac{\varepsilon}{c^4\rho}(\omega_1 \pm \omega_2)^2 B_1 B_2 \\ &\times \cos[(\omega_1 \pm \omega_2)t - (k_1 \mp k_2)x + (\varphi_1 \pm \varphi_2)]. \end{aligned} \tag{5}$$

In the context of the approximate method (2), the four terms on the right-hand side of Eq. (4) can be considered as “external forces” exciting the second-approximation forced waves at the frequencies of second harmonics $2\omega_1$ and $2\omega_2$, as well as at the sum $(\omega_1 + \omega_2)$ and difference $(\omega_1 - \omega_2)$ frequencies.

It is important that the excitation of secondary waves can have a resonant character or a nonresonant one. The first two “forces” given by Eq. (5), $F(2\omega_1)$ and $F(2\omega_2)$, lead to the resonant excitation. The corresponding forced waves

$$\begin{aligned} &p_{1,2}^{(2)} \\ &= -\frac{\varepsilon}{2c^2\rho}B_{1,2}^2(\omega_{1,2}t)\sin[2(\omega_{1,2}t \mp k_{1,2}x + \varphi_{1,2})] \end{aligned} \tag{6}$$

increase in time. The amplitudes grow linearly with time t like the amplitude of forced vibration of a pendulum at the coincidence of the eigen- and driving frequencies.

In contrast to systems with one degree of freedom, the resonance in spatially distributed systems occurs at the coincidence of the velocities of motion of both driving force and exciting wave [9].

Unlike solution (6) that increases in amplitude with t, the partial solution of Eq. (4) corresponding to other two forced waves excited by the forces $F(\omega_1 \pm \omega_2)$ from Eqs. (5)

$$\begin{aligned} p_{3,4}^{(2)} &= \frac{\varepsilon}{c^4\rho}\frac{(\omega_1 \pm \omega_2)^2}{4k_1k_2}B_1B_2 \\ &\times \cos[(\omega_1 \pm \omega_2)t - (k_1 \mp k_2)x + (\varphi_1 \pm \varphi_2)], \end{aligned} \tag{7}$$

have amplitudes independent of t.

The comparison between the resonant (6) and nonresonant (7) solutions shows that after several periods of vibration, $(\omega_{1,2}t) \gg 1$, the waves described by Eq. (7) become much weaker than the resonant waves (6) and cannot participate significantly in the nonlinear energy exchange. Consequently, each of the two waves propagating in opposite directions generates its higher harmonics (6), but the cross-interaction processes (7) can be neglected if the waves are periodic in time. This conclusion is easily seen to be valid for periodic waves intersecting at any sufficiently large angles depending on the acoustic Mach number [8].

Let us now start with the derivation of the simplified evolution equation by taking into account, as the first step, the nonlinear processes only. We consider a plane layer. Its left boundary can vibrate according to the law

$$u(x = 0, t) = Af(\omega t), \tag{8}$$

where A is a characteristic amplitude, u is velocity, and f is a periodic function of its argument with the period 2π. The right boundary is immovable:

$$u(x = L, t) = 0. \tag{9}$$

In order to apply the boundary conditions (8) and (9) to the wave equation (1), we write this equation as a Riemann one for the velocity. This can be done at the same time for right- and leftgoing waves by using in Eq. (1) the relation $p = \pm\rho c u$, where the plus sign is taken for the rightgoing and the minus sign for the leftgoing waves, and making the rescaling $x \longrightarrow \mu x$, where μ is a small parameter. Neglecting the terms $O(\mu^2)$, after the restitution $\mu x \longrightarrow x$, we obtain the nonlinear equation [10] for Riemann waves

$$\frac{\partial u}{\partial x} \pm \frac{1}{c}\frac{\partial u}{\partial t} - \frac{\varepsilon}{c^2}u\frac{\partial u}{\partial t} = 0. \tag{10}$$

The upper (lower) sign in Eq. (10) corresponds to the wave propagating in the positive (negative) direction of the x axis. The solution to Eq. (10) exists in the implicit form. The sum of two solutions can be written as

$$\begin{aligned} u &= F\left[\omega t - \frac{\omega}{c}(x - L) + \frac{\varepsilon}{c^2}\omega(x - L)F\right] \\ &- F\left[\omega t + \frac{\omega}{c}(x - L) - \frac{\varepsilon}{c^2}\omega(x - L)F\right], \end{aligned} \tag{11}$$

where F is an auxiliary function describing the profile of a nonlinear traveling wave. One can see, that solution (11) satisfies the boundary condition (9). Condition (8) applied to Eq. (11) gives the functional equation

$$\begin{aligned} Af(\omega t) &= F\left[\omega t + kL - \frac{\varepsilon}{c}kLF\right] \\ &\quad - F\left[\omega t - kL + \frac{\varepsilon}{c}kLF\right]. \end{aligned} \tag{12}$$

Here, the function $f(\omega t)$ is known, and the function $F(\omega t)$ must be calculated.

The functional equations of implicit form are complicated and cannot be solved analytically. In the simplest case, if we set the nonlinearity $\varepsilon = 0$ and the function $f = \sin(\omega t)$ in Eq. (12), the functional equation

$$F[\omega t + kL] - F[\omega t - kL] = A\sin(\omega t) \tag{13}$$

can be solved easily. Its solution

$$\begin{aligned} F &= -\frac{A\cos(\omega t)}{2\sin(kL)} \\ &\quad + \sum_{n=0}^{\infty}[A_n\cos(n\omega_0 t) + B_n\sin(n\omega_0 t)] \end{aligned} \tag{14}$$

consists of the partial solution of the inhomogeneous equation (13) and the general solution of the corresponding homogeneous equation.

Here,

$$\omega_0 = \pi\frac{c}{L},$$

where

$$L = \frac{\lambda_0}{2}$$

is the fundamental resonance frequency. If the driving frequency approaches a resonance one, $\omega \longrightarrow n\omega_0$, the non-steady-state process comes into play. To show this, let us set in solution (14):

$$A_m = \frac{A}{2\sin(kL)}, \quad B_n = 0, \quad A_n = 0 \quad (n \neq m). \tag{15}$$

Solution (14) with Eq. (15) has an uncertainty of the $\left(\frac{0}{0}\right)$-type. Solving this uncertainty, we obtain

$$\begin{aligned} F &= \frac{A}{2}\lim_{\omega \to n\omega_0}\frac{\cos(n\omega_0 t) - \cos(\omega t)}{\sin\left(\frac{\omega L}{c}\right)} \\ &= \frac{A}{2\pi}(-1)^n(\omega_0 t)\sin(n\omega_0 t). \end{aligned} \tag{16}$$

Solution (16) describes the resonant vibration with an increasing amplitude. This simple example illustrates a surprising, at first sight, fact that the functional equations like Eqs. (12) and (13) can describe not only the steady-state vibration, but also different transient processes.

Let us now pass to the nonlinear functional equation (12). It can be reduced to the simplified evolution equation, if the length of the resonator is small in comparison with the nonlinear length, and the frequency of vibration of the left boundary differs weakly from the resonant frequency

$$\begin{aligned} L \ll \frac{c^2}{\varepsilon\omega F_{\max}}, &\quad kL = \pi + \Delta, \\ \Delta = \pi\frac{\omega - \omega_0}{\omega_0} &\ll 1. \end{aligned} \tag{17}$$

Here, $F_{\max}$ is the maximal value of the function F, and Δ is a discrepancy. The second condition (17) corresponds to the fundamental resonance ($n = 1$), for definiteness. With such restrictions, the right-hand side of Eq. (12) can be expanded in a series:

$$\begin{aligned} F &= \left[\omega t + \pi + \Delta - \pi\frac{\varepsilon}{c}F\right] - F\left[\omega t - \pi - \Delta + \pi\frac{\varepsilon}{c}F\right] \\ &\approx [F(\omega t + \pi) - F(\omega t - \pi)] \\ &\quad + \left(\Delta - \pi\frac{\varepsilon}{c}F\right)[F'(\omega t + \pi) + F'(\omega t - \pi)]. \end{aligned}$$

It is evident that F is a quasi-periodic function whose parameters slowly vary in time. Therefore,

$$F(\omega t + \pi) - F(\omega t - \pi) \approx 2\pi\mu\frac{\partial F}{\partial(\mu\omega t)},$$

where $\mu \ll 1$ is a small parameter the physical meaning of which will be clear later. Equation (12) will have the form

$$\frac{A}{2}f(\omega t) = \mu\frac{\partial F}{\partial\left(\frac{\mu}{\pi}\omega t\right)} + \left(\Delta - \pi\frac{\varepsilon}{c}F\right)\frac{\partial F(\omega t + \pi)}{\partial(\omega t)}. \tag{18}$$

Introducing new dimensionless variables and constants

$$\xi = \omega t + \pi, \quad U = \frac{F}{c}, \quad M = \frac{A}{c}, \quad T = \frac{\omega t}{\pi},$$

one can rewrite Eq. (18) as

$$\frac{\partial U}{\partial T} + \Delta\frac{\partial U}{\partial \xi} - \pi\varepsilon U\frac{\partial U}{\partial \xi} = \frac{M}{2}f(\xi - \pi). \tag{19}$$

It is now evident that the small parameter μ can play the role of any small number: Δ, M, or $U \sim M$.

In recent works [11, 12], an equation similar to Eq. (19) was derived with allowance made for the dis-

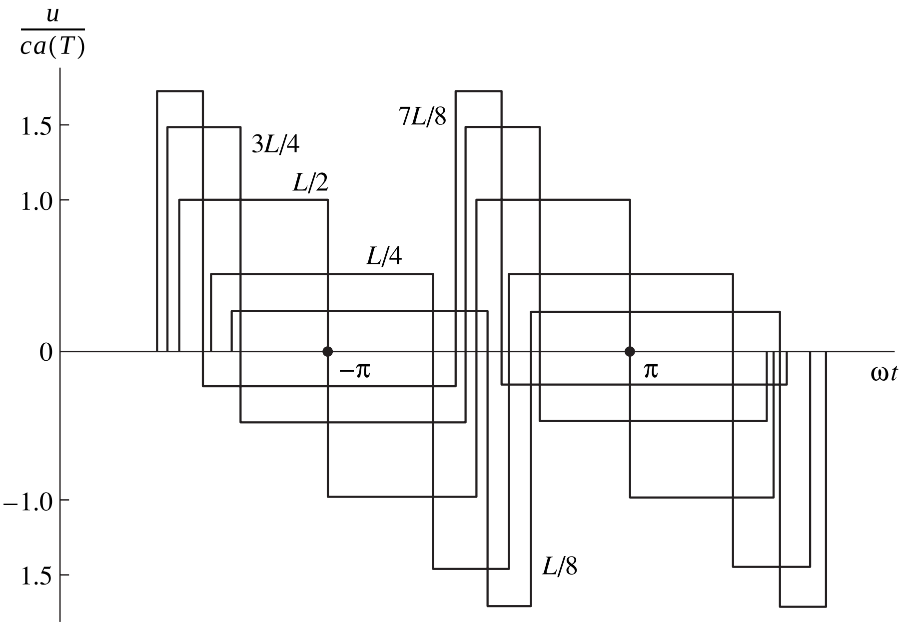

Fig. 1.

sipation and the finite displacement of the vibrating boundary:

$$\frac{\partial U}{\partial T} - D\frac{\partial^2 U}{\partial \xi^2} - M\varphi(\xi)\frac{\partial U}{\partial \xi} + \Delta\frac{\partial U}{\partial \xi} = \frac{M}{2}\varphi'(\xi), \quad (20)$$

where $\varphi'(\xi)$ is a periodic function and

$$D = \frac{b\omega^2}{2c^3\rho}L \ll 1$$

is the dimensionless number determining the weak absorption of a wave passing through the length L of the resonator. However, the volume nonlinearity was not considered in [11, 12].

The main objective of this study is the simultaneous consideration of the weak effects of dissipation and nonlinearity. Because all the phenomena leading to a progressive distortion of the wave are supposed to be weak, the corresponding terms in the evolution equation must be additive [9, 10]. So, combining Eqs. (19) and (20), we obtain:

$$\frac{\partial U}{\partial T} + \Delta\frac{\partial U}{\partial \xi} - \pi\varepsilon U\frac{\partial U}{\partial \xi} - D\frac{\partial^2 U}{\partial \xi^2} = \frac{M}{2}f(\xi - \pi). \quad (21)$$

Equation (21) was named the "inhomogeneous Burgers equation with a discrepancy" [13]. Its main properties were studied in [13–15].

NON-STEADY-STATE SOLUTION FOR A SAWTOOTH-LIKE MOTION OF THE BOUNDARY

Equation (21) can be solved exactly for the most interesting resonant case ($\Delta = 0$) for some special types of vibration of the boundary. These exact solutions can help in understanding the general physical properties of forced nonlinear vibrations of resonators; moreover, the corresponding motion of its wall can be realized in experiments.

Let the boundary execute a sawtooth-like periodic motion:

$$f(\omega t) = \left(1 - \frac{\omega t}{\pi}\right)\operatorname{sgn}(\omega t), \quad -\pi \le \omega t \le \pi. \quad (22)$$

Seeking for the solution to Eq. (21) in the form

$$U = -a(T)\frac{\xi}{\pi}, \quad f = -\frac{\xi}{\pi}, \quad -\pi \le \xi \le \pi, \quad (23)$$

giving $\partial^2 U/\partial\xi^2 = 0$, we obtain the ordinary differential equation

$$\frac{\partial a}{\partial T} + \varepsilon a^2 = \frac{M}{2}. \quad (24)$$

Its solution

$$a = \sqrt{\frac{M}{2\varepsilon}}\tanh\left(\sqrt{\frac{\varepsilon M}{2}}T\right) \quad (25)$$

describes the increase with the time T in the amplitude of the auxiliary function U (Eq. (23)) up to the limiting value $(M/2\varepsilon)^{1/2}$.

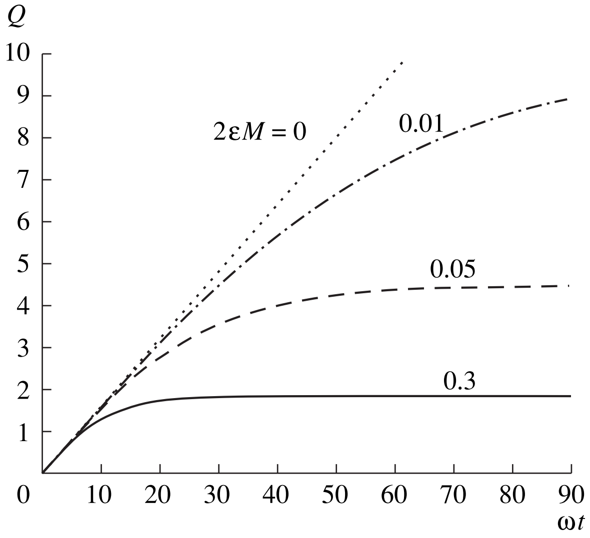

Fig. 2.

The form of the standing wave in the layer is determined by solution (11), where one can neglect small nonlinear terms, if the vibration within a time of order of one period is considered. Taking into account the periodicity of F, we write Eq. (11) as

$$u = cU(\omega t - kx) - cU(\omega t + kx). \tag{26}$$

The temporal profiles of the standing wave given by Eqs. (23), (25), and (26) are shown in Fig. 1 for different cross-sections of the resonator: $x = L/8$, $L/4$, $L/2$, $3L/4$, and $7L/8$. The form of forced nonlinear vibration of the particle velocity varies at the transition from one cross-section to another. In the middle of the layer, each period consists of alternating positive and negative rectangular regions, which have equal durations and "amplitudes".

At approaching the end $x = L$, the positive region becomes narrow, but its height increases up to the magnitude twice exceeding the magnitude in the middle point $x = L/2$. The negative region decreases in magnitude, but expands in duration. The complete area (the integral of u over the period) is equal to zero.

At approaching the other end, $x = 0$, the narrowing and growth of the negative region take place. At both ends, $x = 0$ and L, the motion disappears and $u = 0$ in accordance with the boundary conditions (8) and (9). For the driving wall, this satisfaction of condition (8) should not be taken literally; it means that the amplitude of wall vibration is small in comparison with the characteristic magnitude of u in the layer.

The mean volume density of acoustic energy

$$\rho\overline{u^2} = \frac{\rho}{2\pi}\int_0^{2\pi} u^2 d(\omega\tau) = \rho c^2 \times 8kx\left(1 - \frac{kx}{\pi}\right)a^2(T) \tag{27}$$

has a maximum at the center of the layer, $kx = \pi/2$, and equals zero at both ends. The whole energy in the volume V of the resonator, when calculated by integration of Eq. (27) over x, equals

$$E = \frac{1}{3}\rho c^2 V\frac{M}{\varepsilon}\tanh^2\left(\sqrt{\frac{\varepsilon M}{2}}\frac{\omega t}{\pi}\right). \tag{28}$$

The ratio of "amplitudes" of the standing wave and the vibration of the boundary

$$Q = \frac{a(T)}{M} = \frac{1}{\sqrt{2\varepsilon M}}\tanh\left(\sqrt{2\varepsilon M}\frac{\omega t}{2\pi}\right)$$

is shown in Fig. 2 for different values of $2\varepsilon M$. At steady-state regime,

$$Q = \left(2\varepsilon\frac{A}{c}\right)^{-1/2}. \tag{29}$$

If nonlinear effects were negligible, the Q-factor would not depend on the amplitude A of excitation and would be equal to [12]

$$Q = \frac{1}{2D} = \frac{c^3\rho}{b\omega^2 L} = \frac{c^2\rho}{\pi b\omega}.$$

The linear Q-factor is determined by quite different physical quantities than the nonlinear one (Eq. (29)). In particular, it depends on the effective viscosity b and on the frequency ω.

For the amplitude $A = 10$ cm/s, the nonlinear evaluation is $Q \approx 37$. On the other hand, at typical frequencies about 4 kHz in the air-filled resonator, the linear Q-factor is much higher: it is on the order of 10^3–10^4. However, at high values of the linear Q-factor, the amplitude of the standing wave increases with time, and nonlinear absorption comes into play necessarily, leading to a considerable decrease in the Q-factor.

It must be noted here that some techniques are invented to suppress the nonlinear absorption [1, 2], but this paper is devoted to the common simplest resonators and more complicated systems are not considered here.

The excitation of the layer by a sawtooth-like motion (Eq. (22)) discussed above is similar to that at the harmonic excitation (see below). There exists, however, another form of sawtooth-like vibration providing a radically new regime of amplification of a standing wave. Let us consider the so-called "inverse saw" motion of the driving wall,

$$U = a(T)\frac{\xi}{\pi}, \quad f = \frac{\xi}{\pi}, \quad -\pi \le \xi \le \pi,$$

instead of the "common saw", Eq. (23). The ordinary equation for the amplitude $a(T)$

$$\frac{\partial a}{\partial T} - \varepsilon a^2 = \frac{M}{2}$$

differs from Eq. (24) only by a sign, but it describes a radically different phenomenon:

$$a = \sqrt{\frac{M}{2\varepsilon}}\tan\left(\sqrt{\frac{\varepsilon M}{2}}T\right). \qquad (30)$$

One can see that amplitude (30) increases indefinitely at

$$\omega t \longrightarrow \frac{\pi^2}{\sqrt{2\varepsilon M}}.$$

Such an "explosive instability" in the solution to the inhomogeneous equation (21) was discussed in [15]. This phenomenon can be explained as follows: the energy transmitted from the source to the smooth sections of the profile of the travelling wave U does not have enough time to reach the leading shock front and to be dissipated at it. Therefore, the unlimited growth of amplitude (30) goes on, and only some other nonlinear phenomena (for example, the nonlinearity of the moving boundaries [2]) can be a possible mechanism of limitation. This regime must be investigated in more detail. Anyway, it seems promising for the pumping of high acoustic energy to a limited volume of the medium.

STANDING WAVE EXCITED BY HARMONIC VIBRATION

For the harmonic vibration of the wall, the right-hand side of Eq. (21) takes the form $-(M/2)\sin\xi$. For this case and some other cases, the linearization can help in solving the inhomogeneous Burgers equation (21). Using the transformation

$$U = \frac{2D}{\pi\varepsilon}\frac{\partial}{\partial\xi}\ln W \qquad (31)$$

one can reduce the nonlinear equation (21) to a linear one:

$$\frac{\partial W}{\partial T} + \Delta\frac{\partial W}{\partial\xi} - D\frac{\partial^2 W}{\partial\xi^2} = \frac{1}{2}qD\cos\xi W, \quad q = \frac{\pi\varepsilon M}{2D^2}. \quad (32)$$

By the substitution

$$W = \exp\left(-\frac{1}{4}\lambda DT\right)y\left(z = \frac{\xi}{2}\right),$$

where λ is a constant, we derive an ordinary differential equation for the function $y(z)$:

$$\frac{\partial^2 y}{\partial z^2} - 2\frac{\Delta}{D}\frac{\partial y}{\partial z} + (\lambda + 2q\cos 2z)y = 0. \qquad (33)$$

At zero discrepancy, $\Delta = 0$, Eq. (33) transforms to the canonical form of the differential equation for Mathieu's function. This is exactly the resonant case which must be studied in detail.

For zero initial condition $U(T = 0, \xi) = 0$, the solution to Eq. (32) can be written as a series of even Mathieu's functions [15]:

$$W = \sum_{n=0}^{\infty} a_{2n}\exp\left[-\frac{1}{4}\lambda_{2n}(q)DT\right]ce_{2n}\left(\frac{\xi}{2}, q\right), \qquad (34)$$

where

$$a_{2n} = \left[\int_0^{2\pi} ce_0\left(\frac{\xi}{2}, q\right)d\xi\right] \Bigg/ \left[\int_0^{2\pi} ce_{2n}^2\left(\frac{\xi}{2}, q\right)d\xi\right].$$

The notations used here correspond to those from the book by Strutt [16] (see also [17]).

From Eqs. (31) and (34), the excitation of the travelling wave [15] $U(T, \xi)$ is found, and U is here an auxiliary function for the construction of the standing wave profile during its approaching the steady-state condition. The stationary solution is the limit of Eq. (34) at $T \longrightarrow \infty$ [14]:

$$U = \frac{2D}{\pi\varepsilon}\frac{d}{d\xi}\ln ce_0\left(\frac{\xi}{2}, \frac{\pi\varepsilon M}{2D^2}\right). \qquad (35)$$

At $q \gg 1$, solution (35) takes the form [15]

$$U = \sqrt{\frac{2M}{\pi\varepsilon}}\left[\cos\frac{\xi}{2} - \frac{3\exp(-2\sqrt{q}\xi)}{1 + 2\exp(-2\sqrt{q}\xi)}\right], \quad 0 \le \xi \le \pi,$$

and at $q \longrightarrow \infty$, it does not depend on the linear absorption (i.e., on q) at all:

$$U = \sqrt{\frac{2M}{\pi\varepsilon}}\cos\frac{\xi}{2}\operatorname{sgn}\xi, \quad -\pi \le \xi \le \pi. \qquad (36)$$

In Figs. 3a and 3b, the development of the periodic temporal profiles of the standing wave is shown for the harmonic vibration of the left-hand wall of the resonator, in the middle cross-section ($x = L/2$, Fig. 3a) and near the right-hand end ($x = 7L/8$, Fig. 3b). The profiles are constructed after the calculation of series (34), with allowance for transformations (26) and (31), at the transient moments of slowly varying time: $DT = 0.15$, 0.3, 0.5, and 0.9. For the parameter q (Eq. (32)), the value $q = 20$ was taken.

The curves in Fig. 3, in contrast to the ones in Fig. 1, are smoother, because the formation of the shock front in the travelling wave U at given moments DT is in process. Even at $DT \longrightarrow \infty$, the shock front for $q = 20$ will have a finite width.

At $DT \longrightarrow \infty$, the standing wave reaches its stationary condition. The steady-state profiles are smoothed at finite magnitudes of the parameter q, but discontinuities appear at $q \longrightarrow \infty$.

The steady-state profiles are shown in Fig. 4 for an extremely high harmonic excitation corresponding formally to $q \longrightarrow \infty$. The sum (26) of two travelling waves

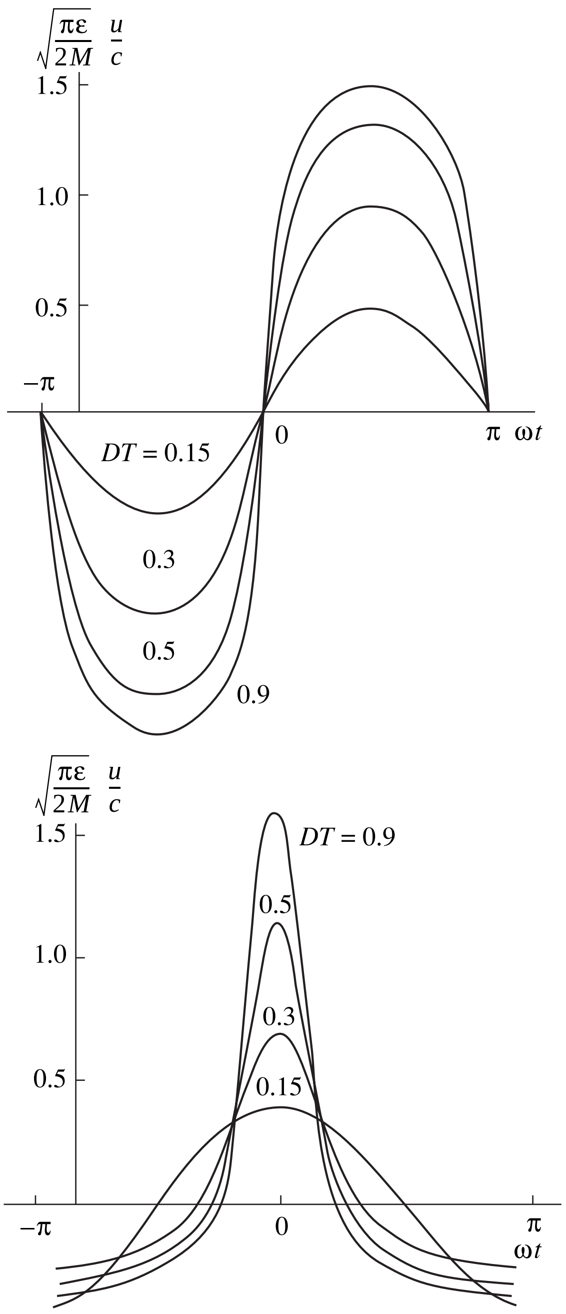

Fig. 3.

described by Eq. (36) is used. The standing wave in Fig. 4 has the shape similar to that in Fig. 1 for sawtooth-like excitation. Only the tops of the positive and negative pulses here are not flat; their form of an arc is described by trigonometric functions. In Fig. 1, the maximal peak of u/c tends (at $T \longrightarrow \infty$) to $\sqrt{2M/\varepsilon}$, and in Fig. 4 it equals to $2\sqrt{2M/\pi\varepsilon}$.

The calculation of the acoustic energy accumulated in the resonator is more complicated here than for sawtooth-like excitation (see above). The steady-state solution (35) is described by the ordinary differential equation

$$D\frac{d^2U}{d\xi^2} + \pi\varepsilon U\frac{dU}{d\xi} = \frac{M}{2}\sin\xi, \qquad (37)$$

which follows from Eq. (21) at $T \longrightarrow \infty$, $\Delta = 0$ and $f(\xi) = -\sin\xi$. Integrating Eq. (37), we obtain

$$D\frac{dU}{d\xi} + \frac{\pi\varepsilon}{2}(U^2 - C) = -\frac{M}{2}\cos\xi. \qquad (38)$$

Since the mean value is $\overline{U} = 0$, it follows from Eq. (38) that the constant C is equal to

$$C = \overline{U^2} = \frac{1}{2\pi}\int_0^{2\pi} U^2(\xi)d\xi.$$

Thus, the constant C is proportional to the density of acoustic energy. Using transformation (31), we reduce the nonlinear equation (38) to a linear one for Mathieu functions:

$$\frac{d^2W}{dz^2} + \left[-\left(\frac{\pi\varepsilon}{D}\right)^2 C + \frac{\pi\varepsilon M}{D^2}\cos 2z\right] = 0, \qquad (39)$$

where $z = \xi/2$. Comparing Eqs. (39) and (33), we conclude that the energy is proportional to the eigenvalue λ_0 of the Mathieu function ce_0 [14]:

$$\overline{U^2} = -\left(\frac{D}{\pi\varepsilon}\right)^2 \lambda_0\left(q = \frac{\pi\varepsilon M}{2D^2}\right).$$

The total energy of the resonator, in accordance with formulas (26) and (27), equals to $E = \rho c^2 V \times 2\overline{U^2}$.

At a weak excitation $\lambda_0 \approx -q^2/2$ [16], a well-known linear result appears:

$$E \approx \left(\frac{M}{2D}\right)^2 \rho c^2 V.$$

Using another asymptotics for the eigenvalue λ_0 at $q \gg 1$ [17], for strong boundary vibration we derive

$$E = \left[\frac{2M}{\pi\varepsilon} - \frac{2D}{(\pi\varepsilon)^2}\sqrt{2\pi\varepsilon M} + \frac{1}{2}\frac{D^2}{(\pi\varepsilon)^2} + \dots\right]\rho c^2 V. \qquad (40)$$

When $q \longrightarrow \infty$, the factor $2/\pi$ in the first leading term in brackets in Eq. (40) differs from the result given by Eq. (28), where at $T \longrightarrow \infty$ the corresponding factor is equal to 1/3.

Thus, the comparison of the results for sawtooth-like and harmonic excitations described above shows their qualitative similarity.

Using solution (34) supplemented by transformations (26) and (31), one can calculate numerically all other characteristics of the standing waves in the layer for both the transient regime and the steady-state one.

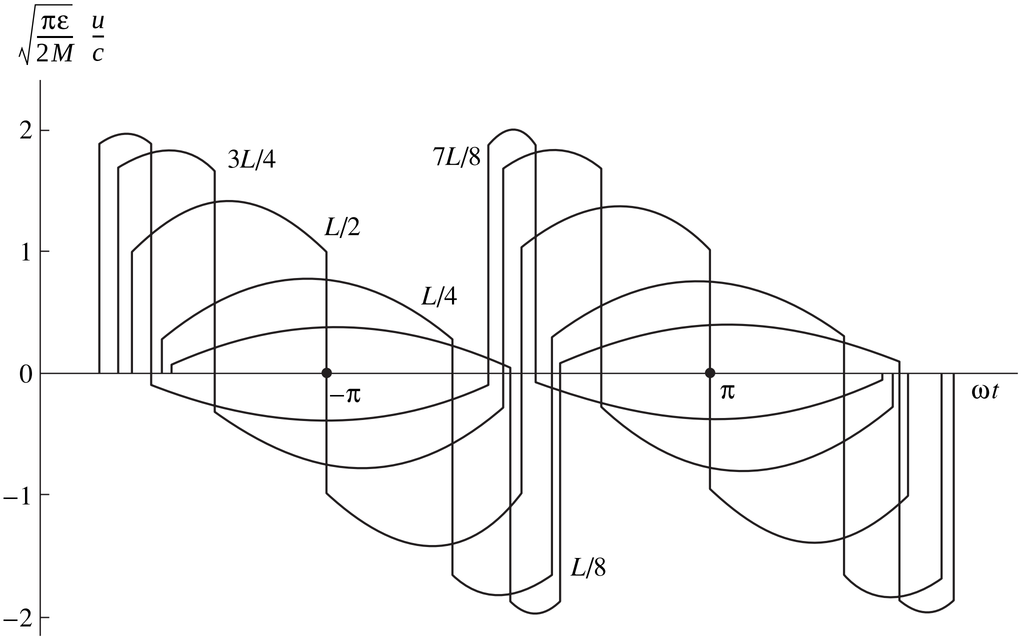

Fig. 4.

The arbitrary relationship between nonlinearity and competitive dissipation processes can be considered. In this paper, however, we have restricted our consideration to the description of the new approach and to the most general analytical results. More particular numerical studies can be performed as a continuation of this work.

CONCLUSIONS

A new analytical approach to the theory of nonsteady-state forced vibration in a layer of a nonlinear dissipative medium is developed on the basis of the simplified evolution equation for the auxiliary function describing two nonlinear waves propagating in opposite directions. This approach is explained and justified for the periodic vibration of a wall. A new equation is derived for standing waves, which is known in the nonlinear wave theory as the “inhomogeneous Burgers equation with a discrepancy”. Three types of the wall motion are considered: (i) the vibration of sawtooth-like form, (ii) the vibration of the form of an “inverse saw”, and (iii) the harmonic vibration. For the “inverse saw” motion, the “explosive instability” is progressing in the resonator, leading to an infinite increase in the standing wave amplitude within a finite time. For the other two regimes, i.e., the sawtooth-like and the harmonic regimes, the transient and steady-state vibrations are studied. The temporal profiles are constructed for different cross-sections of the layer. The nonlinear Q-factor and the total energy in the resonator are calculated. For the harmonic motion, the main characteristics can be expressed through Mathieu functions and their eigenvalues.

ACKNOWLEDGMENT

This work was supported by the Royal Swedish Academy of Sciences, the Russian Foundation for Basic Research, and the INTAS (project no. 97-11134), as well as by a grant under the program “Universities of Russia.”

REFERENCES

1. C. C. Lawrenson, B. Lipkens, T. S. Lucas, *et al.*, J. Acoust. Soc. Am. **104**, 623 (1998).
2. O. V. Rudenko, Akust. Zh. **45**, 397 (1999) [Acoust. Phys. **45**, 351 (1999)].
3. W. Chester, J. Fluid Mech. **18**, 44 (1964).
4. S. Temkin, J. Acoust. Soc. Am. **45**, 224 (1969).
5. A. B. Coppens and A. A. Atchley, in *Encyclopedia of Acoustics* (Wiley, New York, 1997), pp. 237–246.
6. M. A. Ilhamov, R. G. Zaripov, R. G. Galiullin, and V. B. Repin, Appl. Mech. Rev. **49** (3), 137 (1996).
7. V. V. Kaner, O. V. Rudenko, and R. V. Khokhlov, Akust. Zh. **23**, 756 (1977) [Sov. Phys. Acoust. **23**, 432 (1977)].
8. V. V. Kaner and O. V. Rudenko, Vestn. Mosk. Univ., Fiz., Astron., No. 4, 78 (1978).
9. M. B. Vinogradova, O. V. Rudenko, and A. P. Sukhorukov, *The Theory of Waves*, 2nd ed. (Nauka, Moscow, 1990).

10. O. V. Rudenko and S. I. Soluyan, *Theoretical Foundations of Nonlinear Acoustics* (Nauka, Moscow, 1975; Consultants Bureau, New York, 1977).
11. O. V. Rudenko and A. V. Shanin, Abstracts of Papers, *ISNA-15, Goettingen, 1999* (Academic, New York) (to be published).
12. O. V. Rudenko and A. V. Shanin, Akust. Zh. **46**, 392 (2000) [Acoust. Phys. **46**, 334 (2000)].
13. A. A. Karabutov and O. V. Rudenko, Akust. Zh. **25**, 536 (1979) [Sov. Phys. Acoust. **25**, 306 (1980)].
14. O. V. Rudenko, Pis'ma Zh. Éksp. Teor. Fiz. **20**, 445 (1974) [JETP Lett. **20**, 203 (1974)].
15. A. A. Karabutov, E. A. Lapshin, and O. V. Rudenko, Zh. Éksp. Teor. Fiz. **71**, 111 (1976) [Sov. Phys. JETP **44**, 58 (1976)].
16. M. J. O. Strutt, *Lame, Mathieu and Related Functions in Physics and Technology* (Springer, Berlin, 1932; ONTI, Moscow, 1935; Edwards Brothers, New York, 1944).
17. *Handbook of Mathematical Functions*, Ed. by M. Abramowitz and I. A. Stegun (Dover, New York, 1970; Nauka, Moscow, 1979).

Acoustical Physics, Vol. 47, No. 4, 2001, pp. 461–467. Translated from Akusticheskiĭ Zhurnal, Vol. 47, No. 4, 2001, pp. 534–540.
Original Russian Text Copyright © 2001 by Tyutekin.

Simulation and Synthesis of Elastic Wave Absorbers at the Boundary of a Rigid Body: Incidence of Longitudinal Waves

V. V. Tyutekin

Andreev Acoustics Institute, Russian Academy of Sciences,
ul. Shvernika 4, Moscow, 117036 Russia
e-mail: bvp@akin.ru

Received July 26, 2000

Abstract—Results of a computer simulation of an impedance absorber for longitudinal plane elastic waves incident on a free boundary of a rigid body are presented. The absorbing elements are mechanical resonators (of the elasticity–mass type) with two degrees of freedom and, hence, with two resonance frequencies, which correspond to the normal and tangential oscillations of the resonator. Formulas for calculating the absorber efficiency as a function of frequency and angle of incidence of longitudinal waves are derived with allowance for the absorption of both longitudinal and shear waves at their reflection from the absorbing surface. These formulas are used to solve the problem of synthesizing optimal absorbers that are characterized by the maximal average value of the absorption coefficient in preset ranges of frequency and angle of incidence. The possibility of increasing this average value by increasing the loss coefficient of the resonators or by using two types of resonators with different resonance frequencies is studied. The results of the calculations are presented in graphic form. © *2001 MAIK "Nauka/Interperiodica".*

To reduce the levels of reflected waves of different nature, it is common practice to use various absorbing devices specially designed for this purpose and mounted on the surfaces or boundaries of bodies [1–5]. This paper studies the possibility of designing absorbers for plane longitudinal waves incident on a plane free boundary of a rigid body with an arbitrary angle of incidence. This problem is of both theoretical and practical interest. Its solution is important in view of the need for noise and vibration control in thick-walled structures used in construction, as well as the need to develop absorbers for Lamb waves. To our knowledge, such a problem is considered for the first time in this paper.

The problem has a specific feature that complicates its practical solution, namely, the transformation of an incident elastic wave of any polarization into two reflected waves (one longitudinal and one transverse) [6]. The ratio of the amplitudes of the reflected waves strongly depends on the angle of incidence of the initial wave and on Poisson's ratio. The second feature is that regular rigid bodies have large wave impedances for longitudinal and shear waves, i.e., the impedances that can be several ten times as great as the wave impedance of water. These features must be taken into account in selecting the absorbing elements of the absorber. These elements should simultaneously affect the normal and tangential displacements of the surface, and they should have a sufficiently large impedance.

Such elements in the form of mechanical resonators with two oscillation polarizations and, hence, with two resonance frequencies were considered in the previous publications [7, 8]. It was shown that the use of such elements in a wide frequency range and in a wide range of angles of incidence allows one, in particular, to construct special kinds of polarizers for both longitudinal and transverse waves, so that the reflected wave will have the same polarization as the incident wave. The consideration was performed on the assumption that the acoustic loss in the resonators was zero. One can expect that the introduction of a nonzero loss will allow one to use the resonators for the development of absorbers of elastic waves incident on a free boundary of a rigid body. This paper presents a numerical simulation of absorbers for the case of the incidence of longitudinal waves.

The reflection coefficients for an incident longitudinal wave can be calculated by the formulas derived earlier [7]:

$$R_{11} = \frac{D^{-} + Z_{11}^{0} Z_{22}^{0}\cos(\theta_0 + \theta_1) + Z_{11}^{0} b\cos\theta_0 - Z_{22}^{0}\cos\theta_1}{D^{+} + Z_{11}^{0} Z_{22}^{0}\cos(\theta_0 - \theta_1) + Z_{11}^{0} b\cos\theta_0 + Z_{22}^{0}\cos\theta_1}, \tag{1}$$

$$R_{12} = \frac{G + Z_{11}^{0} Z_{22}^{0}\sin 2\theta_0}{D^{+} + Z_{11}^{0} Z_{22}^{0}\cos(\theta_0 - \theta_1) + Z_{11}^{0} b\cos\theta_0 + Z_{22}^{0}\cos\theta_1}, \tag{2}$$

1063-7710/01/4704-0461$21.00 © 2001 MAIK "Nauka/Interperiodica"

where $D^{\pm} = b\sin^4\theta_0[4\cot\theta_0\ \cot\theta_1 \pm (1-\cot\theta_1)^2]$; $G = 4b\cos\theta_0\sin^3\theta_1(1-\cot^2\theta_1)$; and $b = \frac{c_t}{c_l} = \sqrt{\frac{1-2\nu}{2(1-\nu)}}$ (c_t and c_l are the velocities of transverse and longitudinal waves, respectively, and ν is Poisson's ratio. In Eqs. (1) and (2), R_{11} and R_{12} are the reflection coefficients for the longitudinal and transverse waves; θ_0 is the angle of incidence of the longitudinal wave; θ_1 is the angle of reflection of the transverse wave, which is determined as usual from the relation $k_t\sin\theta_1 = k_l\sin\theta_0$; and $Z_{11}^0 = Z_n$ and $Z_{22}^0 = Z_t$ are the normal and tangential impedances of the resonators, respectively. These impedances are expressed in units of the longitudinal wave impedance of the elastic medium, and they can be represented in the form [8]

$$Z_n = \frac{iX\bar{\Omega}}{1-\bar{\Omega}^2/a^2}, \quad Z_t = \frac{iX\bar{\Omega}}{1-\bar{\Omega}^2}, \tag{3}$$

where $\bar{\Omega} = \omega/\bar{\omega}_{0t}$ is the dimensionless complex frequency; $\bar{\omega}_{0t} = \omega_{0t}\sqrt{1+i\eta}$ is the complex resonance frequency of the tangential oscillations of the resonator; the quantity ω_{0r} is defined in [7] (see Eq. (20) there); η is the loss coefficient normalized to the elasticity of the resonator; and a^2 is the ratio of the normal and tangential elasticities of the resonator, so that the complex resonance frequency of its normal oscillations $\bar{\omega}_{0n}$ is determined by the relation $\bar{\omega}_{0n} = a^2\bar{\omega}_{0t}$. The quantity $\bar{\Omega}$ can be represented in the form $\bar{\Omega} = \Omega/\sqrt{1+i\eta}$, where $\Omega = \omega/\omega_{0t}$. The quantity $X = \omega_{0r}ms_0/\rho c_1$ is the dimensionless inertial impedance of the resonator per unit area of the body boundary at the tangential resonance frequency of the resonator; here, m is the specific mass of the resonator and s_0 is the relative area occupied by the resonator. In this notation, the dimensionless resonance frequencies are determined by the equalities $\Omega_r = 1$ and $\Omega_n = a$.

To characterize the efficiency of the simulated absorbers, we will use the absorption coefficient α_l for the incident longitudinal wave. This quantity is related to the corresponding energy fluxes $E_l = |R_{11}|^2$ and $E_t = \frac{b\cos\theta_1}{\cos\theta_0}|R_{12}|^2$ [6] by the formula

$$\alpha_l = 1 - (E_l + E_t). \tag{4}$$

From Eqs. (1)–(4), one can see that the efficiency of the absorbers depends on the angle of incidence θ_0 and the frequency Ω of the wave and on the resonator parameters a^2 and η.

As a generalized measure of the efficiency, one can use the quantity α_l averaged over the frequency range and the range of the angles of incidence. This quantity can be represented in the form

$$\bar{\alpha}_1 = (\mathrm{MN})^{-1}\sum_{n=1}^{\mathrm{N}}\sum_{m=1}^{\mathrm{M}}\alpha_1(\Omega_m, \theta_{0n}), \tag{5}$$

where M and N are the numbers of the frequency values and the values of the angles of incidence within the intervals $\Omega_1 < \Omega < \Omega_2$ and $0° < \theta_0 < 90°$, respectively. The frequencies Ω_1 and Ω_2 are the boundaries of the frequency range of interest. In calculating the values of $\bar{\alpha}_1$, we used a linear scale for the values of θ_0 and a logarithmic scale for the values of Ω with M = N = 50.

In synthesizing an absorber for incident longitudinal waves, we used the following parameters of the resonators: $a^2 = 16$; $\eta = 0.1$, 0.3, 0.6, and 0.9; and $\nu = 0.31$. The dimensionless resonance frequencies were $\Omega_t = 1$ and $\Omega_n = 4$. In addition, we used $\Omega_1 = 0.5$, $\Omega_t = 0.5$ and $\Omega_2 = 2$, $\Omega_n = 8$. Thus, the frequency range over which the absorber efficiency was averaged covered four octaves.

Using Eqs. (1)–(5), we solved the problem of synthesizing an absorber on the basis of the optimization of the quantity $\bar{\alpha}_1$ through selecting the value of the parameter $X = X_m$ that provides the maximal value $\bar{\alpha}_1 = \max$. As an example, Fig. 1 presents a three-dimensional frequency-angular dependence of the quantity α_l for $\eta = 0.1$ (in this case, $X_m \cong 0.15$ and $\bar{\alpha}_1 \cong 0.147$). The x axis represents the quantity θ_0 (in degrees), the y axis represents $\log\Omega$, and the z axis represents the quantity α_l. The resonance frequencies correspond to the values $\log\Omega_t = 0$ and $\log\Omega_n \approx 0.6$. Figure 2, which refines the quantitative relations, represents the sections of the function $\alpha_1(\Omega_m, \theta_{0n})$ in the form of the contours of its constant values indicated by the corresponding numbers. The analysis of the two figures shows that the surface $\alpha_1(\Omega_m, \theta_{0n})$ has two maximums, which correspond to the resonance frequencies of the resonators. The corresponding angular dependence of the absorber efficiency exhibits some specific features: near the tangential resonance, it has a maximum at the angles of incidence $\theta_0 \cong 60°$, while near the longitudinal (normal) resonance, at these angles, a relative minimum is observed. The maximal values at these frequencies occur in the cases of the normal incidence ($\theta_0 = 0°$, $\alpha_1 = 0.4$) and the grazing incidence ($\theta_0 \equiv 85°$, $\alpha_1 = 0.7$).

One of the ways to improve the frequency characteristic of the absorber is the broadening of the resonance curves of the resonators for both tangential and normal resonances. This can be achieved by increasing the loss coefficient of the resonators η. The synthesis of absorbers for the values $\eta = 0.3$, 0.6, and 0.9 was performed as described above. The results of solving this problem are generalized in Table 1.

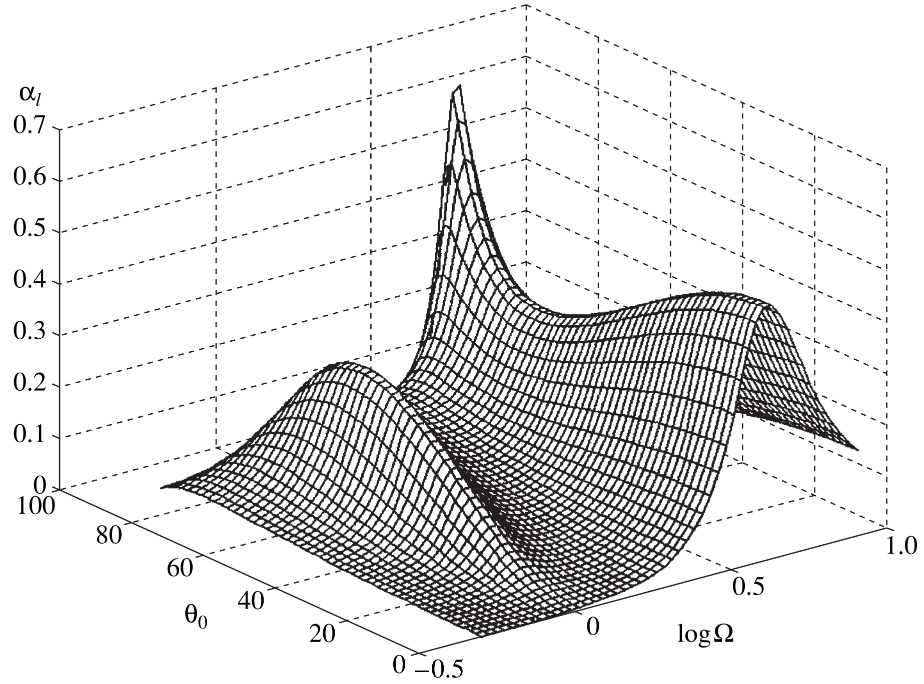

Fig. 1. Efficiency of the optimal absorber for longitudinal waves as a function of frequency and angle of incidence (the loss coefficient of the resonator is $\eta = 0.1$).

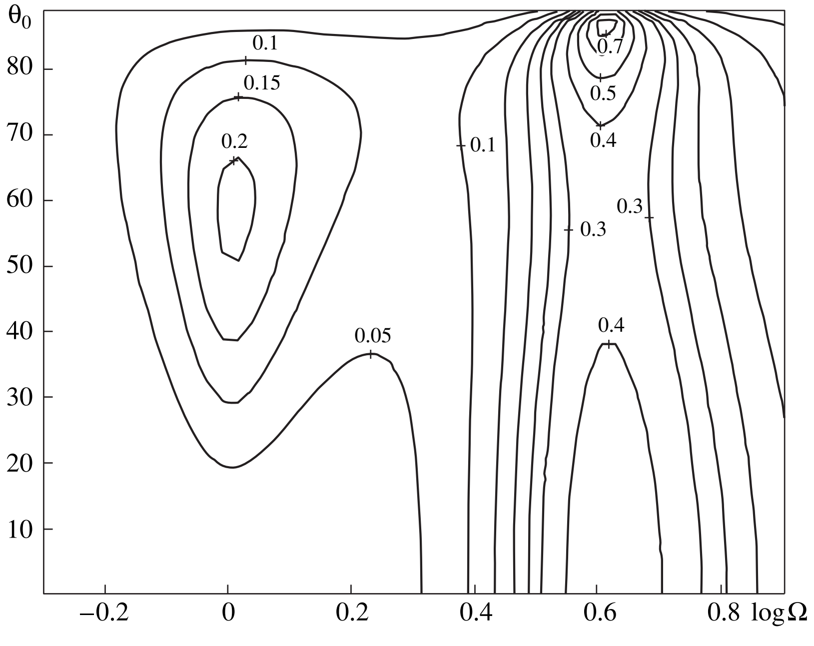

Fig. 2. Constant efficiency lines for the same absorber as in Fig. 1.

From Table 1, one can see that as the loss coefficient increases, the average efficiency of the absorber also increases; however, in this case, it is necessary to increase the optimal value of the inertial impedance of the resonators X_m. It should be noted that when the parameter η increases, the form of the surface $\alpha_1(\Omega_m, \theta_{0n})$ undergoes noticeable changes. This can be seen from Figs. 3 and 4, which are analogous to Figs. 1 and 2, respectively. The main difference consists in the absence of any manifestation of the tangential reso-

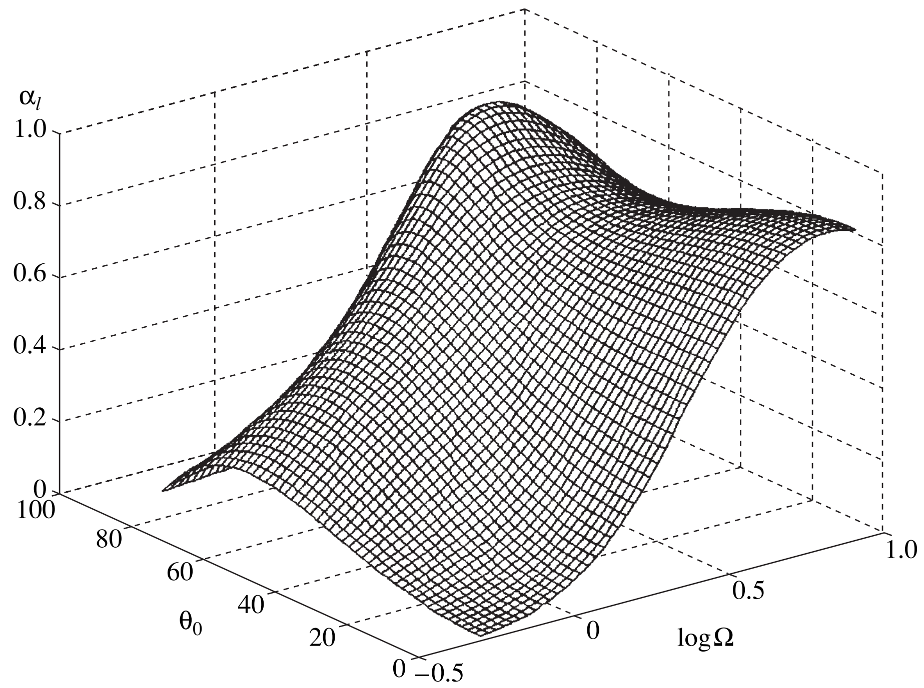

Fig. 3. As in Fig. 1, but for $\eta = 0.9$.

nance at higher η: an increase in frequency is accompanied by an almost steady growth of the efficiency up to the frequencies close to the normal resonance. In this case, the form of the surface with a maximum near $\theta_0 \cong 60°$ is retained; the maximums that occur at the frequencies near the normal resonance are also retained, but their values increase and become close to unity.

We note that when one selects a narrower bandwidth of the absorber efficiency $\Omega_2 - \Omega_1$ and when the frequency band lies near the normal resonance frequency, the average efficiency of the absorber $\bar{\alpha}_1$ can be considerably increased even with relatively small values of η.

One more method of increasing the efficiency of the absorber (especially, when η is small) can be the use of two (or more) types of resonators with different resonance frequencies. For example, to eliminate the dip in the frequency characteristic of the absorber in the middle of the frequency band (Figs. 1, 2) with a simultaneous increase in the entire bandwidth, it is possible to use additional resonators with the normal resonance frequency $\Omega_n = \sqrt{a}$ and, correspondingly, with the tangential resonance frequency $\Omega_t = 1/\sqrt{a}$. Then, the spectrum of the resonance frequencies will be determined by the sequence

$$\Omega_{t1} = 1/\sqrt{a}, \quad \Omega_{t2} = 1, \quad \Omega_{n1} = \sqrt{a}, \quad \Omega_{n2} = a. \tag{6}$$

The subscript 2 refers to the resonators already considered, and the subscript 1 refers to additional resonators.

The formulas for the total impedances of the resonators have the form

$$Z_n = \frac{iX_1\bar{\Omega}}{1-\bar{\Omega}^2/\alpha} + \frac{iX_2\bar{\Omega}}{1-\bar{\Omega}^2/\alpha^2}, \tag{7a}$$

$$Z_r = \frac{iX_1\bar{\Omega}}{1-\alpha\bar{\Omega}^2} + \frac{iX_2\bar{\Omega}}{1-\bar{\Omega}^2}. \tag{7b}$$

Here, the quantities $X_j = \omega_{0t2}m_js_j/\rho c_1$ ($j = 1, 2$) are the inertial impedances of the resonators.

As before, Eqs. (1)–(7) were used to solve the problem of synthesizing the absorber by optimizing the quantity $\bar{\alpha}_1$ through the determination of the parameters $X_j = X_{mj}$, which provide the maximal value $\bar{\alpha}_1 =$

Table 1

η	0.1	0.3	0.6	0.9
X_m	0.1504	0.2290	0.2996	0.4345
$\bar{\alpha}_i$	0.1467	0.3123	0.4393	0.5104

Table 2

η	0.1	0.3	0.6	0.9
X_{m1}	0.2695	0.3566	0.6030	0.6752
X_{m2}	0.1078	0.1458	0.1786	0.2008
$\bar{\alpha}_i$	0.2686	0.4866	0.6030	0.6581

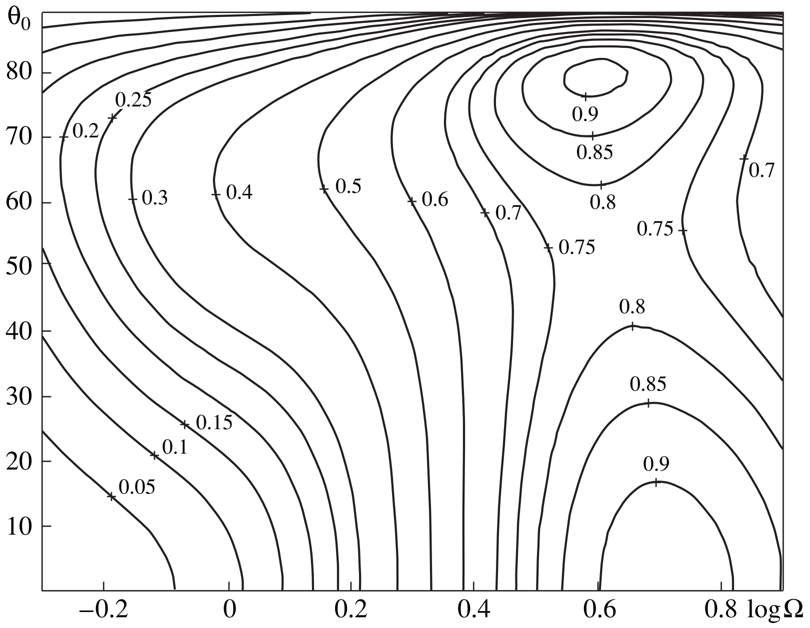

Fig. 4. As in Fig. 2, but for the case of Fig. 3.

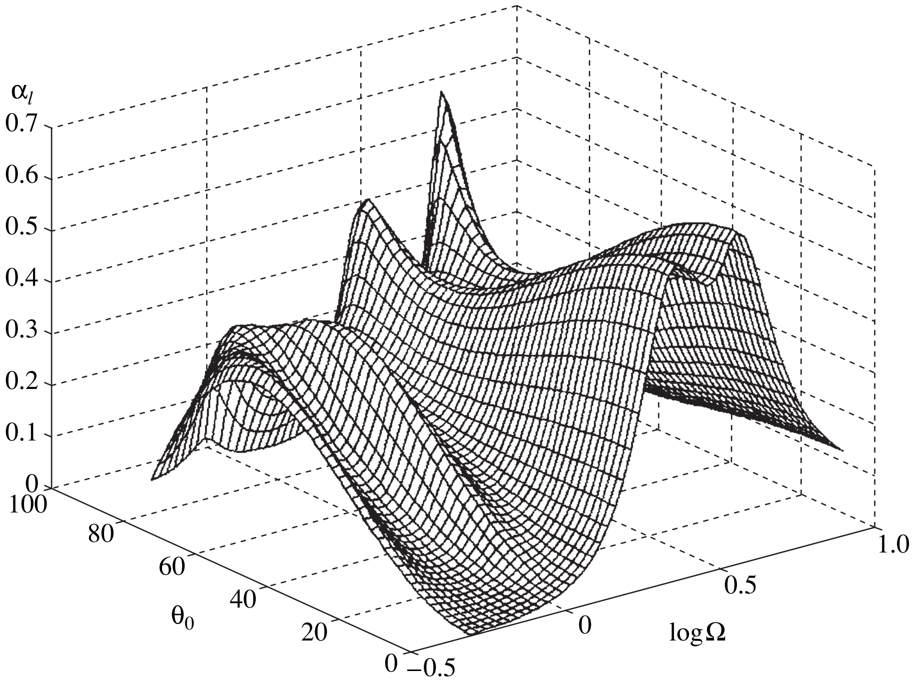

Fig. 5. As in Fig. 1, but with the use of two types of resonators (the loss coefficient of the resonators is $\eta = 0.1$).

max. The results obtained by solving this problem are presented in Table 2, which is analogous to Table 1.

The form of the surface $\alpha_1(\Omega_m, \theta_{0n})$ and its sections are shown in Figs. 5 and 6, respectively, for $\eta = 0.1$. Additionally, we note that $\log\Omega_{t1} \approx 0.3$ and $\log\Omega_{n1} \approx -0.3$. One can see that the latter figures noticeably differ from Figs. 1 and 2: the frequency dependence now has four peaks, although the first two of them (the tangential resonances) almost coincide; the heights of the peaks are approximately 1.5 times greater than in the case with only one type of resonator. The comparison of the data presented in Tables 1 and 2 shows that with two types of resonators, the average value of the effi-

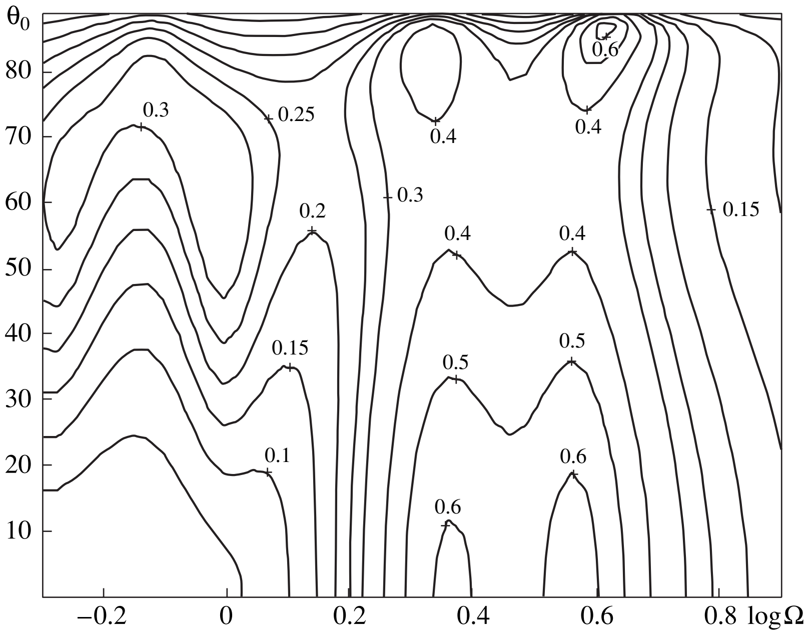

Fig. 6. As in Fig. 2, but for the case of Fig. 5.

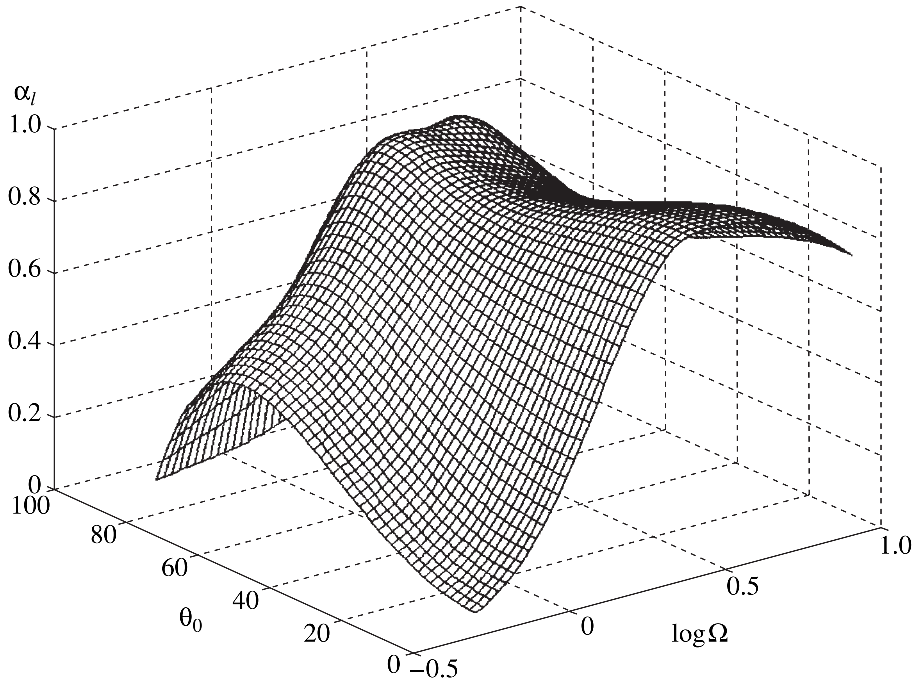

Fig. 7. As in Fig. 5, but for η = 0.9.

ciency has become almost twice as great. For a higher loss coefficient (η = 0.9), the form of the surface changes insignificantly, but the values of $\alpha_1(\Omega_m, \theta_{0n})$ increase, which can be seen from Fig. 7.

In closing, it should be noted that by using the described methods of synthesizing absorbers for longitudinal waves, it is possible to obtain a high efficiency of these absorbers in a preset frequency range and a preset range of the angles of incidence. The narrower these ranges, the higher the efficiency that can be achieved by the proposed methods.

REFERENCES

1. V. V. Tyutekin and A. P. Shkvarnikov, Akust. Zh. **18**, 441 (1972) [Sov. Phys. Acoust. **18**, 369 (1972)].
2. V. I. Kashina, V. V. Tyutekin, and A. P. Shkvarnikov, Akust. Zh. **16**, 257 (1970) [Sov. Phys. Acoust. **16**, 213 (1970)].
3. V. Korotaev and V. V. Tyutekin, Akust. Zh. **46**, 84 (2000) [Acoust. Phys. **46**, 71 (2000)].
4. R. A. Burdisso and J. D. Heilmann, J. Sound Vibr. **214**, 817 (1998).
5. T. M. Chan and S. J. Elliot, Appl. Acoust. **58**, 85 (1999).
6. L. D. Landau and E. M. Lifshits, *Course of Theoretical Physics*, Vol. 7: *Theory of Elasticity* (Nauka, Moscow, 1965; Pergamon, New York, 1986).
7. A. E. Vovk and V. V. Tyutekin, Akust. Zh. **44**, 46 (1998) [Acoust. Phys. **44**, 35 (1998)].
8. V. V. Tyutekin, Akust. Zh. **45**, 110 (1999) [Acoust. Phys. **45**, 98 (1999)].

Translated by E. Golyamina

Acoustical Physics, Vol. 47, No. 4, 2001, pp. 468–475. Translated from Akusticheskiĭ Zhurnal, Vol. 47, No. 4, 2001, pp. 541–549.
Original Russian Text Copyright © 2001 by Filonenko, Khokhlova.

Effect of Acoustic Nonlinearity on Heating of Biological Tissue by High-Intensity Focused Ultrasound

E. A. Filonenko and V. A. Khokhlova
Moscow State University, Vorob'evy gory, Moscow, 119899 Russia
e-mail: vera@acs366b.phys.msu.su

Received June 22, 2000

Abstract—Effect of strong acoustic nonlinearity on the efficiency of heating of a biological tissue by high-intensity focused ultrasound in the modes of operation used in real clinical setups is studied. The spatial distributions of thermal sources and the corresponding temperature increments caused by ultrasonic absorption are analyzed. Numerical algorithms are developed for simulating the nonlinear focusing of ultrasound in the calculations of both the heat sources on the basis of the Khokhlov–Zabolotskaya–Kuznetsov-type equations and the temperature field in a tissue on the basis of an inhomogeneous thermal conduction equation with a relaxation term. It is demonstrated that in the mode of operation typical of acoustic surgery, the nonlinearity improves the locality of heating and leads to an increase in the power of thermal sources in the focus by approximately an order of magnitude. The diffusion phenomena in the tissue lead to a smoothing of the spatial temperature distributions, as compared to the distributions of thermal sources. In the case of one-second exposure in the nonlinear mode of focusing, the maximal temperature in the focus exceeds the values obtained in the approximation of linear wave propagation by a factor of three. *© 2001 MAIK "Nauka/Interperiodica".*

Utilization of high-intensity ultrasound for therapy is a rapidly developing field of modern medical science [1–4]. One of the mechanisms of ultrasonic action on a tissue is its heating due to the absorption of the energy of the ultrasonic waves. The thermal mechanism is used in two modes of operation. The first mode is a hyperthermic one when the tissue is affected by low-intensity ultrasound of about 1–10 W/cm^2 during 30–60 min, which provides the heating of the tissue up to 42–45°C [2]. However, it is difficult to maintain the temperature within the necessary narrow range during the total time of exposure. An alternative is the mode with high-intensity but short-time irradiation. In this mode called acoustic surgery, the irradiation of a tissue is performed over several seconds using an intense focused ultrasonic beam with the intensity in the focus 500–2000 W/cm^2. In this case, localization of the heated region and a rapid increase in temperature up to 60–90°C, which causes the necessary destruction of the tissue, are obtained. For example, the mode of acoustic surgery can be used for therapy of cancerous growths [3, 4].

The effects of acoustic nonlinearity start to play a considerable role in the case of such a high ultrasonic intensity. They lead to the appearance of additional higher harmonics in the initial wave spectrum, the formation of shock fronts in the wave profile, and, correspondingly, the increase in the absorption of the ultrasonic wave energy and in the efficiency of tissue heating [5–8]. Despite the fact that the nonlinear effects in the diagnostic and therapeutic applications of ultrasound have been greatly studied (see the review in [5]), they are rarely taken into account in calculating the irradiation doses and the parameters of ultrasonic setups in real clinical experiments, and they are almost never used for the optimization and increasing the efficiency of heating. The purpose of this work is the investigation of the effects of acoustic nonlinearity in the process of the tissue heating by a high-intensity focused ultrasonic beam in the modes of operation characteristic of real clinical setups [3, 7].

The problem is divided into two parts in order to develop a theoretical model of the heating process. In the first part, the nonlinear propagation of a focused acoustic beam in a tissue is studied and the spatial distribution of thermal sources is calculated. In the second part, the temperature field is calculated for the known distribution of sources. The acoustic field is simulated for the case of a piston piezoelectric radiator with the radius $r_0 = 4.2$ cm, the focal distance $F = 15$ cm, and the frequency $f_0 = 1.7$ MHz (Fig. 1), which is used in the ultrasonic clinical setup at the Institute of Cancer Studies in Sutton [7]. The power of the source is selected in such a way that the field intensity in the focus calculated in the linear approximation is $I_F = 1500$ W/cm^2. It was found experimentally that in the case of the time of ultrasonic irradiation about 1 s, this mode provides the necessary destruction of soft tissues [3]. With the radiator intensity determined in such a way, the calculation of the acoustic field, the thermal sources, and the temperature field is performed both taking and not taking into account the effects of acoustic nonlinearity. The comparison of the simulation results for these two cases provides an opportunity to obtain the quantitative esti-

1063-7710/01/4704-0468$21.00 © 2001 MAIK "Nauka/Interperiodica"

mates of the role of acoustic nonlinearity in the efficiency of thermal action of ultrasound upon a tissue.

ACOUSTIC FIELD

The propagation of an intense focused acoustic wave in a tissue is described in the parabolic approximation by the nonlinear evolution equation of the Khokhlov–Zabolotskaya–Kuznetsov type [8]

$$\frac{\partial}{\partial\tau}\left[\frac{\partial p}{\partial z} - \frac{\varepsilon}{c_0^3\rho_0}p\frac{\partial p}{\partial\tau} - L_{\mathrm{abs}}p)\right] = \frac{c_0}{2}\Delta_\perp p, \qquad (1)$$

where p is the acoustic pressure in the beam; z is the coordinate along the beam axis; $c_0 = 1614$ m/s is the propagation velocity of longitudinal acoustic waves in the tissue; $\rho_0 = 1214$ kg/m^3 is the equilibrium density; $\varepsilon = 4.78$ is the nonlinearity factor of the tissue [7]; $\tau = t - z/c_0$ is the time in the moving coordinate system; and $\Delta_\perp$ is the Laplacian with respect to the transverse coordinates, which, in the case of an axisymmetric beam considered here, has the form $\Delta_\perp = \partial^2/\partial r^2 + 1/r\partial/\partial r$. The linear operator L_{abs} describes the absorption of a wave in compliance with the power law characteristic of biological tissues:

$$\alpha(f) = \alpha_0(f/f_0)^\eta, \qquad (2)$$

where the power index η is close to unity, α is the absorption coefficient at a frequency f, and α_0 is the absorption coefficient at the selected frequency f_0 [2]. For a tissue of liver type, the values of the parameters η and α_0 at the selected radiation frequency 1.7 MHz are equal to $\eta = 1.266$ and $\alpha_0 = 8.42$ m^{-1} [7], respectively. Equation (1) takes into account the nonlinear, dissipative, and diffraction effects.

In the case of a focused piston radiator under study, we have

$$p(z=0, r, \tau) = \begin{cases} p_0\sin[\omega_0(\tau + r^2/2c_0F)], & r \le r_0 \\ 0, & r > r_0 \end{cases} \qquad (3)$$

and an exact analytical solution for the acoustic field can be obtained only at the beam axis and in the focal plane $z = F$ in the linear approximation. It is impossible to obtain an analytical solution for the field in the whole space. Therefore, in order to determine the spatial distribution of thermal sources, the acoustic field of the radiator given by Eq. (3) is simulated numerically in the case of both linear and nonlinear propagation of waves.

Several approaches had been developed for the numerical solution of the problem of the focusing of intense acoustic beams. They use either the temporal finite-difference schemes of a direct integration of equations of the type of Eq. (1) [9–11] or the spectral schemes based on solving a system of coupled nonlinear equations for the amplitudes of the harmonics of the initial wave [7–9, 12–16]. The temporal approach is more suitable for investigating the focusing of pulses [10, 11], and the spectral approach is more suitable for describing periodic waves [12–16], as well as in the case when the frequency power law governing the absorption in the medium differs from the quadratic one and the operator L_{abs} in Eq. (1) has an integral form. In this paper, we use the spectral approach.

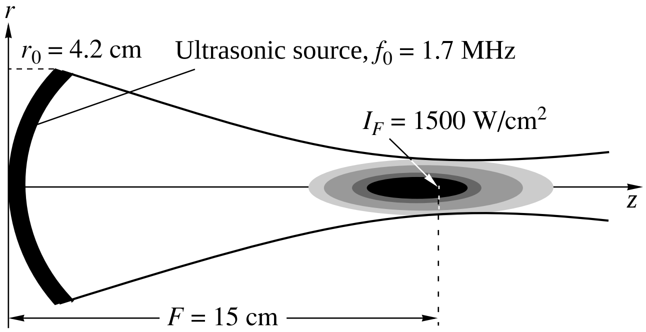

Fig. 1. Geometry of the problem.

In order to construct a numerical algorithm, we change to dimensionless variables in Eq. (1):

$$\frac{\partial}{\partial\theta}\left(\frac{\partial P}{\partial Z} - NV\frac{\partial P}{\partial\theta} - AL_{\mathrm{abs}}P)\right) = \frac{1}{4G}\left(\frac{\partial^2 P}{\partial R^2} + \frac{1}{R}\frac{\partial P}{\partial R}\right). \qquad (4)$$

Here, $P = p/p_0$ is the acoustic pressure normalized to the initial amplitude p_0 at the source; $\theta = \omega_0\tau$ is the dimensionless time, where $\omega_0 = 2\pi f_0$; $Z = z/F$ is the propagation coordinate normalized to the focal length; and $R = r/r_0$ is the transverse coordinate normalized to the radiator radius. Three dimensionless parameters, namely, N (nonlinearity), G (diffraction), and A (absorption),

$$N = \frac{F}{z_{\mathrm{n}}}, \quad G = \frac{z_d}{F}, \quad A = \frac{F}{z_a}, \qquad (5)$$

characterize the relations between the four characteristic spatial scales of the problem: the focal length F, the diffraction length $z_d = \omega_0 r_0^2/2c_0$, the length of shock formation $z_{\mathrm{n}} = c_0^3\rho_0/\varepsilon\omega_0 p_0$, and the absorption length for the radiation frequency $z_a = \alpha_0^{-1}$. Then, the boundary condition given by Eq. (3) can be represented in the form

$$P(Z=0, R, \theta) = \begin{cases} \sin(\theta + GR^2), & R \le 1 \\ 0, & R > 1. \end{cases} \qquad (6)$$

The values of the dimensionless parameters of diffraction and absorption, which are determined by Eq. (5), are equal to $G = 38.7$ and $A = 1.25$, respectively. We use the exact solution to the linearized Eq. (4) at the beam axis for a piston radiator (Eq. (6)) to estimate the intensity at the source $I_0 = p_0^2/2c_0\rho_0$ according to the intensity $I_F = 1500$ W/cm^2 preset in the focus at $Z = 1$:

$$I(Z, R = 0) = \frac{4I_0}{(1-Z)^2}\sin^2\left(G\frac{1-Z}{2Z}\right)\exp(-2AZ). \quad (7)$$

Setting $Z = 1$ in Eq. (7), we obtain $I_0 = I_F\exp(2\alpha_0 F)/G^2 = 12$ W/cm^2, which corresponds to the pressure amplitude $p_0 = 0.7$ MPa and the value of the nonlinearity parameter $N = 1.07$. The parameter N is taken equal to zero in calculating the linear focusing.

We seek the solution to Eq. (4) in the form of the Fourier series expansion:

$$P(Z, R, \theta) = \sum_{n=-\infty}^{\infty} C_n(Z, R)\exp(-in\theta), \quad (8)$$

where C_n is the complex amplitude of the nth harmonic in the spectrum of a propagating wave. Substituting expansion (8) into Eq. (4), we obtain a set of coupled equations for the amplitudes of harmonics

$$\begin{gathered}\frac{\partial C_n}{\partial Z} = \frac{i}{4n}\Delta_\perp C_n - \frac{in}{2}\sum_{k=-\infty}^{\infty} C_k C_{n-k} \\ - K''(n)C_n + iK'(n)C_n = L^{(n)}_{\text{diff}} + L^{(n)}_{\text{nonl}} + L^{(n)}_{\text{abs}},\end{gathered} \quad (9)$$

where $L^{(n)}_{\text{diff}}$, $L^{(n)}_{\text{nonl}}$, and $L^{(n)}_{\text{abs}}$ are the operators describing the diffraction, nonlinear, and dissipative phenomena for the nth harmonic, respectively, and K' and K'' are the dimensionless real and imaginary parts of the wave number; the latter quantities have the following form in the moving coordinate system:

$$\begin{aligned} K(n) &= k(nf_0)F = K' + iK'', \\ K''(n) &= \alpha(nf_0)F = An^{\eta}, \\ K'(n) &= 2\pi nf_0(1/c(nf_0) - 1/c_0)F \\ &= A\frac{2n}{\pi(\eta-1)}(1 - n^{\eta-1}). \end{aligned} \quad (10)$$

The frequency dependence of the absorption K'' is simulated by Eq. (2), and the dispersion of sound velocity K' is calculated according to the known dependence (2) using local dispersion relations of the Kramers–Kronig type [17].

The numerical integration of Eqs. (9) is conducted for a finite number of the first harmonics $n_{\max}$. For $n > n_{\max}$, the amplitudes C_n are assumed to be zero. To provide the stability of the numerical scheme at the stage of the developed shocks, an additional artificial viscosity proportional to the squared frequency is introduced: $K''(n)_{\text{art}} = A_1 n^2$. Since biological tissues consist mainly of water, the coefficient A_1 is selected to be equal to the absorption coefficient in water $\alpha_{\text{w}}(f_0) = 7.23 \times 10^{-4}$ cm^{-1}: $A_1 = 1.08 \times 10^{-2}$.

The method of splitting in the physical factors is used at each step of integration along the axis from the layer Z to the layer $Z + hZ$. This technique is realized in three stages. At the first stage, the diffraction effects described by the operator L_{diff} are taken into account for each harmonic. An absolutely implicit difference scheme is used at the distances close to the radiator, and after that, the Crank–Nicholson scheme is used [18]. The solution obtained for the diffraction problem at a new layer $Z + hZ$ is taken as the initial condition for the second stage of taking into account of the nonlinear effects described by the system of coupled nonlinear equations $\partial C_n/\partial Z = L_{\text{nonl}}$. The system is solved for each node of the grid constructed in R by the Runge–Kutta method with the fourth-order precision [18]. The representation of the solution in the form of the Fourier series in a complex form (Eq. (10)) provides an opportunity to avoid the use of an iteration procedure in simulating the nonlinear operator. The necessity of this procedure arises in the case of the Fourier series expansion in the real form [12, 13]. The solution of the nonlinear problem is used as an initial one for the third stage when the dissipative phenomena described by the set of equations $\partial C_n/\partial Z = L_{\text{abs}}$ are taken into account. Here, the exact result $C_n(Z + hZ, R) = C_n(Z, R)\exp(hZ(-K''(n) + iK''(n) + iK'(n))$ is used for each node of the grid and each harmonic.

From the determined amplitudes of harmonics, the intensity of each nth harmonic $I_n = 4|C_n|^2 I_0$, the total intensity of the wave

$$I(z, r) = \sum_{n=1}^{\infty} I_n(z, r), \quad (11)$$

and the power of thermal sources

$$q_v(z, r) = 2\sum_{n=1}^{\infty}\alpha(nf_0)I_n(z, r), \quad (12)$$

where $\alpha(nf_0)$ is the absorption coefficient at the nth harmonic (Eq. (2)), are calculated.

The following values of the basic parameters of the scheme were used: the limits of integration with respect to the longitudinal coordinate $0 \le Z \le 1.8$, the spatial window in the transverse coordinate $0 \le R \le 2.5$, the step of the grid along the beam axis $hZ = 0.25 \times 10^{-4}$ for the implicit scheme and $hZ = 10^{-4}$ for the Crank–Nicholson scheme, and the step of the grid in the transverse coordinate $hR = 10^{-3}$.

The calculation of the focusing of an acoustic beam in a nonlinear mode when a shock front is formed in the wave profile needs rather long computer time. A variable number of harmonics $n(Z, R)$ is used to reduce the time of calculation in the scheme for different Z and R. The necessary number n is controlled in such way that when the amplitude of the last harmonic exceeds a certain preset value, the number of harmonics is gradually increased up to the maximal value $n_{\max} = 1000$. Even with such an optimization, the time of calculation for the nonlinear problem by a Dec Alpha XP 1000 computer was about 40 h.

One can see from Eq. (12) that a nonlinear transformation of the wave energy up the spectrum leads to an increase in the absorption of the ultrasonic wave energy because of the growth of the absorption coefficient with frequency (Eq. (2)). In the case of a strong manifestation of the nonlinear effects and the appearance of shocks in the wave profile, the heating of the tissue increases most strongly in the focal region. Let us consider some theoretical estimates. As is well known, the absorption at shocks does not depend on the value of the absorption coefficient of the medium and is determined by the wave amplitude and the value of the nonlinear parameter ε [5]. In the case of a linearly propagating harmonic wave, the heat release in the focus, $q_v = 2\alpha_0 I = 2\alpha_0 p_A^2/2c_0\rho_0$, is proportional to the wave intensity or the squared pressure amplitude p_A, whereas in the case of the shock front formation, the heat release at the shock is proportional to the third power of its amplitude A_r:

$$q_{v,\,\mathrm{shock}} = \frac{\omega_0}{2\pi}\frac{\varepsilon A_r^3}{6c_0^4\rho_0^2} = \frac{(A_r/p_A)}{12\pi z_n}\frac{p_A^2}{c_0\rho_0}, \tag{13}$$

where $z_n = c_0^3\rho_0/\varepsilon\omega_0 p_A$ is the length of shock formation in a plane wave with the amplitude p_A. As one can see from Eq. (13), the ratio of absorption at the shock to its linear value is determined by the third power of the shock front amplitude and the ratio of the characteristic scales of absorption and nonlinearity in the tissue:

$$\frac{q_{v,\,\mathrm{shock}}}{q_v} = \frac{(A_r/p_A)^3}{12\pi}\frac{1}{\alpha_0 z_n}. \tag{14}$$

We take into account in Eq. (14) that the shock amplitude in the focus can attain the value $3p_A$ due to the more effective focusing in the nonlinear mode [16] and calculate the nonlinear scale corresponding to the intensity 1500 W/cm^2 in the tissue. As a result, we obtain $z_n = 1.2$ cm and $q_{v,\,\mathrm{shock}}/q_v = 7$. With allowance for the contribution of absorption at low frequencies given by Eq. (2), we can expect that, in the mode of developed shocks, the heating efficiency must increase by approximately an order of magnitude. The longitudinal dimension of the focal region of the considered radiator, which is determined by half the maximal intensity level (7), can be estimated approximately as $6F/G = 2$ cm. Since the size of the focal region is greater than the length of shock formation z_n for a wave with the intensity $I_F = 1500$ W/cm^2, we can expect that the mode of developed shocks is realized in the focus and the efficiency of the tissue heating is considerably increased.

TEMPERATURE FIELD

We use the inhomogeneous Pennes equation of heat conduction [19] to calculate the temperature field

$$\frac{\partial T}{\partial t} = k\Delta(T) - \frac{T - T_0}{\tau} + \frac{q_v}{c_v}, \tag{15}$$

where $T = T(\mathbf{r}, t)$ is the tissue temperature, $T_0 = 36.6$°C is the equilibrium temperature, $c_v = 3.81 \times 10^6$ J/(°C m^3) is the heat capacity of a unit volume, $k = K/c_v = 1.3 \times 10^{-7}$ m^2/s is the thermal diffusivity [7], K is the heat conductivity of the tissue, and Δ is the Laplacian. The first term on the right-hand side of Eq. (15) describes the process of diffusion, and the second term describes the cooling due to the intense heat transfer on account of the blood vessels present in both the heated region and outside it [2]. The characteristic time of the latter process for a liver-type tissue is equal to $\tau = \rho_b c_v/wc_{vb} = 250$ s, where ρ_b, c_{vb}, and w are the density, the heat capacity, and the velocity of the blood flow, respectively [7]. The function $q_v(z, r)$ describes the field of thermal sources caused by the absorption of an ultrasonic wave (Eq. (12)). For a numerical simulation, it is convenient to reduce Eq. (15) to a dimensionless form:

$$\frac{\partial\tilde{T}}{\partial\tilde{t}} = \left[\alpha\frac{\partial^2}{\partial Z^2} + \beta\left(\frac{\partial^2}{\partial R^2} + \frac{1}{R}\frac{\partial}{\partial R}\right)\right]\tilde{T} - \frac{\tilde{T}}{\tau} + \gamma\tilde{q}(R, Z). \tag{16}$$

Here, $\tilde{t} = t/t_0$ is the time normalized to the characteristic heating time $t_0 = 1$ s; $\tilde{T} = (T - T_0)/T_0$ is the dimensionless temperature normalized to the equilibrium value T_0; the dimensionless coefficients $\alpha = kt_0/F^2$ and $\beta = kt_0/r_0^2$ describe the diffusion along and across the beam axis, respectively; and $\gamma = I_0t_0F/(c_vT_0)$ is the dimensionless coefficient characterizing the power of the thermal sources.

As in the case of the acoustic field, we use the technique of splitting with respect to physical parameters in order to solve Eq. (16) numerically. At each time step $h\tilde{t}$ in passing from the time layer $\tilde{t}$ to the layer $\tilde{t} + h\tilde{t}$, the problem is solved in two stages. At the first stage, the influence of the cooling process and the thermal sources is taken into account according to the equation $\partial\tilde{T}/\partial\tilde{t} = -\tilde{T}/\tau + \gamma\tilde{q}(R, Z)$, which has an exact solution

$$\begin{aligned}&\tilde{T}(\tilde{t} + h\tilde{t})\\ &= \tilde{T}(\tilde{t})\exp\left(-h\tilde{t}\frac{t_0}{\tau}\right) + \left[1 - \exp\left(-h\tilde{t}\frac{t_0}{\tau}\right)\right]\frac{\tau\gamma}{t_0}\tilde{q}.\end{aligned} \tag{17}$$

Solution (17) is taken as the initial temperature distribution for solving the diffusion part, which is approximated by the implicit longitudinal–transverse scheme providing the second-order precision in both time and spatial coordinates [18].

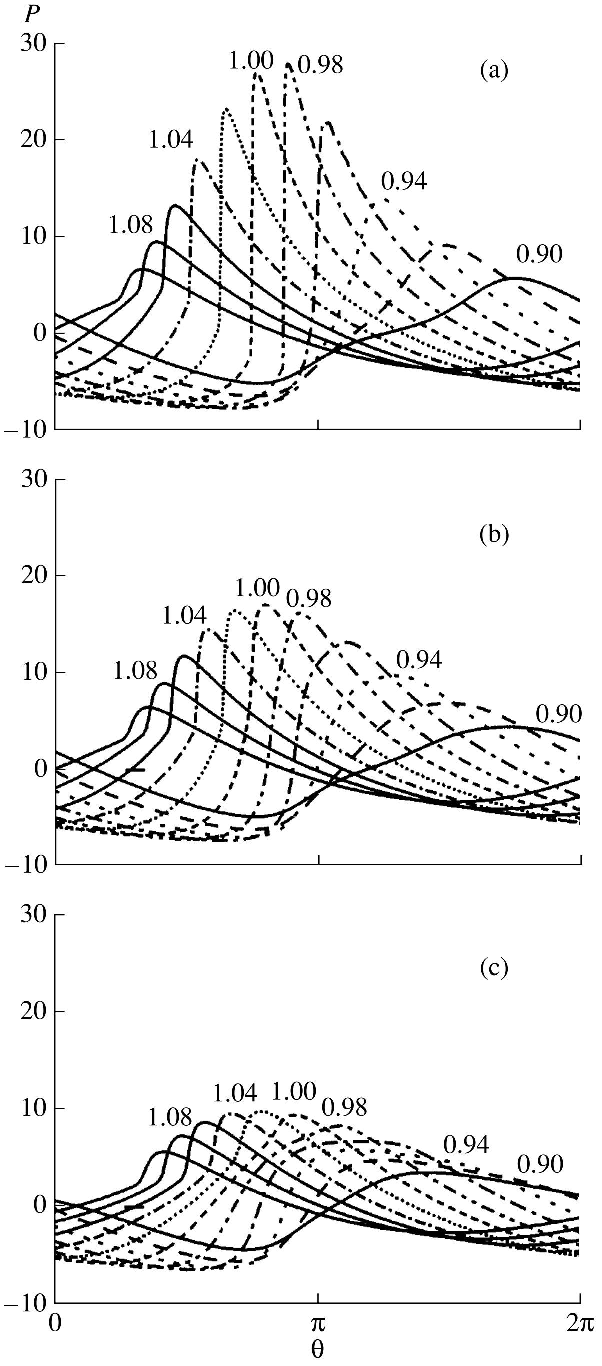

Fig. 2. Wave profiles in the focal region of the beam ($P = p/p_0$) in the case of a nonlinear mode of focusing at various distances from the radiator $Z = z/F$ (numbers at the curves) and from the beam axis: $R = r/r_0$ = (a) 0, (b) 0.01, and (c) 0.02.

The following basic parameters of the scheme were used: the spatial window in the longitudinal coordinate $0.4 \le Z \le 1.6$, the spatial window in the transverse coordinate $0 \le R \le 0.2$, the grid step in the longitudinal coordinate $hZ = 2 \times 10^{-3}$, the grid step in the transverse coordinate $hR = 10^{-3}$, and the time step $h\tilde{t} = 1.5 \times 10^{-2}$.

INFLUENCE OF NONLINEAR EFFECTS ON ACOUSTIC FIELD CHARACTERISTICS AND ON TEMPERATURE DISTRIBUTION IN TISSUE

The results obtained from the simulation of Eqs. (1) and (15) provide an opportunity to investigate the influence of acoustic nonlinearity on the temporal and spatial characteristics of an ultrasonic beam, on the distribution of thermal sources, and on the evolution of the thermal field in the tissue. Figure 2 shows the profiles of an acoustic wave in the focal region at various distances along and across the beam axis, which are calculated with allowance for nonlinear effects. One can see that a shock front arises in the wave profile and the profile shape is characterized by a considerable asymmetry of the positive and negative phases. The positive peak value of the profile in the focus is almost three times as great as the peak value obtained under the approximation of linear wave propagation. The total pressure difference in the profile of a nonlinear wave is one and a half times greater than the corresponding value in the case of the linear wave propagation. One can also see that a considerable manifestation of nonlinear effects occurs only in a small spatial region near the focus: $r/r_0 = 0.02$, $0.95 < z/F < 1.05$, which corresponds to dimension scales of approximately 1.5 mm in the transverse direction and 1.5 cm in the longitudinal direction. One can expect a considerable increase in the efficiency of the tissue heating precisely in this region.

In the nonlinear mode of ultrasonic wave propagation in a tissue, the spectrum of the wave acquires new higher harmonics. Figure 3 presents the distributions of the amplitudes of the first three harmonics in a nonlinear beam (the solid curves *1*, *2*, and *3*) and the distribution of the amplitude of the fundamental harmonic in the case of linear propagation (the dashed curve *1*') in the focal plane and along the beam axis. One can see from these figures that the amplitudes of higher harmonics are sufficiently large and their spatial distributions in the focal region are narrower than the distributions for the fundamental frequency in both longitudinal and transverse directions.

As the frequency grows, the absorption increases. However, at the same time the diffraction effects become weaker and the beam focusing improves. Therefore, we can expect that near the focus, the total intensity of the wave calculated in the nonlinear case by the sum of the intensities of all harmonics differs from the intensity of the first harmonic obtained in the case of linear wave propagation. Figures 4 and 5 present the spatial distributions of the wave intensity and the power of thermal sources in the focal plane $z = F$ and along the beam axis for the linear (curves *1*) and nonlinear (curves *2*) modes of focusing. One can see that in the case of the nonlinear wave propagation, a small (about 15%) increase in the amplification factor in the focus is observed along with an improvement of the spatial localization of the beam in comparison to the linear

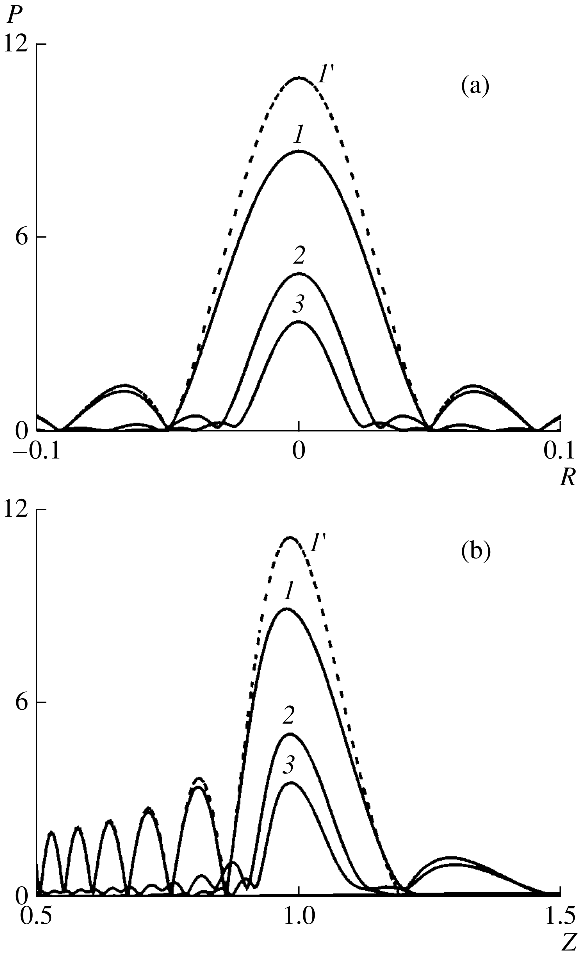

Fig. 3. Spatial distributions of the pressure amplitudes of the first three harmonics $P = 2|C_n|$, n = (*1*) 1, (*2*) 2, and (*3*) 3 in a nonlinear beam and (*1*') the amplitudes of the fundamental harmonic in the case of linear propagation: (a) in the focal plane $z|F| = 1$ and (b) along the beam axis.

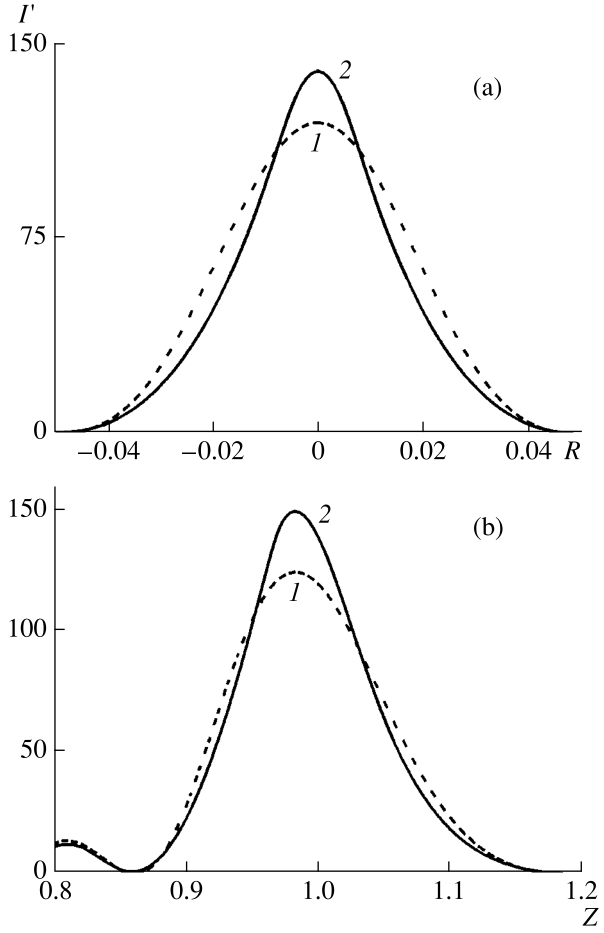

Fig. 4. Spatial distributions of the total intensity $I' = I/I_0$ (a) in the focal plane and (b) along the beam axis for the (*1*) linear and (*2*) nonlinear modes of focusing.

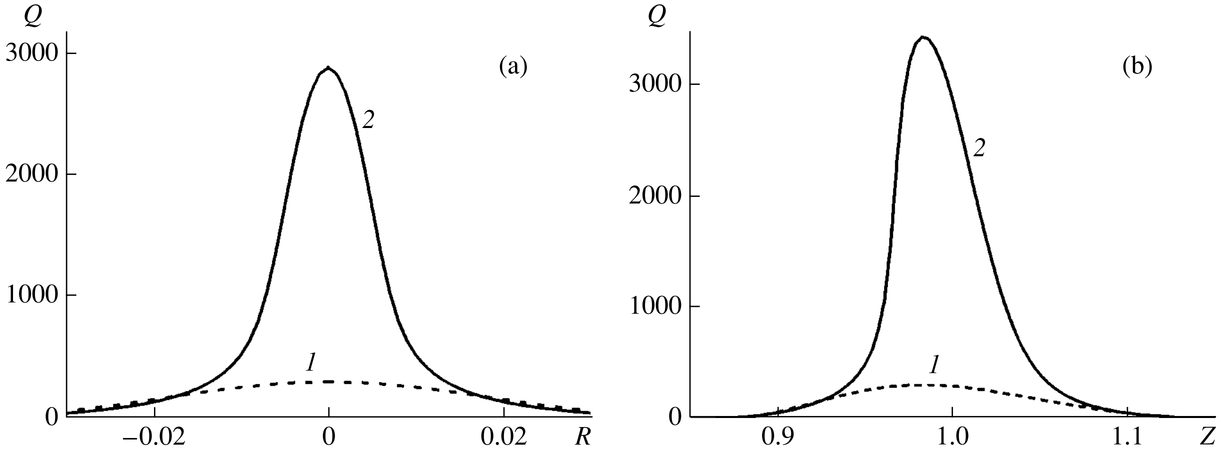

Fig. 5. Distributions of thermal sources $Q = q/q_0$ (a) in the focal plane and (b) along the beam axis for the (*1*) linear and (*2*) nonlinear modes of focusing.

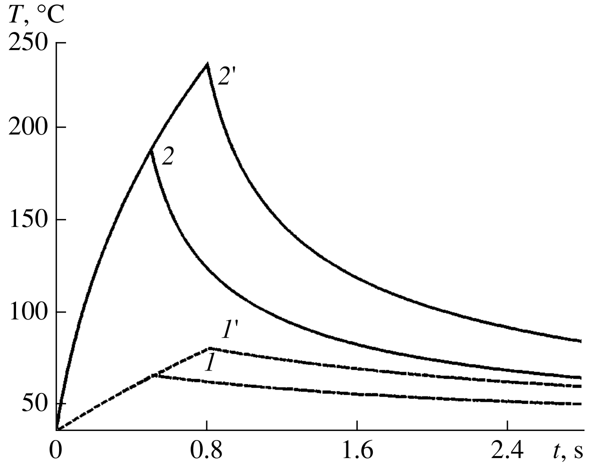

Fig. 6. Dependences of temperature on time in the focus for the (*1*) linear and (*2*) nonlinear modes of focusing and for different times of irradiation: (*1*, *2*) 0.5 and (*1*', *2*') 0.8 s.

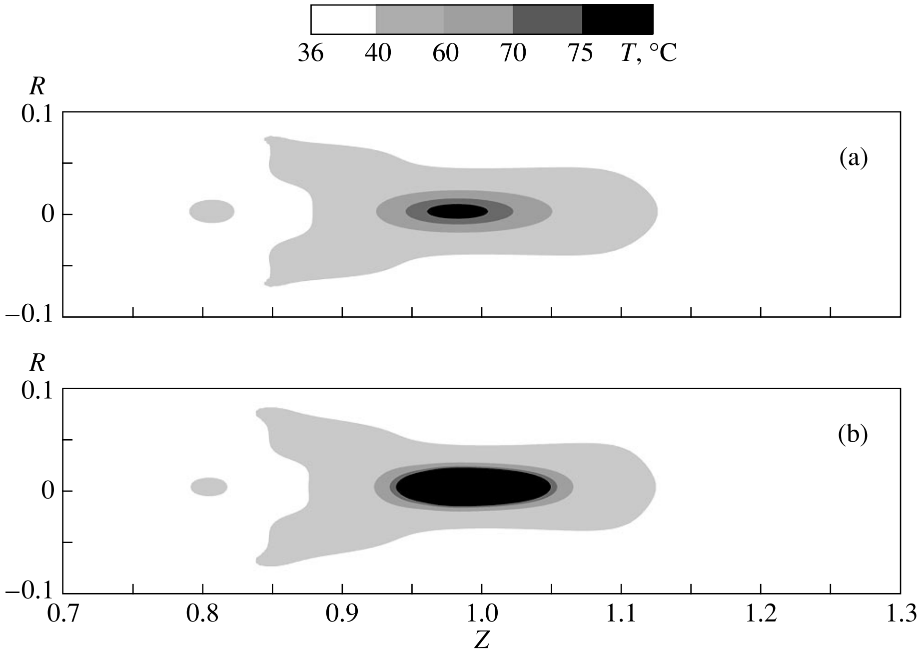

Fig. 7. Spatial temperature distributions in the focal region for the (a) linear and (b) nonlinear modes of focusing in the case of the irradiation time 0.8 s.

case. At the same time, the nonlinear effects lead to a considerable increase in the power of thermal sources in the focal region of the beam. The efficiency of heating increases by almost an order of magnitude, which agrees with the theoretical estimates given above. Thus, the intensity used is close to optimal in terms of the realization of the mode of local tissue heating in the focus due to the absorption at shock fronts. A shock arises close to the focus, and, therefore, one obtains no additional losses of wave energy and no increase in heating in the prefocal region.

Figure 6 shows the dependences of temperature on time in the focus for the linear (curves *1*) and nonlinear (curves *2*) modes of focusing with the exposures 0.5 and 0.8 s. As one can see, even with that short irradiation times, the diffusion of heat manifests itself quite strongly and the dependence $T(t)$ differs from the linear one. The high spatial gradient in the distribution of thermal sources in the nonlinear mode (Fig. 5) amplifies the diffusion process. Therefore, despite the fact that the power of thermal sources in the focus for the linear and nonlinear modes of heating differs by an order of magnitude, the increase in temperature differs by only a factor of three.

Figure 7 illustrates the two-dimensional spatial distributions of temperature calculated for the irradiation time 0.8 s in the linear and nonlinear modes of wave propagation. One can see that in the case of the nonlinear mode, the region of strong heating (over 75°C) is considerably wider in both longitudinal and transverse directions and shifted slightly towards the radiator. In contrast, the region with moderate temperature in the case of the nonlinear propagation is narrower than in the linear mode, which is caused by a better localization of heating.

CONCLUSIONS

The theoretical approach, the numerical algorithm, and the computer codes developed in this study provide an opportunity to effectively investigate the problems of focusing of a high-intensity acoustic beam in a biological tissue and the corresponding tissue heating in the conditions of strong manifestation of the effects of acoustic nonlinearity. A numerical simulation of the acoustic and temperature fields in a biological tissue is conducted for the conditions characteristic of real clinical setups used in ultrasonic surgery. The predictions made with the use of two models, which do and do not take into account the acoustic nonlinearity of the tissue, are compared. It is demonstrated that nonlinear effects lead to an increase in the power of thermal sources in the focus by approximately an order of magnitude and to a certain improvement of the locality of heating. The heat diffusion in the tissue leads to smoothing of the spatial distribution of temperature compared to the distribution of thermal sources, the diffusion processes being more pronounced in the nonlinear mode of focusing. With the acoustic nonlinearity taken into account, the maximal temperature increment in the focus several times exceeds the value obtained in the approximation of linear wave propagation; i.e., the role of nonlinear processes is of fundamental significance.

ACKNOWLEDGMENTS

We are grateful to Dr. G.R. Ter Haar for supporting the idea to conduct this study and to Dr. O.A. Sapozhnikov for useful discussions. The work was supported in part by the Russian Foundation for Basic Research (project no. 98-02-17318) and the Civilian Research and Development Foundation for the independent states of the former Soviet Union (project no. RP2-2099).

REFERENCES

1. J. G. Webster, *Wiley Encyclopedia of Electrical and Electronics Engineering* (Wiley, 1999), pp. 368–386.
2. *Physical Principles of Medical Ultrasonics*, Ed. by C. R. Hill (Ellis Horwood, Chichester, 1986; Mir, Moscow, 1989).
3. G. R. Ter Haar, I. H. Rivens, E. Moskovic, *et al.*, Proc. SPIE **3249**, 270 (1998).
4. J. Y. Chapelon and D. Cathignol, in *Advances in Nonlinear Acoustics: Proceedings of the 13th International Symposium on Nonlinear Acoustics* (Bergen, Norway, 1993), pp. 21–29.
5. M. F. Hamilton and D. T. Blackstock, *Nonlinear Acoustics* (Academic, Boston, 1998), p. 139.
6. V. A. Khokhlova, O. A. Sapozhnikov, and L. A. Crum, J. Acoust. Soc. Am. **102**, 3155 (1997).
7. P. Meaney, M. D. Cahill, and Gail ter Haar, Proc. SPIE **3249**, 246 (1998).
8. F. P. Curra, P. D. Mourad, V. A. Khokhlova, and L. A. Crum, in *Proceedings of the IEEE International Ultrasonics Symposium* (Sendai, Japan, 1998), pp. 1419–1422.
9. N. S. Bakhvalov, Ya. M. Zhileĭkin, and E. A. Zabolotskaya, *Nonlinear Theory of Sound Beams* (Nauka, Moscow, 1982; AIP, New York, 1987).
10. Y. S. Lee and M. F. Hamilton, J. Acoust. Soc. Am. **97**, 906 (1995).
11. J. Tavakkoli, D. Cathignol, R. Souchon, and O. A. Sapozhnikov, J. Acoust. Soc. Am. **104**, 2061 (1998).
12. Tjotta Naze, S. Tjotta, and E. H. Vefring, J. Acoust. Soc. Am. **88**, 2859 (1990).
13. T. S. Hart and M. F. Hamilton, J. Acoust. Soc. Am. **84**, 1488 (1988).
14. P. T. Christopher and K. J. Parker, J. Acoust. Soc. Am. **90**, 488 (1991).
15. Yu. A. Pishchal'nikov, O. A. Sapozhnikov, and V. A. Khokhlova, Akust. Zh. **42**, 412 (1996) [Acoust. Phys. **42**, 362 (1996)].
16. V. A. Khokhlova, M. A. Averkiou, S. J. Younghouse, M. F. Hamilton, and L. A. Crum, in *Proceedings of 16th ICA/135th ASA Meeting* (Seattle, USA, 1998), Vol. 4, p. 2875.
17. S. S. Kashcheeva, V. A. Khokhlova, O. A. Sapozhnikov, *et al.*, Akust. Zh. **46**, 211 (2000) [Acoust. Phys. **46**, 170 (2000)].
18. V. M. Paskonov, V. I. Polezhaev, and L. A. Chudov, *Numerical Simulation of the Processes of Heat and Mass Transfer* (Nauka, Moscow, 1984).
19. W. L. Nyborg, Phys. Med. Biol. **33**, 785 (1988).

Translated by M. Lyamshev

Acoustical Physics, Vol. 47, No. 4, 2001, pp. 476–483. Translated from Akusticheskiĭ Zhurnal, Vol. 47, No. 4, 2001, pp. 550–557.
Original Russian Text Copyright © 2001 by Shenderov.

Directional Properties of an Array of Sound Receivers Positioned in an Impedance Screen Recess

E. L. Shenderov
Morfizpribor Central Research Institute, Chkalovskiĭ pr. 46, St. Petersburg, 197376 Russia
e-mail: shend@peterlink.ru

Received July 17, 2000

Abstract—Expressions for calculating the directional characteristics of an array of sound receivers positioned in a waveguide with impedance walls are obtained from the solution to the problem on the diffraction of a plane sound wave by the waveguide open end with impedance flanges. The waveguide can be of a finite length, and, in this case, it can be considered as an open cavity in an impedance screen. The solution of the integral equation for the sound pressure distribution over the opening area is reduced to the solution of an infinite system of algebraic equations for the coefficients of the field expansion in normal waveguide waves. Examples of calculated directional characteristics are presented for arrays with receivers positioned at different distances from the opening and for different values of the impedances of the waveguide walls and flanges. *© 2001 MAIK “Nauka/Interperiodica”.*

The solution to the problem on the diffraction of a plane sound wave by a flanged open end of a waveguide with impedance walls and impedance flanges was obtained by Shenderov [1]. In the cited paper, this solution was used to calculate the scattering pattern for a wave incident on a screen with a slit, including the backscattering pattern and the “form-function” that describes the backscattered amplitude as a function of the slit width relative to the wavelength. Additionally, this solution can serve as the basis for determining the directional characteristics of an array of sound receivers positioned inside an open waveguide with impedance flanges. Note that for an unflanged waveguide with impedance walls, an exact (but very cumbersome) analytical solution was obtained by Rawlins [2] who used the Wiener–Hopf method. For flanged waveguides, the solution can be obtained only using a numerical procedure that reduces the integral equation governing the sound field in the slit to an infinite system of algebraic equations in the coefficients of the sound field expansion in normal waveguide waves. A similar method was used for waveguides with rigid flanges [3–5]. The sound emission by a source located in an arbitrarily shaped cavity in the impedance screen was considered by Peplow and Chandler-Wilde [6] with the use of integral equations.

This paper deals with the problem schematically represented in Fig. 1. An array of sound receivers is located inside a waveguide of width d with impedance walls. A plane sound wave propagates from the lower halfspace and is incident on an infinite impedance wall (screen) with a slit connected with the waveguide. The waveguide can be both semi-infinite (Fig. 1a) and of a finite length (Fig. 1b). In the latter case, the waveguide appears as an open cavity in the screen. All walls (the screen, every waveguide wall, and the waveguide bottom) can be characterized by different values of impedance. The desired quantity is the directional pattern of the array in the lower halfspace. If we set the depth of the cavity in Fig. 1b to zero, we reduce the problem to the problem on the sound diffraction by an impedance insert in a plane screen whose impedance differs from that of the insert.

We represent the boundary conditions at the screen surface and waveguide walls in the form

$$p = \frac{w_p}{ik\rho c}\frac{\partial p}{\partial y}\bigg|_{y=0} = -\frac{w_p}{ik\rho c}\frac{\partial p}{\partial n}\bigg|_{y=0},$$

$$p_2 = \frac{w_1}{ik}\frac{\partial p_2}{\partial x}\bigg|_{x=d/2}, \quad p_2 = -\frac{w_2}{ik}\frac{\partial p_2}{\partial x}\bigg|_{x=-d/2},$$

$$p_2 = \frac{w_b}{ik}\frac{\partial p_2}{\partial y}\bigg|_{y=h}.$$

Here and below, p is the sound pressure in the lower halfspace; p_2 is the sound pressure in the waveguide; ρc is the wave resistance of the medium; $k = \omega/c$;

$$w_p = Z_p/\rho c; \quad w_1 = Z_1/\rho c;$$

$$w_2 = Z_2/\rho c; \quad w_b = Z_b/\rho c;$$

$$u_1 = w_1/(-ikd); \quad u_2 = w_2/(-ikd),$$

Z_p is the impedance of the screen; Z_1 and Z_2 are the impedances of the left- and right-hand waveguide walls, respectively; and Z_b is the impedance of the bottom of the cavity shown in Fig. 1b. We assume that all quantities vary in time as $\exp(-i\omega t)$.

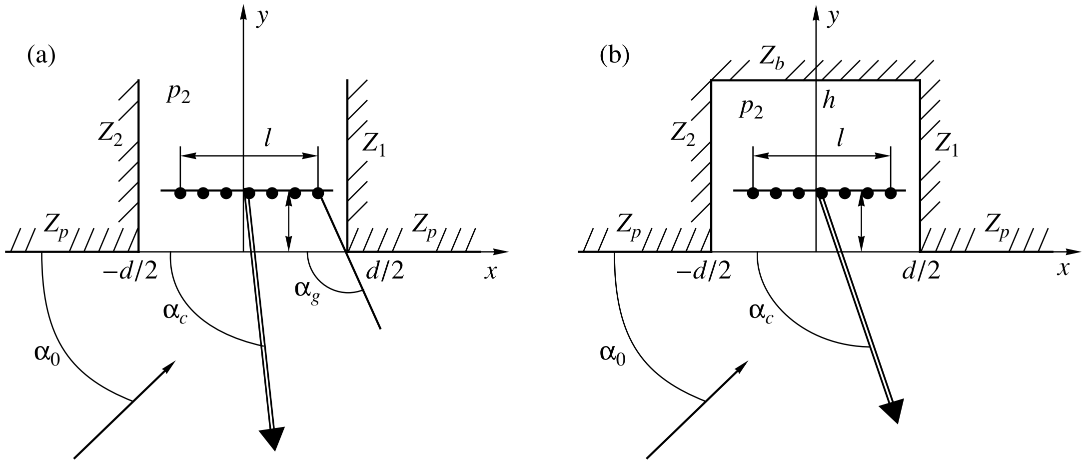

Fig. 1. Reference system. An array of sound receivers in (a) a semi-infinite waveguide and (b) an open cavity. The wide arrow shows the compensation direction.

Inside the waveguide, we represent the field as the expansion in normal waves of the waveguide with impedance walls (see the previous paper [7]):

$$p_2(x,y) = \sum_{n=1}^{\infty} A_n \psi_n(x)$$
$$\times [\exp(ik\gamma_n) + qA_b(\gamma_n)\exp(-ik\gamma_n(y-2h))].$$

Here, $\gamma_n = \sqrt{k^2 - \beta_n^2}$ are the wave numbers of normal waves; $\psi_n(x)$ are the eigenfunctions of the waveguide with impedance walls,

$$\psi_n(x) = u_2\beta_n\cos(\beta_n(x/d+1/2))$$
$$+ \sin(\beta_n(x/d+1/2));$$

and β_n are the eigenvalues obtained as solutions to the transcendental equation

$$(u_1u_2\beta^2 - 1)\sin\beta - \beta(u_1+u_2)\cos\beta = 0.$$

The quantities $A_b(\gamma_n)$ given by the expression

$$A_b(\gamma_n) = (w_b\gamma_n - 1)/(w_b\gamma_n + 1)$$

are the reflection coefficients of the cavity bottom for normal waves. The coefficient q is zero for the semi-infinite waveguide and unity for a finite-length waveguide. Note that the solution for the semi-infinite waveguide cannot be obtained as a particular case of the problem on the finite-length waveguide for $h = \infty$, because backward waves can appear in such an approach for zero-valued losses. In addition, backward waves cannot be eliminated by setting the cavity bottom impedance so as to ensure that the bottom will totally absorb the incident sound, because this approach eliminates a single normal wave rather than all normal waves simultaneously. A specially introduced coefficient q allows a universal representation of the solutions to both problems shown in Figs. 1a and 1b.

The coefficients A_n satisfy the infinite system of equations obtained in [1]

$$A_n + \sum_{m=1}^{\infty} A_m U_{nm} = B_n, \quad n = 1, 2, 3\dots,$$

where

$$B_n = \frac{d_n(\cos\alpha_0)}{H_n(1+q_n)}[1 + A_p(\sin\alpha_0)],$$

$$U_{nm} = \frac{kd[\gamma_m w_p - 1 - q_m(\gamma_m w_p + 1)]}{2\pi H_n(1+q_n)} I_{mn},$$

$$q_m = qA_b(\gamma_m)\exp(2ikh\gamma_m),$$

$$I_{mn} = \int_{-\infty}^{\infty} \frac{d_n(u)d_m(-u)}{w_p\sqrt{1-u^2}+1}du, \tag{1}$$

$$H_n = [1 + u_2 + \beta_n^2u_2^2 - u_2\cos(2\beta_n)$$
$$+ (\beta_n^2u_2^2 - 1)\sin(2\beta_n)/(2\beta_n)]/2,$$

$$d_n(g) = \{[\exp(-ikdg/2) - \cos\beta_n\exp(ikdg/2)]$$
$$\times(ikdg\beta_n u_2 - \beta_n)$$
$$-\sin\beta_n\exp(ikdg/2)(\beta_n^2u_2 + ikdg)\}/((kdg)^2 - \beta_n^2).$$

The function $A_p(\gamma)$ appearing on the right-hand side of the system for argument $\gamma = \sin\alpha_0$ determines the sound reflection coefficient of the screen and is given as follows:

$$A_p(\gamma) = \frac{w_p\gamma - 1}{w_p\gamma + 1}. \tag{2}$$

In order to obtain the directional pattern of the array located inside the waveguide, one must calculate the sound fields at the points where the receivers are

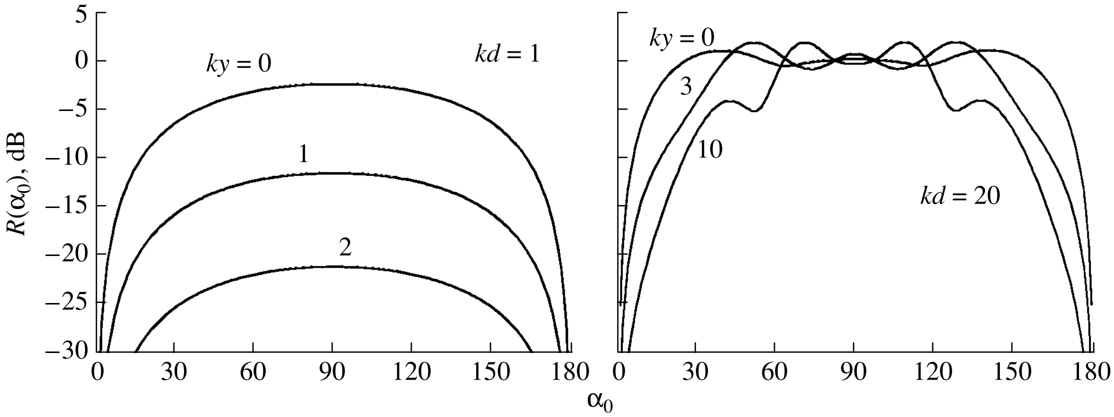

Fig. 2. Directional patterns of a point receiver located at the axis of a semi-infinite waveguide at different wave distances to the slit. The numbers near the curves indicate the wave distance ky; $w_1 = w_2 = w_p = 0.7 - i0.2$; $M = 1$.

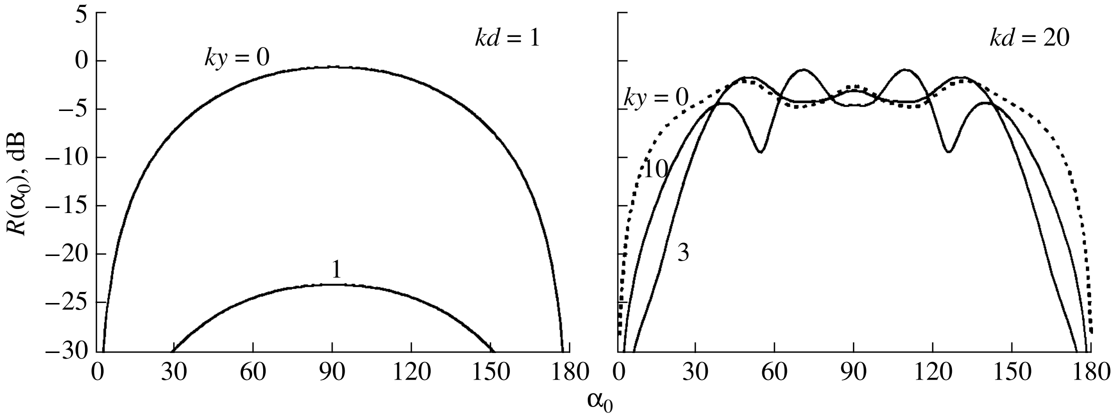

Fig. 3. Directional patterns of a point receiver located at the axis of a semi-infinite waveguide at different wave distances to the slit. The numbers near the curves indicate the wave distance ky. The impedances of all surfaces are close to the impedance of an acoustically soft surface: $w_1 = w_2 = w_p = 0.1 - i0.1$; $\alpha_c = 90°$; and $M = 1$.

located, multiply them by the coefficients f_m and $\exp(i\varphi_m)$, which determine the amplitude and phase distributions of the array, and, finally, add up the resulting values. The coefficients of the amplitude and phase distributions can be introduced to control the form of the directional pattern and the direction of its main lobe. For example, to steer the main lobe of the directional pattern through an angle α_c, one must set $\varphi_m = kx_m\cos\alpha_c$, where x_m are the coordinates of the receivers, $m = 1, 2, \ldots, M$, and M is the number of receivers. Normalizing the directional pattern by its maximal value in the free field, we obtain

$$D(\alpha_0) = \left|\sum_{m=1}^{M} f_m \exp(i\varphi_m) p_2(x_m, y) / \sum_{m=1}^{M} f_m\right|.$$

In decibels, the directional pattern will be determined in the form

$$R(\alpha_0) = 20\log_{10}D(\alpha_0).$$

As in [1], we used the reduction method to solve system (1). The eigenvalues β_n were calculated by the method described in the previous paper [7]. The calculations were carried out using a PC with 450-MHz CPU. The calculation time for the directional pattern at a given value of kd was 0.1 s for $kd < 5$. For $kd = 10$, the calculation time varied between 0.2 and 0.3 s; for $kd = 40$, it was about 2 s; and for $kd = 100$ it varied between 5 and 6 s. All calculations were carried out for the uniform amplitude distribution, i.e., it was assumed that $f_m = 1$.

Figure 2 shows the directional patterns of a point receiver located at the axis of a semi-infinite impedance waveguide for different sizes of the waveguide cross-section and for different wave distances between the receiver and the slit in the screen. In these calculations, we assumed that the waveguide walls are characterized by complex-valued impedances with nonzero real parts in order to take into account the sound absorption by walls. For complex-valued wall impedances, all eigenvalues β_n and wave numbers of normal waves γ_n are complex; therefore, all normal waves attenuate in the waveguide, i.e., no purely propagating waves exist in the waveguide. However, if $\mathrm{Re}\beta_n > k$, the imaginary

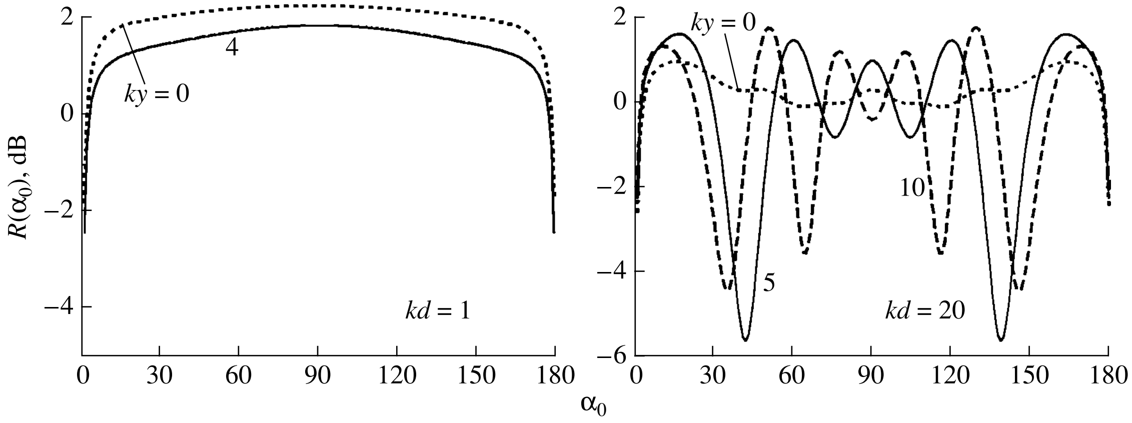

Fig. 4. Directional patterns of a point receiver located at the axis of a semi-infinite waveguide at different wave distances to the slit. The numbers near the curves indicate the wave distance *ky*. The impedances of all surfaces nearly coincide with the impedance of an acoustically hard surface: $w_1 = w_2 = w_p = 100.0 - i0.2$; $\alpha_c = 90°$; and $M = 1$.

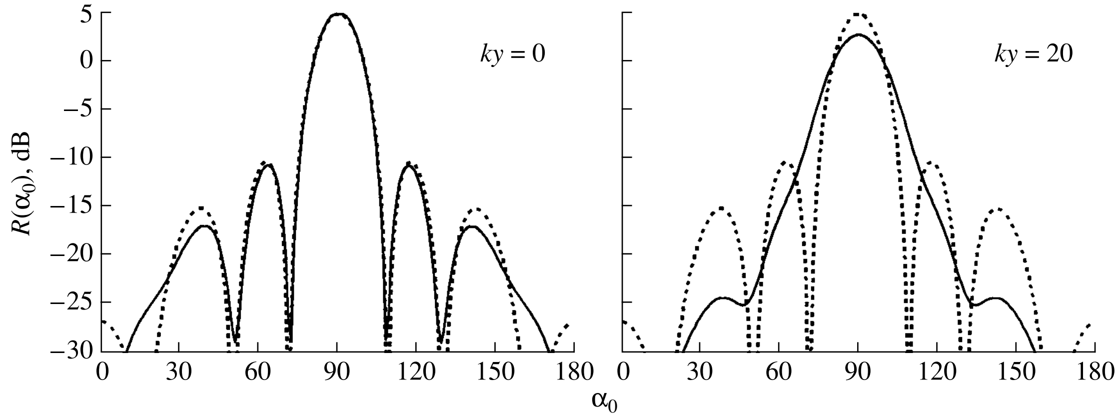

Fig. 5. Directional patterns of a receiver array located inside a semi-infinite waveguide at different wave distances *ky* to the slit; $kd = 20.0$, $kl = 18.0$, $M = 12$, $w_1 = w_2 = w_p = 0.7 - i0.2$, and $\alpha_c = 90°$. The dotted curves correspond to the directional patterns in free space.

part of the wave number γ_n drastically increases, which causes an increase in the attenuation of the corresponding normal wave. This phenomenon is similar to a transition from propagating normal waves to nonpropagating waves in a waveguide with lossless walls. For slits of small wave size ($kd = 1$), the excitation of only the first oscillating mode is noticeable in the waveguide, and even this mode is strongly attenuating. For this reason, the amplitude of the received signal strongly decreases with increasing distance between the receiver and the slit, i.e., with an increase in *ky*.

Owing to the fact that, for slits of small wave size, the amplitudes of all modes with numbers exceeding unity are small, the directional patterns are smooth nonoscillating functions. With an increase in the wave size (see curves for $kd = 20$), higher oscillating modes appear and the directional patterns exhibit an oscillating behavior.

For grazing incidence (at angles close to $\alpha_0 = 0°$ or 180°), the levels of the directional characteristics tend to vanish. This is related to the fact that the reflection coefficient of the screen A_p determined by Eq. (2) tends to –1 with increasing angle of sound incidence, independently of the screen impedance (excluding the case of a perfectly hard screen, i.e., $w = \infty$); i.e., the total sound pressure tends to zero near the screen. The excitation of various modes in the waveguide is characterized by the coefficients B_n, which, according to Eq. (2), are proportional to the magnitude of the total field near the screen. Therefore, the directional patterns are characterized by low levels at grazing angles of incidence.

These features are more prominent when the impedances of the waveguide walls and flanges are close to the impedance of the acoustically soft surface (Fig. 3). At $kd = 1$, the received signal shows a strong decrease (about 25 dB in the example under consideration) even for small distances between the receiver and the slit. At the same time, if the waveguide width exceeds the wavelength, the amplitude of sound pressure in the waveguide varies only slightly even for considerably long distances to the slit; however, the directional patterns become highly nonuniform in this case. The reason

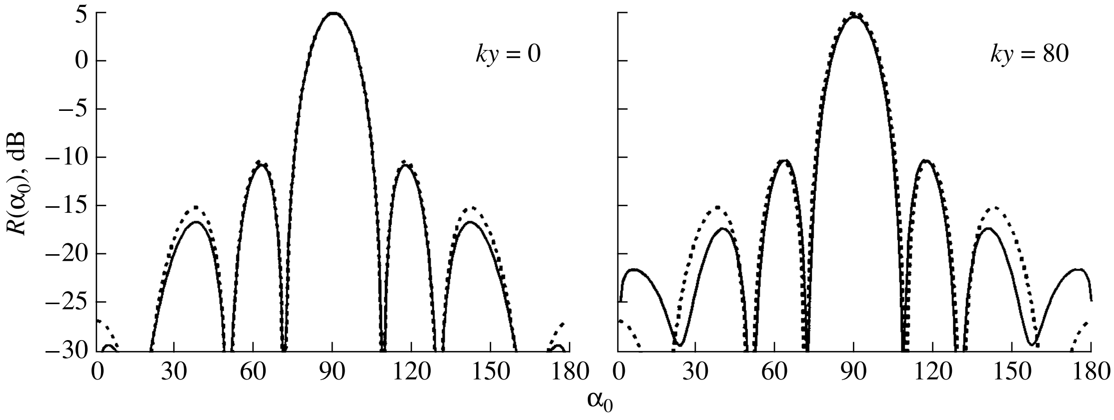

Fig. 6. Directional patterns of the receiver array located inside a semi-infinite waveguide at different wave distances ky to the slit in the case of the surface impedances being close to the impedance of an acoustically hard surface; $kd = 20.0$, $kl = 18.0$, $M = 12$, $w_1 = w_2 = w_p = 100.0 - i0.2$, and $\alpha_c = 90°$. The dotted curves correspond to the directional patterns in free space.

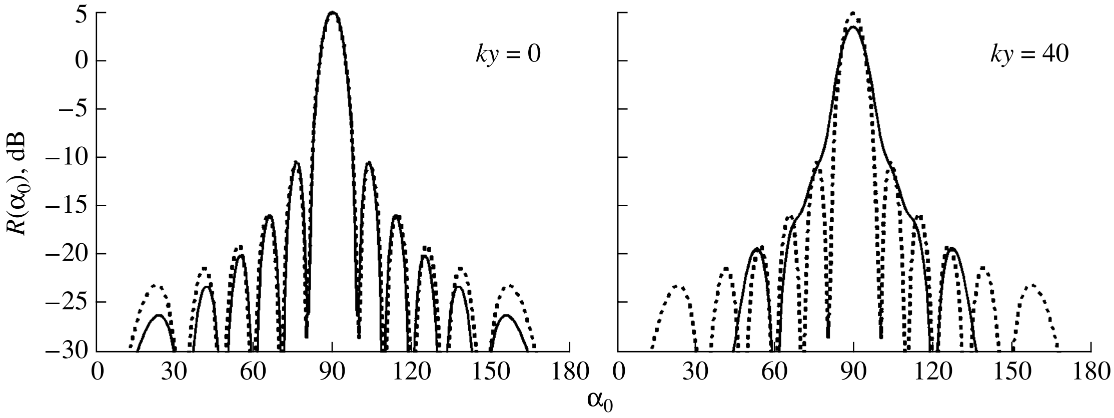

Fig. 7. Directional patterns of the receiver array located inside a semi-infinite waveguide at different wave distances ky to the slit in the case of the surface impedances being close to the impedance of an acoustically soft surface; $kd = 40.0$, $kl = 36.0$, $M = 24$, $w_1 = w_2 = w_p = 0.1 - i0.1$, and $\alpha_c = 90°$. The dotted curves correspond to the directional patterns in free space.

is that a wide waveguide allows low attenuation propagation for several oscillating modes, which can be easily distinguished in the plots corresponding to $kd = 20$.

For a wide waveguide, noticeable oscillations occur also for impedances close to the impedance of the acoustically hard surface (Fig. 4). Note that the zeroth normal wave propagates almost without attenuation in waveguides with such impedance walls. As a result, the received signal shows only small losses even for the observation points located far away from the slit. Unlike the case shown in Fig. 3, the signal here appears quite measurable even for angles deviating from 0° and 180° by only 5°–10°, although the directional characteristic tends, as earlier, to zero for lower grazing angles.

Figure 5 sows directional patterns of a planar array of receivers located inside the waveguide. These curves make it possible to trace the pattern deformation versus the distance between the array and the slit. In this and all subsequent figures, the dashed line corresponds to the directional pattern of the array in free space. In this example, we consider a waveguide of width $kd = 20.0$ and set the wave size of the array (kl) equal to 18.0. The array consists of $M = 12$ elements, so that the interelement wave distance is $kl/(M - 1) = 1.56$. For such an interelement distance, the directional pattern of the array nearly coincides with the pattern of a continuous linear antenna. The array characterized by the above dimensions occupies almost the whole waveguide cross-section.

For large distances between the array and the slit, the main lobe somewhat widens and the lateral lobes become smoother. The signal level in the direction of the main lobe decreases appreciably only for long distances between the array and the slit.

For impedances close to the impedance of the acoustically hard surface (Fig. 6), the pattern is almost independent of the distance between the array and the slit. In this case, almost all energy is carried by the first

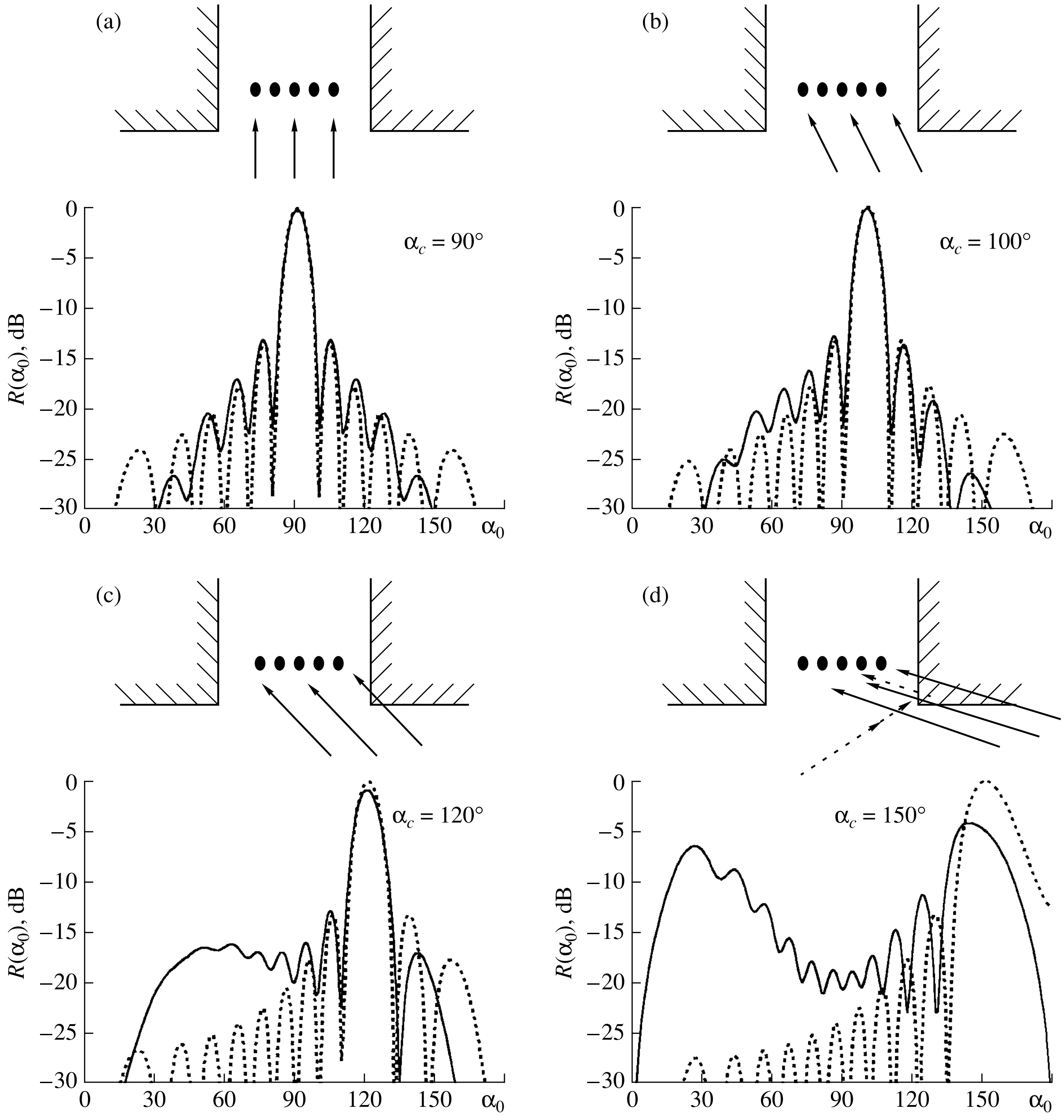

Fig. 8. Directional patterns of the receiver array located inside a semi-infinite waveguide with different compensation angles α_c. The impedances of all surfaces are close to the impedance of an acoustically soft surface. The dotted curves correspond to the directional patterns in free space. Schematic diagrams showing the direction of sound incidence are presented near the corresponding plots: the main lobe steering angle is (a) smaller than the angle of geometric shadowing, (b) coincides with the angle of geometric shadowing, and (c, d) exceeds the angle of geometric shadowing; $kd = 40.0$, $kl = 36.0$, $M = 24$, $w_1 = w_2 = w_p = 0.1 - i0.1$, $ky = 10.0$, and $\alpha_g = 101.3°$.

oscillation mode, which nearly coincides with the piston mode in a waveguide with hard walls. An array of size exceeding the wavelength practically rejects all higher oscillation modes. Therefore, it is impossible to screen the array for decreasing the side-lobe levels with the use of lateral screens with hard walls.

The use of sound-absorbing side walls allows one to decrease the side-lobe levels (Fig. 5), whereas in the case of hard walls (Fig. 6), these levels vary only slightly even if the distance between the array and the slit is twice as large as the waveguide width.

Figure 7 shows similar patterns for an array in a waveguide with walls whose impedances are close to the impedance of an acoustically soft surface. Here, the main lobe somewhat widens and the lateral lobes smooth, as in the case of sound-absorbing walls.

Studying the deformation of the directional pattern is of special practical interest for arrays with an elec-

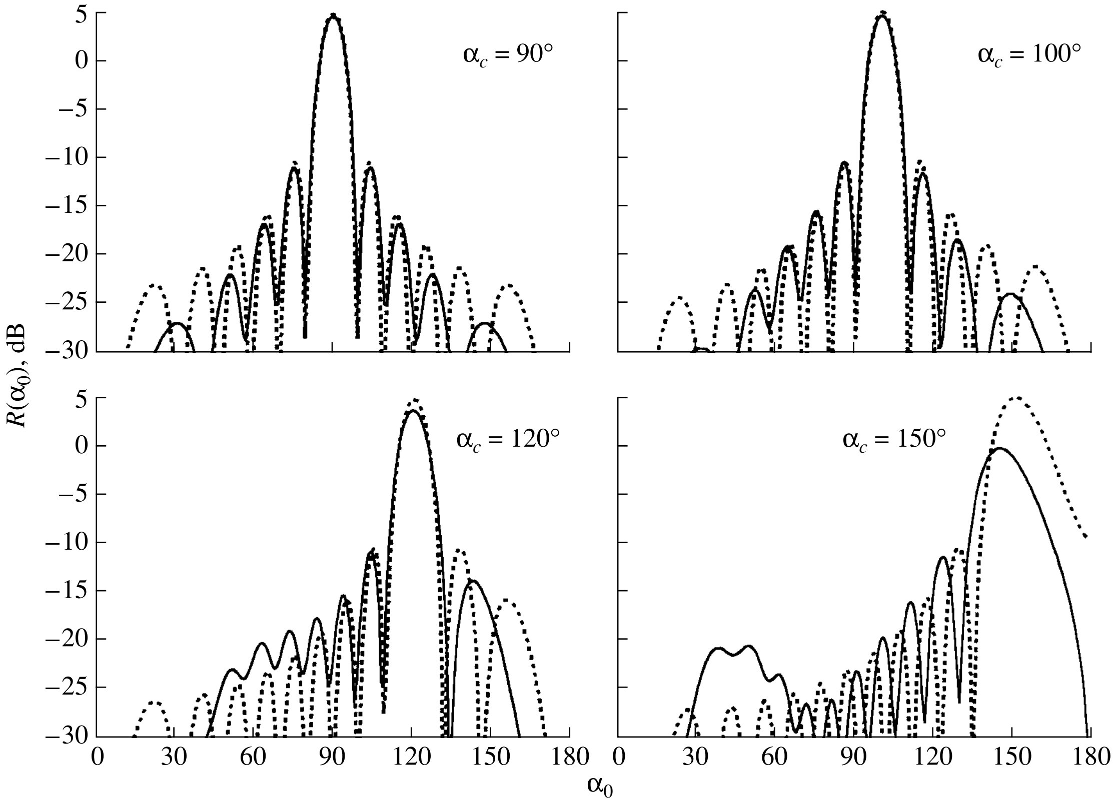

Fig. 9. Directional patterns of the receiver array located inside a semi-infinite waveguide with different compensation angles α_c. The impedances of all surfaces are close to the impedance of a sound absorbing surface. The dotted curves correspond to the directional patterns in free space; $kd = 40.0$, $kl = 36.0$, $M = 24$, $w_1 = w_2 = w_p = 1.0 - i0.1$, $ky = 10.0$, and $\alpha_g = 101.3°$.

tronically steered beam, especially in the case when the beam is partially incident on the waveguide wall. Geometrically, the maximal possible steering angle α_g for which the whole array is seen from the observation point is shown in Fig. 1a. This angle is determined by the relationship $\tan\alpha_g = \pi/2 \pm (d - l)/(2y)$. In the examples shown in Figs. 8 and 9, this angle was 101.3° and the pattern was steered through angles exceeding $\pi/2$.

For steering angles α_c smaller than α_g (see the curves for α_c = 0° and 100°), the diagram varies slightly, as should be expected. With increasing α_c, the array is partially shadowed by the screen edge and the pattern is distorted. For α_c = 150°, almost half of the array is in the geometric shadow. As a result, the amplitude of the received signal decreases, the pattern is strongly distorted, and an additional lobe appears due to the sound reflection from the waveguide wall in the direction specular to the direction of the main lobe. A schematic diagram of sound reflection is shown in Fig. 8.

The curves in Fig. 8 were calculated for impedance walls that nearly perfectly reflect sound. Figure 9 shows another case corresponding to sound-absorbing walls. Calculations were carried out for $w = 1.0 - i0.1$. With this impedance, the side walls are characterized by a reflection coefficient as small as 0.05 for the sound wave incident along the normal to the wall. In this case, the specular lobe decreases and the main lobe level and its width nearly coincide with the corresponding values for the waveguide with sound-absorbing walls.

The results presented in this paper were calculated for a semi-infinite waveguide; however, all above expressions are valid for a finite-length waveguide, i.e., for an open cavity in an impedance screen. Therefore, there is no extra difficulty for determining the effect of a back screen on the directional pattern of the array and on its sensitivity for arbitrary surface impedances. One can determine actual angles of survey by taking into account the diffraction by the edges of lateral screens. In the process of steering the directional pattern, the diffraction causes phase distortions in the received signal, and these distortions are nonsymmetric relative to the direction to the source. As a result, the main lobe is deflected from the compensation direction, i.e., errors occur in the determination of the direction to the source. The above formulas are sufficient for calculating these errors. The results of such calculations will be described in following publications.

ACKNOWLEDGMENTS

This work was supported by the Russian Foundation for Basic Research, project no. 00-02-17840.

REFERENCES

1. E. L. Shenderov, Akust. Zh. **46**, 816 (2000) [Acoust. Phys. **46**, 716 (2000)].
2. A. D. Rawlins, Proc. R. Soc. London, Ser. A **361**, 65 (1978).
3. E. L. Shenderov, *Wave Problems in Hydroacoustics* (Sudostroenie, Leningrad, 1972).
4. E. L. Shenderov, Akust. Zh. **44**, 106 (1998) [Acoust. Phys. **44**, 88 (1998)].
5. A. N. Norris and I. C. Sheng, J. Sound Vibr. **195**, 85 (1989).
6. A. T. Peplow and S. N. Chandler-Wilde, J. Sound Vibr. **223**, 355 (1999).
7. E. L. Shenderov, Akust. Zh. **45**, 661 (1999) [Acoust. Phys. **45**, 589 (1999)].

Translated by A. Vinogradov

Acoustical Physics, Vol. 47, No. 4, 2001, pp. 484–486. Translated from Akusticheskiĭ Zhurnal, Vol. 47, No. 4, 2001, pp. 558–560.
Original Russian Text Copyright © 2001 by Azalinov.

SHORT COMMUNICATIONS

Localized Modes of Vibration of a Plate on the Surface of a Heavy Liquid

D. A. Azalinov

Institute of Problems in Machine Science, Russian Academy of Sciences,
Vasil'evskiĭ Ostrov, Bol'shoĭ pr. 61, St. Petersburg, 199178 Russia
e-mail: azalinov@gp3628.spb.edu; azalinov@euler.ipme.ru

Received August 28, 1999

Much attention is currently attracted to the problems of the determination of the dynamic and acoustic characteristics of floating airdromes and other floating structures on a water surface.

A special feature of contact-boundary problems of this type is the possibility of the localization of waves propagating in the liquid–structure system [1].

The results of solving such problems show the need to determine the conditions for the existence of a discreet spectrum of natural vibration frequencies of such a system (liquid–structure), which can produce the effects of wave localization and resonance. The conditions obtained below are similar to the conditions of the appearance of localized modes of vibration in continuous media with inclusions [2].

The purpose of this paper is to solve the problem of finding the upper and lower boundaries of the discreet spectrum, the cutoff frequencies corresponding to these boundaries, and, consequently, the frequency ranges in which the propagation of flexural gravity waves is possible. The corresponding natural modes of vibration are also determined.

In investigations performed by other authors (for example, in [3, 4]), the possibility of the existence of natural frequencies in such systems was not estimated, not even by the numerical method.

We consider the propagation of flexural gravity waves in a thin plate–liquid system. The propagation of waves occurs in a layer of an ideal incompressible liquid of depth H. A plate of infinite length and a finite width $2a$ floats on the surface of this layer. The coordinate system is chosen so that the y axis is directed along the length of the plate and the z axis is directed upward and passes through the middle of the plate. The upper boundary of the layer outside the region $-a \le x \le a$ is free. The motion of the liquid is assumed to be a potential one. The potential of the velocity of liquid particles is $\Phi(x, y, z, t)$. Disturbances acting in the liquid generate vibrations of the plate that are described by the displacement $\zeta(x, y, t)$. Cooperative vibrations of the liquid and the plate result in a system of surface waves propagating along the x and y axes. The vibrations of the liquid are assumed to be periodic along the y axis with the wave number m and have the frequency ω. We use the approximation of the theory of long waves in shallow water ($kH \ll 1$, where k is the wave number) and seek the potential in the form

$$\Phi(x, y, z, t) = \phi(x)\exp(imy + i\omega t).$$

We divide the region from $-\infty$ to $+\infty$ along the x axis into three parts.

The first and third regions (designated below by the indices 1 and 3) correspond to the free water surface. The velocity potential of water particles in these regions can be written as

$$\frac{\partial^2\phi}{\partial x^2} - \left(m^2 - \frac{1}{gH}\omega^2\right)\phi = 0. \tag{1}$$

For the second region (the plate on the surface of the liquid), we have the system of equations

$$\begin{cases} D\left(\dfrac{\partial^4\zeta}{\partial x^4} + 2\dfrac{\partial^4\zeta}{\partial x^2\partial y^2} + \dfrac{\partial^4\zeta}{\partial y^4}\right) \\ \quad + \rho_1 h\dfrac{\partial^2\zeta}{\partial t^2} + \rho\left(\dfrac{\partial\Phi}{\partial t} + g\zeta\right) = 0 \\ \dfrac{\partial\zeta}{\partial t} = -H\left(\dfrac{\partial^2\Phi}{\partial x^2} + \dfrac{\partial^2\Phi}{\partial y^2}\right), \end{cases} \tag{2}$$

where h is the plate thickness, D is the flexural rigidity, ρ_1 is the density of the plate material, and ρ is the water density.

Using the second equation of system (2), for solving the first equation we derive the following expression with respect to the potential (here, the solution for ζ is taken in the form $\zeta(x, y, t) = \zeta(x)\exp(imy + i\omega t)$):

$$\frac{D}{\rho g}\left(\frac{\partial^6\phi}{\partial x^6} - 3m^2\frac{\partial^4\phi}{\partial y^4} + 3m^4\frac{\partial^2\phi}{\partial x^2} - m^6\phi\right) + \left(\frac{\partial^2\phi}{\partial x^2} - m^2\phi\right)\left(1 - \frac{\rho_1 h}{\rho g}\omega^2\right) + \frac{\omega^2}{gH}\phi = 0. \quad (3)$$

As the boundary conditions, we take the equality of the potentials and paticle velocities of the liquid and the plate for $x = \pm a$ and the zero values of the cutting force (F) and the bending moment (M) at the edges of the plate. For instance, for $x = a$, we have

$$\phi_2 = \phi_3,$$

$$\frac{\partial\phi_2}{\partial x} = \frac{\partial\phi_3}{\partial x},$$

$$M = D\left(\frac{\partial^2\zeta}{\partial x^2} + \sigma\frac{\partial^2\zeta}{\partial y^2}\right) = \frac{\partial^4\phi_2}{\partial x^4} + (1+\sigma)\frac{\partial^4\phi_2}{\partial x^2\partial y^2} + \sigma\frac{\partial^4\phi_2}{\partial y^4} = 0, \quad (4)$$

$$F = -D\left(\frac{\partial^3\zeta}{\partial x^3} + (2-\sigma)\frac{\partial^3\zeta}{\partial x\partial y^2}\right) = \frac{\partial^5\phi_2}{\partial x^5} + (3-\sigma)\frac{\partial^5\phi_2}{\partial x^3\partial y^2} + (2-\sigma)\frac{\partial^5\phi_2}{\partial x\partial y^4} = 0.$$

In addition, the following conditions should be imposed: for $y = \pm\infty$, the potential should be limited and, for $x = \pm\infty$, the Sommerfeld condition should be satisfied.

We seek the solution for the potential in Eqs. (1) and (3) in the form

$$\phi_i(x) = \sum_j e^{\alpha_j x}. \quad (5)$$

Then, Eqs. (1) and (3) are reduced to algebraic equations of the second and sixth degrees with respect to α_j. Omitting the subscript j, we have

$$\alpha^2 - \left(m^2 - \frac{\omega^2}{gH}\right) = 0 \quad \text{for regions 1 and 3}, \quad (6)$$

$$\alpha^6 + A\alpha^4 + B\alpha^2 + C = 0 \quad \text{for region 2}, \quad (7)$$

where

$$A = -3m^2, \quad B = 3m^4 + \frac{\rho g - \rho_1 h\omega^2}{D},$$

$$C = -m^6 + \frac{-H\rho g m^2 + \rho_1 hH\omega^2 m^2 + \omega^2\rho}{DH}.$$

Equation (6) has two roots that are equal in magnitude but opposite in sign; the roots are either real or imaginary. Equation (7) has six roots, four of which are always complex (in the form of $\pm u \pm iv$) and the remaining two are either real or imaginary. The frequency at which the solution passes from the real to the imaginary domain (or in the opposite direction) is the cutoff frequency of the liquid–structure system.

The expression for the cutoff frequency in the regions of free liquid surface on both sides of the plate can be derived from Eq. (1) and is written as

$$\omega_w = m\sqrt{gH}. \quad (8)$$

Similarly, from Eq. (3) we obtain the cutoff frequency for the region corresponding to the infinite plate floating on the water surface:

$$\omega_p = m\sqrt{\frac{H(Dm^4 + \rho g)}{m^2\rho_1 Hh + \rho}}. \quad (9)$$

The lower bound of the discrete spectrum is the cutoff frequency of a waveguide (plate) infinite in one direction, and the upper bound is the cutoff frequency of the medium outside the plate, i.e., in our case, the cutoff frequency of the infinite shallow reservoir.

The localization of waves in the plate region can take place only when the natural real discrete frequency of the system lies within

$$\omega_p < \hat{\omega} < \omega_w. \quad (10)$$

In this case, on the free water surface on both sides of the plate only the attenuation of waves is possible, whereas in the plate itself, travelling waves propagate.

Further analysis of the existence of a discrete spectrum of the system was performed numerically. In the course of solving the problem on eigenvalues, it was established that there is at least one natural frequency of the plate–liquid system that exists only for $\omega_p < \omega_w$ and lies in the range determined by Eq. (10).

As additional investigations showed, the limits of the discrete spectrum, i.e., the corresponding cutoff frequencies, are not natural frequencies of the plate–liquid system.

When the compressibility of the liquid is taken into account, the dispersion dependence representing the frequency versus the wave number will have an additional branch, which begins above the upper cutoff frequency; i.e., this branch lies outside the range in which wave localization is possible.

The figure represents the corresponding mode of natural vibrations. It is symmetric, localized, and attenuates exponentially along the x axis.

In conclusion, we summarize the results obtained from the numerical investigation of the effect of some

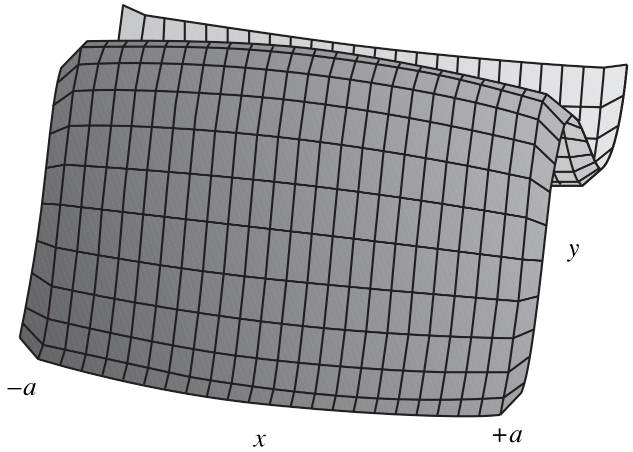

Figure.

parameters of the system on the existence and position of the natural frequency:

(1) As m (the wave number along the y axis) decreases, the natural frequency of the system grows. When the existence of several cutoff frequencies is possible in the range between the cutoff frequencies, the distance between them increases and the range itself is shifted to the left along the frequency axis.

(2) A decrease in the depth of the reservoir results in similar effects.

(3) A decrease in the width of the plate causes a shift of the natural frequency to the right and an increase in the distance between the natural frequencies when there are several.

(4) For the existence of the described localization effect, the plate thickness should fall within a very narrow interval (in the case studied above, it should be within 1 ± 0.2m).

ACKNOWLEDGMENTS

I am grateful to Dr. A.K. Abramyan and Dr. D.A. Indeĭtsev for helpful advice during the investigation.

REFERENCES

1. A. K. Abramian, D. A. Indeitsev, and S. A. Vakulenko, in *Flow, Turbulence and Combustion* (Kluwer Academic, Dordrecht, 1999), Vol. 61, pp. 1–20.
2. A. K. Abramyan and D. A. Indeĭtsev, Akust. Zh. **44**, 437 (1998) [Acoust. Phys. **44**, 371 (1998)].
3. M. Ohkusu and Y. Nanba, in *Proceedings of 11th International Workshop on Water, Waves and Floating Bodies* (Hamburg, 1996).
4. M. Ohkusu and Y. Nanba, in *Proceedings of 13th International Workshop on Water, Waves and Floating Bodies* (Alphen aan den Rijn, 1997), p. 119.

Translated by A. Svechnikov

Acoustical Physics, Vol. 47, No. 4, 2001, pp. 487–489. Translated from Akusticheskiĭ Zhurnal, Vol. 47, No. 4, 2001, pp. 561–563.
Original Russian Text Copyright © 2001 by Badmaev, Damdinov.

SHORT COMMUNICATIONS

Study of the Viscoelastic Properties of Organic Liquids by an Acoustic Method

B. B. Badmaev and B. B. Damdinov
Buryat Scientific Center, Siberian Division, Russian Academy of Sciences,
ul. Sakh'yanovoĭ 8, Ulan-Ude, 670047 Russia
e-mail: lmf@pres.bsc.buryatia.ru

Received August 7, 2000

A special direction of research in molecular physics of liquids is related to the acoustic measurements of their shear viscoelastic properties. The measurements of the shear dynamic properties of liquids represent one of the direct methods for studying the nature and character of the processes of rearrangement of intermolecular structure in them. In recent years, much attention was given to viscoelastic liquids with a non-Newtonian behavior [1–3]. According to the existing concept of the nature of liquids, the shear elasticity of liquids should be observed under shear oscillations with the periods comparable with the time intervals between the liquid particle jumps from the temporary equilibrium states, these intervals being identified with the relaxation time of the nonequilibrium state. The relaxation time is estimated by the self-diffusion rate, and the calculations for low-viscosity liquids yield values of about 10^{-10}–10^{-12} s [1]. Hence, the shear elasticity of such liquids should be observed at the frequencies of shear oscillations of 10^{10}–10^{12} Hz. However, experiments [4, 5] showed that all liquids without exception exhibit shear elasticity at a frequency of 10^5 Hz. This fact suggests that a previously unknown, low-frequency viscoelastic relaxation process occurs in liquids. Presumably, this process is caused by collective interactions of large groups of molecules whose relaxation time can exceed the time intervals corresponding to the temporal stability of individual molecules by many orders of magnitude. One of the characteristic features of the shear mechanical properties of regular liquids is the small value of the mechanical loss tangent ($\tan\theta < 1$). According to the Maxwell rheological model, this means that the relaxation frequency of the process of interest is lower than the frequency used in the experiment. Our previous experiments [6, 7] were performed at a frequency of 74 kHz. Hence, for a better understanding of the nature of the low-frequency viscoelastic relaxation process, one should study the frequency dependence of shear elasticity below 74 kHz.

The presence of the low-frequency shear elasticity was revealed by the resonance method with the use of a piezoelectric quartz resonator. The method is as follows. A 18.5° X-cut quartz crystal with zero Poisson's ratio oscillates at its fundamental resonance frequency. The horizontal surface of the crystal is in contact with a liquid layer covered with a solid strap. The liquid layer experiences shear strains, and shear standing waves are excited in it. The parameters of the resonance curve of the system can vary depending on the thickness of the film. Equating the impedances of the piezoelectric quartz and the liquid, one can derive the following expressions for the complex shift of the resonance frequency of the oscillatory system [6]:

$$\Delta f^* = \frac{SG^*\kappa^*}{4\pi^2 M f_0}\frac{1+\cos(2\kappa^* H-\varphi^*)}{\sin(2\kappa^* H-\varphi^*)}, \qquad (1)$$

where $G^* = G' + iG''$ is the complex shear modulus of the liquid, S is the area of the strap, H is the thickness of the liquid layer, M is the mass of the quartz crystal, f_0 is its resonance frequency, α and β are the attenuation coefficients, κ^* is the complex wave number, and φ^* is the complex phase shift due to the reflection of the shear wave from the liquid–strap boundary. Separating Eq. (1) into the real and imaginary parts, we obtain two expressions for the frequency shifts:

$$\Delta f' = \frac{S}{4\pi^2 M f_0} \times \frac{(G'\beta + G''\alpha)\sin 2\beta H + (G'\alpha - G''\beta)\operatorname{Sh} 2\alpha H}{\operatorname{ch} 2\alpha H - \cos 2\beta H},$$

$$\Delta f'' = \frac{S}{4\pi^2 M f_0} \times \frac{(G''\beta + G'\alpha)\sin 2\beta H + (G''\alpha - G'\beta)\operatorname{Sh} 2\alpha H}{\operatorname{ch} 2\alpha H - \cos 2\beta H}.$$

From these expressions, one can see that the frequency shifts perform damped oscillations, and with the increase in the film thickness, they tend to some limiting values. When the thickness of the liquid layer is

Viscoelastic properties of liquids at the frequencies 40 and 74 kHz

Liquids	40 kHz		74 kHz	
	G'	$\tan\theta$	G'	$\tan\theta$
Petrolatum	1.13	0.60	1.36	0.50
Ethylene glycol	0.39	0.72	0.91	0.24
Diethylene glycol	0.51	0.44	1.22	0.31
Triethylene glycol	0.74	0.65	1.28	0.27
PES-1	1.26	0.18	9.63	0.11
PES-2	0.97	0.19	4.81	0.63
PES-3	0.85	0.21	3.45	0.87
Decane	0.46	0.38	0.54	0.22
Undecane	0.54	0.33	0.58	0.18
Dodecane	0.56	0.32	0.62	0.15
Tridecane	0.58	0.23	0.65	0.15
Pentadecane	0.63	0.13	0.70	0.09
Dibutyl phthalate	0.65	0.29	0.97	0.11
Oleic acid	0.76	0.23	1.63	0.91
Butyl alcohol	0.94	0.22	1.03	0.10

much less than the shear wavelength and the strap is practically at rest, we obtain the following expressions for the real shear modulus and the mechanical loss tangent:

$$G' = \frac{4\pi^2 M f_0 \Delta f' H}{S}, \tag{2}$$

$$\tan\theta = \frac{G''}{G'} = \frac{\Delta f''}{\Delta f'}. \tag{3}$$

The imaginary frequency shift is equal to the variation of the resonance half-width. From Eq. (2), one can see that, if the liquid under study possesses a measurable shear modulus, the real frequency shift must be inversely proportional to the thickness of the liquid layer.

In this paper, we describe the study of the viscoelastic properties of liquids by the resonance method at a frequency of 40 kHz. In studying the shear elasticity of liquids in a wide frequency range, it is impossible to perform all measurements with a single measuring system and even with measuring systems of a single type. For every frequency range, it is necessary to develop special measuring systems. The experiments at 40 kHz were performed by the resonance method using a setup with a piezoelectric crystal whose mass was 13.81 g. The contact area was 0.2 cm^2. An important advantage of the resonance method is that it has no limitations for the viscosity of the liquid under study. The viscosity of the liquid can vary from 10^{-2} to 10^5 P. The disadvantage of the method is that it is realized at a fixed frequency, which cannot be varied. The thickness of the liquid layer is determined by the interference method. The positive shift of the resonance frequency of the oscillatory system testifies to the presence of a shear elasticity. The objects of the studies were different liquids: hydrocarbons, polyethylsiloxanes (PES), glycols, etc. The interest in studying the shear mechanical properties of these liquids is caused, first, by their wide use in engineering. Second, the study of the homologous series of different liquids is of special interest, because a change in the number of links of the chain is accompanied by changes in the shape and size of molecules and in the character of their interaction. All this leads to changes in the viscoelastic properties of liquids of the homologous series. For all liquids studied in our experiment, we obtained linear dependences of the resonance frequency shift on the inverse thickness of the liquid layer. Figure shows the dependences of the frequency shift on the inverse thickness of the liquid layer for three PES liquids. According to Eq. (2), the linearity of the dependences testifies to the presence of the bulk shear elasticity. Using Eqs. (2) and (3), we calculated the values of G' and $\tan\theta$. The results are presented in the table. For comparison, in the second column of the table, we show the values of G' and $\tan\theta$ obtained earlier [7, 8] at a frequency of 74 kHz.

One can see that, for all liquids studied in our experiment, the calculated values of the elastic modulus are smaller than the values obtained at 74 kHz. The mechanical loss tangents are greater than at 74 kHz. For example, for ethylene glycol, the real shear modulus is 0.39×10^5 Pa at the frequency 40 kHz and 0.91×10^5 Pa at 74 kHz. The mechanical loss tangent is 0.72 at 40 kHz and 0.24 at 74 kHz.

From the simple Maxwell rheological model with a single relaxation time, it follows that at the relaxation frequency, the mechanical loss tangent is equal to unity. Hence, the relaxation frequencies of all liquids studied in the experiment lie below 40 kHz. Therefore, it is of interest to study the shear elasticity at lower frequencies.

From the results of this study, we can draw the following conclusions:

(i) All liquids studied in the experiment possess measurable shear moduli at the given frequencies of shear oscillations.

(ii) The presence of the low-frequency shear elasticity in regular and low-viscosity liquids means that the values of the shear stress relaxation time estimated on the basis of the time within which single liquid molecules remain in the temporal equilibrium states are

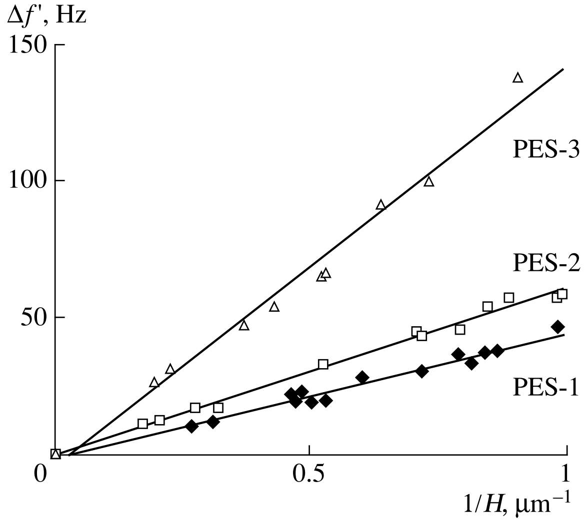

Dependence of the real part of the resonance frequency shift on the inverse thickness of the liquid layer for polyethylsiloxane liquids (PES) at a frequency of 40 kHz.

wrong and confirms the hypothesis that the dominant role is played by the collective interactions of large groups of molecules.

(iii) To obtain a full description of the low-frequency relaxation process in liquids, it is necessary to perform comprehensive studies for different frequencies, temperatures, shear angles, etc.

ACKNOWLEDGMENTS

This work was supported by the Russian Foundation for Basic Research, project nos. 98-01-00503 and 98-01-00504.

REFERENCES

1. J.-C. Majeste, J.-P. Montfort, A. Allal, and G. Marin, Rheol. Acta **37**, 486 (1998).
2. R. B. Mankar, D. N. Saraf, and S. K. Gupta, Rheol. Acta **38**, 84 (1998).
3. N. Phan-Thien and M. Safari-Ardi, J. Non-Newtonian Fluid Mech. **74**, 137 (1998).
4. U. B. Bazaron, B. V. Deryagin, and A. V. Bulgadaev, Zh. Éksp. Teor. Fiz. **51**, 969 (1966) [Sov. Phys. JETP **24**, 645 (1967)].
5. B. V. Derjaguin, B. B. Badmaev, U. B. Bazaron, *et al.*, Phys. Chem. Liq. **29**, 201 (1995).
6. B. B. Badmaev, O. R. Budaev, and T. S. Dembelova, Akust. Zh. **45**, 610 (1999) [Acoust. Phys. **45**, 541 (1999)].
7. B. B. Badmaev, U. B. Bazaron, O. R. Budaev, *et al.*, Kolloidn. Zh. **44**, 841 (1982).
8. B. B. Damdinov, B. B. Badmaev, O. R. Budaev, and M. N. Ivanova, in *Acoustics at the Threshold of the 21st Century* (Mosk. Gorn. Univ., Moscow, 1997), pp. 35–38.

Translated by E. Golyamina

Acoustical Physics, Vol. 47, No. 4, 2001, pp. 490–492. Translated from Akusticheskiĭ Zhurnal, Vol. 47, No. 4, 2001, pp. 564–566.
Original Russian Text Copyright © 2001 by Kalinov, Kondrat'ev, Nikitin, Rimlyand.

SHORT COMMUNICATIONS

Accuracy of Measuring the Levels of Liquids in Tanks by the Acoustic Echo Method

G. A. Kalinov, A. I. Kondrat'ev, O. A. Nikitin, and V. I. Rimlyand
Khabarovsk State Technical University, ul. Tikhookeanskaya 136, Khabarovsk, 680035 Russia
e-mail: riml@fizika.khstu.ru

Received November 12, 1999

Various ultrasonic methods of measuring the levels of liquids in tanks have been actively developed in recent years [1–3]. One of the methods is echo sounding with the use of a reference arm for determining the sound velocity C in air [4, 5]. The use of the reference arm in stationary conditions makes it possible to reduce the measurement errors to the error in determining the length of the reference arm. However, under real conditions, because of heating, high water content, and continuous agitation of the liquid itself, the use of this method for measuring the levels of heavy petroleum products is associated with a number of difficulties, such as the presence of temperature gradients and convection, as well as a high vapor content in air inside a tank. The purpose of this paper is to make an experimental estimate of the errors associated with the use of the method of echo sounding for measuring the level of the liquid in a real tank with fuel oil with allowance for the temperature dependence of the sound velocity. The experiments were performed in a storage tank with fuel oil with a capacity of 1000 t and a height of 10.7 m.

In the measurements, we used a special automated system. An ultrasonic pulse was excited by a radiator and recorded by a receiver of original design made on the basis of piezoceramics with the maximum of the amplitude–frequency response in the range 54–58 kHz. The amplitude of the exciting pulse was about 200 V, and the duration of the pulse was about 20 μs. The radiator and the receiver were installed on a common base with a reference reflector being rigidly attached to it at a distance of $h_r = 1000 \pm 0.2$ mm. From the piezoelectric receiver, the amplified signal was fed to an A/D converter of the controller of a computer and was recorded in a digital form in the computer memory. The clock rate of the A/D converter was 500 kHz. The time of arrival of the reflected signal was calculated by a special algorithm on the basis of the recorded ensembles of realizations. The main operations of the algorithm were as follows: the determination of the level of the background noise for every realization and the detection; the averaging over the given number of realizations N; the determination of the common envelope of the signal (the demodulation); the identification of the pulses corresponding to the reflections from the reference reflector and the liquid surface by integral properties; and the calculation of the times of arrivals of the signals from the reference reflector t_r and from the fuel oil surface t_s (by the level of 1.5% of the pulse amplitude). During the measurements, a base with the radiator, receiver, and reference reflector attached to it was installed in the upper access opening of the tank.

Under laboratory conditions (at a constant temperature and in the absence of convection), the experimental error of measurements did not exceed 1.2 cm for the distance to reflecting surface $h = 10$ m. The sensitivity of the system was 0.2 mm for $h = 2$ m and 1 mm for $h = 10$ m. The measurements in a tank were performed for various levels of fuel oil in winter with the temperature of outside air from –10 to –20°C. The temperature of transducers was 15–25°C and was actually equal to the temperature in the upper part of the tank (T_0). The temperature of the fuel oil surface (T_2) varied from 70°C (for minimal levels) to 35°C (for a full tank).

The position of the level was checked by a special lead-and-line with an accuracy of 0.3 cm. The sensitivity of the measuring system in the case of the measurements in a tank with $h = 10$ m was 5 mm.

For calculating the temperature correction to the sound velocity, the measurements of air temperature variation from the fuel oil surface to the upper part of the tank along the axis of the ultrasonic beam were performed. Figure 1 shows the typical dependences for three values of h (x is the distance from the radiator to the point of measurement). In the dependences obtained for $h \geq 5.5$ m, the variation of the air temperature can be represented in the form of two linear sections (in the upper part of the tank and near the liquid surface) and a section with a relatively constant temperature in the middle part of the tank. The total change in the temperature $\Delta T = T_2 - T_0$ is equal to 40–50°C.

The table shows the experimental values of the temperature and the sound velocities C_s and C_r calculated from t_s and t_r, respectively.

For all h, the experimental values of C_r are 2–3 m/s greater than the values calculated theoretically from the values of T_0 and the temperature profile at $x = 0$–1 m. This result is connected with the fact that the measurement of C_r makes it possible, if only in part, to take into account the influence of uncontrollable parameters (humidity and chemical composition of air) on the speed of sound [1, 6].

Figure 2 displays the experimental dependences of the difference $\Delta C = C_s - C_r$ and the value of the temperature correction to the sound velocity

$$\Delta C_T = \frac{1}{h}\int_0^h C(x)dx - C_0,$$

which was calculated from the temperature profiles, as functions of h. In the calculations, we assumed that $C(x) = C_0\sqrt{[T_0 + \Delta T(x)]/T_0}$, and, for $T = 273$ K, $C = 331.45$ m/s [7]. As is seen from the figure, the temperature correction ΔC_T makes 80–90% of the experimental difference ΔC, and a good correlation between them is observed. In terms of distance, the differences ΔC and ΔC_T for $h = 10$ m correspond to the distances $\Delta h = 43$ cm and $\Delta h_T = 37.5$ cm, respectively. Thus, taking into account the temperature, one can increase the accuracy of the level measurement by a factor of 5–6. The difference $\Delta C_p = \Delta C - \Delta C_T$ (Fig. 2) can be regarded as a systematic error of the considered method due to the influence of humidity varying with height and the air convection, which are difficult to take into account.

The described experiments have shown that, in the measurements in a tank, the value of the root-mean-square deviation of the experimental values of the velocity, $\sigma(C_s)$, which characterizes the random component of the error, considerably increases. The values of $\sigma(C_s)$ were calculated by ten measurements with $N = 100$ for every measurement. The duration of one measurement for $N = 100$ was 5 s, and the interval between the measurements was 100 s. Under laboratory conditions, in the absence of temperature gradients and convection, $\sigma(C_s)$ was 0.2 m/s for $h = 10$ m. The growth of $\sigma(C_s)$ in the tank measurements was determined mainly by the changes in the propagation conditions of the ultrasonic pulse with time due to convective flows.

Figure 2 also displays the summary absolute error in determining the velocity $\Delta C_d + \sigma(C_s)$. When the distance to the fuel oil surface is 10 m, the error is close to 3 m/s, which corresponds to an absolute error of 8.3 cm in determining h, or a relative error of 0.8%. These values are likely to be close to the limiting errors of this method in measuring the level of heavy petroleum products.

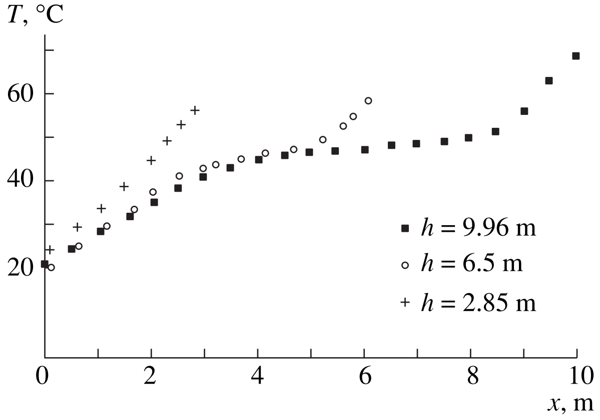

Fig. 1. Temperature of air in a tank for various distances to the surface of fuel oil: (■) 9.96, (○) 6.5, and (+) 2.85 m.

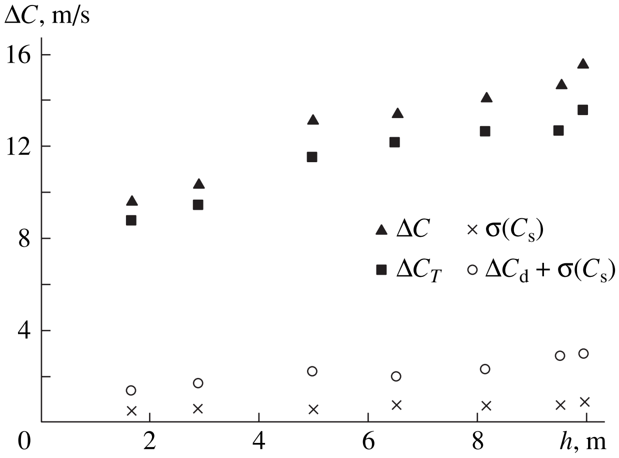

Fig. 2. Dependences of the parameters determining the difference between the theoretical and experimental sound velocities ΔC on the distance h.

In the measurements in a tank for h exceeding 5–6 m, the appearance of false echo-pulses with the amplitudes (U_f) reaching 0.02–0.05 s of the amplitude of the main reflected pulse ($\bar{U}$) was observed in some cases. The false pulse was about 6 ms ahead of the main pulse reflected from the fuel oil surface, which corresponds to two meters of distance and approximately coincides with the beginning of the second region of the sharp increase in temperature (Fig. 1). The appearance of a false pulse can be explained by the formation of a gas layer adjacent to the surface of the fuel oil and characterized by an acoustic impedance (Z_l) noticeably different from the acoustic impedance of the main volume of gas (Z_g). This layer can be caused by steady convective

Experimental values of the temperature and the sound velocities C_s and C_r for various distances to the fuel oil surface h

h, m	T_0, K	ΔT, K	C_s, m/s	C_r, m/s
1.64	296	30	363.6	353.9
2.85	296	33	363.5	353.1
4.97	294	39	360.1	346.9
6.50	293	42	359.2	345.7
8.15	293	43	359.4	345.2
9.53	294	43	360.8	346.3
9.96	294	47	361.3	345.7

flows in a tank, which arise at certain temperature conditions and fuel oil levels. We will estimate the possible changes in the impedance at the boundary of such a layer. The amplitude ratio of the false pulse and the pulse reflected from the fuel oil surface is determined by the relation

$$\frac{U_f}{\overline{U}} = \frac{R}{WW^*} = \frac{(Z_l + Z_g)(Z_l - Z_g)}{4Z_lZ_g} \approx \frac{\rho_lC_l - \rho_gC_g}{2\rho_gC_g}, \qquad (10)$$

where R, W, and W^* are the coefficients of reflection and transmission at the gas–layer boundary, and ρ_l, C_l and ρ_g, C_g are the density and sound velocity corresponding to the layer and the gas above it, respectively.

Using the results of paper [1] and assuming that the changes are caused by the difference in the temperatures of the layer and the adjacent gas δT and by the presence of vapor, we obtain

$$\frac{U_f}{\overline{U}} = \frac{\delta\rho}{2\rho_g} + \frac{\delta C}{2C_g} \approx \frac{\delta\rho}{4\rho_g} \approx -\left[1 + \frac{M_g - M_v}{RT}Q\xi\right]\frac{\delta T}{4T},$$

where $\delta\rho$ and δC are the changes in the density and velocity in passing from gas into the layer; M_v and M_g are the molar masses of vapor and gas, respectively; Q is the specific heat of vaporization; and ξ is the mass fraction of vapor in the mixture.

For fixed values of $U/\overline{U}$ and $\xi = 0.12$ (which corresponds to a temperature of 50°C), the temperature difference δT is 10–20 K, which is in good agreement with the results of the temperature measurements.

From the results of this study, we draw the following conclusions on the possibility of using the method under consideration for measuring the levels of heavy petroleum products:

(1) Taking into account the temperature profile of the air column above the liquid, it is possible to considerably reduce the error of measurement. However, the presence of convective flows of air with high vapor content restricts the accuracy of the level measurement to the value of the order of 10 cm for a base of 10 m.

(2) In tanks of large capacity with low levels of liquid and sufficiently high temperature gradients, the appearance of additional reflections is possible due to the gas stratification in temperature and density of saturated vapor above the liquid.

REFERENCES

1. M. S. Klyuev, S. P. Klyuev, and V. V. Krasnoborod'ko, Akust. Zh. **45**, 825 (1999) [Acoust. Phys. **45**, 743 (1999)].
2. V. A. Kabatchikov, Patent of the Russian Federation No. 2064666 (1996).
3. D. S. Nyce, M. G. Togneri, and R. S. Bulkowski, U.S. Patent No. 5848549 (1998).
4. V. K. Khamidullin, *Ultrasonic Control and Measuring Devices and Systems* (Leningr. Gos. Univ., Leningrad, 1989).
5. Stapleton *et al.*, U.S. Patent No. 5085077 (1992).
6. O. Cramer, J. Acoust. Soc. Am. **93**, 2510 (1993).
7. *Tables of Physical Data: Handbook*, Ed. by I. K. Kikoin (Atomizdat, Moscow, 1976).

Translated by A. Svechnikov

Acoustical Physics, Vol. 47, No. 4, 2001, p. 493. Translated from Akusticheskiĭ Zhurnal, Vol. 47, No. 4, 2001, p. 567.
Original Russian Text Copyright © 2001 by the Editorial Board.

CHRONICLE

Rostislav Yur'evich Popov (On His 70th Birthday)

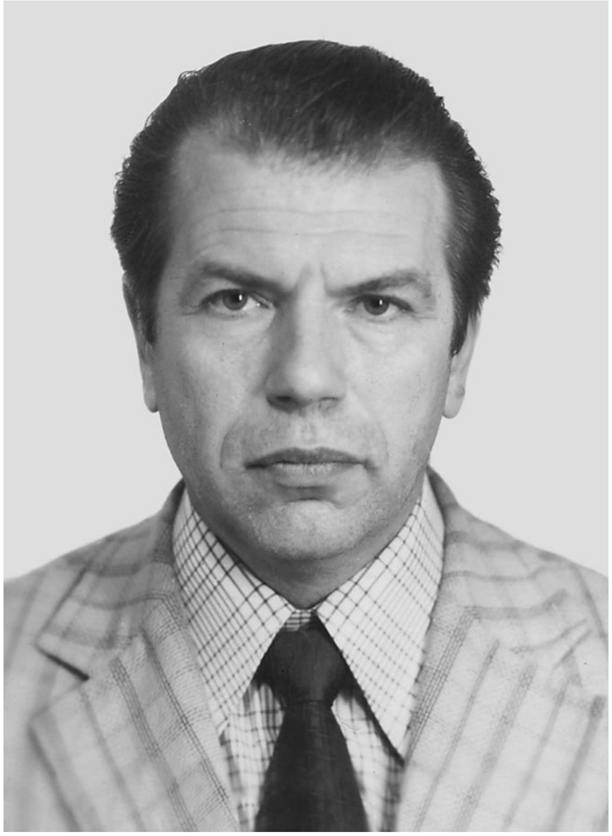

On January 21, 2001, Rostislav Yur'evich Popov, a well-known scientist working in ocean acoustics and the head of a laboratory of the Andreev Acoustics Institute, turned seventy.

Popov graduated from the Physics faculty of Moscow State University in 1954. His first job was at the Publishing House for Foreign Literature where he held the position of a scientific editor in physics until 1962. Then, he moved to the Acoustics Institute, which has become his permanent place of work.

Popov's scientific interests lie with the basic problems of ocean acoustics. Popov has studied the space–time variability of sound fields in the ocean, the fluctuations of tone and broadband signals transmitted through long distances in the deep ocean and on the coastal shelf, the characteristics of reverberation signals and the specific features of bottom reverberation, the correlation between different kinds of signals, and many other phenomena. He obtained a number of important results that have found practical application. In 1975, Popov defended his candidate dissertation. In 1981, he received the title of senior researcher. Popov is the author of about 100 scientific papers and reports; he supervises the work of postgraduate students and applicants for scientific degrees.

Ocean acoustics is a science mainly based on the results of experimental studies. Being one of the leading specialists in underwater acoustics, Popov headed many oceanic expeditions that were carried out on the research ships of the Acoustics Institute to the Atlantic, Indian, and Pacific oceans. He prepared and supervised the experimental studies of acoustic characteristics of several ocean regions under large cooperative projects of different organizations, such as the Vostok-81 project. Popov also supervised comprehensive research projects, the results of which were used in the development of new underwater acoustic systems.

Rostislav Yur'evich Popov has authority with his colleagues as a competent scientist and a benevolent and kind person. We wish him good health, success, and further achievements in his creative work.

Translated by E. Golyamina

1063-7710/01/4704-0493$21.00 © 2001 MAIK "Nauka/Interperiodica"

Acoustical Physics, Vol. 47, No. 4, 2001, pp. 494–495. Translated from Akusticheskiĭ Zhurnal, Vol. 47, No. 4, 2001, pp. 568–569.
Original Russian Text Copyright © 2001 by the Editorial Board.

Konstantin Dmitrievich Sabinin (On His 70th Birthday)

November 26, 2000 marked the 70th birthday of the well-known Russian oceanologist Konstantin Dmitrievich Sabinin, Doctor of Physics and Mathematics, Professor, and head of the Oceanology Laboratory of the Andreev Acoustics Institute.

Sabinin was born in 1930 to the family of an outstanding biologist Dmitriĭ Anatol’evich Sabinin. In 1953 he graduated with honors from Moscow State University, as one of the first graduates of the Oceanology department. Then he joined the staff of the department and taught and conducted research under the guidance of one of the founders of Russian oceanology, Nikolaĭ Nikolaevich Zubov. Sabinin received his Candidate of Science degree in 1960. His thesis was based on oceanographic observations in the Arctic.

Starting from 1961 and continuing up to this day, Sabinin’s scientific activities have been connected with the Andreev Acoustics Institute where he heads the laboratory founded on the suggestion by Leonid Maksimovich Brekhovskikh for acoustic-oceanologic research. In 1978 Sabinin defended his thesis for the degree of Doctor of Science, which was devoted to the properties of internal waves in the ocean. It included the results of multiple original full-scale observations in the Atlantic, Pacific, and Indian oceans. Sabinin received the title of Professor of Acoustics in 1988. During the past few years, he has combined his job at the Acoustics Institute with research activities at the Institute of Space Research, Russian Academy of Sciences, where he is developing new techniques of sea monitoring which combine remote satellite and acoustical methods.

The major topic of Sabinin’s work for many years was specifically internal waves in the ocean. However, the area of his research interests was always very broad and included the wave variability of the ocean, synoptic eddies and lenses, processes on the shelf, various interactions of waves, techniques of oceanic measurements, and the influence of various wave motions on sound propagation in the ocean. At the same time, acoustic signals were considered by Sabinin as a powerful tool for investigation of the ocean.

Almost from the very start of his research expeditions in the ocean, Sabinin turned his attention to short internal waves, which were on average hardly noticeable and therefore escaped the attention of many observers. Short internal waves have a nonlinear nature and play an important role in the formation of the appearance of the ocean. The work in this direction of research coincided with the growth of interest in nonlinear waves in general and in nonlinear effects in oceanic motions in particular. Later on, observations on short internal waves allowed him to reveal the relationship between these waves and the currents and thermocline structure in the ocean. A logical consequence of these studies was the discovery and detailed description of intense nonlinear waves that arise under the effect of tides in the Indian Ocean and have the character of internal solitons. Short internal waves together with internal tides considerably influence the propagation of acoustic signals in the ocean due to their relatively large intensity and regular structure.

In the last decade, Sabinin has been giving more and more attention to the application of acoustic methods to the investigation and monitoring of the ocean. Under his initiative, the research vessel *Akademik Nicolaĭ Andreev* took part in the first international global experiment on acoustic thermometry of the ocean in 1990, which was headed by Walter Munk. This experiment

1063-7710/01/4704-0494$21.00 © 2001 MAIK “Nauka/Interperiodica”

was the start of a long-term research program ATOC (Acoustic Thermometry of the Oceanic Climate). Collaborating actively in the Arctic part of this program, Sabinin has shown that using the acoustic halinometry developed by him, it is possible to monitor the salinity of the upper layer of icy seas, which is especially important for the Arctic Ocean, where monitoring of this characteristic (which is very important for the oceanic climate) by other methods is almost impossible.

Nowadays, using his vast knowledge of various fields of oceanology and abundant experience in oceanic research, Sabinin is successfully developing a complex monitoring of sea areas that combines acoustic, satellite, and traditional oceanographic measurements into a unified system of observations on the state of the sea medium and the processes in it.

Many of Sabinin's publications are devoted to various features of internal waves and other oceanic motions. He realized his long-term desire to illustratively explain the observed properties of internal waves and processes in the ocean in the book *Waves within the Ocean* (Gidrometeoizdat, 1992; in collaboration with K.V. Konyaev). Seven of Sabinin's students have received the degrees of Candidate of Science under his supervision, and three of his close collaborators became Doctors of Science.

Sabinin is a cochairman of the seminar "Dynamics of Natural Media." He is a member of the Scientific Council of the Andreev Acoustics Institute and the qualification councils at the Acoustics Institute and Moscow State University. He is a member of the National Oceanographic Committee, the Russian Acoustical Society, and the Editorial Board of the *Morskoĭ Gidrofizicheskiĭ Zhurnal* (Marine Hydrophysical Journal) of the National Academy of Sciences of Ukraine. Sabinin collaborates actively with many foreign researchers and in particular with researchers from the Woods Hole Oceanographic Institute (USA), where he carried out long-term studies.

We wish Konstantin Dmitrievich Sabinin further success in his creative work.

Translated by M. Lyamshev

Acoustical Physics, Vol. 47, No. 4, 2001, pp. 496–498. Translated from Akusticheskiĭ Zhurnal, Vol. 47, No. 4, 2001, pp. 570–572.
Original Russian Text Copyright © 2001 by Kouzov, Shenderov.

INFORMATION

St. Petersburg Workshop on Computational and Theoretical Acoustics Held in 2000 by the Scientific Council on Acoustics of the Russian Academy of Sciences

In 2000, the regular session of the St. Petersburg workshop on computational and theoretical acoustics of the Scientific Council on Acoustics of the Russian Academy of Sciences took place. The information on the previous sessions was published in *Acoustical Physics*: **43**, 575 (1997) and **46**, 718 (2000). Below, we briefly review the reports presented at the workshop in 2000.

Two reports by I.V. Andronov were devoted to wave propagation along a narrow crack in an elastic plate in contact with an acoustic medium. The author studied the propagation of symmetric and antisymmetric waves an showed that a symmetric wave exists at any parameters of the plate–medium system and at any frequencies, whereas an antisymmetric wave is possible only when the density of the acoustic medium is not too high and only in a limited frequency range. The author considered the energy flows transferred by symmetric and antisymmetric waves and also the forms of the plate displacements corresponding to these waves.

The propagation of waves of different origin in smoothly inhomogeneous stratified media was considered by A.V. Aref’ev. This study was based on the space–time ray approach and the use of the two-scale asymptotic expansion technique. Aref’ev studied surface waves propagating along a free boundary of an isotropic viscoelastic halfspace (the vector problem) and high-frequency acoustic oscillations in a weakly nonstationary acoustic waveguide (the scalar problem). The author called the latter quasi-normal waves. Aref’ev determined the factor describing the wave attenuation along the ray for Love and Rayleigh waves and derived the expression for their stray components. He obtained the high-frequency asymptotic expansions for quasi-normal waves of a surface oceanic waveguide in the case of the violation of adiabatic conditions.

The report presented by V.S. Buldyrev and N.G. Gel’freĭkh was devoted to the study of the asymptotics of the scattered field in the insonified region in the context of the problem of sound diffraction by a thin elastic shell. The boundary condition for the sound pressure was derived for the case of sound diffraction by a convex cylindrical shell described by the Kirchhoff–Love equations. The method of reference problems was used to obtain the formal asymptotic solution in the insonified region. This solution contained a wave associated with the propagation of longitudinal vibrations along the shell. In his other report, V.S. Buldyrev considered the equations with pseudo-differential operators in the theory of wave propagation and constructed asymptotic solutions to such equations.

S.V. Romashkin studied the scattering properties of an infinite periodic plane lattice of elastic cylinders with the linear-slip boundary conditions between the cylinders and the elastic medium. Such a model can be used for simulating the scattering properties of a system of inclusions in a medium when the interface between them is not clearly defined. The problem on the interaction of a longitudinal elastic plane wave with such a lattice was solved by the method of separation of variables. An infinite system of linear algebraic equations was obtained in a matrix form, which included the matrix characterizing the state of the interface. A numerical analysis of the transmission and reflection factors was performed for different combinations of the parameters of the lattice, the interface, and the medium. The results of this study can be used in the applied problems of nondestructive testing of metal products.

M.A. Lyalinov considered the scattering of a steady-state plane acoustic wave by the vertex of an arbitrary pyramid (a regular trihedral cone) with the Dirichlet boundary conditions at its faces. An integral transform was used to separate the radial variable, and the Dirichlet boundary problem was formulated for the Laplace–Beltrami–type operator on a unit sphere containing a hole made by an infinite cone. The main result of this study is related to the explicit solution of the problem on the diffraction by a sphere with a triangular hole. At first, the author considered the axisymmetric incidence of a plane wave and constructed the exact solution to the problem for the spectral function. Then, he discussed the generalization of the solution to the case with a nonaxisymmetric incidence and a poly-

1063-7710/01/4704-0496$21.00 © 2001 MAIK “Nauka/Interperiodica”

hedral regular pyramid. A closed expression was proposed for the scattering diagram of a diverging spherical wave originating from the pyramid vertex.

The report by V.D. Luk'yanov and G.L. Nikitin was concerned with the solution of the problem on the acoustic wave radiation by a spherical shell surrounding the vertex of a perfectly rigid infinite cone. The shell separates two different acoustic media, which occupy the space outside the cone. The oscillations that occur in the system are excited by an external force applied to the shell. An exact analytical solution of this problem is derived, and on its basis, the directional patterns of the acoustic radiation produced by the shell are obtained. The dependences of the excitation coefficients of spherical harmonics on the frequency of the driving force are calculated.

V.D. Luk'yanov considered the problem on the acoustic wave excitation by thin elastic bodies and obtained the energy relation that follows from the energy conservation law and relates the characteristics of the driving force applied to the body to the parameters of the acoustic field generated by this body. To obtain an identity of the type of the optical theorem, the problem of wave radiation is replaced by the equivalent problem on the scattering of specially selected waves and then the energy conservation law is applied to the scattering problem.

The report by É.P. Babaĭlov was concerned with the determination of the natural frequencies of a thin spherical shell in a compressible medium for the first two modes of vibration. The author determined the conditions at which the natural vibrations of the shell are aperiodic in the absence of losses in both the shell material and the surrounding medium.

The report presented by S.A. Nazarov and I.V. Kamotskiĭ was devoted to the edge effects in the theory of thin plates and to the localization of eigenfunctions near the edges. The authors determined and justified the asymptotic representations of the eigenfunctions localized in the vicinity of the edge of a thin plate, or near a single point at the edge (away from the aforementioned sets, the functions attenuate according to the exponential law). These eigenfunctions are closely related to the boundary layer phenomenon. They appear when the region is of a trap type. Specific examples were calculated for the Helmholtz equation in a thin cylinder with a small perturbation of the lateral surface; the Dirichlet boundary conditions were set at the cylinder ends, and the Neumann conditions were set at the edge.

E.L. Shenderov considered the diffraction of sound by an elastic cylinder placed near an elastic halfspace. The solution of the problem is based on a relation of the Helmholtz integral equation type and on the use of the Green's function for an elastic halfspace. Such a function is represented in the form of a Sommerfeld integral along a contour on the complex plane of the angles of the wave incidence on the halfspace boundary. An integral equation is obtained for the distribution of the sound pressure on the cylinder surface; this equation is reduced to an infinite system of equations in the expansion coefficients of the Fourier series expansion of the aforementioned distribution. The results are valid for the diffraction of cylindrical and plane waves. In addition, they describe the scattered field in the case of the diffraction of a spherical wave when the transmission and reception points are far from the cylinder and lie in one plane that is perpendicular to the cylinder axis. The author calculated the two-point scattering diagrams and the backscattering diagrams as well as the frequency characteristics of the backscattered wave amplitude. The results show that the dependences of the scattered wave amplitude on the angle of incidence and on frequency exhibit an oscillatory behavior, which is explained by the resonance properties of the cylinder and by the interference of multiply scattered waves between the cylinder and the plane.

The report presented by E.V. Ivanova was concerned with high-frequency free vibrations of plates in the Reissner-type theory. This theory is known to contain three spectra of natural frequencies: one low-frequency spectrum and two high-frequency ones. Ivanova considered the high-frequency natural vibrations of plates. Using an asymptotic analysis, she showed that the changes that occur in the quantities determining the stress–strain state of the plate in the cases of high-frequency and low-frequency vibrations are essentially different. In the case of high-frequency vibrations, functions of the boundary-layer type are absent, whereas other functions, which rapidly vary with the spatial coordinates and penetrate through the whole plate region, are present. An approximate formulation of the problem on high-frequency natural vibrations of a plate was proposed, this formulation containing only the functions that slowly vary with the spatial coordinates. The proposed formulation of the problem is of the fourth order in time and describes only the high-frequency vibrations.

A.V. Pyshin obtained some strict solutions for the forced vibrations of bounded rods and beams. He analyzed the possibility of an analytical solution of the problem on the longitudinal vibrations of a rod with a varying cross-section. He determined two classes of dependences of the rod cross-section on the longitudinal coordinate for which the differential equation describing the longitudinal vibrations of the rod had a solution representable in terms of elementary functions. It was shown that, for a particular case of a rod being a fusiform body of revolution, the differential equation describing its longitudinal vibrations can also be solved in terms of elementary functions. The author determined the eigenvalues of the problem on the longitudinal vibrations of a rod with free ends. He considered the problem on the forced longitudinal vibrations of a fusiform rod with free ends under a concentrated longitudinal force applied in an arbitrary cross-section of the rod. The solution to the problem (the Green's function) was obtained in the form of an infinite series expansion in eigenfunctions, and it was also represented in terms of elementary functions.

The participants of the workshop are grateful to the Deputy Director of the Institute of Problems of Machine Science of the Russian Academy of Sciences D.A. Indeĭtsev for his assistance in organizing the workshop. We invite all those interested in the workshop to join in the next session.

D.P. Kouzov and E.L. Shenderov

Translated by E. Golyamina

Acoustical Physics, Vol. 47, No. 4, 2001, pp. 499–502. Translated from Akusticheskiĭ Zhurnal, Vol. 47, No. 4, 2001, pp. 573–576.
Original Russian Text Copyright © 2001 by Lyamshev.

INFORMATION

The 8th International Workshop on Modern Acoustics—Nondestructive Evaluation

The 8th International Workshop on Modern Acoustics—Nondestructive Evaluation was held in Nanjing (China) October 28–31, 2000. It was organized by Nanjing University and supported by the National Science and Technology Ministry, the National Natural Science Foundation, and other institutions from China, as well as by foreign institutions and societies. Professor Shu-Yi Zhang (China) and Dr. R.L. Thomas (USA) co-chaired the workshop. Over 120 researchers and experts from Belarus, Belgium, Great Britain, Germany, Canada, China, Korea, Malaysia, Russia, Singapore, the United States, the Republic of South Africa, and Japan took part, and over 120 papers in physical acoustics, nondestructive evaluation, laser ultrasonics, photoacoustics, medical acoustics, and other fields were presented. Invited lecturers delivered over 30 lectures. Oral presentations and poster papers were also given.

Below we give a brief review of several papers which characterize to a certain extent the workshop agenda and its scientific level.

A paper by R. Wei (China), “Unity of Soliton and Chaos in Faraday Wave Experiment,” presented the results of numerical experiments characterizing the formation of solitons and chaos in Faraday waves. A possibility of coexistence of solitons and chaos was demonstrated. It was stressed that solitons and chaos are the phenomena prevailing in the experiments with Faraday waves.

W. Eisenmenger (Germany) presented a paper “High Precision Acoustic Measurements in ESWL, HIFU, and SBSL with the Fiber Optic Probe Hydrophone (FOPH)” that was devoted to the description of a fiber-optic probe hydrophone (FOPH) and its applications to extracorporeal shock-wave lithotripsy (ESWL), highly focused ultrasound (HIFU), and single bubble sonoluminescence (SBSL). The characteristics of a fiber-optic probe hydrophone were compared with the parameters of a probe hydrophone manufactured using a PVDF piezoelectric polymer film. The fiber-optic hydrophones developed by Eisenmenger provide an opportunity to measure an acoustic field with a spatial resolution of ±0.05 mm within the frequency band up to 60 MHz. They have a broad dynamic range and can be used to measure shock waves in fluids with amplitudes up to 5 atm.

A paper by L. Sui, G. Miao, and R. Wei (China) “The Surface Wave and Transport in Oscillated Granular Materials” aroused considerable interest. The paper presents the results of an experimental investigation of the surface instability in a granular medium and of the transport of its particles (grains) under the effect of vibrations in an oscillating medium. A phenomenon of grain transfer upwards, along an oblique plane, under the effect of vibrations was discovered. A diagram in the f–Γ phase plane, which describes the transport of granular materials, was presented. Here, f is the vibration frequency, $\Gamma = 4\pi^2 f^2 A/g$ is the dimensionless acceleration, A is the vibration amplitude, and g is the acceleration of gravity. It was found that the rate of grain transport increases with the growth of the acceleration Γ. The dispersion of the velocity of a surface wave in quartz sand was measured and compared to the dispersion of surface waves in water and viscous oil. It was demonstrated that the viscosity coefficient in a granular medium increases with the increase of vibration frequency, whereas it is frequency independent in the aforementioned liquids. It was also found that the value of the dimensionless acceleration Γ increases with the growth of vibration frequency at a constant depth of the granular medium, the surface wavelength increases with the increase in depth at a constant vibration frequency, and the value of the dimensionless acceleration is almost independent of the surface wavelength. The authors explained the discovered phenomenon theoretically.

Q. Cheng and M. L. Qian (China) delivered the lecture “Laser-Interferometric Technique for the Acoustic Pressure in the Spherical Resonant Field.” Pressure at the center of a spherical vessel filled with a liquid and performing resonant spherically symmetric oscillations was measured. These measurements may be important for the investigation of sonoluminescence arising in the process of ultrasonic cavitation. The study is especially important in the case of the collapse of a single cavitation bubble. A laser interferometric technique was used to measure the pressure without violating the field pattern. The technique was based on the observation of the refraction index of light in a liquid within the region of varying pressure. Measurements and calculations were conducted. The numerical and experimental data were compared with the experimental results obtained by

1063-7710/01/4704-0499$21.00 © 2001 MAIK “Nauka/Interperiodica”

using a miniature hydrophone made on the basis of a piezoelectric film.

The paper "Study of the Characters of Acoustic Fields Radiated by a Bifrequency Focused Ultrasonic Transducer" by H. Shi and Z. Shang (China) presented the results of theoretical and experimental studies of an acoustic field in water that was generated by a radiator operating at two frequencies simultaneously and provided the focusing of sound waves. The calculations were performed under the assumption that the electromechanical coupling within the radiator is absent; i.e., the radiation and focusing of sound fields at two frequencies is performed as if by two identical independent transducers positioned in the same region of the liquid and operating at different frequencies. The calculations and experiments were conducted for the frequencies 400 and 800 kHz in water. A good agreement of theoretical and experimental results was observed. For example, the calculated value of the position of the focal region was $z = 4.2$ cm, and the experimental one was $z = 4.4$ cm. The diameter of the focal region was 0.61 cm. The spectrum of the sound field in the focal region was studied. As should be expected, the components of the combination frequencies caused by the nonlinear interaction of sound waves at basic frequencies were observed along with oscillations at two basic frequencies 400 and 800 kHz. The importance of investigating the acoustic field in the case of simultaneous focusing of sound waves at two frequencies was stressed. The reason for this is the fact that the efficiency of two-frequency ultrasonic cavitation is 2–5 times higher than the cavitation efficiency in the case of a single frequency. This fact is important for medical applications including the problems of the control of malignant growths and their destruction.

H. D. Liang, M. Halliwell, and P. N. T. Wells (Great Britain) presented a paper "Continuous-Wave Ultrasonic Tomography in Nondestructive Testing." The paper describes a technique for nondestructive testing of defects in rotating parts of machines in the case of the excitation of ultrasonic vibrations in them by probing signals of large duration. Such signals can be treated as continuous tone signals. It was noted that the scattering of an ultrasonic wave by the defects located in various parts of a tested object is accompanied by different Doppler frequency shifts, and this effect serves as the distinguishing feature. It is possible to plot the pattern of the distribution of defect locations according to the trajectories of the frequency shifts of ultrasonic signals, and, from the scattered signal amplitude, one can judge the defect size.

A paper by X. Liu, Z. Liu, and C. Li (China) "The Application of Solitons in the Ultrasonic Testing Signal Processing" shows the possibility of using a soliton as a testing signal in ultrasonic nondestructive testing. It is noted that, in the case of ultrasonic testing of parts made of coarse-grained materials, difficulties arise because of the very small signal-to-noise ratio, which is governed by the high noise level due to the scattering of the testing signal by the structural inhomogeneities of the material. It is demonstrated that the application of a soliton as a testing signal leads to the increase of the signal-to-noise ratio and to a considerable decrease in the noise influence. This provides an opportunity to increase the efficiency of the flaw detection. The increase in the signal-to-noise ratio is connected with the specific features of the soliton propagation in a granular medium. Results of numerical simulations and experiments are presented.

In his paper "Time-Varying Diffraction Tomography: A New Form of Acoustic Imaging," W. S. Gan (Singapore) developed a theory for a new type of ultrasonic tomography in nondestructive testing. A soliton is used as a probing signal. The soliton signal has an advantage over the commonly used signals, since a soliton propagates to relatively longer distances without distortions. The theory is based on the solution of a nonlinear Schrödinger equation. The time variability of the function describing the probing signal is taken into account. The solution of the inverse problem is performed using the reconstruction algorithm based on the solution of the Marchenko equation. It is possible to obtain an exact solution describing the reconstructed wave field. In this case, it is also possible to reconstruct the wave field arising in the presence of a time-varying object in the medium. The theory describes the processes in four dimensions (space–time scales). The developed theoretical approach is realized in the experiments on monitoring the work of a human heart. A method for obtaining a solitonlike probing signal with the help of an array of ultrasonic transducers was discussed.

Three papers presented the results of the application of the wavelet analysis to signal processing in ultrasonic nondestructive testing. A paper "Wavelet-Transform Analysis of Ultrasonic Guided Waves in Pipes with Defects" by D. Ta, Y. Liang, and Z. Liu (China) can be an example. Pipes are the main element of structures and devices used in oil, chemical, and other industries. Flaw detection in pipes is a very important issue. Two waves (modes) can propagate in a pipe at moderate frequencies. The signals propagating in a pipe by different modes have different group velocities. The signals reflected by defects are nonstationary and can propagate with different group velocities. The application of the wavelet analysis provides an opportunity to analyze the nonstationary signals reflected by the defects and to determine the defect positions.

Several papers considered various problems of laser ultrasonics and optoacoustics. In the paper "Laser and

Particle Beam Ultrasonics" by L. M. Lyamshev (Russia), the generation of ultrasound in condensed media by harmonically modulated or pulsed laser and penetrating radiation, i.e., beams of particles (electrons, protons, heavy ions, and synchrotron radiation), and also by single high-energy particles, was considered. The basic laws governing the formation of acoustic signals and directivity patterns of acoustic sources excited by laser radiation and particle beams were discussed. The influence of the particular features of radiation absorption in a medium on the characteristics of acoustic signals and on the formation of sound sources was considered. Laser optoacoustic diagnostics of the radiation structure of an unstable cavity laser was discussed. A possibility of the detection of dark matter particles with the help of space-borne acoustic sensors was considered. The dark matter constitutes up to 90% of the substance in the Universe, but it is still "invisible" to researchers. There is only a so-called circumstantial evidence of its existence.

A paper by M. Somekh, M. Clark, and S. D. Sharples (Great Britain) "Laser Ultrasonic Microscopy" discussed a possibility for the development of laser-acoustic microscopy grounded on the laser excitation and focusing of surface acoustic waves. According to the authors, laser-acoustic microscopy using surface waves will provide an opportunity to increase the sensitivity, selectivity, and noise immunity of ultrasonic microscopy. Examples of applications of the suggested laser ultrasonic microscopy technique to the investigation of the structure of various objects were given.

M. Mackenzie (Great Britain) described some important applications of laser pulsed photoacoustics in his paper "Applications of Pulsed Photoacoustics." These applications concern medicine and environmental monitoring. In the first case, a noninvasive optoacoustic technique for blood tests was described. The technique is based on the study of the characteristics of an acoustic signal excited optically in the tissues of a human finger inserted into a special photoacoustic cell. It is possible to determine the glucose content in blood and monitor in real time the dynamics of its variations. The second example concerned the monitoring of hydrocarbons in water.

The paper "Interfacial Acoustic Waves in Gas and Liquid excited by the Surface Transient Grating Method" by H. Bill, E. Ivakin, E. Chernukho, V. Krylovich, A. Rubanov, and A. Sukhodolov (Belarus) presented the results of theoretical and experimental studies of acoustic waves at the solid–gas and solid–liquid interfaces. Acoustic waves were excited by a thermal grating produced by laser radiation in a solid at the interface. Calculations and experiments were conducted for acoustic waves in a gas (from 2 to 6 MHz) and liquids (from 6 to 15 MHz).

A paper by K. Van de Rostyne, C. Glorieux, W. Lauriks, and J. Thoen (Belgium) "Laser Ultrasonics Generated Interface Waves for Soft Matter Investigation" was devoted to a similar problem. Rayleigh and Scholte waves can be excited by laser radiation at the solid–gas and solid–liquid interfaces. Rayleigh waves propagate mainly in a solid, while Scholte waves propagate in a liquid. If the parameters of a liquid and a solid are close to each other, the characteristics of the Scholte waves become sensitive to the changes in the parameters of the media, as do the Rayleigh waves in a solid. The surface waves were excited by laser pulses. The major attention was given to the study of acoustic waves and the media parameters in the case when surface acoustic waves were excited at the interface between a liquid and a "soft" solid.

Two papers on medical acoustics should be mentioned. A paper by T. Li (Japan) "Theoretical Modeling and Error Analysis of Measurement of the Artery Elasticity" presented a theory of propagation of acoustic oscillations in a tube simulating an artery. The propagation velocity of oscillations in a tube was studied as a function of the pressure inside the tube, its diameter, wall thickness, and the elasticity modulus of the tube material. The purpose of the study was to estimate when one should expect changes in the artery (tube) parameters in the case of atherosclerosis, when the thickness of artery walls and the value of arterial pressure change depending on the stage of the illness (atherosclerosis).

W. T. Shi, F. Forsberg, J. B. Liu, and B. B. Goldberg (USA) presented the paper "Nonlinear Imaging Using Subharmonic Signals from Microbubble Contrast Agents." According to the authors, a new method for ultrasonic imaging of objects is suggested. Its basis is the utilization of microbubbles introduced into an object, testing of the object with bubbles by a two-frequency ultrasonic signal, and the detection of the subharmonic signal arising due to the nonlinear scattering of ultrasonic waves by a resonant bubble. Multiple experiments were conducted, including experiments on dogs. The experiments demonstrated high efficiency of the new method of ultrasonic imaging. This fact is determined in particular by the high signal-to-noise ratio. It was noted that the suggested method can be effective for monitoring small-volume flows of blood in deep biological tissues.

A paper by Y. Yan, D. Zhang, and X. Gong (China) "Acoustic Nonlinear Parameter Tomography of Biological Tissues in the Reflection Mode" described the technique of nonlinear acoustic tomography using a reflected mode or reflected waves, which was suggested by the authors. The acoustic nonlinear parametric tomography was described in the literature for the first time in 1980. It involved the observation of changes of the nonlinear parameter of a medium (a biological tissue) in the transmission mode, i.e., in an acoustic wave of finite amplitude transmitted through an object. The authors of this paper considered the possibility of developing the nonlinear parameter tomography of a biological tissue using a reflected finite-amplitude wave. They also took into account the fact that a biological tissue is a layered medium. The results of a theoretical analysis and experiments using samples of biological tissues (pig liver, tongue, and adipose tissues) were presented.

The workshop was well organized. Excursions around some places of interest in Nanjing were offered. The participants appreciated greatly the efforts undertaken by the organizers and, first of all, by Prof. Shu-Yi Zhang, the cochairperson of the workshop and Director of the Institute of Acoustics of Nanjing University.

L. M. Lyamshev

Translated by M. Lyamshev